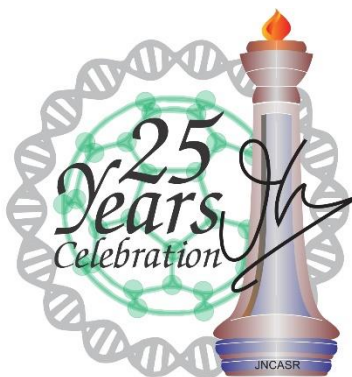

Design, synthesis, *in vitro* and *in vivo* studies of therapeutic and diagnostic agents for Alzheimer's disease

A Thesis Submitted for the Degree of

Doctor of Philosophy

By

Sourav Samanta



Bioorganic Chemistry Laboratory, New Chemistry Unit

Jawaharlal Nehru Centre for Advanced Scientific Research

(A Deemed University)

Bengaluru-560064, India

November 2020

Dedicated to my Parents



TABLE OF CONTENTS

| | |
|---|-----------|
| Certificate | i |
| Declaration | iii |
| Acknowledgements | v |
| Preface | ix |
| | |
| <i>Chapter 1: Introduction</i> | 1 |
| 1.1 APP and A β | 4 |
| 1.2 Amyloidogenesis | 6 |
| 1.3 Multifaceted amyloid toxicity | 8 |
| 1.4 Biomarkers and Diagnosis | 11 |
| 1.5 AD phenotype mouse model (APP/PS1) | 13 |
| 1.6 Multifunctional Therapeutic strategy | 14 |
| 1.7 Objective | 21 |
| 1.8 References | 22 |
| | |
| <i>Chapter 2: Small molecule inhibits metal-dependent and independent multifaceted toxicity of Alzheimer's disease</i> | 33 |
| | |
| 2.1 Design strategy of natural tripeptide-inspired small molecule MFM | 38 |
| 2.2 Synthesis of compounds 1-4 | 40 |
| 2.3 Chelation of redox-active metal ions | 41 |
| 2.4 Metal-dependent antioxidant assay | 46 |
| 2.5 Metal-independent antioxidant assay | 50 |
| 2.6 Modulation of Nrf2 signaling under oxidative stress conditions | 54 |
| 2.7 Inhibition of amyloid aggregation | 55 |
| 2.8 Molecular-Level Interaction of 4 with A β 42 | 61 |
| 2.9 Impairment of neuroinflammation and mitochondrial dysfunction | 62 |



| | |
|---------------------------|----|
| 2.10 Conclusion | 64 |
| 2.11 Experimental methods | 67 |
| 2.12 Appendix | 81 |
| 2.13 References | 91 |

| | |
|--|----|
| <i>Chapter 3: Small molecule with naphthalene monoimide scaffold ameliorates amyloid burden and cognitive decline in a mouse model of Alzheimer's disease</i> | 97 |
|--|----|

| | |
|--|-----|
| 3.1. Design and synthesis of small molecules with naphthalene monoimide scaffold | 101 |
| 3.2 <i>In vitro</i> modulation of amyloid aggregation and probable mechanism | 102 |
| 3.3 Inhibition of A β aggregation and associated toxicity: microscopy and dot blot analysis | 111 |
| 3.4 Pharmacokinetics study of TGR63 | 117 |
| 3.5 <i>In vivo</i> amelioration of amyloid burden | 121 |
| 3.6 Recovery of cognitive functions | 126 |
| 3.7 Discussion | 132 |
| 3.8. Limitation | 138 |
| 3.9. Experimental methods | 138 |
| 3.10. Appendix | 151 |
| 3.11. References | 172 |

| | |
|--|-----|
| <i>Chapter 4. Fluorescent tripeptide to probe Cu^{II}-induced amyloid toxicity in Alzheimer's disease</i> | 177 |
| 4.1 Design strategy | 180 |
| 4.2 Synthesis of NTP | 182 |
| 4.3 Cu ^{II} chelation by NTP | 184 |
| 4.4 The selectivity of NTP towards Cu ^{II} | 187 |
| 4.5 Structural assessment of amyloid species | 188 |



| | |
|--|-----|
| 4.6 Sequestration of Cu ^{II} from A β aggregation species | 189 |
| 4.7 Conclusion | 192 |
| 4.8 Experimental methods | 192 |
| 4.9 Appendix | 198 |
| 4.10 References | 200 |

| | |
|--|-----|
| <i>Chapter 5: Unambiguous detection of elevated levels of HOCl and its proximal localization with Aβ plaques in double transgenic AD mouse brain</i> | 205 |
| 5.1 Design and synthesis of CM probes | 208 |
| 5.2 Regioselective oxidation of CM2 and HOCl detection | 211 |
| 5.3 Specific detection of HOCl over other ROS | 212 |
| 5.4 Detection of HOCl in SHSY5Y cells using CM2 | 213 |
| 5.5 Detection, imaging, and quantification of HOCl in APP/PS1 mouse model | 219 |
| 5.6 Conclusion | 223 |
| 5.7 Experimental methods | 223 |
| 5.8 Appendix | 231 |
| 5.9 Reference | 241 |
| <i>List of publications</i> | 245 |



CERTIFICATE

I hereby certify that the work described in this thesis entitled “**Design, synthesis, *in vitro* and *in vivo* studies of therapeutic and diagnostic agents for Alzheimer’s disease**” has been carried out by **Mr. Sourav Samanta** under my supervision at the Bioorganic Chemistry Laboratory, New Chemistry Unit, Jawaharlal Nehru Centre for Advanced Scientific Research, Bengaluru, India and that it has not been submitted elsewhere for the award of any degree or diploma.



Prof. T. Govindaraju
(Research Guide)

DECLARATION

I hereby declare that the matter embodied in the thesis entitled “**Design, synthesis, *in vitro* and *in vivo* studies of therapeutic and diagnostic agents for Alzheimer’s disease**” is the resultant of the investigations carried out by me at the Bioorganic Chemistry Laboratory, New Chemistry Unit, Jawaharlal Nehru Centre for Advanced Scientific Research, Bengaluru, India under the supervision of **Prof. T. Govindaraju** and that it has not been submitted elsewhere for the award of any degree or diploma.

In keeping with the general practice in reporting the scientific observations, due acknowledgment has been made whenever the work described is based on the findings of other investigators. Any omission that might have occurred due to oversight or error in judgment is regretted.

Sourav Samanta

Sourav Samanta

(PhD Student)



ACKNOWLEDGEMENTS

First and foremost, I would like to express my sincere gratitude to my research supervisor Prof. T. Govindaraju, Bioorganic Chemistry Laboratory, New Chemistry Unit, JNCASR, for his continuous support, motivation, infinite patience, and guidance throughout my PhD tenure. It has been a great privilege and honor to be associated with him.

I would like to thank Bharat Ratna Prof. C. N. R. Rao, FRS, for being the source of inspiration, generous support, and encouragement throughout my stay in JNCASR. I also thank him for providing the infrastructure and facilities to carry out my research work.

I would like to thank the present and past Chairs, New Chemistry Unit, for providing excellent facilities to carry out my research work.

I would like to thank my collaborators Dr. James Chelliah and Dr. Arul Murugan, for their constant support and fruitful scientific discussions.

I would like to thank Dr. Sridhar Rajaram, Dr. Sebastian C. Peter, Prof. R. Varadarajan (IISc, India), and Dr. H. K. Gowda (Karnataka Veterinary, Animal and Fisheries University, Karnataka) for helping me in various experiments and fruitful scientific discussions.

I would like to thank Prof. A. Anand, Dr. R. G. Prakash, and the JNCASR animal facility for helping us in maintaining Alzheimer's mouse model and executing the in vivo work.

I am thankful to my wonderful lab mates Dr. Debabrata, Dr. Avinash, Dr. Pandeewar, Dr. Shivaprasad, Dr. Nagarjun, Dr. Rajasekhar, Dr. Suseela, Mr. Debasis, Mr. Sumon, Mr. Biswanath, Mr. Satyajit, Mr. Harshit, Mr. Madhu, Dr. Madhu, Dr. Chandrasekhar, Dr. Abhaya, Dr. Pardasaradhi, Dr. Shadab, Dr. Bappaditya, Dr. Mahesh, Dr. Sangita, Dr. Balachandra, Mr. Vardhaman, Mr. Ashish, Mr. Hariharan, Ms. Dikshaa, Dr. Lakshmi, Dr. Mouli, Dr. Tanmay, Mr. Sai Gautham, Mr. Pradhresh for their help and friendly environment in the lab.



I am thankful to Prof. Hemalatha Balaram, Prof. Chandrabhas Narayana, Dr. Sridhar Rajaram, Dr. Tapas. K. Maji, Dr. Jayanta Haldar, Dr. James Chelliah, Dr. Sheeba Vasu, and Dr. Sebastian C. Peter, Dr. Sarit S. Agasti for their valuable courses.

I would like to thank all my friends for their love and support throughout my stay at JNCASR.

I would like to thank the wardens (Dr. Tapas. K. Maji, Dr. Ranjani Viswanatha, Dr. Jayanta Haldar, and Dr. Sheeba Vasu) and all the student representative (2019-20) group for helping and supporting me during my student representative period.

I would like to thank Academics, Administration and NCU Office staff for their constant help.

I would like to express my sincere thanks to the Chemistry department of the Indian Institute of Technology, Guwahati, to inspire me in Science.

It is indeed a great pleasure to express my sincere thanks to the Bangabasi College, Kolkata, for the most memorable moments of life.

I thank JNCASR Library, Comp Lab, Hostel, Security, and Health Center to provide and maintain the various facilities that have helped me immensely.

Finally, and most importantly, I am grateful to my family, especially my parents (Dilip Samanta and Chhanda Samanta) and sisters (Tota and Munna), for their love, moral support, and constant encouragement throughout my life. Their love, blessings, and affection made me what I am today. This thesis is dedicated to my parents for their love and support.

PREFACE

This Ph.D thesis is divided into five chapters. The overall objective of the research is to develop and validate (*in vitro*, *ex vivo*, and *in vivo*) novel therapeutic and diagnostic tools for multifaceted amyloid toxicity in Alzheimer's disease (AD). In brief, chapter 1 provides a comprehensive outlook on the multifactorial nature of AD. The production, misfolding, and aggregation of amyloid beta (A β) peptides, one of the major contributors to multifaceted toxicity of AD, is comprehensively described. The current status of available biomarkers and the importance of multiplexing in AD diagnosis, and suitability of APP/PS1 mice model with AD phenotype for the study of AD are discussed. Recent developments on multifunctional therapeutic molecules to modulate A β -induced multifaceted toxicity are presented.

Chapter 2 presents small molecule-based multifunctional modulators of multifaceted A β toxicity. Synthesis of four small molecule analogs (**1-4**) of natural tripeptide GHK of human origin is described. Compound **1-4** were found to complex and ameliorated Cu and Fe mediated multifaceted A β toxicity in contrast to parent tripeptide (GHK), which can only modulate Cu-dependent toxicity. *In vitro* studies have revealed that compound **4** effectively modulate metal-dependent and -independent A β aggregation, reactive oxygen species (ROS), and oxidative stress to rescue neuronal cells. The antioxidant property of compound **4** was evaluated through nuclear factor erythroid 2-related factor 2 (*Nrf2*) protein signaling, which is a hallmark of oxidative stress in cells. Compound **4** showed excellent anti-inflammatory activity and effectively ameliorated lipopolysaccharide (LPS) induced inflammation in cultured microglial cells (BV2). Compound **4** was found to rescue PC12 cells from oxidative stress by preventing mitochondrial dysfunction and DNA damage.

In chapter 3, detailed *in vitro*, *in silico*, *ex vivo*, and *in vivo* evaluation of synthetic naphthalene monoamide derivatives (TGR60-65) to identify a potent anti-AD drug candidate are described. The *in vitro*, *in silico*, and *in cellulo* studies have revealed that TGR63 is the most potent candidate to ameliorate amyloid induced neurotoxicity in PC12 and SHSY5Y cell lines. TGR63 modulate A β aggregation species (oligomers and fibrils) by disrupting non-covalent interactions such as intermolecular hydrogen bonding and salt bridges among the A β peptides. The inhibition of plasma membrane toxicity of A β aggregation species by TGR63 is demonstrated in SHSY5Y cells. The working modalities of the APP/PS1 AD mice model to evaluate the *in vivo* efficacy of TGR63 as an anti-AD therapeutic candidate is described. The pharmacokinetics studies revealed serum stability, BBB permeability, and biocompatibility of TGR63, which proved the suitability of TGR63 for long-term *in vivo* treatment. TGR63 treatment showed a significant reduction of amyloid burden (cortical and hippocampal) in the progressive stages of APP/PS1 AD mice brain. Various behavioral



tests revealed that the reduction in amyloid burden resulted in a promising reversal of learning deficiency, memory impairment, behavioral debility, cognitive decline, and neuropsychiatric symptoms.

Chapter 4 deals with the study of Cu^{II}-induced amyloid toxicity. The design, synthesis, characterization, and evaluation of a novel peptide-based fluorescent probe (NTP) for the selective chelation of Cu^{II} are discussed. NTP effectively sequesters Cu^{II} from Cu^{II}-induced A β species (oligomers and fibrils). The sequestration of Cu^{II} from Cu^{II}-induced A β fibrils is found to be significantly facile compared to Cu^{II}-induced A β oligomers under similar conditions. The kinetics of Cu^{II} sequestration revealed important insights into the mechanism of metal chelation-based antioxidant molecules and provided basic understanding for the design of antioxidant-based multifunctional inhibitors to target multifaceted amyloid toxicity.

In chapter 5, identification and validation of novel AD biomarker for multiplexed AD diagnosis has been discussed. The production and proximal localization of excess hypochlorous acid (HOCl) with amyloid plaques in the AD brain are identified and validated to serve as a reliable biomarker for progressive AD pathogenesis. The design, synthesis, characterization, and evaluation of coumarin-morpholine (CM) based fluorescence probe for the specific detection, imaging, and quantification of HOCl, and its proximal localization with amyloid plaques is described. The nonfluorescent thioamide probe CM2 undergoes regioselective transformation to fluorescent amide probe CM1 in the presence of HOCl under *in vitro*, *ex vivo*, and *in vivo* conditions. The excellent cellular uptake and BBB crossing ability of CM2 allowed facile and differential detection, imaging, and quantification of HOCl in the cellular milieu as well as in the mouse brain (WT and AD). The *in vivo* study revealed elevated levels of HOCl proximally localized with A β plaques in the AD brain and a potential biomarker to expand the list of definite biomarkers for the multiplexed diagnosis of AD.

In summary, the proposed thesis presents current developments in AD diagnosis and therapeutic strategies, *in vivo* study model, and objectives of the work in the introduction chapter. The second chapter describes natural tripeptide inspired small molecule multifunctional therapeutic agents to ameliorate multifaceted A β toxicity. The third chapter deals with a detailed evaluation of the therapeutic efficacy of a synthetic molecule in a double transgenic AD mice model. The fourth and fifth chapters present our understanding of metal-induced amyloid toxicity during AD pathogenesis, which helped us to establish novel biomarkers for multiplexed AD diagnosis and to develop effective antioxidant-based multifunctional therapeutic agents.



Chapter 1

Introduction

Peptides and proteins are the most abundant biomacromolecules in living organisms. They are the real workhorses and perform all the functions of cells, including cell growth, division, differentiation, transformation, enzyme, transport, structure, hormones, defence, contractile, storage survival, and death.¹⁻³ The term 'protein' was originated from the Greek word '*protos*' that implies the first element. In the cellular process, the proteins are synthesized by the linear polymerization of amino acids on ribosomal RNA using mRNA template codons. The nascent polypeptides/proteins undergo various post-translational modifications to adopt functional three-dimensional conformations.⁴⁻⁶ An appropriately folded protein is functionally active and maintains healthy physiological conditions.^{7,8} The conformational transition to achieve native state is known as on-pathway protein folding. Nevertheless, peptides or proteins can adopt various non-native conformations *via* off-pathway folding, commonly referred to as protein misfolding.^{6,9,10} The misfolded proteins often appear as aberrantly exposed with hydrophobic regions that drive protein aggregation. The misfolding and corresponding aggregation of proteins leads to various disease conditions.^{6,9,11,12} In particular, protein aggregation is associated with several neurodegenerative diseases such as Alzheimer's disease (AD), Parkinson's disease (PD), and Huntington's diseases (HD), among others.¹³⁻¹⁸ The aggregation-prone amyloid- β (A β) peptides and hyperphosphorylated tau protein (p-tau) are the major pathological factors of AD.^{13,17,19-22} In PD, the felon protein is α -synuclein, which aggregate to form Lewy body in the dopaminergic neurons of substantia nigra.²³ The aggregation of polyglutamine-containing huntingtin protein is responsible for HD.²⁴

AD was first identified by a German physician Alois Alzheimer (1906).²⁵ It is the most prevalent form of neurodegeneration, contributing to 70-80% of all dementia cases.²⁶ Aging

is identified as one of the leading risk factors of AD, although family heredity and genetic mutations have a significant role in AD development.^{27,28} Irrespective of the causes (genetic or environment), all AD positive individuals suffer from common symptoms like short-term memory (STM) impairment at the early onset of AD and progressively lose their thinking, decision making, problem-solving ability, and communication aptitude.²⁹⁻³¹ Other symptoms include aggression, irritability, confusion, mood swings, behavioral changes, language problems, and long-term potential (LTP) impairment. In advanced stages, the AD patients have experienced severe neuronal degeneration, nervous system collapse, and multi-organ failure, ultimately leading to death.²⁹ Currently, around 50 million people are affected by AD, while this number is expected to reach more than 130 million by 2050.¹⁹ Recent statistics showed that AD has contributed to 146% rise in deaths between 2000 and 2018 compared to a considerable decline in the number of deaths caused by other disease conditions such as heart disease, stroke, AIDS, prostate, and breast cancer.³⁰ The rapid rise of AD cases and associated death is attributed to the complex disease etiology and lack of reliable diagnosis and effective treatments.

1.1 APP and A β

The production, misfolding, aggregation, and accumulation of A β peptides in the brain are considered as the major pathological hallmarks of AD.^{11,21,32,33} Monomeric A β peptides are produced from amyloid precursor protein (APP) present in various cell types of our body, including neuronal cells in the CNS.³⁴ APP is a member of the amyloid precursor-like proteins (APLP1 and APLP2) family in mammals.²⁵ This class of proteins is considered as single-pass transmembrane proteins with the larger extracellular domain involved in various physiological

functions, including transport through the cell membrane, cell survival, neuronal growth, motility, neurite outgrowth, and neuronal development.³⁵ The APP transcript produces eight different protein isoforms, of which three are most commonly observed. APP isoform containing 695 amino acids is the most abundant in the CNS, and the other two (751 and 770 amino acids) isoforms are

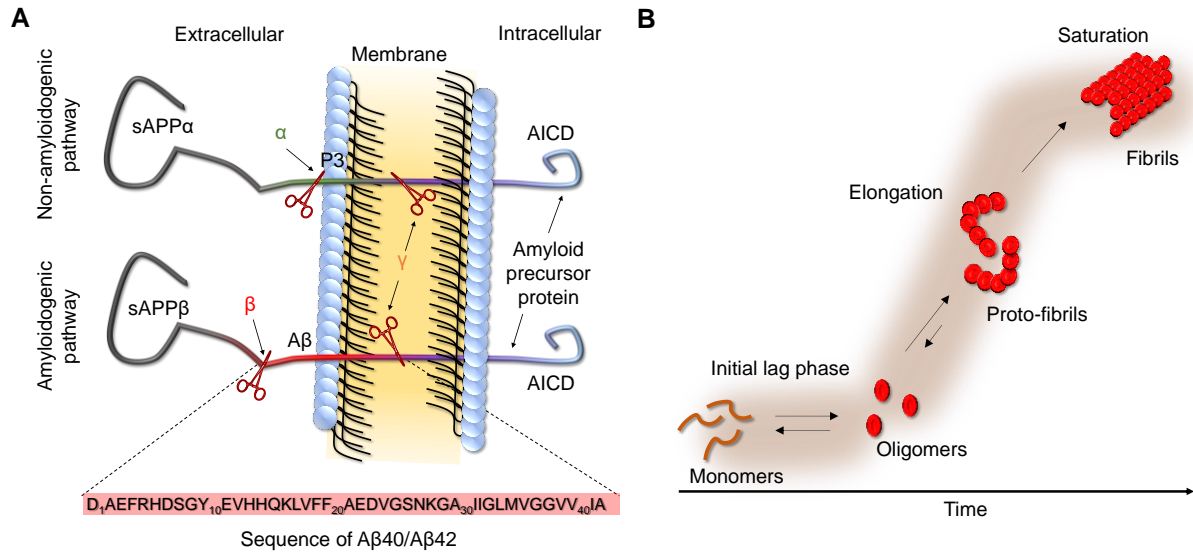


Figure 1. (A) Proteolytic processing of APP. In the non-amyloidogenic pathway, α - and γ -secretase act on APP and produce sAPP α , P3, and intracellular C-terminal fragments (AICD). In the amyloidogenic pathway, β - and γ -secretase act on APP and produce sAPP β , A β , and AICD. The amino acid sequence of A β 40/A β 42 is shown. (B) Typical aggregation kinetics of A β to form soluble and insoluble aggregation species.

expressed more ubiquitously in the body. The neuronal APP undergoes proteolytic degradation through multiple alternate pathways. One of the pathways (amyloidogenic) leads to the generation of pathogenic A β peptides, while other pathways (non-amyloidogenic) generate nontoxic peptides (Figure 1A).⁸ Two proteolytic enzymes, namely β -secretase (BACE1: β -site APP-cleaving enzyme 1) and γ -secretase, are involved in the amyloidogenic processing of APP. At first, β -secretase cleaves APP to produce sAPP β and β C-terminal fragment (β -CTF), followed by the successive

cleavage of the membrane-bound domain by γ -secretase to produce $A\beta$ peptides (37-43 amino acids) and amyloid precursor protein intracellular domain (AICD). Under the non-amyloidogenic pathway, α -secretase cleaves APP into APPs α and α -CTF fragments, and successive cleavage of the membrane-bound domain (α -CTF) by γ -secretase generate soluble P3 peptide and AICD.^{6,8,19} Among the $A\beta$ peptides, 42 amino acids containing peptide ($A\beta$ 42) is the most aggregation-prone peptide and a leading contributor to multifaceted AD toxicity (Figure 1A).

1.2 Amyloidogenesis

The presence of $A\beta$ peptides in human brain throughout the lifespan, revealing its importance in healthy brain functioning by associating with various critical physiological processes.⁷ Experimentally, it is demonstrated that $A\beta$ acts as an antimicrobial peptide, a class of immune (innate) peptides with broad-spectrum antimicrobial activity. The available literature reveals that $A\beta$ has putative functions in repairing the blood-brain barrier, regulating synaptic function, and promoting recovery from the injury besides protecting the brain from external infections.²⁵ $A\beta$ peptides misfolded into ordered secondary (β -sheet) structures through self-aggregation to form toxic polymorphic $A\beta$ species (oligomers, protofibrils, and fibrils) in the brain (Figure 1B).³⁶ $A\beta$ 40 is the most common form of $A\beta$ peptides and contributes to about 80% of total $A\beta$ in the healthy human brain.^{5,21} Under pathological conditions, $A\beta$ 42 is produced in excess and predominantly accumulate as insoluble $A\beta$ plaques due to its self-aggregating nature.

The $A\beta$ aggregation follows typical kinetics with an initial lag phase, aggregation elongation phase, and saturation phase or mature fibrils formation (Figure 1B).³⁷ The native $A\beta$ peptides can also form stable soluble oligomeric species, which are the most toxic form of $A\beta$ aggregates.³⁸ The formation of soluble oligomers promotes the stepwise formation of protofibrils and fibrils that

suggests the nucleation growth mechanism in the elongation phase. The aggregation process is mostly governed by the noncovalent interactions to form paranucleus and subsequently converting into higher-order aggregates, namely protofibrils.⁸ The protofibrils are further interacting among themselves in the elongation phase to form fully grown A β fibrils.³⁹ Oligomers act as nucleation

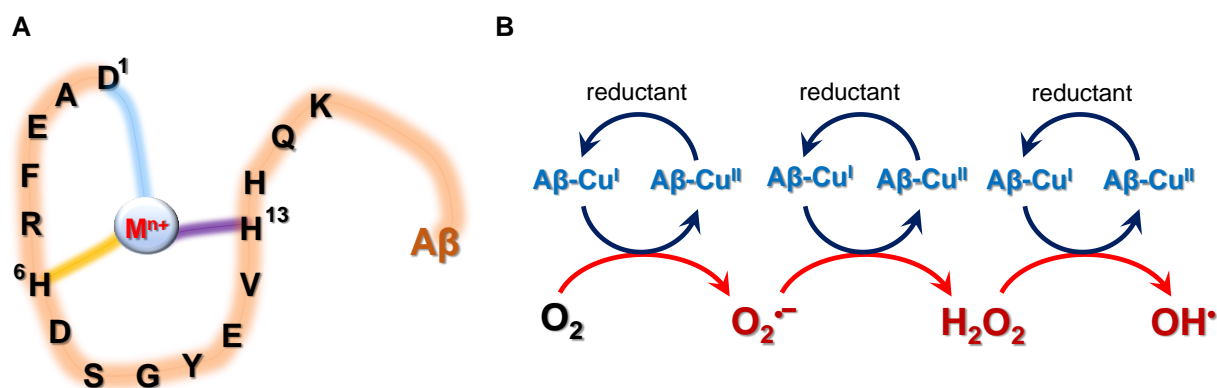


Figure 2. (A) The amino acid sequence of A β ₁₋₁₆, which is mostly responsible for metal-A β inclusion complex formation. (B) Typical redox cycle of A β -Cu complexes in the presence of reducing agents and oxygen and one of the main causative factors of oxidative stress and inflammation in the AD brain.

centers to form higher-order aggregates in the AD brain. The pathogenic A β ₄₂ (D₁AEFRH₆DSGYEVH₁₃H₁₄QKLVFFAEDVGSNKGAIIGLMVGGVVIA₄₂) binds to biological metals (Cu, Zn, and Fe) and elevates their levels in the AD brain, which was confirmed by the post-mortem study of the AD brain (Figure 2).⁴⁰⁻⁴⁵ The unstructured N-terminal fragment is mainly involved in metal ion chelation and experimental evidence demonstrated the importance of histidine (His-6, His-13, and His-14), tyrosine (Tyr-10), and aspartic acid (Asp-1) in metal chelation and promoting metal-dependent A β aggregation.⁴¹ As a result, studies have revealed that metal ions accelerate the A β aggregation and stabilize the toxic oligomeric species.⁴¹ The redox-active metal ions (Cu^{II} and Fe^{III}) bound A β species act as depots and anticipated to continuously produce reactive oxygen

species (ROS).⁴⁶⁻⁴⁸ This is speculated as one of the leading causes of oxidative stress and inflammation in the brain that contributes to the multifactorial toxicity in AD (Figure 3).^{49,50}

1.3 Multifaceted Amyloid Toxicity

Numerous studies employing multidisciplinary approaches have demonstrated the multifactorial nature of AD, where multifaceted toxicity associated with A β plays a central role in the disease onset and progression.^{19,20} Nerve cells are involved in acquiring, storing, and retrieving information (memory) through the synapse, allowing neurons to pass chemical or electrical signals to the target cell.⁵¹⁻⁵⁴ A β aggregation species under pathological conditions impair the synaptic function and damage the neuronal circuits in the CNS. The A β oligomers are shown to damage the neural synapse by blocking the essential synaptic receptors at the synaptic cleft, while the mechanism of synaptic disruption by A β is not completely understood. Experimental studies have demonstrated that A β oligomers bind and block the essential glutamate receptors such as N-methyl-D-aspartate (NMDA) and α -amino-3-hydroxy-5-methyl-4-isoxazolepropionic acid (AMPA), leading to the impairment in synaptic plasticity, learning, memory formation, and cognition.⁵³ The α 7- nicotinic receptors are also affected by the soluble A β oligomers and trigger the cognitive deficits and AD development. Thus, substantial improvement of neuronal synaptic function and receptors activity can be achieved by eliminating or reducing the A β burden in the AD brain. The plasma membrane separates and protects the interior part of the cells from the extracellular matrix. The neuronal plasma membrane maintains the balance between intracellular and extracellular metal ions (Na⁺, K⁺, and Ca^{II}) concentrations, which is essential for the axonal potential and signal transformation.^{41,42} The A β aggregation species interact with the neuronal plasma membrane and create pores causing uncontrolled flow of ions through the membrane. In

particular, the influx of excess Ca^{II} into the neurons leads to neuronal degeneration.¹⁹ The mechanism of the pore formation by $\text{A}\beta$ in the neuronal membrane is similar to the action of antimicrobial peptides (AMPs). $\text{A}\beta$ species also interact with the mitochondrial membrane to form mitochondrial permeability transition pore (mPTP), resulting in mitochondrial dysfunction. The

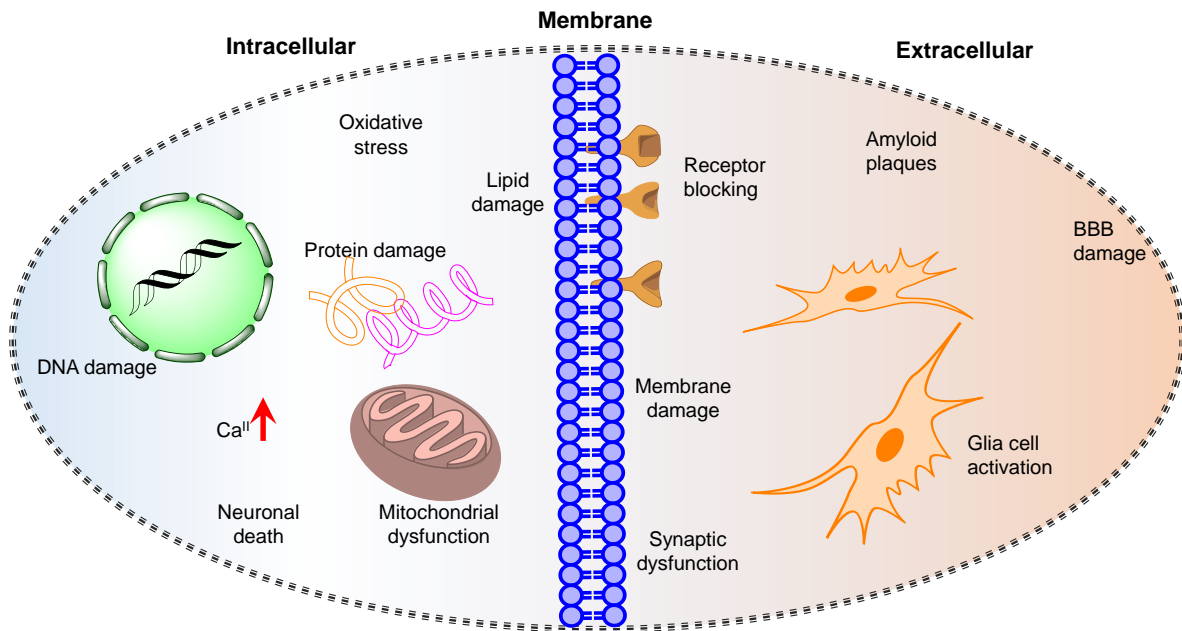


Figure 3. The amyloid burden is one of the leading causes of the multifaceted toxicity of AD. The list of various intracellular (neuron) and extracellular (brain matrix) toxicities that are associated with amyloid burden in the AD brain.

damaged mitochondria contribute to the impairment in ATP production, ROS balance, mitochondrial biogenesis, and neuronal functions. Further, $\text{A}\beta$ damages nuclear DNA by blocking telomerase activity.⁵⁵ Telomerase is a ribonucleoprotein enzyme that plays a crucial role during cell division and incorporates the repeated TTAGGG sequence in the telomere regions of DNA strands (3' end).⁵⁶ The blocking of telomerase activity by $\text{A}\beta$ causes shortening of telomere regions related to biological aging and age-related diseases. Thus, reducing the $\text{A}\beta$ burden is believed to improve telomerase activity and a potential therapeutic strategy to treat AD.⁸

The reactive intermediate species (RIS) play a vital role in the immune system and cell signaling cascades in the human body. However, excessive production and accumulation of RIS lead to oxidative stress and inflammation. Elevated levels of RIS in the brain are observed in the pathophysiological conditions of AD.⁵⁷ The redox-active metal-A β complexes produce excess RIS such as superoxide radical ($O_2^{\cdot-}$), hydrogen peroxide (H_2O_2), hydroxyl radicals (HO^{\cdot}), nitric oxide (NO), peroxynitrite ($ONOO^{\cdot}$), and hypochlorous acid (HOCl). A β -Cu^{II} and A β -Fe^{III} undergo a Fenton type reaction in the presence of reducing agents to generate H_2O_2 from molecular oxygen. The oxidative damage of essential biomacromolecules (DNA, lipids, and proteins) under oxidative stress conditions is a significant contributor to neuronal death.⁵⁸ Therefore, targeting the neuronal redox imbalance by reducing the metal-dependent and independent A β aggregation related toxicity employing synthetic and hybrid antioxidant compounds is a promising approach to target AD. Under physiological conditions, the brain immune system (microglia) response towards senile plaques results in microglia migration and activation to clear the toxic plaques.^{8,19} The persistent A β plaques deposition activates the mounted immune system for a prolonged time, and eventually, the adeptness of A β clearance declines. These circumstances accelerate the insoluble plaques deposition and persistent microglial activation in the AD brain that triggers the neurotoxins and pro-inflammatory cytokines release.⁵⁹

The amyloidogenic proteolysis of the most abundant APP isoform (695 amino acids) is the source of amyloid peptides in the CNS. Although A β 40 is the most common form of A β , the AD pathology is mainly governed by A β 42, produced extensively in the AD brain. A β 42 rapidly self-aggregates to form polymorphic species such as oligomers, protofibrils, and senile plaques in the extracellular matrix. The A β aggregation species severely affect the neuronal synapse and synaptic plasticity, causing impairment in the STM and LTP formation and cognitive function.^{58,60} The

clinicopathological studies directly correlate the cognitive decline or sequence of AD pathology with the deposition of widespread A β plaques and associated toxicity (NFTs) in the brain. As a result, the amyloid burden became a potential therapeutic target to ameliorate multifaceted toxicity and cognitive decline in AD.^{8,19,20}

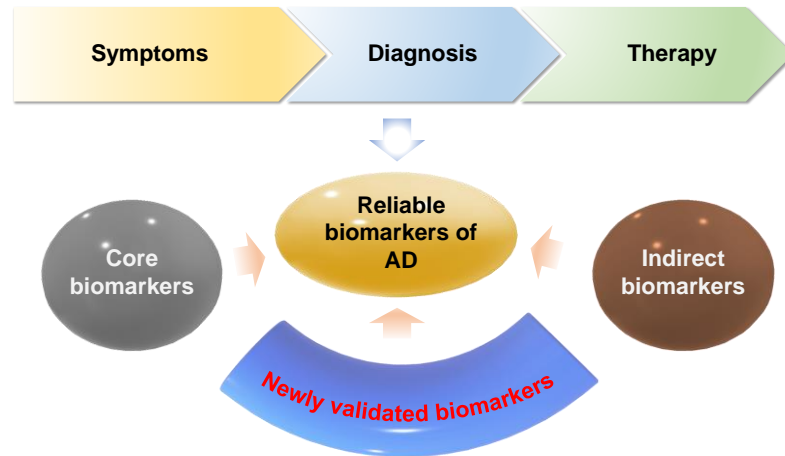


Figure 4. Schematic representation of diagnosis and therapy of AD and the importance of core and indirect biomarkers.

1.4 Biomarkers and Diagnosis

For any disease, including AD, a reliable diagnosis with precision is necessary to ensure timely treatment and management. Currently, the assessment of behavioural and neuropathological symptoms is used as a tool for AD diagnosis. The accuracy of AD diagnosis is determined from the clinical and neuropathological data of the National Alzheimer's Coordinating Center (NACC), collaborating with National Institute on Aging (NIA)-sponsored Alzheimer's Disease Centers (ADCs).^{61,62} The visible neuropathological hallmarks (A β and Tau) correspond to the advanced stage of the disease, and treatment options are limited at this stage. In brief, to assess the progressive cognitive decline Alzheimer's disease assessment scale–cognitive subscale (ADAS-

Cog) was established in the 1980s.⁶³ Eight different AD categories were proposed: prodromal AD, AD dementia, typical AD, atypical AD, mixed AD, preclinical states of AD, Alzheimer's pathology, and mild cognitive impairment (MCI). In prodromal AD stages, the clinical symptoms such as hippocampal-mediated memory loss are observable, which predicts the AD symptomatic patients. Quite a few severe cognitive dysfunctions (abnormalities in daily and social life) are present in AD dementia stages. The typical AD symptom includes progressive memory impairment, which dominates and coexists with other cognitive dysfunctions such as language problems, praxis, and impairments in complex visual processing. These are the most promising clinical symptoms of AD development. The atypical AD is observed with one in around 20 AD patients, they have distinct early symptoms. Similar type of alterations in the brain have caused these symptoms as typical AD. However, the specific changes start in different sections of the AD brain (posterior cortical atrophy) that are causing distinct symptoms compared to typical AD. Mixed AD is a complicated condition in which AD coexists with other diseases like cerebrovascular or Lewy Body diseases. The preclinical stages are further classified into asymptomatic and presymptomatic AD. The asymptomatic stage is a phase between early pathogenic events and the most initial cognitive failure, subsequently AD develops in the presymptomatic stages. Alzheimer's pathology stages demonstrate important neuropathological events such as synaptic dysfunctions and vascular A β deposits, along with cognitive decline. The MCI is a phase between the anticipated and more severe cognitive decline by normal aging and dementia. MCI is mostly characterized by difficulties with language, memory, judgment, and thinking. Clinical diagnosis of AD mainly relies on the described cognitive decline and memory impairments with disease progression. Recent AD research has established that AD is a multifaceted disease that involves multiple biomarkers, and multiplexed imaging is anticipated to

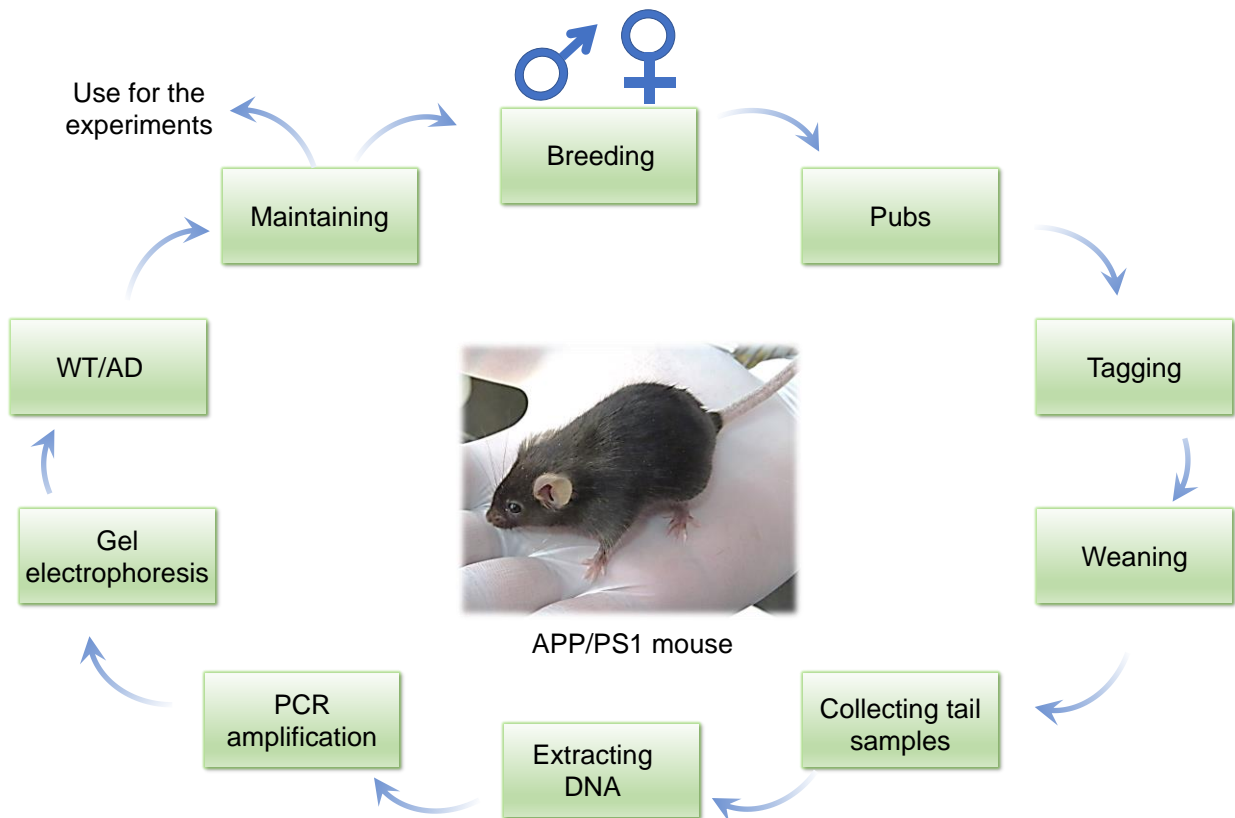


Figure 5. A schematic representation of the maintenance of AD phenotypic mice (APP/PS1) and WT/AD mice preparation for the *in vivo* experiments.

provide an accurate diagnosis (Figure 4).^{27,64-67} The National Institute on Aging and Alzheimer's Association (NIA-AA) Research Framework report (2018) proposed A β , tau, and related neurodegeneration as core biomarkers along with cognitive tests. Interestingly, the NIA-AA Research Framework left the biomarkers list open-ended to allow the addition of new biomarkers as and when identified and validated.⁶⁸ In this context, our work involved the prediction, validation, and establishment of novel biomarkers for AD development that will help in multiplexed and reliable AD diagnosis.⁶⁴

1.5 AD Phenotype Mouse Model (APP/PS1)

The genomic analysis has emphasized the impressive genetic homologies among human and mouse. Therefore, many available inbred mice strains are used as models of several human diseases. These animal models have contributed enormously in understanding the disease pathology and assessing the efficacy of drug candidates in the preclinical stages. The APP/PS1 mouse model (B6C3-Tg (APP^{swe}, PSEN 1dE9)85Dbo/J) is a double transgenic AD phenotype mouse extensively used in AD research.^{69,70} These mice express the mutated (Swedish) human APP transgene 3-fold higher than the murine APP. The Swedish mutation (K595N/M596L) in APP protein elevates A β production in the CNS. The presenilin 1 (PSEN1) contains L166P mutation leading to the formation of a mutated γ -complex, which facilitates the preferential production of A β 42 peptide. As a result, A β plaque deposition is found in the neocortex, thalamus, brainstem, striatum, and hippocampus regions with advancing age. The A β 42 levels in the CSF of these mice decrease to ~50 and 80% by 6 and 18 months of age, respectively.⁷¹ This observation confirms the chronic deposition of A β plaque in the CNS of these mice.⁷² The cortex- and hippocampus- mediated cognitive and memory functions get impaired at the age of ~7 months.⁷³ The APP/PS1 mouse is one of the best *in vivo* models to understand the amyloid burden-mediated AD development and associated multifaceted toxicity.⁶⁹ The APP/PS1 mouse model is obtained from the Jackson Laboratory and bred and maintained in the in-house animal facility for our experiments (Figure 5).

1.6 Multifunctional Therapeutic Strategy

Several therapeutic strategies have been pursued to halt or cure AD progression, albeit most of these efforts met with continuous failures. These unsuccessful attempts and failure of various drug candidates in different stages of clinical trials have confirmed the multifaceted nature of AD

pathology.⁷⁴ The advancements in AD research over the years show that A β aggregation in the brain is the key contributor to this multifaceted toxicity of AD.^{8,19,20} The multifaceted toxicity includes neurotoxic metal accumulation, metal-A β inclusion complex, extensive RIS production, oxidative stress, biomolecule (DNA, lipids, and proteins) damage, mitochondrial dysfunction, neuroinflammation, premature apoptosis, synaptic dysfunctions, memory impairment, neuronal loss, and cell death. Besides, A β plays a critical role in forming and spreading neurofibrillary tangles and Lewy Body (LB) under AD conditions. It was observed that more than 50% of AD patients also exhibit LB dementia. Thus, production, misfolding, aggregation, and parenchymal plaques deposition become one of the potential therapeutic targets for AD.⁷⁵ The production of A β can be suppressed by blocking the APP expression and secretase (β and γ) activity. However, APP is engaged with an assortment of physiological functions such as cellular transport, neurite development, cellular motility, cell growth, and survival. Therefore, the blocking of its expression directly affects basal brain functions. Inhibition of β or γ -secretase is a promising approach pursued to reduce pathogenic A β production. Unfortunately, targeting β or γ -secretase have severely affected their physiological functions causing undesired toxicity. The immunization of AD patients to accelerate the A β plaques clearance significantly triggers the neuroinflammatory response by activating the immune cells. Therefore, modulation of A β misfolding, aggregation and associated neuronal toxicity using small molecules and peptidomimetics became a promising therapeutic strategy to cure or halt the AD progression. In recent years, multifunctional drug candidates are being developed to ameliorate amyloid-induced AD toxicity.⁷⁶⁻⁸¹

The accumulation of metal ions as inclusion complexes in A β aggregates in the AD brain is one of the key contributors to multifaceted amyloid toxicity. As a result, metal chelators have turned into a potential therapeutic candidate to ameliorate AD toxicity (Figure 6).^{41,82} Clioquinol

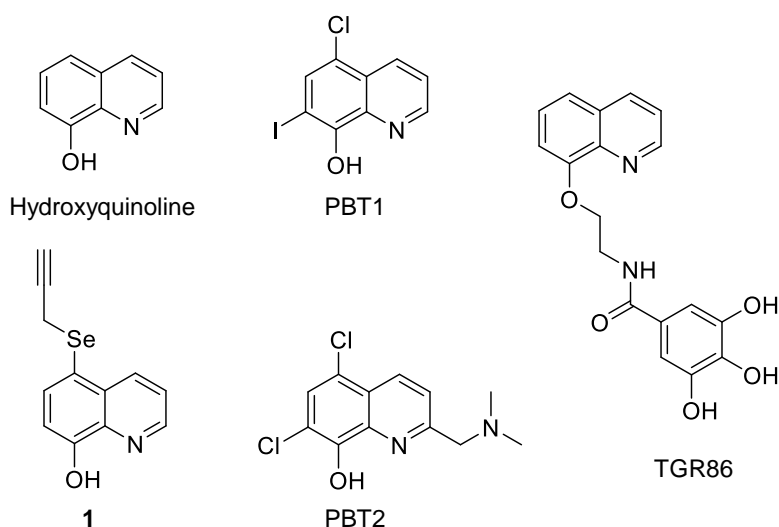


Figure 6. The chemical structures of metal chelator-based modulators of amyloid toxicity. The development of multifunctional modulators starting from a metal chelator to target multifaceted toxicity of AD.

(5-chloro-7-iodo-8-hydroxyquinoline) (PBT1), a hydroxyquinoline derivative is an excellent metal ion chelator evaluated as a drug candidate for AD. Hydroxyquinoline showed moderate success in sequestering the toxic metal ions (Cu^{II} and Zn^{II}) from $\text{A}\beta$ aggregation species.⁸³ The selenium (Se) containing clioquinol (**1**) derivative was more effective than its parent compound in inhibiting the excess ROS production, and Cu^{II} induced $\text{A}\beta$ aggregation.⁸⁴ PBT2, the second generation hydroxyquinoline derivative, showed excellent inhibition of metal-dependent $\text{A}\beta$ aggregation and redox cycle of Cu^{II} .⁸⁵ PBT2 also prevents the formation of the oligomers and dissolves the preformed oligomer under *in vivo* conditions.⁸⁶ As a result, the treatment with PBT2 effectively improved the cognitive function in clinical trials. Unfortunately, PBT2 failed in phase II clinical trial due to multiple factors. However, it firmly established the need to develop multifunctional

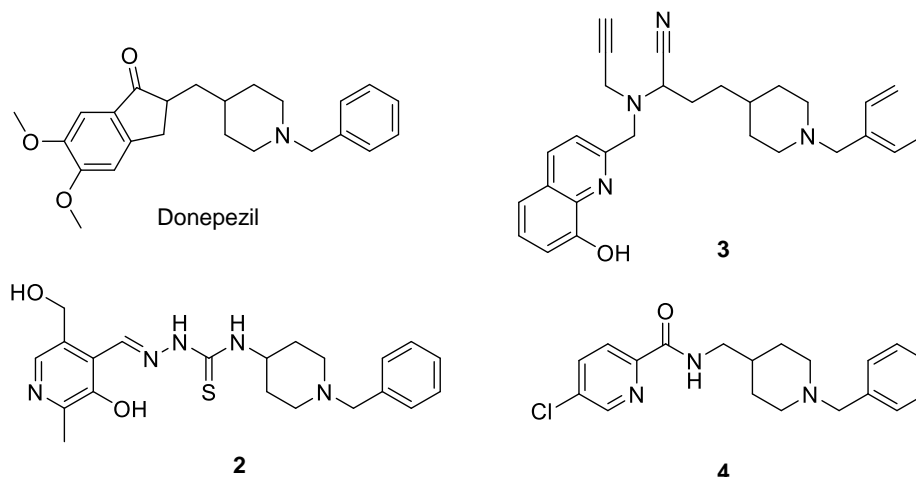


Figure 7. The chemical structures of donepezil and the donepezil-based multifunctional modulators to target multifaceted AD toxicity.

modulators to tackle multifaceted AD toxicity. A hybrid multifunctional inhibitor (TGR86) was developed by strategically combining the structural and functional components of hydroxyquinoline and natural antioxidant epigallocatechin gallate (EGCG) found in green tea.⁷⁸ TGR86 showed excellent modulation of metal-dependent and -independent A β aggregation and arrests the redox cycle of Cu^{II}, thus preventing oxidative DNA and protein damage. These attributes have resulted in the rescue of neuronal cells from A β toxicity and mitochondria dysfunction.

The Food and Drug Administration (FDA) has approved four different drugs (Aricept[®], Exelon[®], Razadyne[®], and Namenda[®]) for the preliminary medication of AD patients. These drugs mainly inhibit cholinesterase (AChE) and are prescribed to treat cognitive abnormalities, such as difficulty with memory, language, judgment, and other thinking activities. Notably, these drugs improve memory and cognitive impairments by modulating the levels of neurotransmitters such as acetylcholine by inhibiting the action of AChE to

breakdown acetylcholine. Researchers are actively involved in modifying these drug molecules to improve their therapeutic potential (Figure 7). Various bioactive moieties were integrated with Aricept[®] (donepezil) to develop effective multifunctional drug candidates.⁸⁷ Compound **2** was synthesized by incorporating the active unit of donepezil and iron metal ions chelator.⁸⁸ The compound **2** showed inhibition of AChE (IC₅₀= 4.93 μM), Aβ aggregation, oxidative stress, and Fe^{II} mediated toxicity. Monoamine oxidase (MAO) overactivation is directly involved in anxiety, depression, cognitive deficits, and neurodegenerative diseases.⁸⁸ Compound **3** was developed by integrating the inhibitory activity of AChE and MAO enzymes with metal chelators. Excellent inhibition of hAChE (IC₅₀ = 29 nM), and hMAO-A (IC₅₀ = 10 mM), and modulation of metal (Cu and Zn)-dependent Aβ toxicity was observed. Further, compound **4** was developed to improve the activity of **3**.⁸⁹ Similar to **3**, compound **4** inhibited AChE (IC₅₀= 22 nM), butyrylcholinesterase (IC₅₀= 1.23 mM), MAO-A (IC₅₀= 13.4 mM), and MAO-B (IC₅₀= 3.14 mM) with improved efficacy.⁹⁰

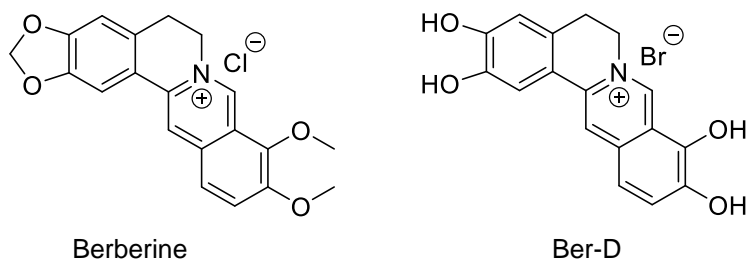


Figure 8. The chemical structures of berberine and its derivative (Ber-D). The development of multifunctional modulators derived from natural products to target multifaceted AD toxicity.

The natural products, such as EGCG, curcumin, ascorbic acid, gallic acid, and α-tocopherol, have a potential role in improving the brain functions, indicating that these

natural products are capable of protecting AD (Figure 8). Berberine is an isoquinoline alkaloid with tremendous therapeutic potential to treat various diseases (tumours, hypertension, diarrhoea, and inflammation).⁹¹ The therapeutic activity of berberine was assessed against AD, and the results show that berberine reduces A β generation by blocking APP processing, restores gliosis, decreases oxidative stress, and prevents inflammation. However, berberine has very low aqueous solubility and cytotoxic to cells, as it induces mitochondrial fragmentation, which resulted in poor therapeutic efficacy for AD. Researchers are actively involved in overcoming this limitation *via* appropriate chemical modifications. Demethylation of berberine yielded a soluble and multifunctional berberine derivative (Ber-D).⁸¹ Ber-D has been found to be an excellent multifunctional modulator for multifaceted amyloid toxicity. Ber-D showed a significant reduction in Cu^{II}-induced oxidative damage and rescued cultured neurons from metal-dependent and -independent A β toxicity. Interestingly, the treatment of neuronal cells with Ber-D prevented premature apoptosis and mitochondrial dysfunction under AD conditions.

As discussed earlier, A β undergoes β -sheet-guided misfolding and aggregation, which is initiated from the A β 16-20 hydrophobic core (KLVFF) and serves as a recognition unit for its fibrillar elongation (Figure 1). Thus, the peptide-based inhibitors were initially designed by targeting the KLVFF unit to modulate the A β aggregation.⁹² The KLVFF (Figure 9) and derived peptide **5** (LPFFD) have been studied, and the results showed effective inhibition of A β aggregation under *in vitro* and *in vivo* condition.⁹³ Various modifications involving the incorporation of unnatural amino acids or organic moieties in the N- or C-terminal have been adopted to develop peptide-based multifunctional modulators.⁹⁴ In this context, Servoss *et al.* have reported a peptoid-based modulator, JPT1, a mimic of the KLVFF

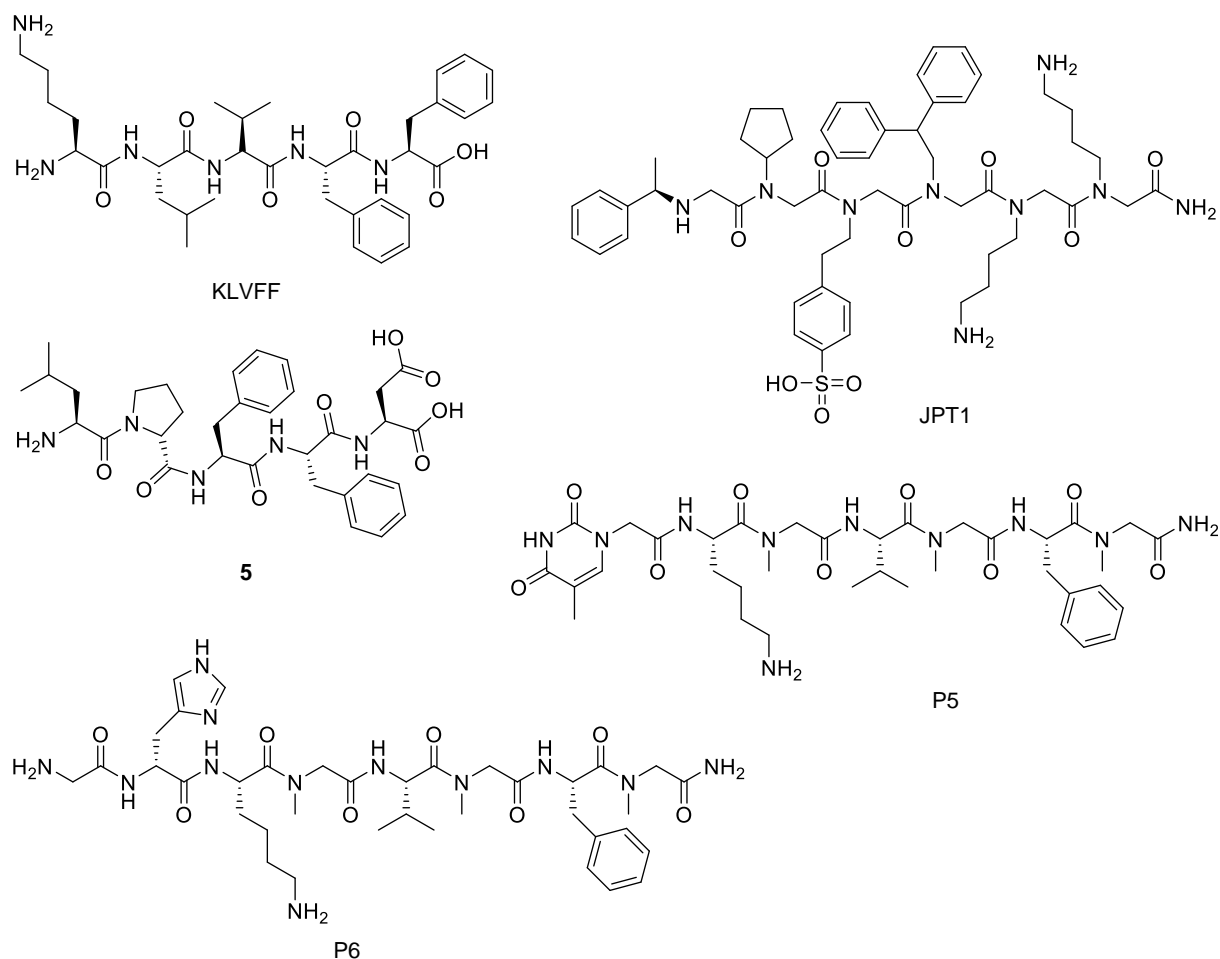


Figure 9. The chemical structures of peptide-based modulators of amyloid toxicity. Multifunctional modulators developed based on KLVFF to target multifaceted AD toxicity.

recognition unit. JPT1 exhibited an α -helical state that facilitates the noncovalent interactions along with $A\beta$.⁹⁵ Interestingly, JPT1 effectively reduces the $A\beta_{40}$ aggregation compared to its parent peptide KLVFF. The use of hybrid peptide-peptoid-based inhibitors (P5) was studied against multifaceted amyloid toxicity.⁷⁶ Interestingly, P5 effectively inhibits the amyloid aggregation and associated toxicity, which was validated in the yeast model. Next, multifunctional inhibitor P6 (Gly-His-Lys-Sr-Val-Sr-Phe-Sr, GHKSrVSrFSr,

Sr= sarcosine) was designed, synthesized, and assessed against AD toxicity.⁷⁷ The C-terminal SrVSrFSr unit, an aggregation modulator peptoid, and the N-terminal GHK, a metal ions chelating unit in P6, provide multifunctionality to target multifaceted A β toxicity. The GHK peptide is associated with several physiological functions in our body, including maintaining Cu homeostasis, activation of wound healing and attraction of immune cells, and oxidative stress and inflammation control. Interestingly, GHK can easily sequester the redox-active metal ion (Cu^{II}) from the A β -Cu^{II} inclusion complex without affecting metalloenzymes. Moreover, Cu^{II} bound to GHK stays in the redox-silent state. P6 inhibits the formation of both fibrillar and oligomeric aggregation species. Its effective sequestration of Cu^{II} from the A β -Cu^{II} inclusion complex prevents the ROS generation, oxidative stress and rescues neuronal cells from amyloid toxicity.⁷⁷ The contemporary research activity and directions in developing anti-AD agents highlight the importance of the multifunctional strategies, which we have adopted in this thesis work.

1.7 Objective

AD is the most devastating chronic disorder and contributes to more than 70-80% of all dementia. The multifactorial nature eludes researchers from the development of accurate diagnosis methods and promising therapeutic tools to tackle AD. In the absence of reliable diagnosis and treatment, the number of deaths caused by AD increased by 146% over the last two decades. The amyloid toxicity caused by the misfolding and aggregation of A β peptide in the CNS is one of the major sources of multifaceted toxicity and pathology of AD. In this context, we have designed, synthesized, and validated the multifunctional therapeutic agents to target multifaceted amyloid toxicity under *in vitro* and *in vivo* AD

conditions. We also identified, validated, and established a novel biomarker recipe (HOCl produced and proximally localized with A β plaques) by understanding the multifaceted metal-A β toxicity, which has the potential to aid multiplexed AD diagnosis (Figure 10).

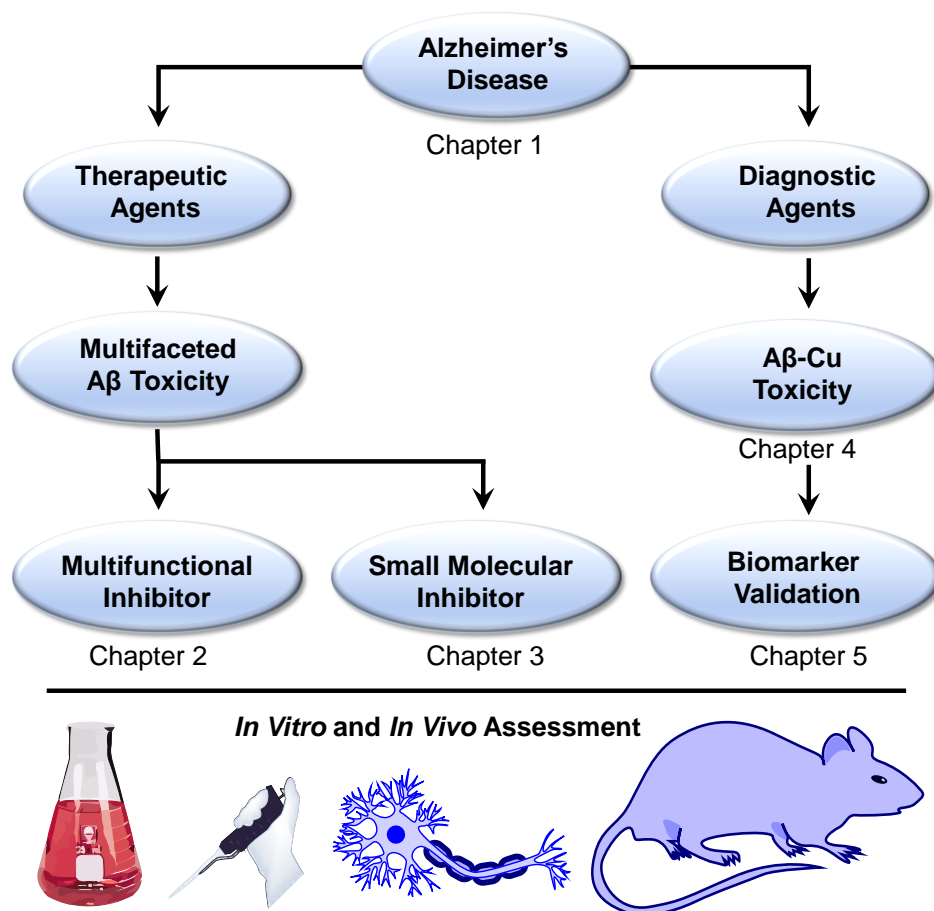


Figure 10. Outline of the thesis (Chapter 1-5).

1.8 References

1. Silverbush, D.; Sharan, R., A systematic approach to orient the human protein-protein interaction network. *Nat. Commun.* **2019**, *10* (1), 3015.
2. Zhong, Q.; Pevzner, S. J.; Hao, T.; Wang, Y.; Mosca, R.; Menche, J.; Taipale, M.; Tasan, M.; Fan, C.; Yang, X.; Haley, P.; Murray, R. R.; Mer, F.; Gebreab, F.; Tam, S.; MacWilliams, A.; Dricot, A.; Reichert, P.; Santhanam, B.; Ghamsari, L.; Calderwood, M.

- A.; Rolland, T.; Charlotheaux, B.; Lindquist, S.; Barabasi, A. L.; Hill, D. E.; Aloy, P.; Cusick, M. E.; Xia, Y.; Roth, F. P.; Vidal, M., An inter-species protein-protein interaction network across vast evolutionary distance. *Mol. Syst. Biol.* **2016**, *12* (4), 865.
3. Kim, M. S.; Pinto, S. M.; Getnet, D.; Nirujogi, R. S.; Manda, S. S.; Chaerkady, R.; Madugundu, A. K.; Kelkar, D. S.; Isserlin, R.; Jain, S.; Thomas, J. K.; Muthusamy, B.; Leal-Rojas, P.; Kumar, P.; Sahasrabudhe, N. A.; Balakrishnan, L.; Advani, J.; George, B.; Renuse, S.; Selvan, L. D.; Patil, A. H.; Nanjappa, V.; Radhakrishnan, A.; Prasad, S.; Subbannayya, T.; Raju, R.; Kumar, M.; Sreenivasamurthy, S. K.; Marimuthu, A.; Sathe, G. J.; Chavan, S.; Datta, K. K.; Subbannayya, Y.; Sahu, A.; Yelamanchi, S. D.; Jayaram, S.; Rajagopalan, P.; Sharma, J.; Murthy, K. R.; Syed, N.; Goel, R.; Khan, A. A.; Ahmad, S.; Dey, G.; Mudgal, K.; Chatterjee, A.; Huang, T. C.; Zhong, J.; Wu, X.; Shaw, P. G.; Freed, D.; Zahari, M. S.; Mukherjee, K. K.; Shankar, S.; Mahadevan, A.; Lam, H.; Mitchell, C. J.; Shankar, S. K.; Satishchandra, P.; Schroeder, J. T.; Sirdeshmukh, R.; Maitra, A.; Leach, S. D.; Drake, C. G.; Halushka, M. K.; Prasad, T. S.; Hruban, R. H.; Kerr, C. L.; Bader, G. D.; Iacobuzio-Donahue, C. A.; Gowda, H.; Pandey, A., A draft map of the human proteome. *Nature* **2014**, *509* (7502), 575-581.
 4. Bitran, A.; Jacobs, W. M.; Zhai, X.; Shakhnovich, E., Cotranslational folding allows misfolding-prone proteins to circumvent deep kinetic traps. *Proc. Natl. Acad. Sci.* **2020**, *117* (3), 1485-1495.
 5. Marinko, J. T.; Huang, H.; Penn, W. D.; Capra, J. A.; Schleich, J. P.; Sanders, C. R., Folding and misfolding of human membrane proteins in health and disease: from single molecules to cellular proteostasis. *Chem. Rev.* **2019**, *119* (9), 5537-5606.
 6. Dobson, C. M., Protein folding and misfolding. *Nature* **2003**, *426* (6968), 884-90.
 7. Brothers, H. M.; Gosztyla, M. L.; Robinson, S. R., The physiological roles of amyloid-beta peptide hint at new ways to treat Alzheimer's disease. *Front. Aging Neurosci.* **2018**, *10*, 118.
 8. Rajasekhar, K.; Chakrabarti, M.; Govindaraju, T., Function and toxicity of amyloid beta and recent therapeutic interventions targeting amyloid beta in Alzheimer's disease. *Chem. Commun. (Camb)* **2015**, *51* (70), 13434-1350.
 9. Soto, C., Unfolding the role of protein misfolding in neurodegenerative diseases. *Nat. Rev. Neurosci.* **2003**, *4* (1), 49-60.
-

10. Selkoe, D. J., Folding proteins in fatal ways. *Nature* **2003**, 426 (6968), 900-904.
11. DeMattos, R. B.; Bales, K. R.; Cummins, D. J.; Dodart, J. C.; Paul, S. M.; Holtzman, D. M., Peripheral anti-A beta antibody alters CNS and plasma A beta clearance and decreases brain A beta burden in a mouse model of Alzheimer's disease. *Proc. Natl. Acad. Sci.* **2001**, 98 (15), 8850-8855.
12. Knowles, T. P.; Vendruscolo, M.; Dobson, C. M., The amyloid state and its association with protein misfolding diseases. *Nat. Rev. Mol. Cell. Biol.* **2014**, 15 (6), 384-396.
13. Wells, C.; Brennan, S. E.; Keon, M.; Saksena, N. K., Prionoid proteins in the pathogenesis of neurodegenerative diseases. *Front. Mol. Neurosci.* **2019**, 12, 271.
14. Soto, C.; Pritzkow, S., Protein misfolding, aggregation, and conformational strains in neurodegenerative diseases. *Nat. Neurosci.* **2018**, 21 (10), 1332-1340.
15. Chung, C. G.; Lee, H.; Lee, S. B., Mechanisms of protein toxicity in neurodegenerative diseases. *Cell Mol. Life Sci.* **2018**, 75 (17), 3159-3180.
16. Jucker, M.; Walker, L. C., Pathogenic protein seeding in Alzheimer disease and other neurodegenerative disorders. *Ann. Neurol.* **2011**, 70 (4), 532-540.
17. Ballard, C.; Gauthier, S.; Corbett, A.; Brayne, C.; Aarsland, D.; Jones, E., Alzheimer's disease. *Lancet* **2011**, 377 (9770), 1019-1031.
18. Jucker, M.; Walker, L. C., Self-propagation of pathogenic protein aggregates in neurodegenerative diseases. *Nature* **2013**, 501 (7465), 45-51.
19. Rajasekhar, K.; Govindaraju, T., Current progress, challenges and future prospects of diagnostic and therapeutic interventions in Alzheimer's disease. *RSC Adv.* **2018**, 8 (42), 23780-23804.
20. Huang, Y.; Mucke, L., Alzheimer mechanisms and therapeutic strategies. *Cell* **2012**, 148 (6), 1204-1222.
21. Schnabel, J., Amyloid: little proteins, big clues. *Nature* **2011**, 475 (7355), 12-14.
22. Rushworth, J. V.; Hooper, N. M., Lipid rafts: linking Alzheimer's amyloid-beta production, aggregation, and toxicity at neuronal membranes. *Int. J Alzheimers Dis.* **2010**, 2011, 603052.
23. Ffytche, D. H.; Creese, B.; Politis, M.; Chaudhuri, K. R.; Weintraub, D.; Ballard, C.; Aarsland, D., The psychosis spectrum in Parkinson disease. *Nat. Rev. Neurol.* **2017**, 13 (2), 81-95.

24. Chaganti, S. S.; McCusker, E. A.; Loy, C. T., What do we know about late onset Huntington's disease? *J Huntingtons Dis.* **2017**, *6* (2), 95-103.
25. Anliker, B.; Muller, U., The functions of mammalian amyloid precursor protein and related amyloid precursor-like proteins. *Neurodegener Dis.* **2006**, *3* (4-5), 239-246.
26. Alzheimer's Association, 2013 Alzheimer's disease facts and figures. *Alzheimers Dement* **2013**, *9* (2), 208-245.
27. Scheltens, P.; Blennow, K.; Breteler, M. M.; de Strooper, B.; Frisoni, G. B.; Salloway, S.; Van der Flier, W. M., Alzheimer's disease. *Lancet* **2016**, *388* (10043), 505-517.
28. Panpalli Ates, M.; Karaman, Y.; Guntekin, S.; Ergun, M. A., Analysis of genetics and risk factors of Alzheimer's disease. *Neuroscience* **2016**, *325*, 124-131.
29. Chung, H. Y.; Wickel, J.; Brunkhorst, F. M.; Geis, C., Sepsis-associated encephalopathy: from delirium to dementia? *J Clin. Med.* **2020**, *9* (3), 703.
30. Alzheimer's Association, 2020 Alzheimer's disease facts and figures. *Alzheimers dement* **2020**. doi: 10.1002/alz.12068.
31. Alzheimer's Association, 2018 Alzheimer's disease facts and figures. *Alzheimers Dement* **2018**, *14* (5), 701-701.
32. Crescenzi, O.; Tomaselli, S.; Guerrini, R.; Salvadori, S.; D'Ursi, A. M.; Temussi, P. A.; Picone, D., Solution structure of the Alzheimer amyloid beta-peptide (1-42) in an apolar microenvironment. Similarity with a virus fusion domain. *Eur. J Biochem.* **2002**, *269* (22), 5642-5648.
33. Mandelkow, E., Alzheimer's disease. The tangled tale of tau. *Nature* **1999**, *402* (6762), 588-599.
34. Muller, U. C.; Zheng, H., Physiological functions of APP family proteins. *Cold Spring Harb Perspect. Med.* **2012**, *2* (2), a006288.
35. Truong, P. H.; Ciccotosto, G. D.; Cappai, R., Analysis of motor function in amyloid precursor-like protein 2 knockout mice: the effects of ageing and sex. *Neurochem. Res.* **2019**, *44* (6), 1356-1366.
36. Scheidt, H. A.; Morgado, I.; Huster, D., Solid-state NMR reveals a close structural relationship between amyloid-beta protofibrils and oligomers. *J Biol. Chem.* **2012**, *287* (27), 22822-22826.

37. Walti, M. A.; Ravotti, F.; Arai, H.; Glabe, C. G.; Wall, J. S.; Bockmann, A.; Guntert, P.; Meier, B. H.; Riek, R., Atomic-resolution structure of a disease-relevant Abeta(1-42) amyloid fibril. *Proc. Natl. Acad. Sci.* **2016**, *113* (34), e4976-4984.
38. Selkoe, D. J.; Hardy, J., The amyloid hypothesis of Alzheimer's disease at 25 years. *EMBO Mol. Med.* **2016**, *8* (6), 595-608.
39. Colvin, M. T.; Silvers, R.; Ni, Q. Z.; Can, T. V.; Sergeev, I.; Rosay, M.; Donovan, K. J.; Michael, B.; Wall, J.; Linse, S.; Griffin, R. G., Atomic resolution structure of monomorphic Abeta42 amyloid fibrils. *J Am. Chem. Soc.* **2016**, *138* (30), 9663-9674.
40. Huy, P. D.; Vuong, Q. V.; La Penna, G.; Faller, P.; Li, M. S., Impact of Cu(II) binding on structures and dynamics of abeta42 monomer and dimer: molecular dynamics study. *ACS Chem. Neurosci.* **2016**, *7* (10), 1348-1363.
41. Barnham, K. J.; Bush, A. I., Biological metals and metal-targeting compounds in major neurodegenerative diseases. *Chem. Soc. Rev.* **2014**, *43* (19), 6727-6749.
42. Crouch, P. J.; Barnham, K. J., Therapeutic redistribution of metal ions to treat Alzheimer's disease. *Acc. Chem. Res.* **2012**, *45* (9), 1604-1611.
43. Bourassa, M. W.; Miller, L. M., Metal imaging in neurodegenerative diseases. *Metallomics* **2012**, *4* (8), 721-738.
44. Rauk, A., The chemistry of Alzheimer's disease. *Chem. Soc. Rev.* **2009**, *38* (9), 2698-715.
45. Bush, A. I., The metallobiology of Alzheimer's disease. *Trends Neurosci.* **2003**, *26* (4), 207-214.
46. Gonzalez, P.; Bossak-Ahmad, K.; Vileno, B.; Wezynfeld, N. E.; El Khoury, Y.; Hellwig, P.; Hureau, C.; Bal, W.; Faller, P., Triggering Cu-coordination change in Cu(ii)-Ala-His-His by external ligands. *Chem. Commun. (Camb)* **2019**, *55* (56), 8110-8113.
47. Okita, Y.; Rcom-H'cheo-Gauthier, A. N.; Goulding, M.; Chung, R. S.; Faller, P.; Pountney, D. L., Metallothionein, copper and alpha-synuclein in alpha-synucleinopathies. *Front Neurosci.* **2017**, *11*, 114.
48. Atrian-Blasco, E.; Santoro, A.; Pountney, D. L.; Meloni, G.; Hureau, C.; Faller, P., Chemistry of mammalian metallothioneins and their interaction with amyloidogenic peptides and proteins. *Chem. Soc. Rev.* **2017**, *46* (24), 7683-7693.
49. Barnham, K. J.; Masters, C. L.; Bush, A. I., Neurodegenerative diseases and oxidative stress. *Nat. Rev. Drug Discov.* **2004**, *3* (3), 205-214.

50. Butterfield, D. A.; Sultana, R., Methionine-35 of Abeta(1-42): importance for oxidative stress in Alzheimer disease. *J Amino Acids* **2011**, *2011*, 198430.
51. Ranasinghe, K. G.; Cha, J.; Iaccarino, L.; Hinkley, L. B.; Beagle, A. J.; Pham, J.; Jagust, W. J.; Miller, B. L.; Rankin, K. P.; Rabinovici, G. D.; Vessel, K. A.; Nagarajan, S. S., Neurophysiological signatures in Alzheimer's disease are distinctly associated with tau, amyloid-beta accumulation, and cognitive decline. *Sci. Trans. Med.* **2020**, *12* (534).
52. Nortley, R.; Korte, N.; Izquierdo, P.; Hirunpattarasilp, C.; Mishra, A.; Jaunmuktane, Z.; Kyrargyri, V.; Pfeiffer, T.; Khennouf, L.; Madry, C.; Gong, H.; Richard-Loendt, A.; Huang, W.; Saito, T.; Saido, T. C.; Brandner, S.; Sethi, H.; Attwell, D., Amyloid beta oligomers constrict human capillaries in Alzheimer's disease via signaling to pericytes. *Science* **2019**, *365* (6450).
53. Snyder, E. M.; Nong, Y.; Almeida, C. G.; Paul, S.; Moran, T.; Choi, E. Y.; Nairn, A. C.; Salter, M. W.; Lombroso, P. J.; Gouras, G. K.; Greengard, P., Regulation of NMDA receptor trafficking by amyloid-beta. *Nat. Neurosci.* **2005**, *8* (8), 1051-1058.
54. Yan, S. D.; Zhu, H.; Zhu, A.; Golabek, A.; Du, H.; Roher, A.; Yu, J.; Soto, C.; Schmidt, A. M.; Stern, D.; Kindy, M., Receptor-dependent cell stress and amyloid accumulation in systemic amyloidosis. *Nat. Med.* **2000**, *6* (6), 643-651.
55. Wang, J.; Zhao, C.; Zhao, A.; Li, M.; Ren, J.; Qu, X., New insights in amyloid beta interactions with human telomerase. *J Am. Chem. Soc.* **2015**, *137* (3), 1213-1219.
56. Forero, D. A.; Gonzalez-Giraldo, Y.; Lopez-Quintero, C.; Castro-Vega, L. J.; Barreto, G. E.; Perry, G., Meta-analysis of telomere length in Alzheimer's disease. *J. Gerontol. A Biol. Sci. Med. Sci.* **2016**, *71* (8), 1069-1073.
57. Butterfield, D. A.; Boyd-Kimball, D., Oxidative stress, amyloid-beta peptide, and altered key molecular pathways in the pathogenesis and progression of Alzheimer's disease. *J Alzheimers Dis.* **2018**, *62* (3), 1345-1367.
58. Alies, B.; Sasaki, I.; Proux, O.; Sayen, S.; Guillon, E.; Faller, P.; Hureau, C., Zn impacts Cu coordination to amyloid-beta, the Alzheimer's peptide, but not the ROS production and the associated cell toxicity. *Chem. Commun. (Camb)* **2013**, *49* (12), 1214-1216.
59. Kinney, J. W.; Bemiller, S. M.; Murtishaw, A. S.; Leisgang, A. M.; Salazar, A. M.; Lamb, B. T., Inflammation as a central mechanism in Alzheimer's disease. *Alzheimers Dement* **2018**, *4*, 575-590.

60. Lauren, J.; Gimbel, D. A.; Nygaard, H. B.; Gilbert, J. W.; Strittmatter, S. M., Cellular prion protein mediates impairment of synaptic plasticity by amyloid-beta oligomers. *Nature* **2009**, *457* (7233), 1128-1132.
61. Beekly, D. L.; Ramos, E. M.; Lee, W. W.; Deitrich, W. D.; Jacka, M. E.; Wu, J.; Hubbard, J. L.; Koepsell, T. D.; Morris, J. C.; Kukull, W. A.; Centers, N. I. A. A. s. D., The national Alzheimer's coordinating center (nacc) database: the uniform data set. *Alzheimer Dis. Assoc. Disord.* **2007**, *21* (3), 249-258.
62. Beekly, D. L.; Ramos, E. M.; van Belle, G.; Deitrich, W.; Clark, A. D.; Jacka, M. E.; Kukull, W. A.; Centers, N. I.-A. s. D., The National Alzheimer's Coordinating Center (NACC) Database: an Alzheimer disease database. *Alzheimer Dis. Assoc. Disord.* **2004**, *18* (4), 270-277.
63. Kueper, J. K.; Speechley, M.; Montero-Odasso, M., The Alzheimer's disease assessment scale-cognitive subscale (adas-cog): modifications and responsiveness in pre-dementia populations. a narrative review. *J Alzheimers Dis.* **2018**, *63* (2), 423-444.
64. Arora, H.; Ramesh, M.; Rajasekhar, K.; Govindaraju, T., Molecular tools to detect alloforms of A β and tau: implications for multiplexing and multimodal diagnosis of Alzheimer's disease. *Bull. Chem. Soc. Jpn.* **2020**, *93* (4), 507-546.
65. Marcus, C.; Mena, E.; Subramaniam, R. M., Brain PET in the diagnosis of Alzheimer's disease. *Clin. Nucl. Med.* **2014**, *39* (10), e413-22.
66. Rajasekhar, K.; Narayanaswamy, N.; Murugan, N. A.; Kuang, G.; Agren, H.; Govindaraju, T., A high affinity red fluorescence and colorimetric probe for amyloid beta aggregates. *Sci. Rep.* **2016**, *6*, 23668.
67. Rajasekhar, K.; Narayanaswamy, N.; Murugan, N. A.; Viccaro, K.; Lee, H. G.; Shah, K.; Govindaraju, T., Abeta plaque-selective NIR fluorescence probe to differentiate Alzheimer's disease from tauopathies. *Biosens. Bioelectron.* **2017**, *98*, 54-61.
68. Jack, C. R., Jr.; Bennett, D. A.; Blennow, K.; Carrillo, M. C.; Dunn, B.; Haeberlein, S. B.; Holtzman, D. M.; Jagust, W.; Jessen, F.; Karlawish, J.; Liu, E.; Molinuevo, J. L.; Montine, T.; Phelps, C.; Rankin, K. P.; Rowe, C. C.; Scheltens, P.; Siemers, E.; Snyder, H. M.; Sperling, R.; Contributors, NIA-AA research framework: toward a biological definition of Alzheimer's disease. *Alzheimers Dement* **2018**, *14* (4), 535-562.

69. Lok, K.; Zhao, H.; Shen, H.; Wang, Z.; Gao, X.; Zhao, W.; Yin, M., Characterization of the APP/PS1 mouse model of Alzheimer's disease in senescence accelerated background. *Neurosci. Lett.* **2013**, *557*, 84-9.
70. Samanta, S.; Govindaraju, T., Unambiguous detection of elevated levels of hypochlorous acid in double transgenic ad mouse brain. *ACS Chem. Neurosci.* **2019**, *10* (12), 4847-4853.
71. Maia, L. F.; Kaeser, S. A.; Reichwald, J.; Hruscha, M.; Martus, P.; Staufenbiel, M.; Jucker, M., Changes in amyloid-beta and tau in the cerebrospinal fluid of transgenic mice overexpressing amyloid precursor protein. *Sci. Trans. Med.* **2013**, *5* (194), 194re2.
72. Radde, R.; Bolmont, T.; Kaeser, S. A.; Coomaraswamy, J.; Lindau, D.; Stoltze, L.; Calhoun, M. E.; Jaggi, F.; Wolburg, H.; Gengler, S.; Haass, C.; Ghetti, B.; Czech, C.; Holscher, C.; Mathews, P. M.; Jucker, M., Abeta42-driven cerebral amyloidosis in transgenic mice reveals early and robust pathology. *EMBO Rep.* **2006**, *7* (9), 940-946.
73. Serneels, L.; Van Biervliet, J.; Craessaerts, K.; Dejaegere, T.; Horre, K.; Van Houtvin, T.; Esselmann, H.; Paul, S.; Schafer, M. K.; Berezovska, O.; Hyman, B. T.; Sprangers, B.; Sciot, R.; Moons, L.; Jucker, M.; Yang, Z.; May, P. C.; Karran, E.; Wiltfang, J.; D'Hooge, R.; De Strooper, B., gamma-Secretase heterogeneity in the Aph1 subunit: relevance for Alzheimer's disease. *Science* **2009**, *324* (5927), 639-642.
74. Aguzzi, A.; O'Connor, T., Protein aggregation diseases: pathogenicity and therapeutic perspectives. *Nat. Rev. Drug Discov.* **2010**, *9* (3), 237-248.
75. Landy, K. M.; Salmon, D. P.; Galasko, D.; Filoteo, J. V.; Festa, E. K.; Heindel, W. C.; Hansen, L. A.; Hamilton, J. M., Motion discrimination in dementia with Lewy bodies and Alzheimer disease. *Neurology.* **2015**, *85* (16), 1376-1382.
76. Rajasekhar, K.; Suresh, S. N.; Manjithaya, R.; Govindaraju, T., Rationally designed peptidomimetic modulators of abeta toxicity in Alzheimer's disease. *Sci. Rep.* **2015**, *5*, 8139.
77. Rajasekhar, K.; Madhu, C.; Govindaraju, T., Natural tripeptide-based inhibitor of multifaceted amyloid beta toxicity. *ACS Chem. Neurosci.* **2016**, *7* (9), 1300-1310.
78. Rajasekhar, K.; Mehta, K.; Govindaraju, T., Hybrid multifunctional modulators inhibit multifaceted Abeta toxicity and prevent mitochondrial damage. *ACS Chem. Neurosci.* **2018**, *9* (6), 1432-1440.

79. Samanta, S.; Rajasekhar, K.; Babagond, V.; Govindaraju, T., Small molecule inhibits metal-dependent and -independent multifaceted toxicity of Alzheimer's disease. *ACS Chem. Neurosci.* **2019**, *10* (8), 3611-3621.
80. Datta, L. P.; Samanta, S.; Govindaraju, T., Polyampholyte-based synthetic chaperone modulate amyloid aggregation and lithium delivery. *ACS Chem. Neurosci.* **2020**, *11* (18), 2812-2826.
81. Rajasekhar, K.; Samanta, S.; Bagoband, V.; Murugan, N. A.; Govindaraju, T., Antioxidant berberine-derivative inhibits multifaceted amyloid toxicity. *iScience* **2020**, *23* (4), 101005.
82. Hung, L. W.; Barnham, K. J., Modulating metals as a therapeutic strategy for Alzheimer's disease. *Future Med. Chem.* **2012**, *4* (8), 955-969.
83. Di Vaira, M.; Bazzicalupi, C.; Orioli, P.; Messori, L.; Bruni, B.; Zatta, P., Clioquinol, a drug for Alzheimer's disease specifically interfering with brain metal metabolism: structural characterization of its zinc(II) and copper(II) complexes. *Inorg. Chem.* **2004**, *43* (13), 3795-3797.
84. Wang, Z.; Wang, Y.; Li, W.; Mao, F.; Sun, Y.; Huang, L.; Li, X., Design, synthesis, and evaluation of multitarget-directed selenium-containing clioquinol derivatives for the treatment of Alzheimer's disease. *ACS Chem. Neurosci.* **2014**, *5* (10), 952-962.
85. Johanssen, T.; Suphantarida, N.; Donnelly, P. S.; Liu, X. M.; Petrou, S.; Hill, A. F.; Barnham, K. J., PBT2 inhibits glutamate-induced excitotoxicity in neurons through metal-mediated preconditioning. *Neurobiol. Dis.* **2015**, *81*, 176-185.
86. Adlard, P. A.; Cherny, R. A.; Finkelstein, D. I.; Gautier, E.; Robb, E.; Cortes, M.; Volitakis, I.; Liu, X.; Smith, J. P.; Perez, K.; Laughton, K.; Li, Q. X.; Charman, S. A.; Nicolazzo, J. A.; Wilkins, S.; Deleva, K.; Lynch, T.; Kok, G.; Ritchie, C. W.; Tanzi, R. E.; Cappai, R.; Masters, C. L.; Barnham, K. J.; Bush, A. I., Rapid restoration of cognition in Alzheimer's transgenic mice with 8-hydroxy quinoline analogs is associated with decreased interstitial Abeta. *Neuron* **2008**, *59* (1), 43-55.
87. Adunsky, A.; Chesnin, V.; Ravona, R.; Harats, D.; Davidson, M., Plasma lipid levels in Alzheimer's disease patients treated by Donepezil hydrochloride: a cross-sectional study. *Arch. Gerontol. Geriatr.* **2004**, *38* (1), 61-68.
88. Palanimuthu, D.; Poon, R.; Sahni, S.; Anjum, R.; Hibbs, D.; Lin, H. Y.; Bernhardt, P. V.; Kalinowski, D. S.; Richardson, D. R., A novel class of thiosemicarbazones show multi-

- functional activity for the treatment of Alzheimer's disease. *Eur. J Med. Chem.* **2017**, *139*, 612-632.
89. Wu, M. Y.; Esteban, G.; Brogi, S.; Shionoya, M.; Wang, L.; Campiani, G.; Unzeta, M.; Inokuchi, T.; Butini, S.; Marco-Contelles, J., Donepezil-like multifunctional agents: design, synthesis, molecular modeling and biological evaluation. *Eur. J Med. Chem.* **2016**, *121*, 864-879.
90. Li, F.; Wang, Z. M.; Wu, J. J.; Wang, J.; Xie, S. S.; Lan, J. S.; Xu, W.; Kong, L. Y.; Wang, X. B., Synthesis and pharmacological evaluation of donepezil-based agents as new cholinesterase/monoamine oxidase inhibitors for the potential application against Alzheimer's disease. *J Enzyme Inhib. Med. Chem.* **2016**, *31* (3), 41-53.
91. Imenshahidi, M.; Hosseinzadeh, H., Berberis vulgaris and berberine: an update review. *Phytother. Res.* **2016**, *30* (11), 1745-1764.
92. Tjernberg, L. O.; Naslund, J.; Lindqvist, F.; Johansson, J.; Karlstrom, A. R.; Thyberg, J.; Terenius, L.; Nordstedt, C., Arrest of beta-amyloid fibril formation by a pentapeptide ligand. *J Biol. Chem.* **1996**, *271* (15), 8545-8548.
93. Viet, M. H.; Ngo, S. T.; Lam, N. S.; Li, M. S., Inhibition of aggregation of amyloid peptides by beta-sheet breaker peptides and their binding affinity. *J Phys. Chem. B* **2011**, *115* (22), 7433-7446.
94. Simon, R. J.; Kania, R. S.; Zuckermann, R. N.; Huebner, V. D.; Jewell, D. A.; Banville, S.; Ng, S.; Wang, L.; Rosenberg, S.; Marlowe, C. K.; et al., Peptoids: a modular approach to drug discovery. *Proc. Natl. Acad. Sci.* **1992**, *89* (20), 9367-9371.
95. Turner, J. P.; Lutz-Rechtin, T.; Moore, K. A.; Rogers, L.; Bhave, O.; Moss, M. A.; Servoss, S. L., Rationally designed peptoids modulate aggregation of amyloid-beta 40. *ACS Chem. Neurosci.* **2014**, *5* (7), 552-558.

Chapter 2

**Small Molecule Inhibits Metal-dependent and
Independent Multifaceted Toxicity of Alzheimer's
Disease**

AD symptoms include cognitive decline, memory loss, and behavioural disability, all of which ultimately lead to death.¹⁻³ This devastating ailment has reached epidemic proportions worldwide owing to the lack of effective drugs.⁴ Although the precise etiology of the disease is poorly understood, production, aggregation, and deposition of A β peptides in the brain as senile plaques is strongly implicated in AD progression.⁵⁻⁷ This A β 42 is highly amyloidogenic and exhibits high propensity to undergo aggregation through hydrophobic interactions and ordered β -sheet formation to form polymorphic soluble oligomers, protofibrils, and insoluble fibrillar aggregates.^{5,7-10} The A β toxicity is aggravated in the presence of metal ions such as copper and iron owing to the formation of A β -metal complexes, which accelerate the process of aggregation to generate highly toxic polymorphic A β -metal species.^{11,12} These polymorphic A β species are implicated in membrane toxicity and mitochondrial dysfunction and trigger various neurotoxic cascade processes.^{9,13} Furthermore, the inclusion of redox-active metal ions (Cu^{II} and Fe^{III}) in A β species triggers Fenton-type reaction in the reducing environment to generate reactive oxygen and nitrogen species (ROS and RNS, respectively), which induce neuronal oxidative stress.^{5,9,14} The generation of excess ROS damages DNA, which contributes to additional toxicity and neuronal death.^{7,11,14} The failure of cellular redox homeostasis (oxidative stress) is governed by Nrf2 signaling, a nuclear transcription factor, which adjusts redox homeostasis by activating an array of antioxidant genes.¹⁵ Further, polymorphic A β species activate neuroglia cells via the toll like receptor **4** (TLR4) signaling pathway, leading to neuroinflammation.^{16,17} Therefore, neuronal impairment through oxidative stress, inflammation, and mitochondrial dysfunction are the manifestations of multifaceted toxicity induced by A β -metal aggregation species in the AD brain.^{5,18,19} This emphasizes the need for a novel drug design strategy to develop multifunctional modulators (MFMs) to effectively target multiple disease routes associated with AD.²⁰⁻²² In recent

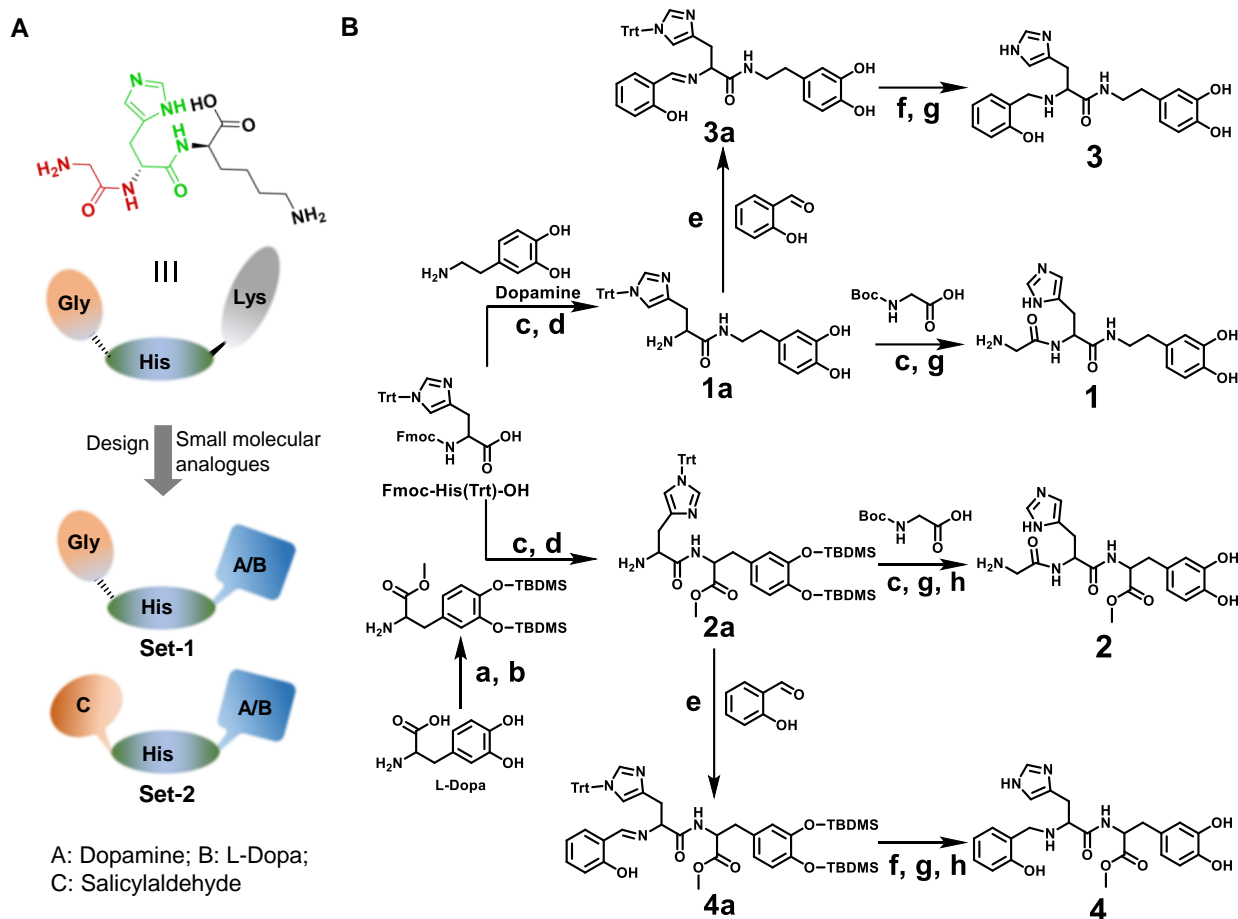


Figure 1. (A) Design strategy for MFMs. (B) Syntheses of multifunctional compounds 1–4. Reagents and conditions: (a) SOCl_2 , MeOH; (b) TBDMSCl, DBU, DMF; (c) HBTU, HOBt, DIPEA, DMF; (d) diethylamine, DCM; (e) DIPEA, ACN, 65 °C; (f) NaBH_4 , MeOH; (g) TFA, DCM; (h) $(\text{tBu})_4\text{N}^+\cdot\text{F}^-$, THF.

years, notwithstanding the design constraints, researchers have undertaken the task of developing therapeutic candidates targeting multifaceted $\text{A}\beta$ toxicity.^{23–26} We earlier reported KLVFF-based hybrid peptoid inhibitors, a multifunctional inhibitor, by conjugating the hybrid peptoid, $\text{A}\beta$ aggregation inhibitor, and a natural tripeptide (Gly-His-Lys, GHK) of human origin and a known Cu^{II} chelator.^{27,28} Further, we developed small molecule-based hybrid multifunctional modulators (HMMs) designed by integrating the structural and functional features of clioquinol.²⁹ The potential HMM was found to modulate mitochondrial damage and metal-dependent and -

independent multifaceted A β toxicity.^{19,30} The aforementioned multifunctional inhibitor and HMM were not equipped to inhibit the Fe-A β inclusion complex-induced toxicity and neuroinflammation. Therefore, any strategy to design novel MFMs for AD must consider incorporation of functional features that inhibit multiple toxicities including neuroinflammation.^{5,20} Herein, we report a unique design of natural peptide-inspired small molecule MFMs to ameliorate the multifaceted A β toxicity. The MFM is anticipated to (i) chelate and sequester metal ions (Cu^{II} and Fe^{II}) from their A β inclusion complexes and arrest their redox cycle, (ii) inhibit the generation of excessive ROS through both metal-dependent and metal-independent pathways, (iii) inhibit the metal-dependent and metal-independent A β aggregation species, (iv) reduce oxidative stress in the neuronal cells, (v) protect DNA from ROS, (vi) prevent mitochondrial dysfunction and oxidative damage, (vii)

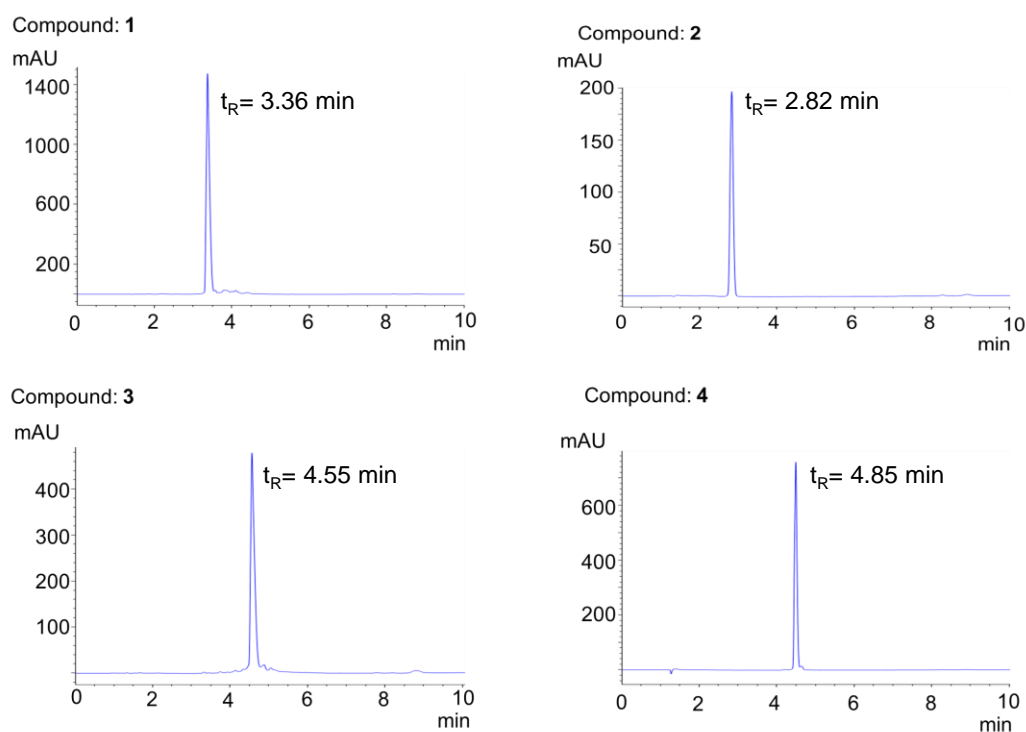


Figure 2. HPLC trace and purity of compound 1-4.

inhibit neuroglia activation and provide anti-inflammatory effects, and (viii) provide overall neuroprotection and rescue neuronal cells from metal-dependent and metal-independent A β -mediated multifaceted toxicity.

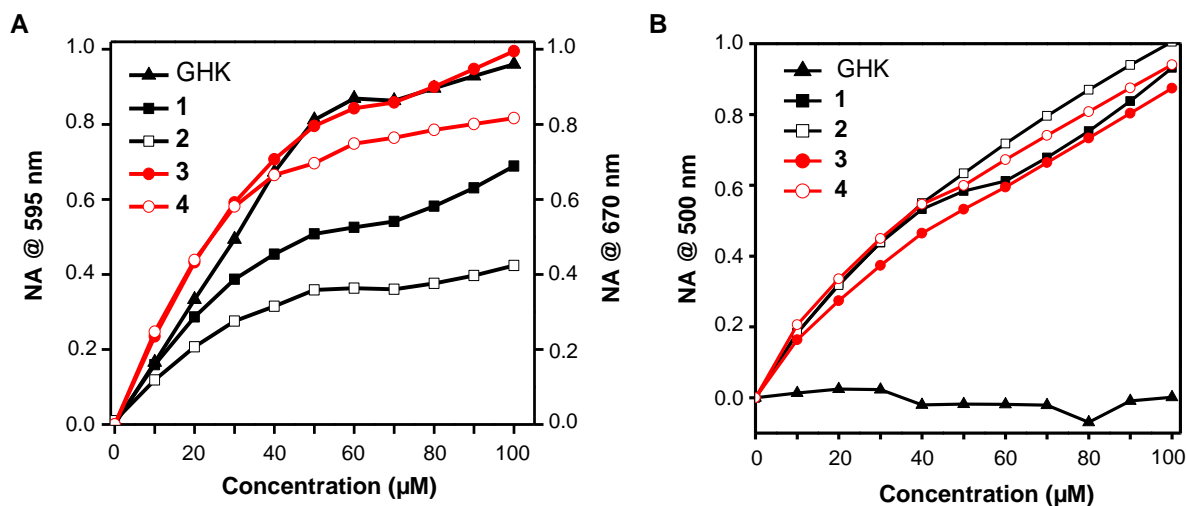


Figure 3. Chelation of redox active metal ions (Cu^{II} and Fe^{III}) by compounds 1-4. (A) The plot of absorbance intensity at 595 and 670 nm for Cu^{II} complex of 1-4 and GHK. (B) The plot of absorbance intensity at 500 nm for Fe^{III} complex of compounds 1-4 and GHK.

2.1 Design Strategy of Natural Tripeptide-Inspired Small Molecule MFM

We designed a set of small molecules to identify a potential MFM by undertaking strategic structural and functional modifications to GHK, a natural tripeptide known for many biological functions in humans.^{30,31} One of the major revelations here is that ~200 μg/L of GHK is found in adult human serum, which decreases to <80 μg/L with aging.³⁰ Remarkably, GHK exhibits higher binding affinity ($K_a \approx 10^{14}$) compared to A β 42 ($K_a \approx 10^9$) for Cu^{II} but lower than that of metalloproteins ($K_a \approx 10^{15}$ to 10^{17}) in the biological milieu.³¹ In other words, GHK can effectively sequester Cu^{II} from A β 42-Cu^{II} complex without interfering with copper-based metalloproteins, a

highly desirable property that has been exploited in our earlier work.³⁰ However, GHK and its conjugates function as anti-AD agents only in the presence of Cu^{II} and are grossly ineffective in

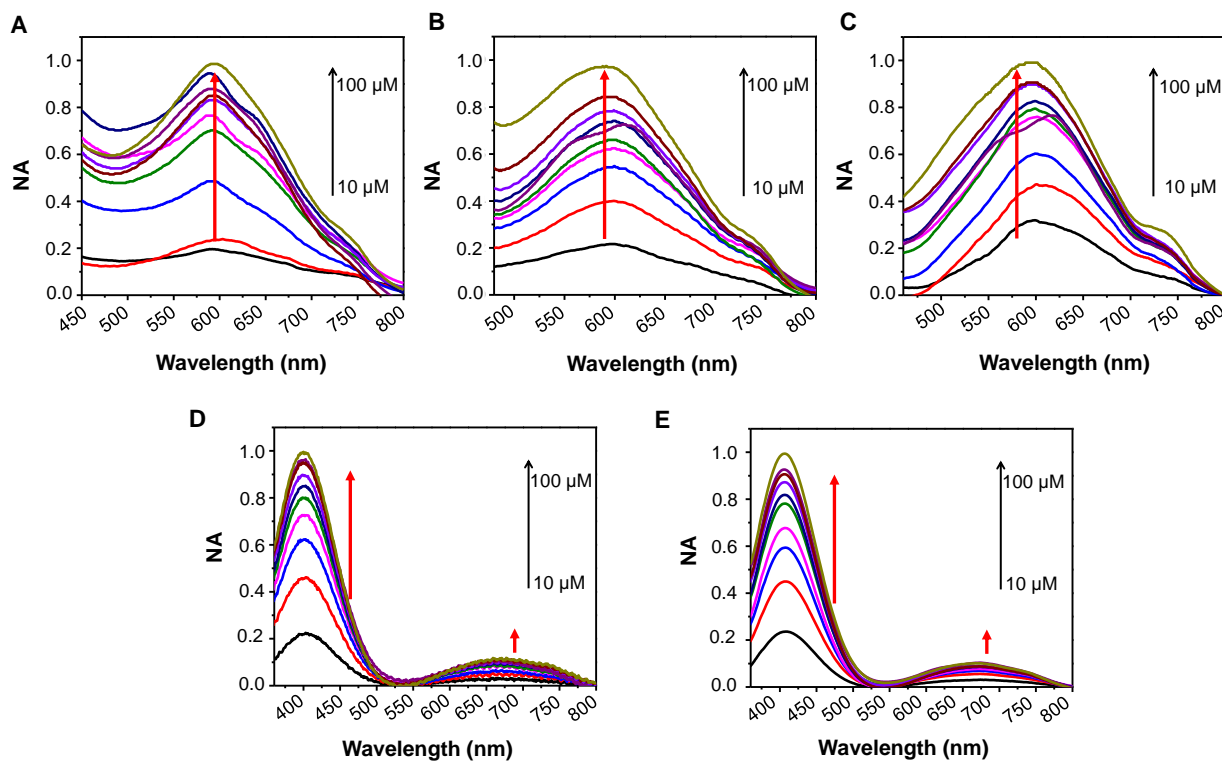


Figure 4. Metal ion chelation study. Absorption spectra of Cu^{II} treated with GHK (A), 1 (B), 2 (C), 3 (D) and 4 (E). NA: Normalized absorbance.

the inhibition of ROS generation, oxidative stress and neuroinflammation arising from Fe-dependent and metal (Cu^{II} and Fe^{III})-independent processes. In this context, we embarked on pertinent and unique structural and functional modifications to GHK to generate novel small molecule MFMs capable of modulating the metal-dependent and independent generation of excessive ROS, as well as $\text{A}\beta$ aggregation, and controlling the related oxidative stress and neuroinflammation, thereby protecting DNA and mitochondria. In GHK, glycine (G) and histidine (H) are indispensable for Cu^{II} chelation while lysine (K) mostly assists in membrane anchoring to transport Cu^{II} efficiently inside the cells.³¹ In our design, the metal ion chelation property of GH

(in GHK) was integrated with polyphenolic moieties such as L-DOPA and dopamine to obtain compounds **1** and **2** (Figure 1). To further enhance the metal chelation ability toward Cu and Fe, antioxidant properties, and inhibition of A β aggregation, glycine was substituted with a salicylaldehyde moiety to produce **3** and **4** (Figure 1).

2.2 Synthesis of Compounds 1-4

The synthetic route followed for the preparation of **1-4** is shown in Figure 1B. Fmoc-His(Trt)-OH was coupled to dopamine using HBTU and HOBT in DMF, and the product was subjected to Fmoc deprotection to obtain histidine-dopamine conjugate **1a**. The intermediate **1a** was coupled to Boc-Gly-OH in DMF followed by Boc and Trt deprotection giving compound **1**. Next, intermediate **1a** was conjugated with salicylaldehyde in DMF to obtain Schiff base **3a**. The Schiff base **3a** was treated with NaBH₄, followed by trifluoroacetic acid to obtain the target compound **3**. The L-

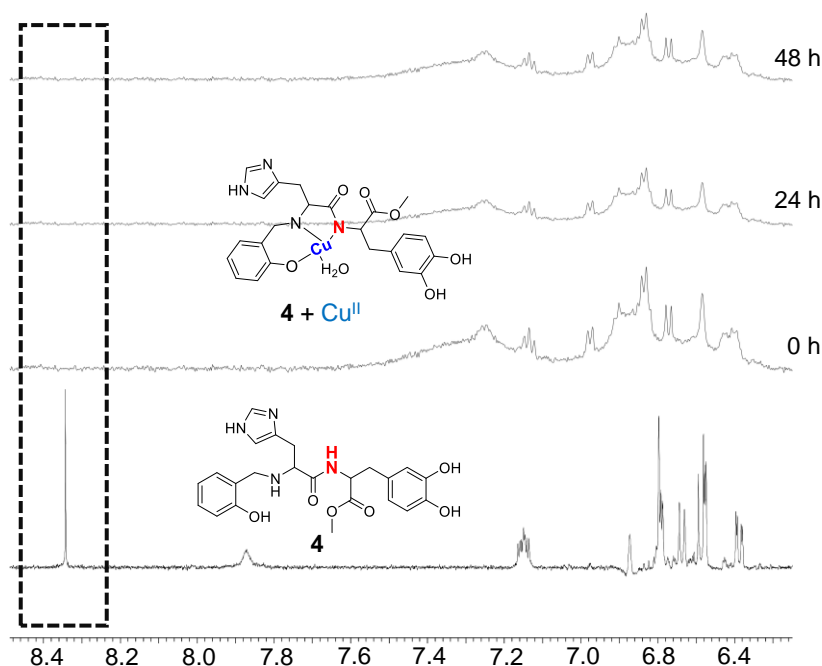


Figure 5. ¹H NMR study of **4** and **4+Cu^{II}** reveal the deprotonation of amide and its involvement in the chelation of Cu^{II}.

DOPA methyl ester was treated with tertbutyldimethylchlorosilane (TBDMSCl), and the resulting product was coupled with Fmoc-His(Trt)-OH using HBTU and HOBt in DMF followed by Fmoc deprotection, which gave the intermediate 2a. The intermediate 2a was treated with Boc-Gly-OH in DMF followed by treatment with trifluoroacetic acid and ammonium fluoride (NH_4^+F^-) to obtain the target compound **2**. The intermediate 2a was treated with salicylaldehyde in DMF to obtain Schiff base (4a). The Schiff base intermediate 4a was treated with NaBH_4 , followed by trifluoroacetic acid and NH_4^+F^- to obtain the target compound. The integrity of all the compounds were characterized using high performance liquid chromatography (HPLC), nuclear magnetic resonance (NMR), and high-resolution mass spectrometry (HRMS) (Figure 2).

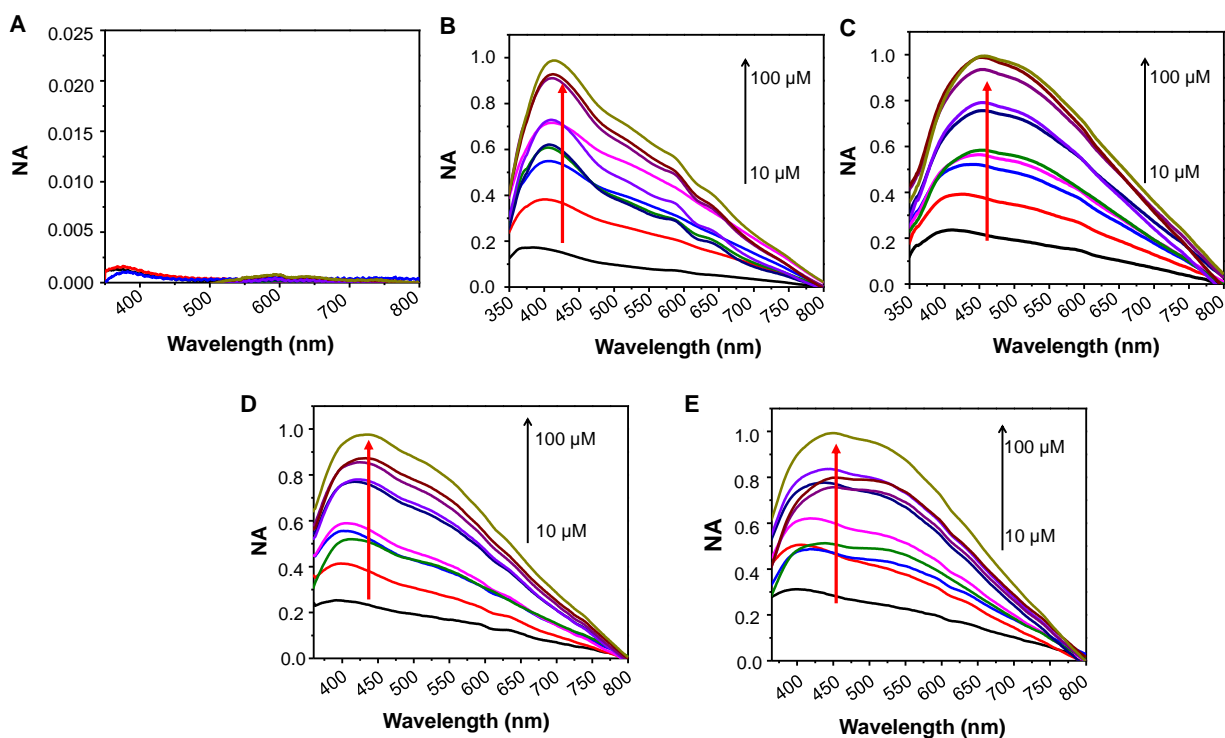


Figure 6. Metal ion chelation study. Absorption spectra of Fe^{III} treated with GHK (A), **1** (B), **2** (C), **3** (D) and **4** (E). NA: Normalized Absorbance.

2.3 Chelation of Redox-Active Metal Ions

Coordination of redox-active metal ions (Cu^{II} and Fe^{III}) with $\text{A}\beta$ has been shown to enhance the aggregation and stabilization of the oligomeric state and generation of excessive ROS through a continuous redox cycling process.^{9,32-34} The effective chelation and sequestration of redox-metal

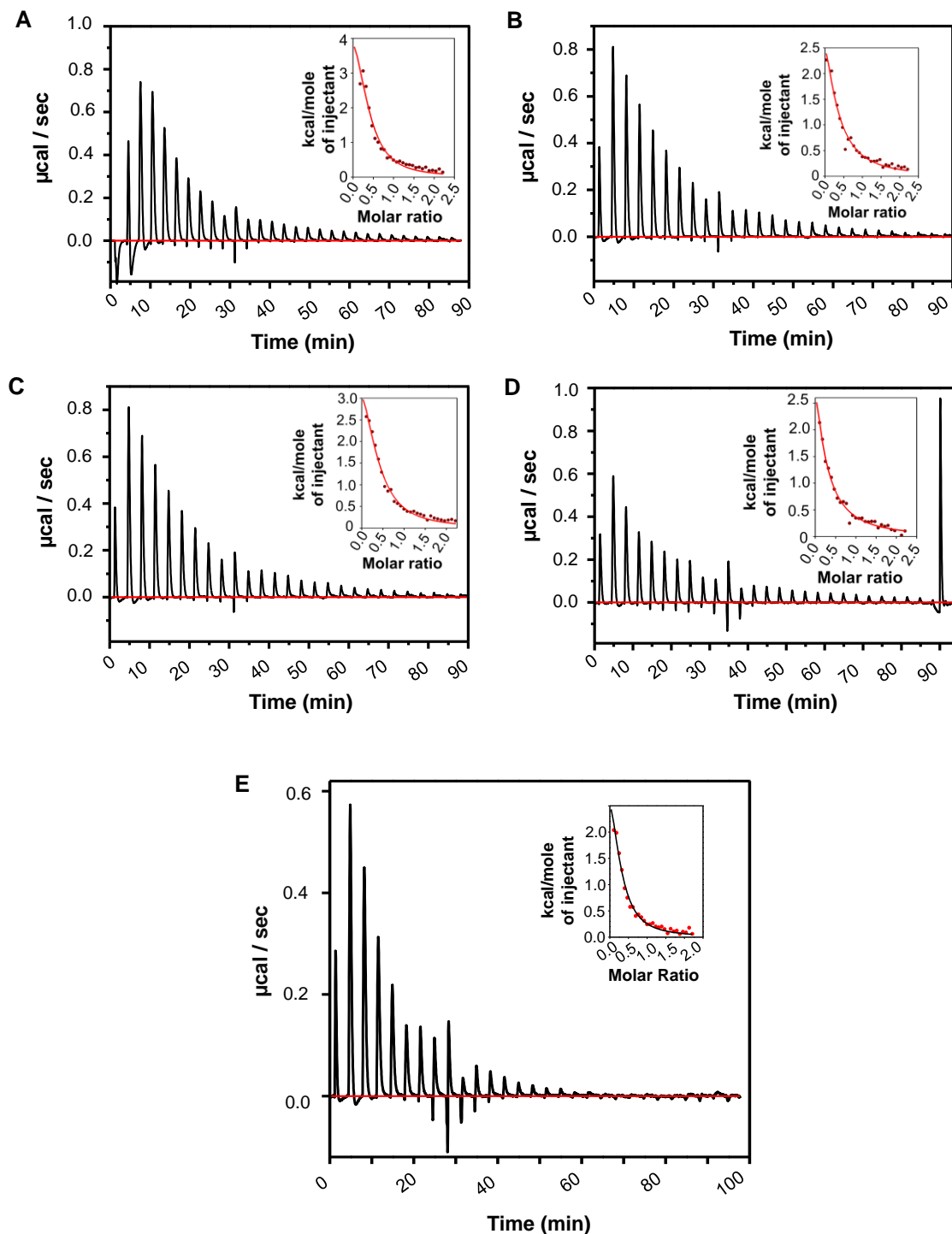


Figure 7. ITC binding isotherms of interaction of Cu^{II} with GHK (A), 1 (B), 2 (C), 3 (D) and 4 (E).

ions from A β -metal inclusion complexes and subsequent reduction of excessive ROS are key strategies to ameliorate the burden of multifaceted A β toxicity including oxidative stress.³³⁻³⁶ The chelating ability of the compounds 1-4 toward redox-active metal ions (Cu^{II} and Fe^{III}) was studied

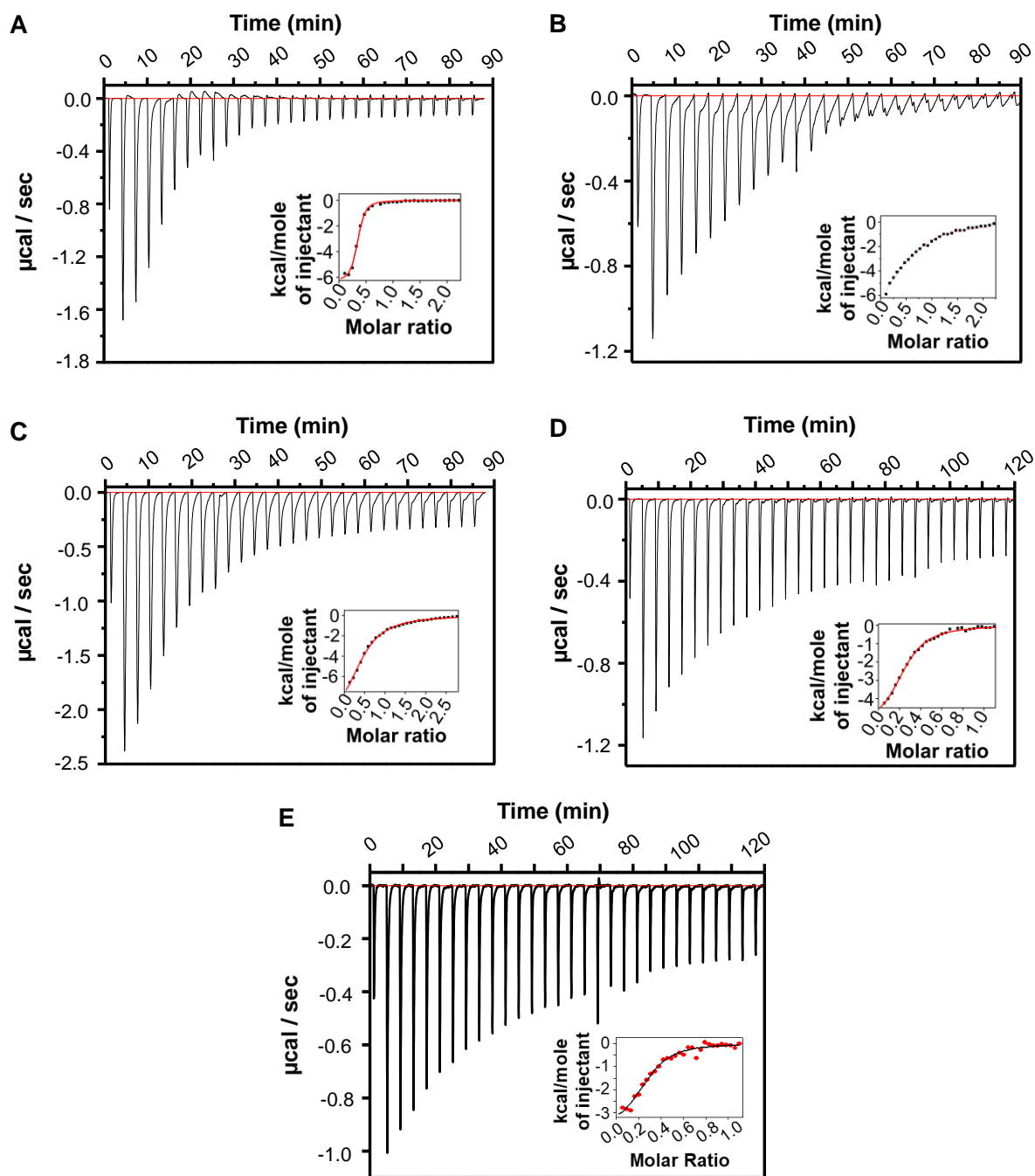


Figure 8. ITC binding isotherms of interaction of Fe^{III} with GHK (A), 1 (B), 2 (C), 3 (D) and 4 (E).

by the absorption measurements. Compounds **1** and **2** with the GH dipeptide unit exhibited broad absorption bands ($\lambda_{\text{max}} = 595 \text{ nm}$) in the presence of Cu^{II} , which indicated the formation of corresponding distorted square-planar complexes like GHK (Figure 3A).³⁷ On the other hand, **3** and **4** showed two distinct characteristic absorption bands with the maxima at 415 and 690 nm, respectively. The strong absorption intensity at 415 nm and a large bathochromic shift ($\sim 75 \text{ nm}$) compared to GHK ($\lambda_{\text{max}} = 595 \text{ nm}$) indicated the possible involvement of phenolic hydroxyl groups in Cu^{II} chelation (Figure 4). Evidently, ^1H NMR spectra showed the deprotonation of amide hydrogen at 8.35 ppm, which confirmed the involvement of the deprotonated amide nitrogen of **4** in complexation with Cu^{II} , similar to GHK- Cu^{II} complexation (Figure 5).⁴² Next, we assessed the ability of our compounds to chelate Fe^{III} and inhibit its redox activity, an inherent drawback of GHK. Remarkably, all the compounds (**1-4**) showed intense broad absorption bands in the visible region ($\lambda_{\text{max}} = 500 \text{ nm}$) in the presence of Fe^{III} (Figure 3B). The new absorption band in the visible region was attributed to the formation of an Fe^{III} complex, possibly through hydroxyl groups.³⁸ Remarkably, GHK did not show any absorbance change in the presence of Fe^{III} (Figure 6). In isothermal titration calorimetry (ITC) measurements, all the compounds including GHK showed endothermic binding with Cu^{II} (Figure 7) and dissociation constants (K_{d}) in the nanomolar range, 33.49×10^{-9} , 44.25×10^{-9} , 26.70×10^{-9} , 22.11×10^{-9} , and $19.44 \times 10^{-9} \text{ M}$ for GHK and compounds **1-4**, respectively (Figure 7). On the other hand, exothermic binding interaction was observed for the complexation of Fe^{III} (Figure 8) with compounds **1-4** with dissociation constants (K_{d}) in the nanomolar range, 34.30×10^{-9} , 27.60×10^{-9} , 5.05×10^{-9} , and $6.66 \times 10^{-9} \text{ M}$, respectively (Figure 8). Surprisingly, GHK also showed binding interaction with Fe^{III} in the ITC measurements with the dissociation constant value of $1.37 \times 10^{-9} \text{ M}$. Despite the binding interaction observed in ITC data, GHK was found to be ineffective in modulating the generation

of ROS through Fenton-type reaction, possibly due to its inability to keep Fe^{III} in a redox-dormant state (Figure 10). Further, mass spectrometry data supported the complex formation between compounds **1-4** and the metal ions (Cu^{II} and Fe^{III}) (Table 1). MALDI analysis of compound **4** and Cu^{II} showed m/z peaks corresponding to strong [M + Cu^{II}], [M + 2Cu^{II}], and [M + 3Cu^{II}] interactions (517.11, 580.04, and 642.97, respectively). Similarly, complexation of **4** and Fe^{III} was confirmed by the m/z peaks corresponding to [M + Fe^{III}], [M + 2Fe^{III}], and [M + 3Fe^{III}] interactions (510.12, 566.05, and 621.99, respectively). The absorbance, NMR, ITC, and mass analysis data together underscore the fact that we achieved the first goal of designing compounds that can chelate both Cu^{II} and Fe^{III} to tackle the metal-dependent ROS generation and related adverse effects. Thus, we explored the effect of our compounds on the redox metal dependent A β toxicity.

Table 1. MALDI mass analysis of complexes of compounds **1-4** with Cu^{II} and Fe^{III}.

| | [1-Cu ^{II}] | [1-2Cu ^{II}] | [1-3Cu ^{II}] | [1-Fe ^{III}] | [1-2Fe ^{III}] | [1-3Fe ^{III}] |
|------------|-----------------------|------------------------|------------------------|------------------------|-------------------------|-------------------------|
| Calculated | 410.08 | 473.01 | 535.94 | 403.09 | 459.02 | 514.96 |
| Observed | 410.07 | 474.01 | 535.24 | - | - | - |
| | [2-Cu ^{II}] | [2-2Cu ^{II}] | [2-3Cu ^{II}] | [2-Fe ^{III}] | [2-2Fe ^{III}] | [2-3Fe ^{III}] |
| Calculated | 468.09 | 531.02 | 593.95 | 461.09 | 517.03 | 572.96 |
| Observed | 468.14 | 530.08 | 593.30 | 460.08 | - | - |
| | [3-Cu ^{II}] | [3-2Cu ^{II}] | [3-3Cu ^{II}] | [3-Fe ^{III}] | [3-2Fe ^{III}] | [3-3Fe ^{III}] |
| Calculated | 459.10 | 522.03 | 584.96 | 452.11 | 508.04 | 563.98 |
| Observed | 459.13 | 521.04 | 584.28 | 451.11 | - | 564.91 |
| | [4-Cu ^{II}] | [4-2Cu ^{II}] | [4-3Cu ^{II}] | [4-Fe ^{III}] | [4-2Fe ^{III}] | [4-3Fe ^{III}] |
| Calculated | 517.11 | 580.04 | 642.97 | 510.12 | 566.05 | 621.99 |
| Observed | 517.15 | 580.10 | 642.28 | 509.13 | 568.13 | 622.10 |

2.4 Metal-Dependent Antioxidant Assay

The inclusion complex of redox-active metal ions (Cu^{II} and Fe^{III}) in $\text{A}\beta$ species instigates the Fenton-type reaction to generate excessive ROS (H_2O_2 and OH^\bullet), leading to oxidative stress and

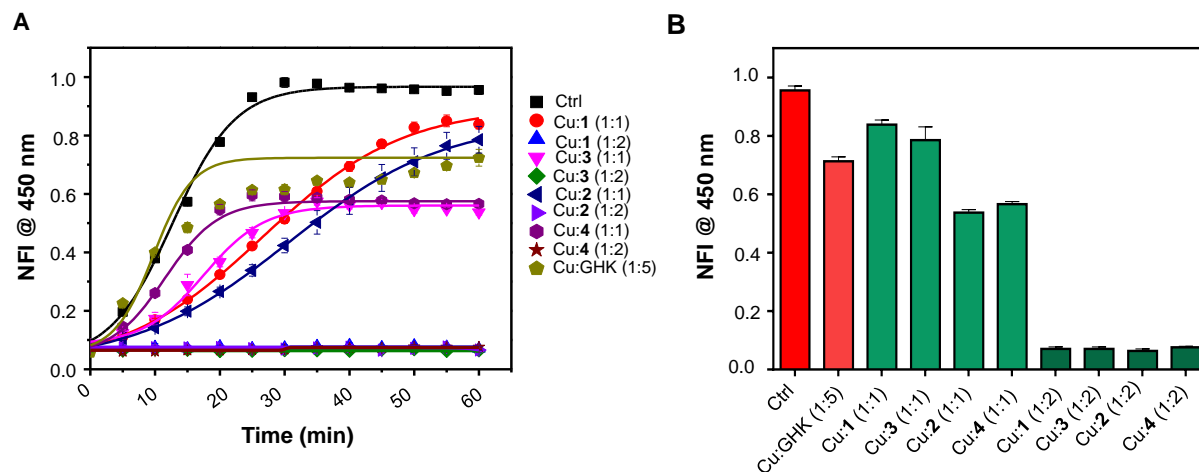


Figure 9. (A) Plot of normalized fluorescence intensity (NFI) of 7-OH-CCA ($\lambda_{\text{em}} = 450 \text{ nm}$) containing Cu^{II} -Asc system as function of time in the absence (ctrl) and presence of compounds **1-4** and GHK at 37°C . (B) NFI of 7-OH-CCA generated in solution containing Cu^{II} -Asc system, in the absence (control) and presence of compounds **1-4** and GHK after 1 h at 37°C . Ctrl: Control.

related toxicity.^{9,16,35} Therefore, chelation of redox-active metal ions (Cu^{II} and Fe^{III}) and keeping them in the redox-dormant state under a reducing environment is crucial to prevent excessive ROS generation and oxidative stress.^{5,20,39,40} We performed *in vitro* and *in cellulo* antioxidant assays using redox metal ion (Cu^{II} or Fe^{III}) and ascorbate (Asc) to validate the redox-silencing ability of our compounds (**1-4**). Figure 9 shows that sample incubated with Cu^{II} -Asc in the absence of our compounds showed maximum 7-HO-CCA fluorescence emission (100%). Addition of compounds **1-4** ($\geq 20 \mu\text{M}$) considerably reduced the fluorescence emission to $<10\%$, whereas the control GHK showed significant 7-HO-CCA fluorescence (71%) at a concentration as high as $50 \mu\text{M}$. To check the production of excessive OH^\bullet more efficiently as compared at lower concentration ($10 \mu\text{M}$) of

compounds **3** and **4**, the samples showed 7-HO-CCA fluorescence emission of 48% and 54%, respectively, compared to 83% and 78% for **1** and **2**, respectively, which indicates that **3** and **4** were superior to the others, which showed moderate activity (Figure 9). Next, we assessed the effect of compounds **1-4** on the production of OH^\bullet from the Fenton-type reaction of Fe^{III} (Figure 10). As expected, the disproportionation reaction occurred in the sample containing H_2O_2 alone and did not show any 7-HO-CCA fluorescence enhancement. However, in the presence of Fe^{III} , a strong fluorescence enhancement was observed owing to the production of excess OH^\bullet (Fenton-

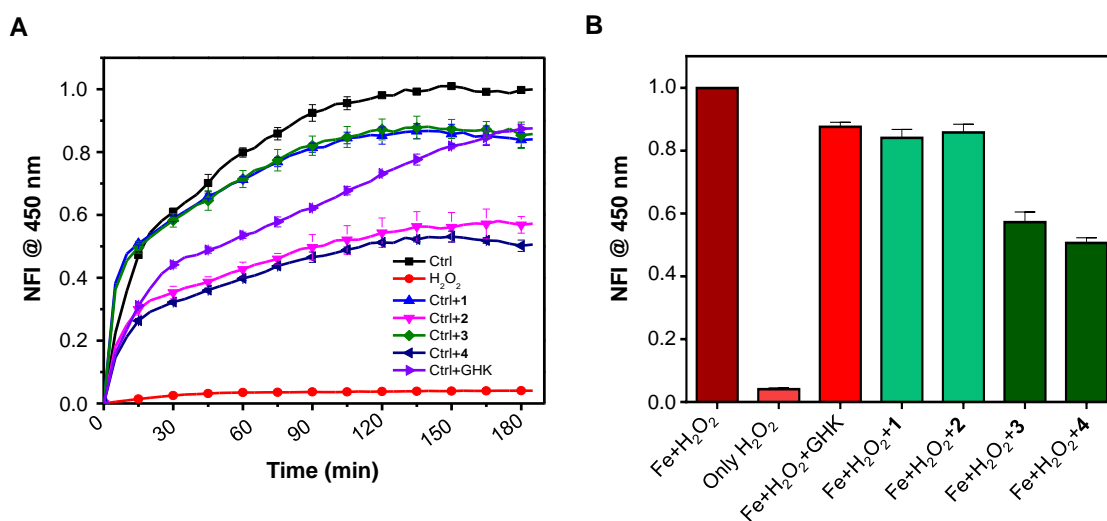


Figure 10. (A) Plot of NFI of 7-OH-CCA ($\lambda_{\text{em}} = 450 \text{ nm}$) generated in solution containing Fe^{III} - H_2O_2 -Asc system as function of time in the absence (ctrl) and presence of compounds **1-4** and GHK at 37°C . (B) NFI of 7-OH-CCA generated in solution containing Fe^{III} - H_2O_2 -Asc system, in the absence and presence of compounds **1-4** and GHK after 3 h at 37°C .

type reaction). Remarkably, samples treated with compounds **3** and **4** showed 50% and 55% reduction, respectively, in 7-Hydroxycoumarin carboxylic acid (7-HO-CCA) fluorescence emission; **1**, **2**, and GHK (16%, 15%, and 13% reduction, respectively) showed minimal reduction compared to the control (100%). This is a clear indication that **3**- and **4** bound Fe^{III} was not involved in the redox process to generate OH^\bullet in the presence of H_2O_2 . On the other hand,

compounds **1**, **2**, and GHK were found to have minimal interference in the Fe^{III} redox process for checking ROS generation. DNA oxidative damage by elevated ROS under AD conditions is one of the most dreadful consequences that aggravate the neuronal toxicity.³⁰ The chemical reaction of ROS with DNA caused breaking of the phosphate backbone or nucleobase modifications, leading to cellular death.⁵ We assessed the ability of compounds **1-4** and GHK to protect the DNA from oxidative damage using plasmid DNA (pUC19) as a model system (Figure 11). Agarose gel data showed that DNA sample treated with Cu^{II}-Asc (ctrl) exhibited ~100% noncoiled (NC) form

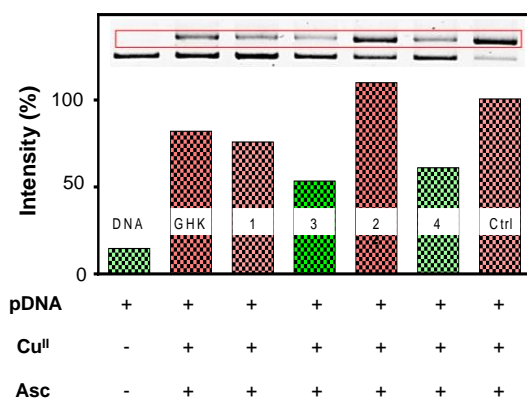


Figure 11. DNA cleavage and rescue studies on pDNA in the presence of Cu^{II}-Asc redox system by compounds **1-4**, monitored by gel electrophoresis.

while pDNA (PBS treated) contained ~14% NC (existing mostly as supercoiled form, SC), which is attributed to oxidative DNA damage by the in situ generated OH[•]. Under similar conditions, pDNA samples treated with GHK showed ~74% NC form when compared to samples treated with Cu^{II}-Asc alone (100%). Interestingly, compound **3** and **4** treated samples showed lower percentage of the NC form of pDNA (~48% and 55%, respectively) compared to the control sample treated with Cu^{II}-Asc (~100%), which was indicative of minimal oxidative damage to DNA (Figure 11). This result revealed that the compounds **3** and **4** protected DNA by chelating Cu^{II} and interrupting

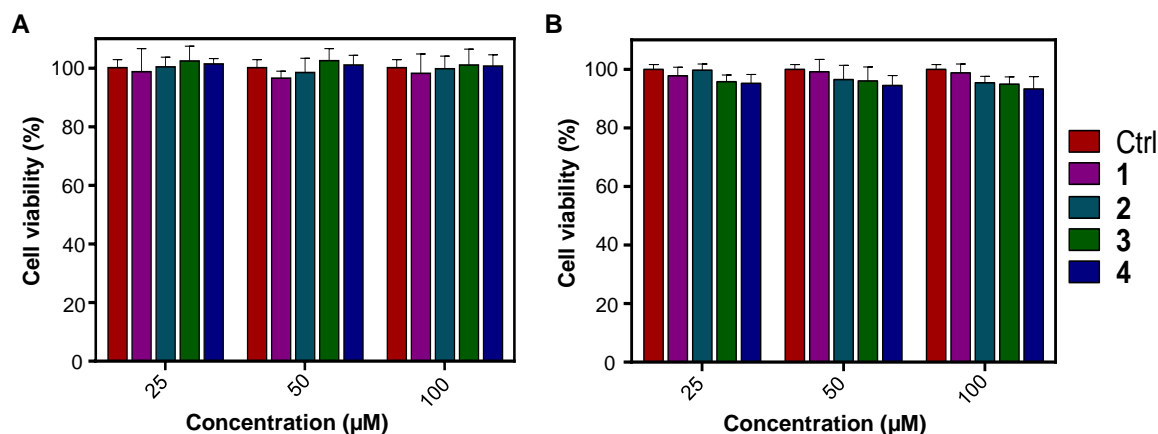


Figure 12. Viability data of PC12 (A) and BV2 (B) cell lines after exposing (24 h) to different concentrations of compound **1-4** (25, 50 and 100 μM), respectively.

its redox process. The inhibition ability of compounds **1-4** against ROS and DNA damage encouraged us to evaluate their antioxidant properties under in cellulo conditions. First, we assessed the cytotoxicity of compounds **1-4** on neuroblastoma (PC12) and neuroglia (BV2) cells. The cytotoxicity assay showed that cells treated with compounds **1-4** exhibited good viability in the concentration range of 10-100 μM (Figure 12). To check the antioxidant properties under in cellulo conditions, PC12 cells were incubated with Cu^{II} -Asc redox pair in the absence and presence of compounds **1-4** or GHK. Only Cu^{II} -Asc treated wells exhibited 65% cell viability compared to untreated control cells (100%) (Figure 13A). The cells in the media consisting of Cu^{II} -Asc redox system showed remarkable improvement in viability (97%) upon treatment with **4**, while **1-3** and GHK exhibited 79%, 73%, 86%, and 70%, respectively. The observed rescue, as revealed by the excellent cell viability of PC12 cells under stress from Cu^{II} -Asc redox system, confirmed that compound **4** effectively reduced the OH^{\cdot} production ($\sim 91\%$) by chelating Cu^{II} and maintaining it in a redox-dormant state. Similarly, cellular toxicity from OH^{\cdot} produced from the Fe^{III} - H_2O_2 system was studied in the presence of compounds **1-4** (Figure 13B). EDTA- Fe^{III} and H_2O_2 treated

cells showed 60% cytotoxicity compared to untreated control cells (0%). The PC12 cells treated with EDTA-Fe^{III} complex and compounds **1-4** showed a significant reduction in the cytotoxicity by 36%, 35%, 30%, and 25%, respectively. Under similar conditions, cells treated with GHK showed 52% cytotoxicity. The cytotoxicity data showed that compound **4** effectively inhibited cellular toxicity arising from the Fe^{III} redox system with overall cytotoxicity reduction by 35%. As expected, GHK did not have a significant effect in modulating the cellular toxicity (8%) arising from the Fe^{III} redox system as it failed to keep the Fe^{III} system in a redox-dormant state. These metal-dependent antioxidant studies clearly demonstrated that our compounds, in particular **4**, were excellent antioxidant molecules that effectively inhibited ROS production by chelating with redox active Cu^{II} and Fe^{III} and maintaining them in the redox dormant states.

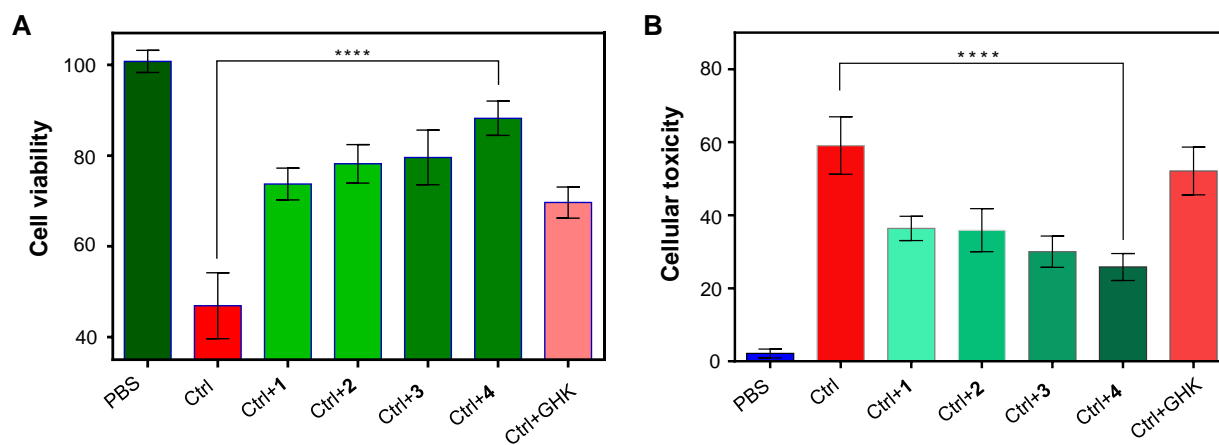


Figure 13. (A) The cell viability study of PC12 cell lines after exposing to Cu^{II}-Asc system, in absence (Ctrl) and presence of compounds **1-4** and GHK. (B) Cellular toxicity of EDTA-Fe^{III}-H₂O₂ redox system after exposing PC12 cell lines with EDTA-Fe^{III} and H₂O₂, in the absence (ctrl), and presence of compounds **1-4** or GHK.

2.5 Metal-Independent Antioxidant Assay

Under AD conditions, mitochondrial dysfunction alters the electron chain and subsequently produces excess ROS.^{9,19,22,41} Therefore, scavenging the reactive intermediates using antioxidants is considered a promising approach to confront oxidative stress, and we validated the radical

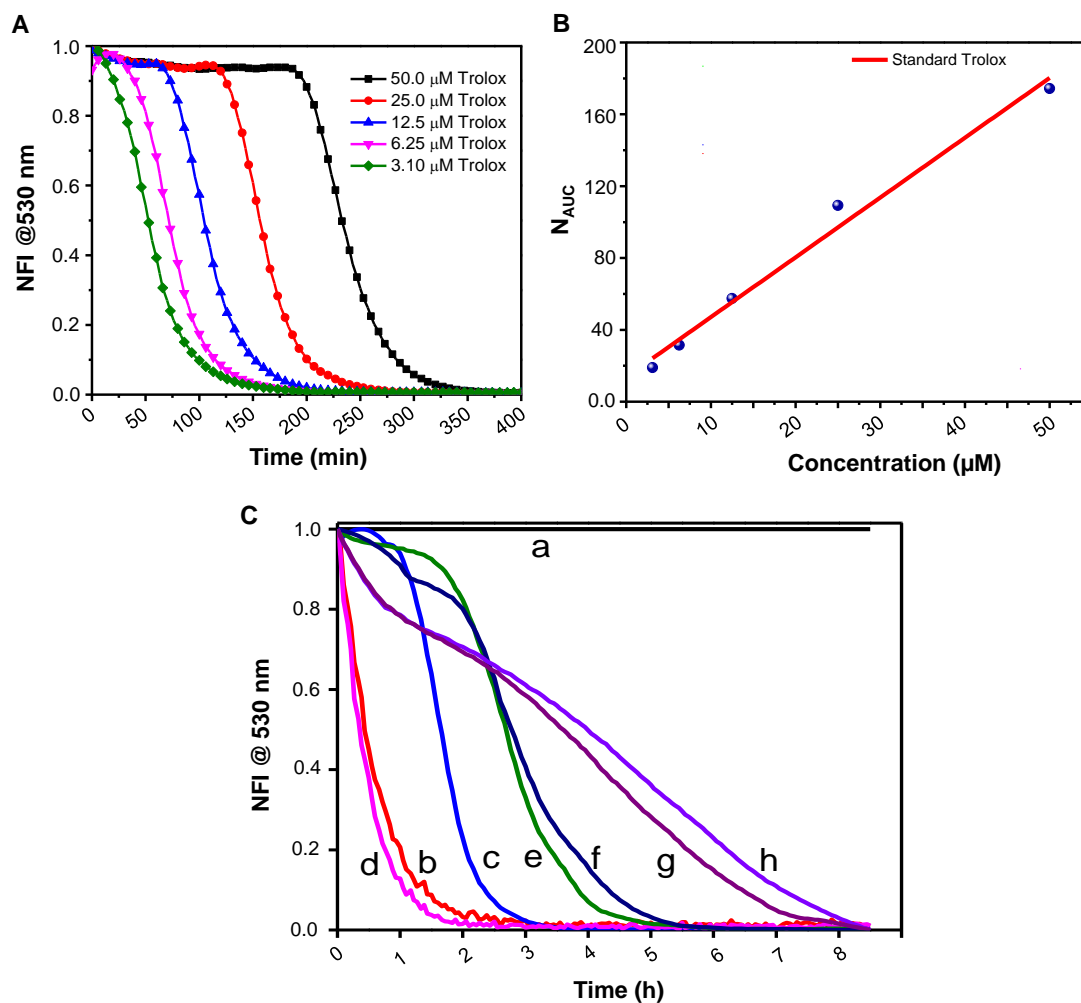


Figure 14. (A) Plot of NFI of fluorescein at 530 nm measured upon incubating with APPH (200 µM) and in presence of Trolox (3.1 to 50 µM). (B) The plot of net area under the curve (N_{AUC}) in plot (A) as function of Trolox concentration. (C) NFI of fluorescein (a) at 530 nm measured upon incubating with APPH (200 µM) in the absence (b) and the presence of 12.5 µM Trolox (c), 1 (e), 2 (f), 3 (g), 4 (h), and GHK (d). NFI: Normalized fluorescence intensity, APPH: 2,2'-Azobis(2-amidinopropane) dihydrochloride.

scavenging ability of compounds **1-4** (Figure 14). At first, Trolox equivalent antioxidant capacity (TEAC) assay was performed, and the data in Figure 14C show that APPH radicals rapidly

quenched the fluorescence (fluorescein) at 530 nm, whereas Trolox and compounds **1-4** delayed the fluorescence quenching by efficiently scavenging the radicals. Remarkably, compound **4** showed the highest TEAC value of 4.96 compared to **1-3** and GHK (2.60, 2.67, 3.70, and 0.11, respectively), which is an indication that **4** is an efficient scavenger of the radicals or RIS. Further, we evaluated the radical scavenging ability of compounds **1-4** through 2,2'-azino-bis(3-ethylbenzothiazoline-6-sulfonic acid) (ABTS) and 2,2-diphenyl-1-picrylhydrazyl (DPPH)

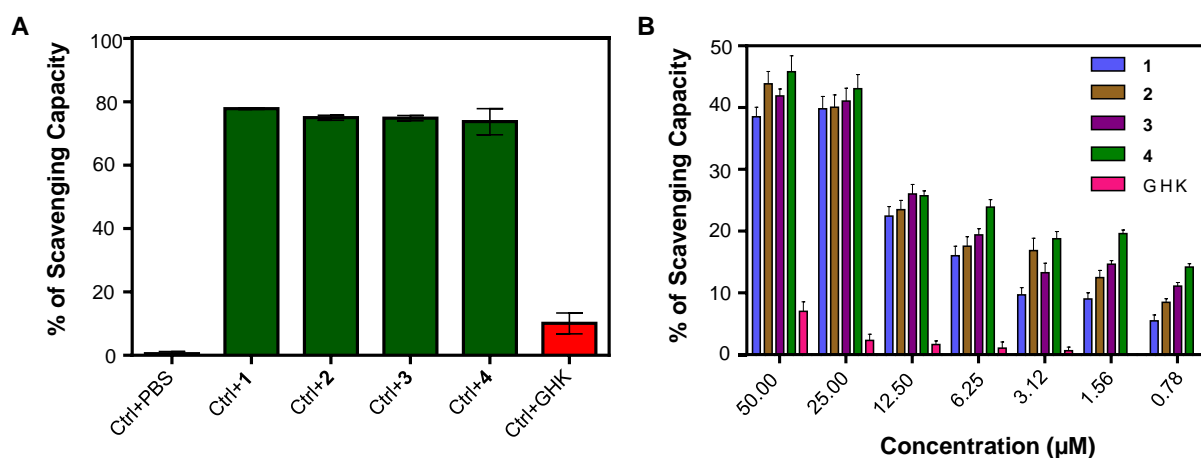


Figure 15. (A) Radical scavenging capacity of compounds **1-4** and GHK assessed against of ABTS^{•+}. ABTS: 2,2'-azino-bis(3-ethylbenzothiazoline-6-sulphonic acid). (B) Antioxidant scavenging ability (radical scavenging capacity) of compounds **1-4** and GHK at different concentrations (50, 25, 12.5, 6.25, 3.12, 1.56 and 0.78 μM) assessed against DPPH. DPPH: 2,2-Diphenyl-1-(2,4,6-trinitrophenyl) hydrazyl.

assays.^{19,41,42} In ABTS assay, the control sample showed 0%, while GHK exhibited negligible scavenging efficiency (SE) of 10%; compounds **1-4** exhibited good SE of 77%, 75%, 74%, and 73%, respectively, attributed to their polyphenolic nature (Figure 15A). Compounds **1-4** (50.0 μM) showed appreciable SE (38%, 43%, 41%, and 45%, respectively) compared to the control (0%) in DPPH assay. Interestingly, compound **4** showed significant SE (14%) at a concentration as low as 0.78 μM, at which GHK remains completely inactive in scavenging DPPH radical (Figure 15B).

These results also reveal that compound **4** is an excellent radical scavenger at sub-micromolar concentrations when compared to **1-3** and GHK.

Next, 2',7'-dichlorodihydrofluorescein diacetate (DCFDA) assay was performed to assess the total amount of intracellular ROS in the absence and presence of compounds **1-4** and GHK. GHK-treated cells (97%) did not show significant effect on the DCF fluorescence while compounds **1-4** treated cells showed 52%, 52%, 38%, and 20%, respectively, compared to cells treated only with H₂O₂ (100%). Remarkably, compound **4** exhibited ~80% reduction in intracellular ROS and emerged as the most efficient ROS scavenger compared to **1-3** and GHK (48%, 48%, 62%, and 3%, respectively) (Figure 16A). In cell rescue assay, only H₂O₂ (150 μM) treated cells showed ~35% reduction in cell viability compared to untreated control (100%), which increased to ~97%

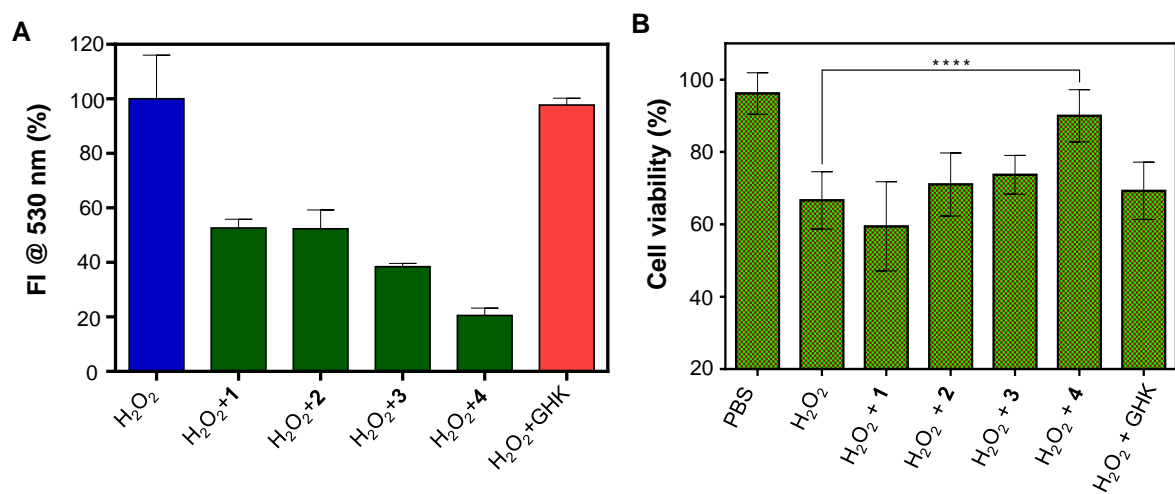


Figure 16. (A) In cellulo ROS quenching assay. The cell viability of PC12 cells assessed after exposure to H₂O₂ in the absence (ctrl) and presence compounds **1-4** and GHK. (B) Fluorescence intensity (FI) of DCF at 530 nm measured in PC12 cells upon incubating (4 h) with H₂O₂ in absence and presence of compounds **1-4** and GHK. DCF: 2',7'-dichlorofluorescein.

in the presence of compound **4** (Figure 16B). These metal-independent antioxidant studies show that compounds **1-4** were better antioxidants than Trolox and could efficiently rescue the cells by scavenging the ROS under in cellulo conditions. Remarkably, this effectively overcame the

critical limitations of GHK, that is, its inability to inhibit Fe^{III} -dependent and metal-independent ROS generation and oxidative stress.

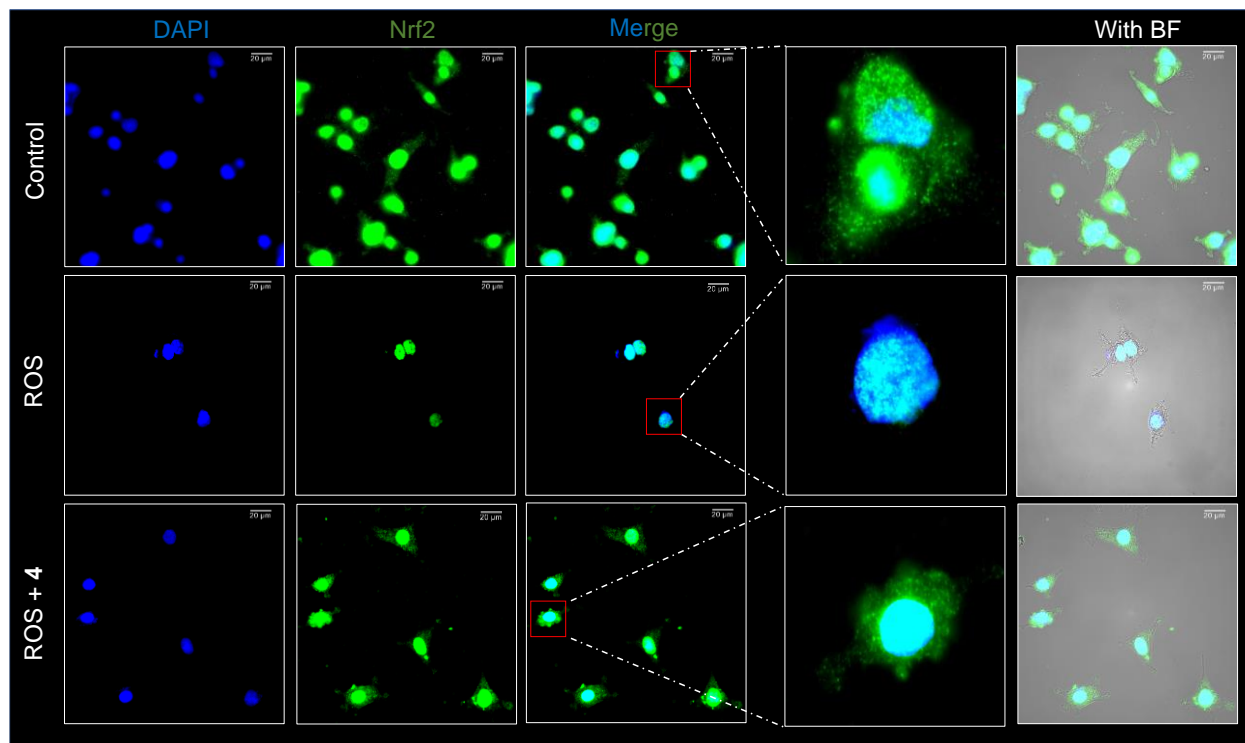


Figure 17. Fluorescence optical microscopy images of PC12 cells stained with DAPI and Nrf2 specific antibody after exposure of the cells to PBS (control), exogenous ROS (H_2O_2 , 100 μM), and H_2O_2 (100 μM) + **4** (100 μM). Scale bar: 20 μm .

2.6 Modulation of Nrf2 Signaling Under Oxidative Stress Conditions

The antioxidant defense mechanism effectively cut down the toxic ROS in the cells, and this defense mechanism is controlled by nuclear factor erythroid 2-related factor 2 (Nrf2)/antioxidant response element (ARE) signaling pathway.¹⁵ In this context, we assessed the Nrf2 signaling under oxidative stress conditions to demonstrate the antioxidant ability of **4**. Figure 17 shows that under normal physiological conditions Nrf2 is found in both nuclear and cytosolic matrix. However, under oxidative stress conditions, it is mostly localized inside the nucleus to activate the endogenous antioxidant defense mechanism, which shows the imbalance of redox homeostasis in

the cells. Remarkably, the cells under oxidative stress conditions upon treatment with **4** showed localization of Nrf2 in both nuclear and cytosolic matrix. This restoration of nuclear and cytosolic Nrf2 localization shows that **4** effectively modulates the oxidative stress by scavenging toxic ROS. The excellent antioxidant properties and ability to restore the in cellulo redox home stasis validate that MFM **4** is able to maintain the intracellular redox homeostasis and modulate the multifaceted toxicity in AD conditions (Figure 17).

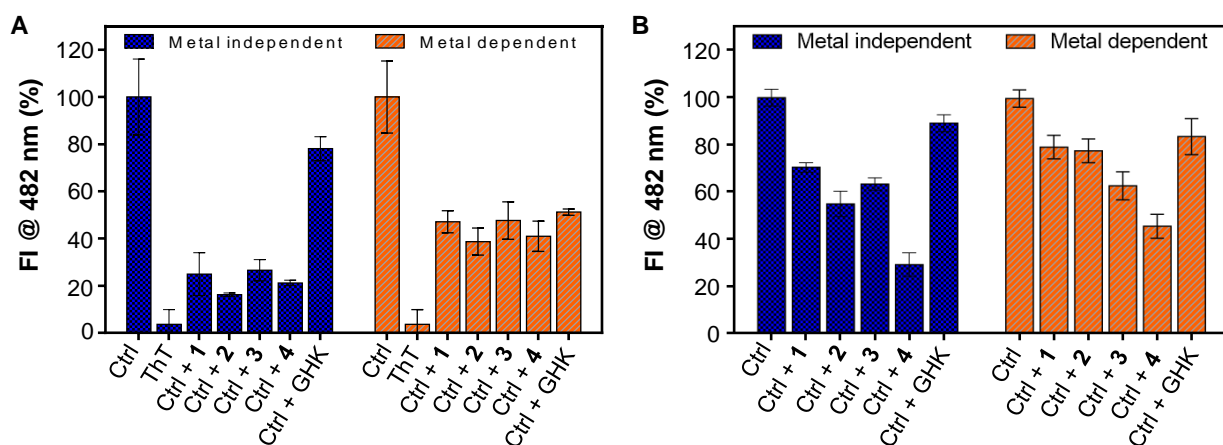


Figure 18. (A) The percentage of ThT fluorescence ($\lambda_{em}=482$ nm) intensity is plotted for Cu^{II} -independent (deep blue) and dependent (orange) $\text{A}\beta_{42}$ aggregation, in absence and presence of compounds **1-4** and GHK. (B) The change in ThT fluorescence emission intensity (dissolution activity) plotted for Cu^{II} -independent (deep blue) and dependent (orange) $\text{A}\beta_{42}$ fibrils, in the absence and presence of compounds **1-4** and GHK.

2.7 Inhibition of Amyloid Aggregation

Inhibition of polymorphic $\text{A}\beta$ aggregation is a promising approach to developing effective therapeutic agents for AD.^{22,43-48} In this context, we studied the effect of our compounds **1-4** on metal-independent and -dependent $\text{A}\beta_{42}$ aggregation, and compounds **1-4** showed minimal ThT fluorescence (24%, 17%, 26% and 18%, respectively) in comparison to that of $\text{A}\beta_{42}$ alone, which

is considered as 100%; GHK exhibited 78% ThT fluorescence (Figure 18A). The data also revealed that the most promising antioxidant **4** inhibited A β 42 aggregation by >80% compared to ~20% by GHK. Further, GHK, a well-known Cu^{II} chelator, showed 51% fluorescence emission, whereas compounds **1-4** displayed approximately 47%, 36%, 47% and 38%, respectively, in comparison to A β 42–Cu^{II} (100%) (Figure 18A). This result demonstrates that our best modulator, **4**, inhibited the metal-mediated A β 42 aggregation by >60%, which corresponds to 50% improvement in the inhibition activity compared to GHK. To further strengthen these findings, TEM analysis was performed, which showed distinct morphologies for Cu^{II}-dependent and –

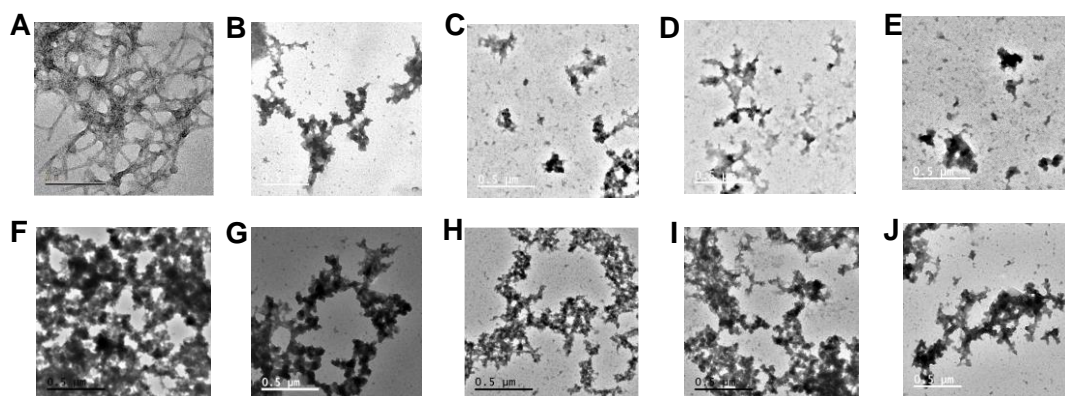


Figure 19. TEM images of metal-independent A β 42 fibrils (A) and upon treatment with compounds **1-4** (B, C, D and E, respectively). TEM images of metal-dependent A β 42 fibrils (F) and upon treatment with compounds **1-4** (G, H, I and J, respectively).

independent A β 42 aggregates with the former showed highly intertwined fibrillar structure (Figure 19). Interestingly, upon treatment with **4**, the amount of aggregates drastically decreased both in the absence and in the presence of Cu^{II}, which is in good agreement with the results from ThT assay. To evaluate the ability of **4** to modulate Zn^{II} dependent A β 42 aggregation, we performed an inhibition study tracked by ThT fluorescence assay (Figure 20). Compound **4** showed moderate inhibition of ~30% against Zn^{II}-induced A β 42 aggregation. These data confirmed that compound

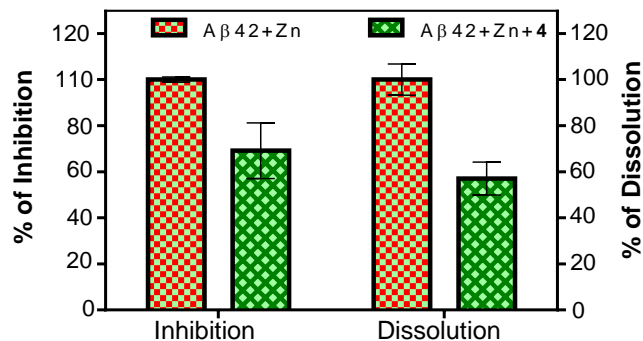


Figure 20. The percentage of ThT fluorescence ($\lambda_{em}=482$ nm) intensity is plotted for Zn^{II} -dependent A β 42 aggregation modulation (inhibition and dissolution), in presence of compounds **4**.

4 is capable of modulating metal-dependent and -independent A β 42 aggregation by interacting with the different forms of A β 42 species.

Next, we evaluated the effect of compounds **1-4** against Cu^{II} -dependent and -independent A β 42 aggregates in dissolution assay. The untreated sample containing only A β 42 aggregates showed maximum ThT fluorescence, while the samples treated with compounds **1-4** showed significant decrease in fluorescence (Figure 18B). Compound **4** was found to be most efficient in dissolving the toxic A β 42 aggregates (~71%), while compounds **1-3** and GHK showed 30%, 45%, 37%, and 11% dissolution efficiency, respectively. Compound **4** was found to be the most efficient

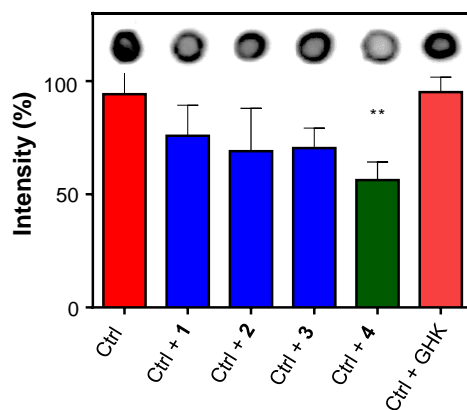


Figure 21. Dot blot assay (dissolution activity): blot intensity of A β 42 fibrils before and after treatment with compounds **1-4** or GHK.

modulator (dissolution) of Cu^{II} -dependent $\text{A}\beta_{42}$ fibrils as it showed $\sim 55\%$ decrease in fluorescence compared to untreated sample, which exhibited maximum fluorescence ($\sim 100\%$). In contrast, compounds **1-3** and GHK showed 22%, 23%, 38%, and 17% decrease in fluorescence, respectively. Figure 21, the dot blot image showed that the sample treated with **4** dissolved $\sim 50\%$ of $\text{A}\beta_{42}$ fibrils, while compounds **1-3** and GHK exhibited minimal dissolution ability (approximately 20%, 30%, 30%, and 2%, respectively) when compared to PBS (control, 0%). Next, the ability of **4** to dissolve Zn^{II} -dependent $\text{A}\beta_{42}$ fibrils was studied (Figure 20). $\text{A}\beta_{42}$ - Zn^{II} fibrils treated with compound **4** showed decrease in the ThT fluorescence, which corresponds to $\sim 43\%$ dissolution efficiency. Overall, the potential modulator **4** inhibited $\text{A}\beta_{42}$ fibrillar aggregate formation as well as dissolved the preformed toxic fibrils more efficiently than GHK. In continuation, we demonstrated effective redox silencing of Cu^{II} from the $\text{A}\beta$ - Cu^{II} complex by compounds **1-4**. These results are in good agreement with the Cu^{II} -Asc assay and further support the observation that **4** effectively sequestered $\text{A}\beta_{42}$ -bound Cu^{II} and maintained it in a redox-

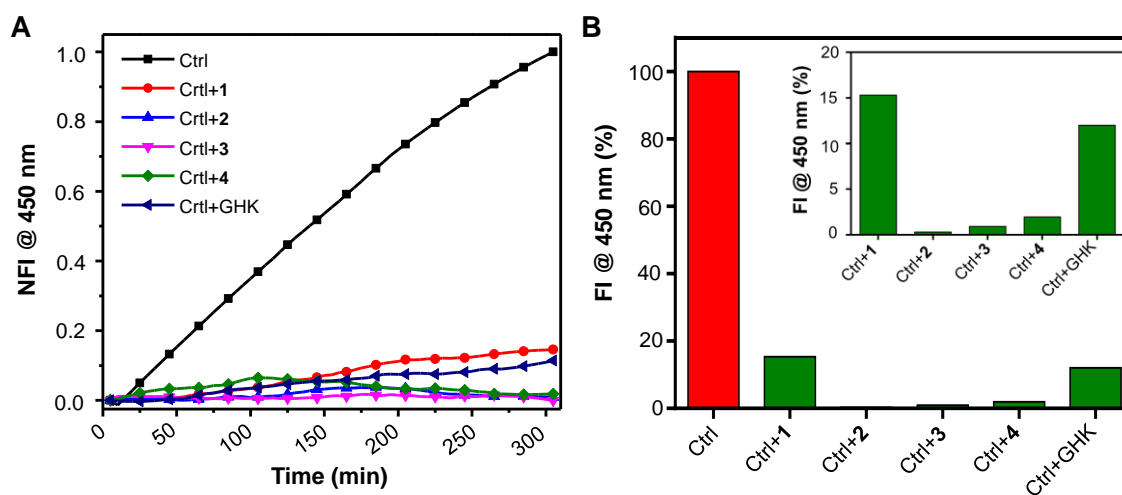


Figure 22. (A) Plot of NFI of 7-OH-CCA ($\lambda_{\text{em}} = 450$ nm) containing $\text{A}\beta_{42}$ - Cu^{II} -Asc in the absence (ctrl) and presence of compounds **1-4** and GHK at 37°C . (B) FI of 7-OH-CCA generated in solution containing $\text{A}\beta_{42}$ - Cu^{II} -Asc system, in the absence (ctrl) and presence of compounds **1-4** and GHK after 5 h at 37°C .

dormant state, thereby arresting excess ROS production and oxidative DNA damage (Figures 22 and 23). Compounds **1-4** were evaluated under in cellulo conditions to assess their inhibition efficacy against A β toxicity.^{5,20,22} To evaluate the ability of our compounds to ameliorate A β toxicity, AD-like situations were simulated by the addition of A β 42 to cultured PC12 cells. A β 42 monomers formed toxic aggregation species in the cell growth media, which damaged the cultured cells; as a result, cell viability was decreased by 48% compared to untreated cells (control) with

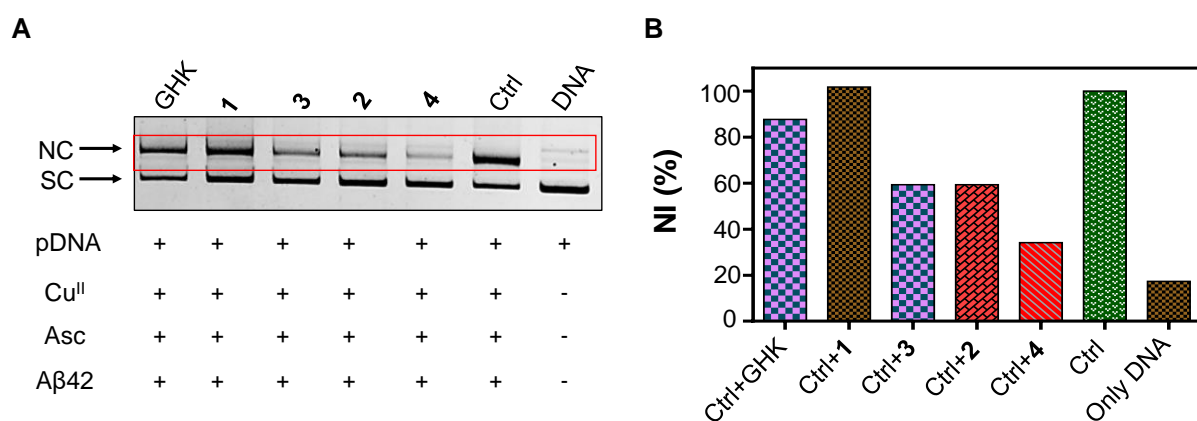


Figure 23. (A) DNA (pDNA: pUC19) cleavage in presence of A β 42-Cu^{II}-Asc redox system and evaluation of DNA protection by compounds **1-4** and GHK, monitored by gel electrophoresis. (B) Normalized intensity (NI) of non-coiled (NC) from of pDNA after treating with A β 42-Cu^{II}-Asc in the absence (ctrl) and presence of compounds **1-4** and GHK.

100% viability (Figure 24A). The treatment of cells affected by A β 42 toxicity with compounds **1-4** showed improved cell viability. Specifically, compounds **2** and **4** effectively inhibited the A β 42 aggregation process and rescued the cells, thereby increasing the cell viability by 21% and 17%, respectively (total cell viability of 69% and 65%, respectively) (Figure 24A). Subsequently, PC12 cells were cultured and treated with fibrillar aggregates formed in the absence and presence of Cu^{II} or modulated fibrillar aggregates (Cu^{II}-independent and -mediated) by compounds **1-4** or GHK.

The cells treated with Cu^{II}-independent A β 42 fibrillar aggregates (10 μ M) in the cell media showed ~50% reduction in viability when compared to untreated cells (100% viability) (Figure 24B). Interestingly, the viability of cells treated with A β 42 fibrillar aggregates (10 μ M) was effectively inhibited by compound **4** (50 μ M), increasing the viability to 84%, while compounds **1-3** and GHK showed 48%, 68%, 77%, and 64% improvement when compared to the control (100%). Cu^{II}-induced A β 42 fibrillar aggregates were more toxic and showed ~45% cell viability compared to Cu^{II}-independent A β 42 fibrillar aggregates (50%), treated cells and untreated control (100%) (Figure 24B). This result indicates that modulator **4** reduced the Cu^{II}-induced A β 42 fibrillar toxicity by ~77% (cell viability 88%), while compounds **1-3** and GHK were found to reduce the same by approximately 50%, 59% , 61%, and 42%, respectively. These in cellulo experiments confirmed that compound **4** protected cells against Cu^{II}-induced and -independent A β toxicity and, hence, was the best MFM candidate, which encouraged us to explore the molecular-level interactions between **4** and A β 42.

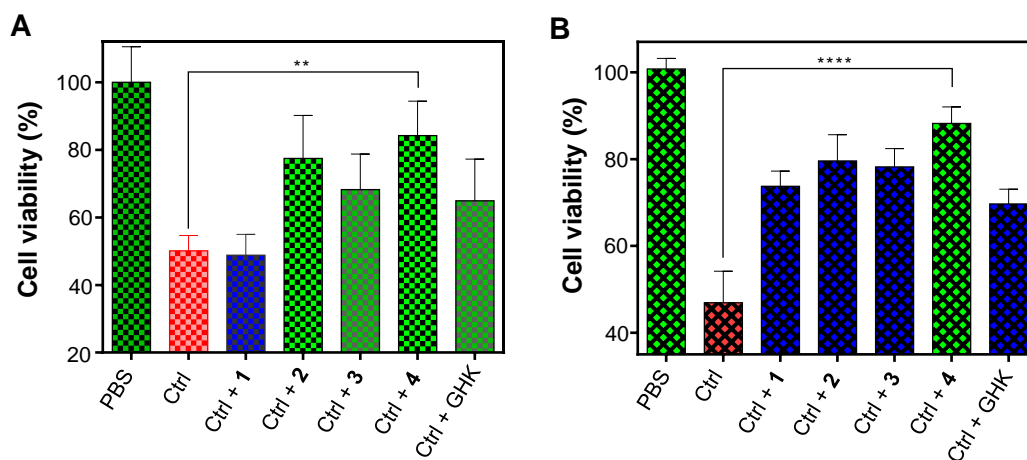


Figure 24. (A) Modulation of A β 42 toxicity in neuronal cells. The cell viability of PC12 cells assessed after exposing to A β 42, in the absence (only PBS) and presence of compounds **1-4** or GHK. (B) Modulation of A β 42 toxicity in neuronal cells: The cell viability of PC12 cell lines after exposing to Cu^{II}-independent A β 42 fibrils (ctrl) and inhibited Cu^{II}-independent A β 42 fibrils with compounds **1-4** or GHK.

2.8 Molecular-Level Interaction of **4** with A β 42

We performed nuclear magnetic resonance (NMR) spectroscopy measurements to understand the molecular interactions between the lead compound **4** and A β 42 (Figure 25). NMR spectra at different time points showed that peaks for exchangeable hydrogen atoms (e and m) of **4** at 7.95 and 8.05 ppm, respectively, were missing in the NMR spectrum and appeared upon the addition of A β 42; this was attributed to the formation of hydrogen bonds between **4** and A β 42 (Figure 25A). The ^1H NMR spectra revealed that aromatic protons of L-DOPA (j, k, and l) and salicylaldehyde

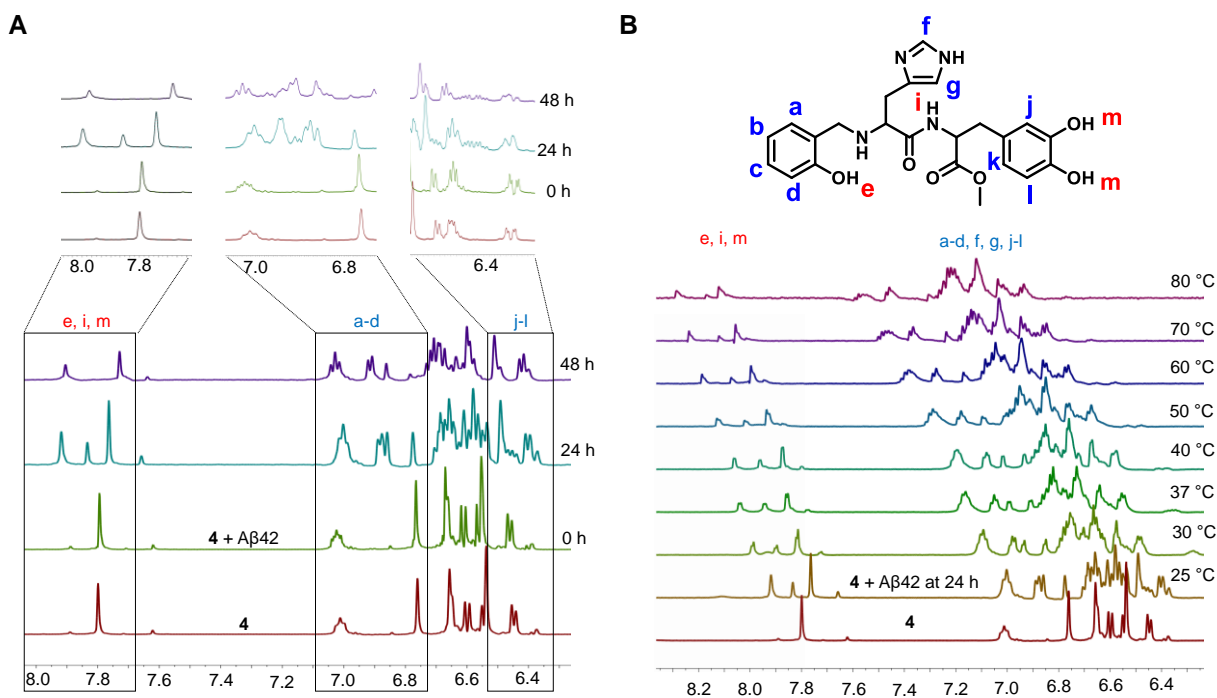


Figure 25. (A) ^1H NMR spectra of **4** and in the presence of A β 42, recorded at different time points (0, 24, and 48 h). The significant changes (downfield shift) of the NMR peaks in the shaded regions show that **4** interacts with A β 42 through hydrogen bonding and hydrophobic interactions. (B) Sample containing compound **4** and A β 42 was incubated for 24 h, and temperature-dependent ^1H NMR spectra were recorded from 25 °C to 80 °C. Structure of compound **4** with protons labeled is inserted.

(a, b, c, and d) moieties appearing in the aromatic region (6.45-6.65 and 6.85-7.15 ppm, respectively) completely rearranged and underwent upfield shift in the presence of A β 42, which

confirmed the interaction of π -electron-rich aromatic moieties of **4** with A β 42. ^1H NMR spectra of **4** in the presence of A β 42 was recorded at different temperatures; Figure 25B shows that with increasing temperature, the exchangeable hydrogen (e and m) peaks at 7.95 and 8.05 ppm, respectively, became broad and downfield shifted, which demonstrated hydrogen bonding interactions of **4** with A β 42. The 2D NMR spectra of **4** showed significant correlation among aromatic and aliphatic protons (Figure 26). Interestingly, the aromatic ^1H correlations completely disappeared in the presence of A β 42, which indicates that **4** interacted and interfered with the A β 42 aggregation process. Therefore, NMR study clearly showed the molecular interactions between **4** and A β 42 that led to its efficient inhibition of A β 42 aggregation.

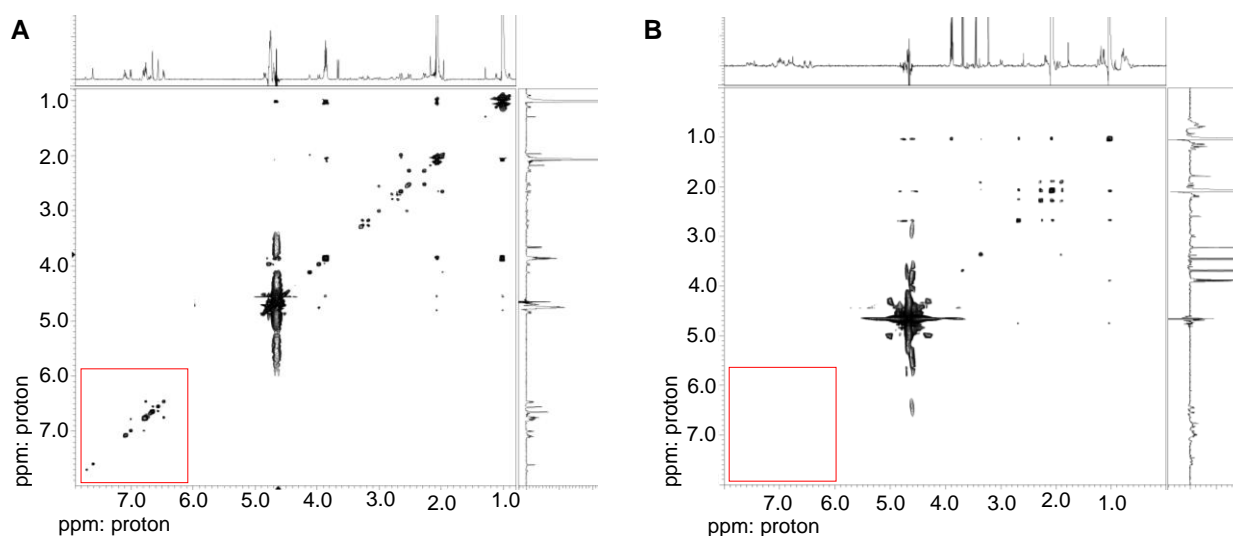


Figure 26. Two-dimensional ^1H correlation spectroscopy (2D COSY) of compound **4**, in the absence (A) and presence to A β 42 (B).

2.9 Impairment of Neuroinflammation and Mitochondrial Dysfunction

Hyperactivation of neuroglia in AD pathogenesis contributes to neuroinflammation, an additional trait of neuronal toxicity in AD.^{16,16,20} Inhibition of activated neuroglia cells using anti-inflammatory compounds can potentially halt AD progression and may prevent irreversible

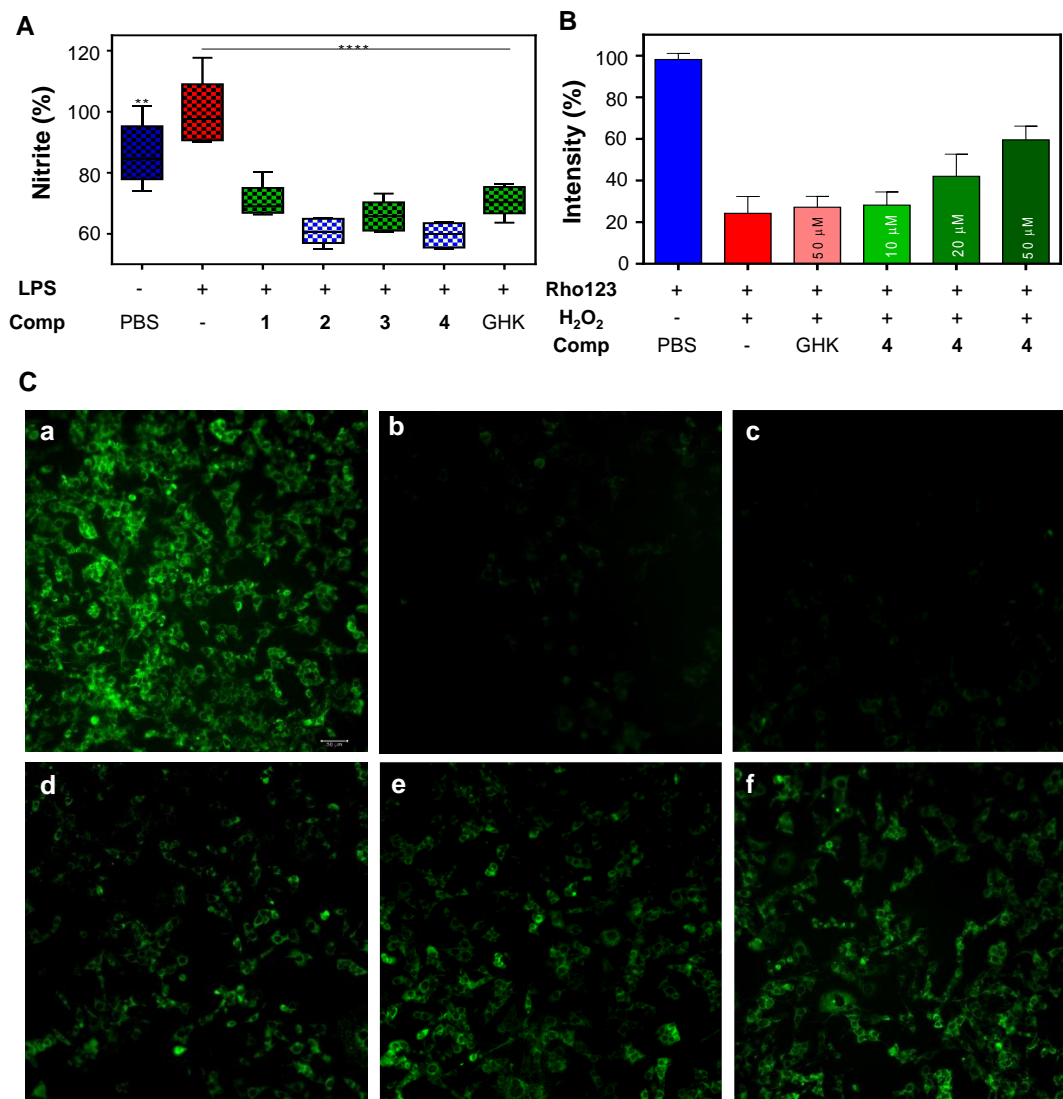


Figure 27. (A) Total nitrite concentration (percentage) measured in cell media, exposed to LPS and upon treatment with compounds **1-4** or GHK for 24 h. (B) Quantification of Rho123 fluorescence at 530 nm ($\lambda_{ex}=509$ nm) (corresponding to MMP) for PC12 cells with media containing H₂O₂ and treated with variable concentrations of **4** and GHK. (C) Fluorescence optical microscopy images of PC12 cells treated with Rho123 (MMP probe): (a) only PBS, (b) only H₂O₂, (c) H₂O₂ + GHK, (d) H₂O₂ + **4** (10 μM), (e) H₂O₂ + **4** (20 μM), and (f) H₂O₂ + **4** (50 μM). Each experiment was performed in triplicate, and data points are shown as mean \pm SD (* $p < 0.05$). LPS, lipopolysaccharides.

damage caused to the AD brain.^{20,22} We assessed the antiinflammatory activity of compounds **1-4** through the Griess assay to estimate the NO levels in the form of nitrite (NO²⁻) (Figure 27).⁴⁹ The

untreated cell media showed 84% nitrite, while samples treated with compounds **1–4** samples were found to reduce the nitrite production to 68%, 61%, 65%, and 60%, respectively, compared to the LPS-treated control sample (100%) (Figure 27A). The nitrite content in the cell media treated with GHK was determined to be 70%, which is higher than the media treated with our compounds, especially **4** (60%). Thus, **4** effectively inhibited the LPS-mediated neuroglia activation and suppressed the inflammatory response (NO production). Next, we studied the effect of **4** to avert the oxidative stress-mediated mitochondrial dysfunction in PC12 cells by measuring MMP through the rhodamine 123 (Rho123) fluorescence assay.¹⁹ The cells incubated with H₂O₂ exhibited 24% Rho123 fluorescence emission as compared to the untreated control (100%), which is indicative of the oxidative stress-induced mitochondrial dysfunction (MMP reduction). The cells treated with H₂O₂ and compound **4** (10, 20, and 50 μM) showed enhanced Rho123 fluorescence emission (implying the corresponding improvement in MMP) up to 29%, 45%, and 60% respectively, by scavenging the toxic radicals, while GHK (50 μM) failed to show any significant improvement in MMP (Figure 27B and C). These observed results suggest that **4** rescued mitochondria by restoring its MMP, which was attributed to efficient inhibition of oxidative stress by scavenging the excess ROS produced in the cells (Figure 28).

2.10 Conclusion

We have demonstrated our rational design and synthesis of natural tripeptide-inspired small molecule MFMs by successfully integrating multifunctional properties to target metal-dependent and -independent multifaceted Aβ toxicity associated with Alzheimer's disease pathology. The detailed evaluation study revealed that compound **4** was the most potent and effective modulator of multifaceted Aβ toxicity encompassing metal ion dyshomeostasis, metal-dependent ROS

generation, metal-dependent and -independent A β 42 toxicity, oxidative stress, DNA damage, mitochondrial dysfunction, and neuroinflammation, which are the major hurdles in the development of therapeutic agents for multifactorial AD. The absorption studies, ITC measurements, and metal-dependent antioxidant assays demonstrated that **4** chelated redox-active metal ions and kept them in the redox-dormant state to arrest the production of excessive ROS, thereby modulating oxidative stress. Interestingly, the nanomolar affinities of MFM toward redox

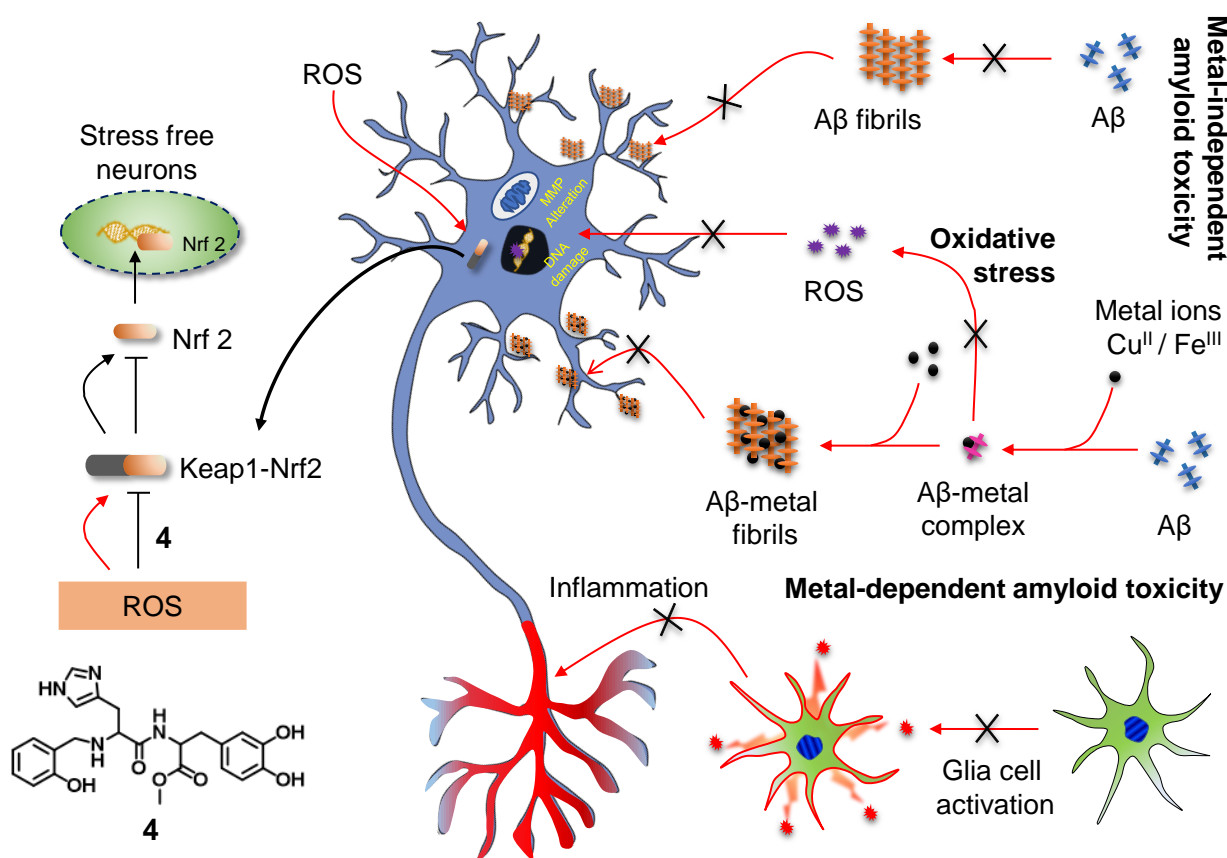


Figure 28. Schematic representation to show the inhibition of multifaceted A β toxicity by MFM 4.

metal ions (Cu^{II} and Fe^{III}), as revealed by the ITC data, confirmed the sequestration of these metal ions. The polyphenolic moiety of **4** contributed to efficient radical quenching ability as shown by

Trolox, ABTS, and DPPH assays. Further, ThT fluorescence assay, TEM, and dot blot analysis clearly revealed that the MFM efficiently inhibited both metal-dependent and metal-independent A β 42 aggregation in both inhibition and dissolution assays. The NMR study revealed molecular-level interactions between the MFM and A β 42 through hydrogen bonding and hydrophobic interactions, which disrupt the assembly of A β 42 to form toxic aggregates. Further, in cellulo studies were in good agreement and supported the in vitro assays, where MFM rescued cells from multifaceted A β toxicity by modulating the metal-dependent and -independent A β 42 aggregation, ROS production, oxidative stress, and DNA damage. Remarkably, **4** rescued mitochondria from dysfunction by restoring its MMP, which was attributed to efficient scavenging of excessive ROS and inhibition of oxidative stress in the cells, further supported by the restoration of nuclear and cytosolic Nrf2 localization under the oxidative stress conditions (Figure 28). In addition, MFM significantly reduced the LPS-mediated glial cell activation, NO production, and inflammation. Overall, the good cell viability, prevention of metal ion (Cu^{II} and Fe^{III}) dependent and -independent generation of excessive ROS, protection of DNA and mitochondria, antioxidant and antiinflammatory properties, and inhibition of metal ion-dependent and -independent A β 42 aggregation make compound **4** a highly desirable MFM for developing therapeutic agents to ameliorate multifaceted A β toxicity in AD (Figure 7). We have witnessed a series of drug candidates fail at various stages of clinical trials possibly due to their inability to interfere with multifaceted toxicity of AD. In this context, our multifunctional modulator (MFM) strategy is anticipated to inspire the development of potential therapeutic candidates to treat AD in the near future.

2.11 Experimental Methods

2.11.1 General Methods

All starting materials, reagents, and solvents were obtained from Sigma-Aldrich and used without any further purification unless otherwise mentioned. Argon or nitrogen atmosphere was maintained for the air and moisture-sensitive reactions. Agilent Cary series UV-Vis-NIR absorption, Agilent Cary eclipse fluorescence spectrophotometers and microplate reader was used for all absorption and fluorescence measurements, respectively. All the raw data was processed and analyzed in Prism 6 or Origin 8.5 software. ^1H and ^{13}C NMR of all synthesized compounds were recorded by a Bruker AV-400 spectrometer with tetramethylsilane as an internal standard. HRMS spectra were acquired on Agilent 6538 UHD HRMS/Q-TOF high-resolution spectrometer, respectively. The stock solutions of all the compounds were prepared by dissolving the calculated amount of corresponding solids in deionized Milli Q water and stored at $-20\text{ }^\circ\text{C}$. For experiments, samples were prepared by diluting the stock solutions in same deionized Milli Q water. Cu^{II} and Fe^{III} samples were obtained by dissolving the calculated amount of copper sulfate (CuSO_4) and ferric chloride (FeCl_3) in deionized Milli Q water, respectively. Freshly prepared ascorbate solution was used for all the experiments. ThT solution was prepared by dissolving the calculated amount of solid ThT in filtered PBS buffer ($\text{pH}= 7.4$, 50 mM). The live cell images were captured using optical fluorescence microscope (LEICA DMi8).

2.11.2 Synthesis of Compounds 1-4

To a stirred solution of FmocHis(Trt)-OH (3.0 g, 4.8 mmol) in dimethyl formamide (DMF, 6 mL) at $0\text{ }^\circ\text{C}$. Diisopropylethylamine (DIPEA, 1.03 mL, 5.8 mmol), Tetramethyl-O-(1H-benzotriazol-1-yl)uronium hexafluorophosphate (HBTU, 2.20 g, 5.8 mmol), and hydroxybenzotriazole (HOBt,

0.78 g, 5.8 mmol) were added. The reaction mixture was kept for stirring about 15 min under nitrogen atmosphere. 3,4Dihydroxyphenethylamine (dopamine, 1.83 g, 9.68 mmol) and methyl 3-(3,4-bis(tert-butyldimethylsilyloxy)phenyl)-2-aminopropanoate (3.0 g, 6.8 mmol) were added to above solution, and the reaction was left to stir for 5-6 h. After the completion of the reaction (monitored by TLC), the solvent was removed, the crude was diluted with water (30 mL), and the residue was extracted into EtOAc (3 × 30 mL). The combined organic phase was washed with water (1 × 30 mL) and brine (1 × 30 mL). The organic layers were collected, dried over anhydrous Na₂SO₄, and evaporated in vacuum to afford the crude peptide. The products were purified by column chromatography using DCM and methanol as eluent. Next, 1a (0.5 g, 0.93 mmol) and 2b (1.5 g, 1.83 mmol) were dissolved in DMF (3 mL), which was cooled to 0 °C, and DIPEA (0.33 mL, 1.87 mmol), HBTU (0.42 g, 1.12 mmol), and HOBt (0.17 g, 1.12 mmol) were added. The reaction mixture was kept stirring about 15 min under nitrogen atmosphere, Boc-Gly-OH (0.2 g, 1.12 mmol) was added, and the reaction was left to stir for 5-6 h at room temperature. After the completion of the reaction (monitored by TLC), solvent was removed, the crude was diluted with water (25 mL), and the residue was extracted into EtOAc (3 × 25 mL). The combined organic phase was washed with water (1 × 30 mL) and brine (1 × 25 mL). The organic layers were collected, dried over anhydrous Na₂SO₄, and evaporated. This was purified by column chromatography using dichloromethane (DCM) and methanol as eluent. Finally, the above crude compounds **1** and **2** were purified using a reverse-phase (RP) semipreparative HPLC on C18 column at 40 °C. Further, to synthesize compounds **3** and **4**, intermediates 1b (0.4 g, 0.75 mmol) and 2b (1.0 g, 1.22 mmol) in acetonitrile (10 mL) were added to 2hydroxybenzaldehyde (0.2 mL, 1.83 mmol) and DIPEA (0.5 mL, 2.44 mmol). The reaction mixture was kept stirring about 10 min at room temperature under nitrogen atmosphere, was heated up to 65 °C, and then was left to stir for 12 h. After the completion

of the reaction (monitored by TLC), the solvent was then removed, azeotrope distillation with toluene was performed, and the resulting product was dried completely and was used as such for the next step without purification. Then the crude intermediates 3a (0.3 g, 0.47 mmol) and 4a (0.5 g, 0.54 mmol) were dissolved in dry methanol (3 mL), which was cooled to 0 °C, and sodium triacetoxy borohydride (STAB, 100 mg, 0.47 mmol) was added. The reaction mixture was kept stirring about 2 h under nitrogen atmosphere. After the completion of the reaction (monitored by TLC), solvent was removed, the crude was diluted with water (3 mL), and the residue was extracted into EtOAc (2 × 5 mL). The combined organic phase was washed with water (1 × 3 mL) and brine (1 × 3 mL). The organic layers were collected, dried over anhydrous Na₂SO₄, and evaporated in vacuum to afford the crude peptide, and the resulting residue was reprecipitated using DCM and hexane, followed by trituration with diethyl ether to yield the crude. The crude compound was dissolved in DCM (3 mL), TFA (10% sol in DCM) was added, and the reaction was monitored by TLC and was complete within 20 min. The solvent was then removed, and the residue was triturated with diethyl ether to yield crude compounds **3** and **4**. Crude compounds **3** and **4** were purified using a reverse-phase (RP) semipreparative HPLC on a C18 column at 40 °C.

Compound 1. ¹H NMR (DMSO-d₆, 400 MHz): δ 14.35 (s, 1H), 8.94 (s, 1H), 8.71 (d, J = 8 Hz 3 H), 8.17 (t J = 11.2 Hz 1H), 8.03 (s, 2 H), 7.32 (s, 1H), 6.64–6.56 (m 1H), 6.41 (q, J = 8 Hz, 1H), 4.60–4.55 (m, 1H), 3.65–3.55 (m, 3H), 3.23–3.05 (m, 3H), 2.94–2.88 (m, 1H). ¹³C NMR (DMSO-d₆, 100 MHz) δ 169.0, 166.0, 145.1, 143.6, 133.8, 129.8, 129.0, 119.2, 116.9, 115.9, 115.5, 34.5. HRMS (ESI-MS): m/z calculated for C₁₆H₂₂N₅O₄ [M + H]⁺ 348.1662, observed 348.1664.

Compound 2. ¹H NMR (DMSO-d₆, 400 MHz): δ 14.26 (s, 1H), 8.96 (s, 1H), 8.78 (d, J = 9.6 Hz,

1H), 8.66 (d, J = 8.4 Hz, 1H), 8.53 (d, J = 7.2 Hz, 1H), 7.96 (s, 1H), 7.30 (s, 1H), 6.62 (d, J = 8.0 Hz, 1H), 6.55 (d, J = 2.0 Hz, 1H), 6.42 (q, J = 8 Hz, 1H), 4.72 (q, J = 13.6 Hz, 1H), 4.38 (q, J = 14 Hz, 1H), 3.58 (s., 3H), 3.03 (q, J = 15.2 Hz, 1H), 2.94–2.821 (m, 2H), 2.72 (q, J = 14 Hz, 1H). ¹³C NMR (DMSO-d₆, 100 MHz) δ 169.0, 166.0, 158.6, 158.3, 158.0, 145.1, 143.6, 133.8, 129.8, 129.1, 119.1, 118.4, 118.39, 115.9, 115.5, 51.9, 34.5, 27.2. HRMS (ESI-MS): m/z calculated for C₁₈H₂₄N₅O₆ [M + H]⁺ 406.1721, observed 406.1708.

Compound 3. ¹H NMR (DMSO-d₆, 400 MHz): δ 14.17 (s, 1H), 8.90 (s, 1H), 8.72 (s, 1H), 8.54 (t, J = 11.2 Hz, 1H), 7.37 (s, 1H), 7.26–7.22 (m, 2H), 6.92–6.84 (m, 1H), 6.82 (q, J = 7.6 Hz, 1H), 6.62 (d, J = 8 Hz, 1H), 6.56 (d, J = 2 Hz, 1H), 6.39 (q, J = 8 Hz, 1H), 4.04–3.94 (m, 3H), 3.27–3.12 (m, 5H), 2.46–2.38 (m, 2H). ¹³C NMR (DMSO-d₆, 100 MHz) δ 165.8, 158.3, 158.0, 156.1, 145.1, 143.6, 134.3, 131.6, 130.6, 129.5, 119.0, 119.0, 118.41, 117.6, 115.8, 115.4, 115.2, 58.2, 44.7, 34.1, 25.5. HRMS (ESI-MS): m/z calculated for C₂₁H₂₄N₄O₄ [M + H]⁺ 397.1875, observed 397.1871.

Compound 4. ¹H NMR (DMSO-d₆, 400 MHz): δ 14.06 (s, 1H), 9.01 (d, J = 8 Hz, 1H), 8.88–8.74 (m, 4H), 7.356 (s, 1H), 7.251–7.213 (m, 1H), 7.08 (d, J = 6.8 Hz, 1H), 6.90 (d, J = 8 Hz, 1H), 6.81 (d, J = 7.6 Hz, 1H), 6.58 (dd, J = 5.6, 4.0 Hz, 2H), 6.42 (q, J = 8 Hz, 2H), 4.557 (q, J = 14 Hz, 1H), 4.07 (q, J = 7.6 Hz, 1H), 3.75 (d, J = 2 Hz, 3H), 3.24 (dd, J = 13.6, 14.8 Hz, 1H), 3.10 (q, J = 14.6 Hz, 2H), 2.88 (dd, J = 14, 13.6 Hz, 1H), 2.71 (dd, J = 14, 13.6 Hz, 2H). ¹³C NMR (DMSO-d₆, 100 MHz) δ 171.1, 158.4, 156.1, 145.1, 144.1, 134.2, 131.6, 130.6, 127.0, 119.7, 119.0, 116.2, 115.3, 115.1, 58.3, 53.7, 52.0, 45.0, 36.3. HRMS (ESI-MS): m/z calculated for C₂₃H₂₇N₄O₆ [M + H]⁺ 455.1925, observed 455.1923.

2.11.3 Absorption Spectroscopy

UV-Visible spectroscopy measurements were carried out using single beam Agilent 8453 UV-Vis spectrophotometer at room temperature. 1 cm path length quartz cuvette (1 mL) was used for the absorbance measurement (200-800 nm).

2.11.4 Binding Constant Measurement

Isothermal titration calorimetry (ITC) measurements were performed at constant temperature (298 K) and atmospheric pressure using a VP-ITC micro calorimeter (Microcal). The metal ions (Cu^{II} and Fe^{III}) and compounds **1-4** or GHK are dissolved in MQ water, and all the samples were degassed to remove the air bubbles. During the experiment, the sample was stirred at constant speed (300 rpm) to achieve homogeneous mixing in the cell. The reference power was set at 25 $\mu\text{cal}/\text{sec}$, to obtain accurate baseline. A 100 seconds pre-titration delay was set to allow the pre-titration baseline. 10 μL metal solutions (Cu^{II} and Fe^{III}) was injected up to 30 times with a spacing of 200 seconds. Whereas, for **2-Fe^{III}** and **4-Fe^{III}** interaction study 10 μL aliquots of metal solution (Fe^{III}) was injected up to 30 times with a spacing of 300 seconds. The titration data were analyzed using Origin software.

2.11.5 MTT Assay

MTT (3-(4,5-dimethylthiazol-2-yl)-2,5-diphenyltetrazolium bromide) assay was performed in two different cell lines (PC12 and BV2) to assess the cytotoxicity of our compounds. 15,000 cells/well were seeded in a 96-well plate in RPMI (Roswell Park Memorial Institute) medium (Gibco, Invitrogen) with fetal bovine serum (FBS, 10%), horse serum (HS, 5%), and pen-strep (1%) and at 37 °C temperature within 5% CO_2 atmosphere for 24 h. The cultured media was exchanged with

low serum RPMI media (2% FBS) and incubated for 6 h. The different concentrations of our compounds (25, 50 and 100 μM) added and incubated for 24 h under similar conditions. Then 15 mL of MTT solution (5 mg/mL) was added to each wells; all the medium was removed and 1:1 DMSO-MeOH (100 μL) was added after 3 h of incubation. The absorbance was measured at 570 nm after 30 min of shaking in the dark. The absorbance measurement was carried out using a microplate reader, and the data was plotted and analyzed by GraphPad Prism 6 software.

2.11.6 Preparation of A β 42 Monomer and Fibrils

A β 42 (Cat: PP69- 0.25 MG) peptide was dissolved in 250 μL of hexafluoro-2-propanol (HFIP). After incubation of (1 h) at room temperature, HFIP was first removed by nitrogen gas flow and then under vacuum condition. A β 42 peptide concentration was calculated by UV-Visible absorbance study using molar extinction coefficient $1450 \text{ cm}^{-1} \text{ M}^{-1}$. A β 42 peptide was dissolved in PBS buffer (50 mM, pH= 7.4) containing 2% DMSO or NaOH solution (100 mM) to obtain a final concentration of 100 μM , which is used as a stock solution. The A β 42 fibrils were prepared by incubating A β 42 monomers with and without metal ion (Cu^{II}) for 5 days in PBS buffer (50 mM, 150 μM NaCl, pH = 7.4). The formation of A β 42 fibrils was confirmed by ThT fluorescence.

2.11.7 Modulation of A β Toxicity in Cells

To demonstrate the modulation of A β toxicity by our compounds, *in cellulo* assay was performed with PC12 cells using monomeric and fibrillar A β 42. PC12 cells were cultured in a 96-well plate (15,000 per well) in RPMI (Roswell Park Memorial Institute) medium (Gibco, Invitrogen) with fetal bovine serum (FBS, 10%), horse serum (HS, 5%), and pen-strep (1%) at 37 °C temperature within 5% CO_2 atmosphere. The cultured media was exchanged with low serum RPMI media (2%

FBS) and cells were treated with monomeric A β 42 in absence and presence of our compounds or GHK for 24 h. For fibrils modulation assay, cells treated with metal-dependent and independent A β fibrils were incubated with our compounds or GHK for 24 h. The cell viability was determined through MTT assay. The absorbance measurement was done using MicroPlate Reader and data is plotted and analyzed by GraphPad Prism 6 software.

2.11.8 Anti-inflammatory Assay

To check the anti-inflammatory activity of our compounds and GHK, Griess assay was performed in BV2 cells. BV2 cells (1.5×10^5) were cultured in DMEM medium (Dulbecco's Modified Eagle's medium, Gibco, Invitrogen) with fetal bovine serum (FBS, 10%), horse serum (HS, 5%), and pen-strep (1%) at 37 °C temperature within 5% CO₂ atmosphere. The cultured media was exchanged with low serum phenol red free DMEM media (2% FBS) and cells were exposed to polysaccharide (LPS) (30 μ M) in the absence and presence of our compounds or GHK (100 μ M) for 24 h. Next, Griess reagent was added to culture media and incubated on a shaker for 30 min in the dark. The absorbance of the media at 530 nm measured and analyzed.

2.11.9 MMP Measurement

To study the protective nature of our compounds towards mitochondria from the A β toxicity, a fluorescence assay was performed using Rho123 dye, and a relative change in MMT was determined. PC12 cells were cultured in a 96-well plate (15,000 per well) in RPMI (Roswell Park Memorial Institute) medium, Gibco, Invitrogen) with fetal bovine serum (FBS, 10%), horse serum (HS, 5%), and pen-strep (1%) at 37 °C temperature within 5% CO₂ atmosphere. The cultured media was exchanged with low serum RPMI media (2% FBS), and cells were treated with either A β -Cu^{II}

(10 μ M) complex or H₂O₂ (100 μ M) in the absence and presence of compound **4** for 12 h at 37 °C. The cell media was subsequently treated with Rho123 (500 nM) and incubated for 15 min. The cells were carefully washed with PBS buffer (3 times), and imaged under the fluorescence optical microscope, and the total fluorescence intensity of each well was measured using microplate reader ($\lambda_{\text{ex}} = 509$ nm, $\lambda_{\text{em}} = 530$ nm).

2.11.10 pDNA Damage Analysis by Gel Electrophoresis

To demonstrate the effective redox-silencing of Cu^{II} and arresting the production of ROS by compounds **1-4**, DNA damage assay was performed. The plasmid DNA (pDNA: pUC19) was exposed with two different redox pairs Cu^{II}-Asc and A β 42-Cu^{II}-Asc in the presence and absence of our compounds and GHK to validate their DNA protecting ability from toxic OH \cdot . The incubated pDNA samples were loaded on 0.7% agarose gel, which is pre-stained with ethidium bromide and electrophoresed for 50 min at 120 V and room temperature. The electrophoresed agarose gels were imaged using in Gel documentation System.

2.11.11 Trolox Equivalent Antioxidant Capacity Measurement (Trolox Assay)

To demonstrate the effective antioxidant property and inhibition activity against ROS produced independent of redox active metals Trolox equivalent antioxidant capacity of our compounds was measured (Trolox assay). In Trolox assay, fluorescein (30 nM) and 6-hydroxy-2,5,7,8-tetramethylchroman-2-carboxylic acid (Trolox) / our compounds or GHK (3.1, 6.25, 12.5, 25 and 50 μ M) was incubated in PBS (75 mM, pH = 7.4), and the fluorescence emission of fluorescein ($\lambda_{\text{em}} = 510$ nm) was measured in the presence of 2,2'-azobis (2-methylpropionamide) dihydrochloride (AAPH) (200 μ M). Standard Trolox plot was obtained from the area under the

curve (N_{AUC}) for different Trolox concentration curve and that was used to calculate TEAC of our compounds. $N_{AUC} = (\text{Sample or Trolox AUC} - \text{blank AUC})$.

2.11.12 DPPH Radical Scavenging Assay

Di-(phenyl)-(2,4,6-trinitrophenyl)iminoazanium (DPPH) radical quenching assay was performed to demonstrate the radical scavenging ability of our compounds. DPPH (100 μM) was incubated alone or with different concentration of our compounds and GHK (0.78, 1.56, 3.12, 6.25, 12.50 and 50.00 μM) in MeOH:H₂O (1:1) at 37 °C for 30 min. The absorbance at 540 nm was measured using microplate reader and data was plotted and analyzed by GraphPad Prism 6 software.

2.11.13 Intracellular ROS Measurement

To demonstrate the *in cellulo* ROS scavenging ability of our compounds 2',7'-Dichlorofluorescein diacetate (DCFDA) assay was performed in cultured cells. PC12 cells were seeded in a 96-well plate (15,000 per well) in RPMI (Roswell Park Memorial Institute) medium (Gibco, Invitrogen) with fetal bovine serum (FBS, 10%), horse serum (HS, 5%), and pen-strep (1%) at 37 °C temperature within 5% CO₂ atmosphere. The cultured media was exchanged with low serum RPMI media (2% FBS) and incubated with DCFDA (10 μM) for 30 min. The cells were washed with PBS and H₂O₂ (400 μM) and treated with our compounds and GHK (100 μM) and incubated for 4 h. The media was removed, and cells were washed with PBS (3 times), the total fluorescence ($\lambda_{em} = 530 \text{ nm}$) of the entire well (in well plate) was measured using microplate reader.

2.11.14 Redox Silencing of Cu^{II} (Cu^{II}-Asc Assay)

To assess the redox silencing (Cu^{II}) and ROS inhibition ability of compounds **1-4** or GHK, we performed *in vitro* Cu^{II} -Asc assay. Coumarin-3-carboxylic acid (3-CCA, 150 μM), Cu^{II} (10 μM) and compounds **1-4** or GHK was incubated independently in PBS (10 mM, pH = 7.4) at 37 °C with high concentration of ascorbate (200 μM). 3-CCA was used to assess the OH^\cdot generation, which transformed from non-fluorescent to fluorescent, 7-OH-CCA ($\lambda_{\text{ex}} = 385 \text{ nm}$, $\lambda_{\text{em}} = 450 \text{ nm}$). The fluorescence emission intensity of 7-OH-CCA was measured as a function of time using the MicroPlate Reader and result was plotted and analyzed using origin 8.5 software.

2.11.15 Redox Silencing of Fe^{III} (Fe^{III} -Asc Assay)

To assess the antioxidant and redox silencing (Fe^{III}) activity of compounds **1-4** or GHK, we performed *in vitro* Fe^{III} -Asc assay. 3-CCA (150 μM), Fe^{III} (10 μM) and H_2O_2 (50 μM) was incubated with compounds **1-4** and GHK in PBS (10 mM, pH = 7.4) at 37 °C. The fluorescence emission intensity of 7-OH-CCA ($\lambda_{\text{ex}} = 385 \text{ nm}$, $\lambda_{\text{em}} = 450 \text{ nm}$) was measured as a function of time after the addition of ascorbate (200 μM) using MicroPlate Reader and data was plotted and analyzed in origin 8.5 software.

2.11.16 In Cellulo Redox Silencing (Cu^{II})

To assess the redox silencing ability of our compounds, *in cellulo* assay was performed with PC12 cells using Cu^{II} -Asc redox pair. PC12 cells were cultured in a 96-well plate (15,000 per well) in RPMI (Roswell Park Memorial Institute) medium (Gibco, Invitrogen) with fetal bovine serum (FBS, 10%), horse serum (HS, 5%), and pen-strep (1%) at 37 °C temperature within 5% CO_2 atmosphere. The cultured media was exchanged with low serum RPMI media (2% FBS) and cells were treated with Cu^{II} (25 μM) and ascorbate (200 μM) in absence and presence of compounds **1-**

4 or GHK for 24 h. The cell viability was determined through MTT assay. The absorbance measurement was done using MicroPlate Reader and data is plotted and analyzed by GraphPad Prism 6 software.

2.11.17 Inhibition of *In Cellulo* Fe^{III}-H₂O₂ Toxicity

To evaluate the inhibition ability of our compounds against Fe^{III}-H₂O₂ toxicity, *in cellulo* assay was performed in PC12 cell lines using EDTA-Fe^{III}-H₂O₂-Asc redox pair. PC12 cells were cultured in a 96-well plate (15,000 per well) in RPMI (Roswell Park Memorial Institute) medium (Gibco, Invitrogen) with FBS (10%), horse serum (HS, 5%), and pen-strep (1%) at 37 °C temperature within 5% CO₂ atmosphere. The cultured media was exchanged with low serum RPMI media (2% FBS) and cells were treated with EDTA-Fe^{III} (100 μM), H₂O₂ (50 μM) and ascorbate (200 μM) in absence and presence of our compounds **1-4** or GHK for 36 h. The cell viability was determined through MTT assay. The absorbance measurement was done using MicroPlate Reader and data is plotted and analyzed by GraphPad Prism 6 software.

2.11.18 *In Cellulo* Radical Scavenging Assay

To evaluate the radical scavenging ability of our compounds in a cellular context, *in cellulo* assay was performed with PC12 cells using toxic H₂O₂. PC12 cells were cultured in a 96-well plate (15,000 per well) in RPMI (Roswell Park Memorial Institute) medium (Gibco, Invitrogen) with FBS (10%), horse serum (HS, 5%), and pen-strep (1%) at 37 °C temperature within 5% CO₂ atmosphere. The cultured media was exchanged with low serum RPMI media (2% FBS) and cells were treated with H₂O₂ (150 μM) in absence and presence of compounds **1-4** or GHK for 24 h.

The cell viability was determined through MTT assay. The absorbance measurement was done using MicroPlate Reader and data is plotted and analyzed by GraphPad Prism 6 software.

2.11.19 ABTS Radical Scavenging Assay

2,2'-Azinobis-(3-ethylbenzothiazoline-6-sulfonic acid (ABTS) radical quenching assay was performed to evaluate the radical scavenging ability of our compounds **1-4**. Deep green colored ABTS radical cation (ABTS^{•+}) was formed by the reaction of ABTS and potassium persulfate for 12 h. ABTS^{•+} (100 μM) was incubated alone or with compounds **1-4** or GHK (100 μM) in PBS at 37 °C for 30 min. The absorbance at 734 nm was measured using MicroPlate Reader and data was plotted and analyzed by GraphPad Prism 6 software.

2.11.20 Nrf2 Protein Imaging

To demonstrate the antioxidant property of compound **4** we assayed the location of Nrf2 protein in cultured PC12 cells. The cells were seeded in a confocal dish in RPMI (Roswell Park Memorial Institute) medium (Gibco, Invitrogen) with fetal bovine serum (FBS, 10%), horse serum (HS, 5%), and pen-strep (1%) and at 37 °C temperature within 5% CO₂ atmosphere for 48 h. The cultured media was exchanged with low serum RPMI media (2% FBS) and incubated for 6 h. Then the cells were exposed with H₂O₂ (100 μM) in the absence and presence of compound **4** (100 μM) for 30 min under similar conditions. Then the treated cells were fixed using 100% methanol for 20 min and blocked with 5% bovine serum albumin for 1 h at room temperature after removing the methanol with PBS. The fixed cells were incubated with anti-Nrf2 antibody (1:100, dilution) for 2 h at room temperature in PBS. Unbound anti-Nrf2 antibody was washed out and the cells were further incubated with FITC conjugated secondary antibody (1:400, dilution) for 30 min at room

temperature. Finally, the cells were washed with PBS for several times and DAPI was used to verify the integrity and location of nucleus. The stained, fixed cell images were captured using optical fluorescence microscope (LEICA DMI8).

2.11.21 A β Aggregation Inhibition Assay

To evaluate the inhibition ability of our compounds against metal-independent and -dependent A β aggregation, thioflavin T (ThT) assay was performed. Freshly reconstituted A β 42 (20 μ M) was incubated alone and with our compounds **1-4** or GHK (100 μ M) in PBS (50 mM, P^H=7.4, 150 μ M NaCl) at 37 °C for 48 h. For metal-dependent aggregation inhibition, A β 42-Cu^{II} (20 μ M) was incubated alone and with our compounds **1-4** or GHK (100 μ M) in PBS (50 mM, pH = 6.6, 150 μ M NaCl) at 37 °C for 72 h. Finally, ThT (20 μ M) was added to the samples and ThT fluorescence emission intensity was measured at 482 nm ($\lambda_{\text{ex}} = 442$ nm) using MicroPlate reader, and plotted and analyzed by GraphPad Prism 6 software.

2.11.22 TEM Imaging

To visualize the inhibition of metal-independent and -dependent A β aggregation by our compounds, transmission electron microscopy (TEM) imaging was performed. Freshly reconstituted A β 42 (10 μ M) was incubated alone and with our compounds **1-4** (50 μ M). For metal-dependent aggregation, A β 42-Cu^{II} (10 μ M) was incubated alone and with our compounds **1-4** or GHK (100 μ M). The incubated sample was deposited on TEM grid and the grid was washed with Milli-Q water to remove excess salt. Finally, the samples deposited on the grids were stained with uranyl acetate and TEM images were captured.

2.11.23 A β -Cu^{II} Redox Silencing Assay

To evaluate the inhibition of A β -Cu^{II} toxicity and redox silencing (bound Cu^{II}) activity of our compounds **1-4** or GHK, we performed *in vitro* A β 42-Cu^{II}-Asc assay. Cu^{II} (10 μ M) and A β 42 (12.5 μ M) was incubated for 2 h to form the A β 42-Cu^{II} complex in PBS (10 mM, pH = 7.4) at 37 °C. Then A β 42-Cu^{II} complex, 3-CCA (150 μ M) and compounds **1-4** or GHK was incubated independently in PBS (10 mM, pH = 7.4) at 37 °C. The fluorescence emission intensity of 7-OH-CCA (λ_{em} = 450 nm) was measured after adding ascorbate (200 μ M) as a function of time using the MicroPlate Reader and result was plotted and analyzed in origin 8.5 software.

2.11.24 A β Fibrils Dissolution Assay

To assess the inhibition ability of our compounds **1-4** AGAINST metal-independent and -dependent A β fibrillar aggregates, we performed thioflavin T (ThT) assay. The freshly prepared metal-independent and -dependent A β 42 fibrils were incubated alone, and with compounds **1-4** and GHK (100 μ M) in presence of ThT. The ThT fluorescence emission intensity was measured after 10 h of incubation using MicroPlate Reader at 37 °C. The data was plotted and analyzed by GraphPad Prism 6 software.

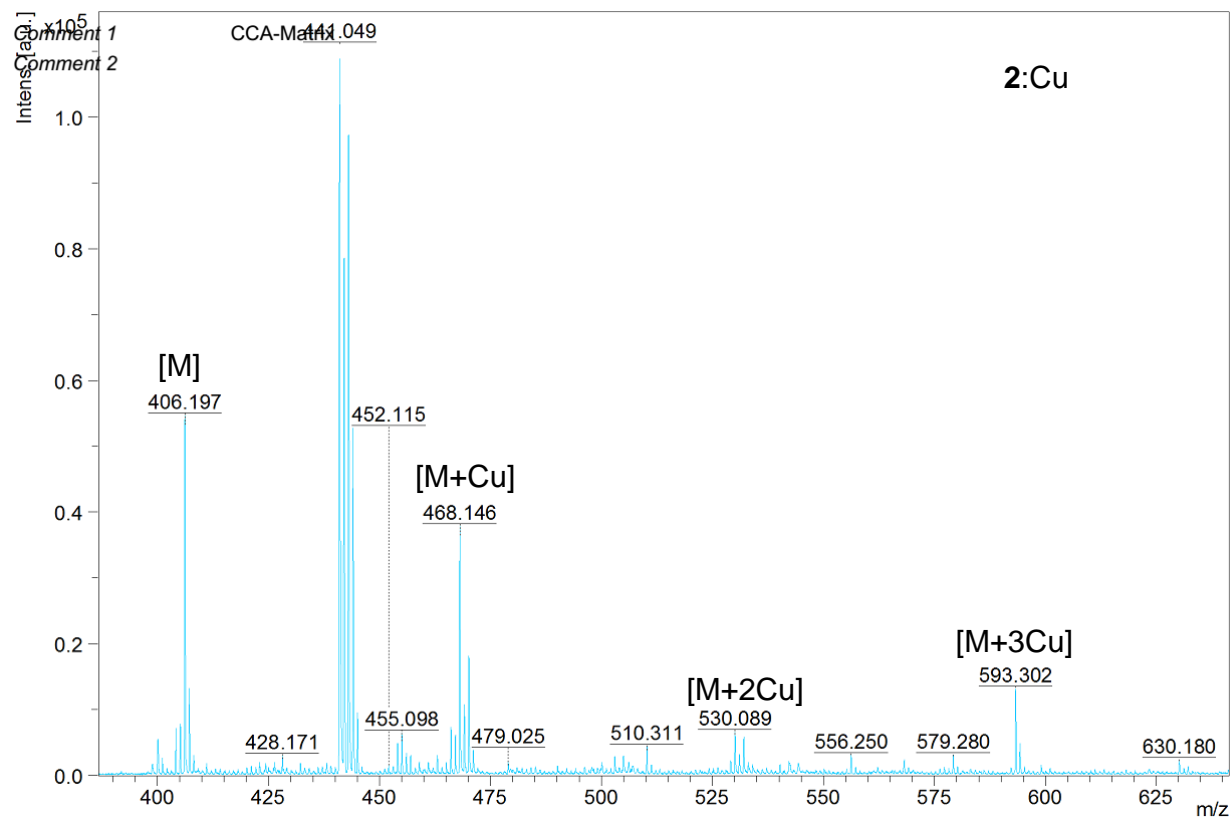
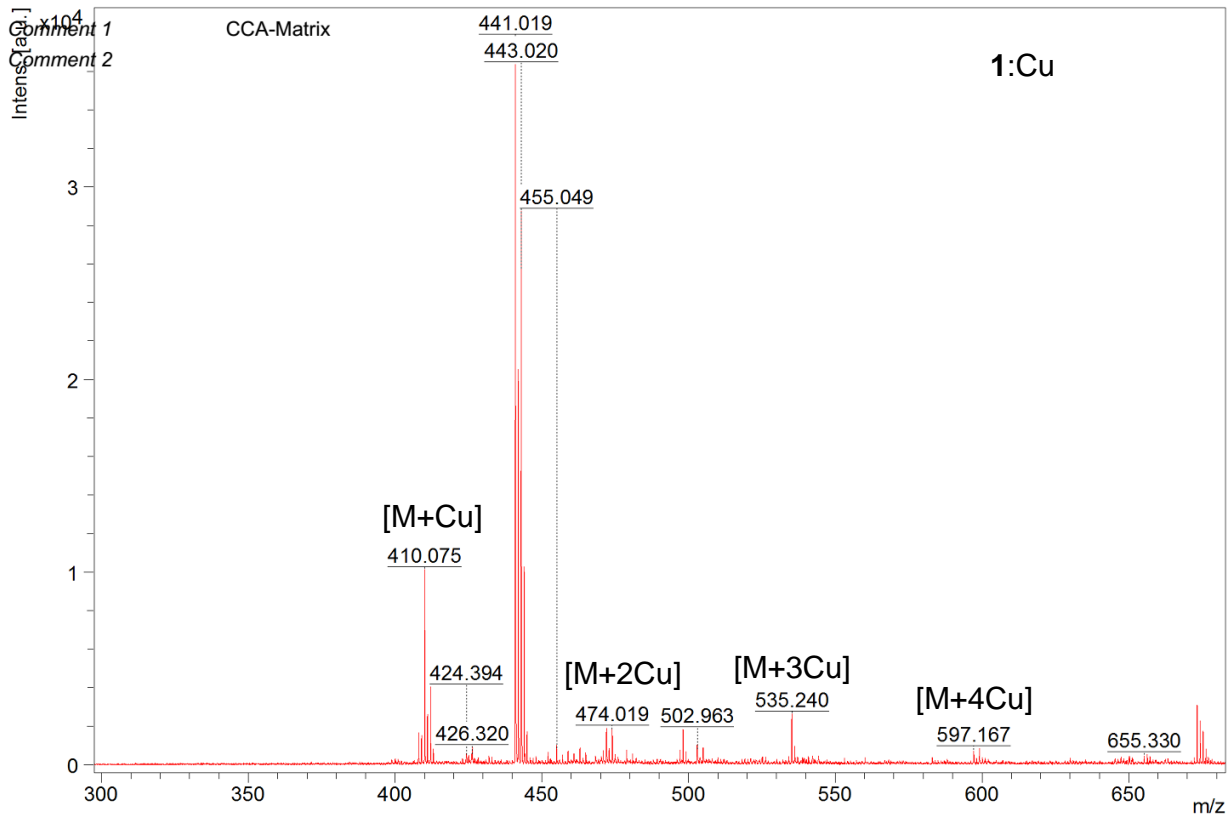
2.11.25 Dot Blot Analysis

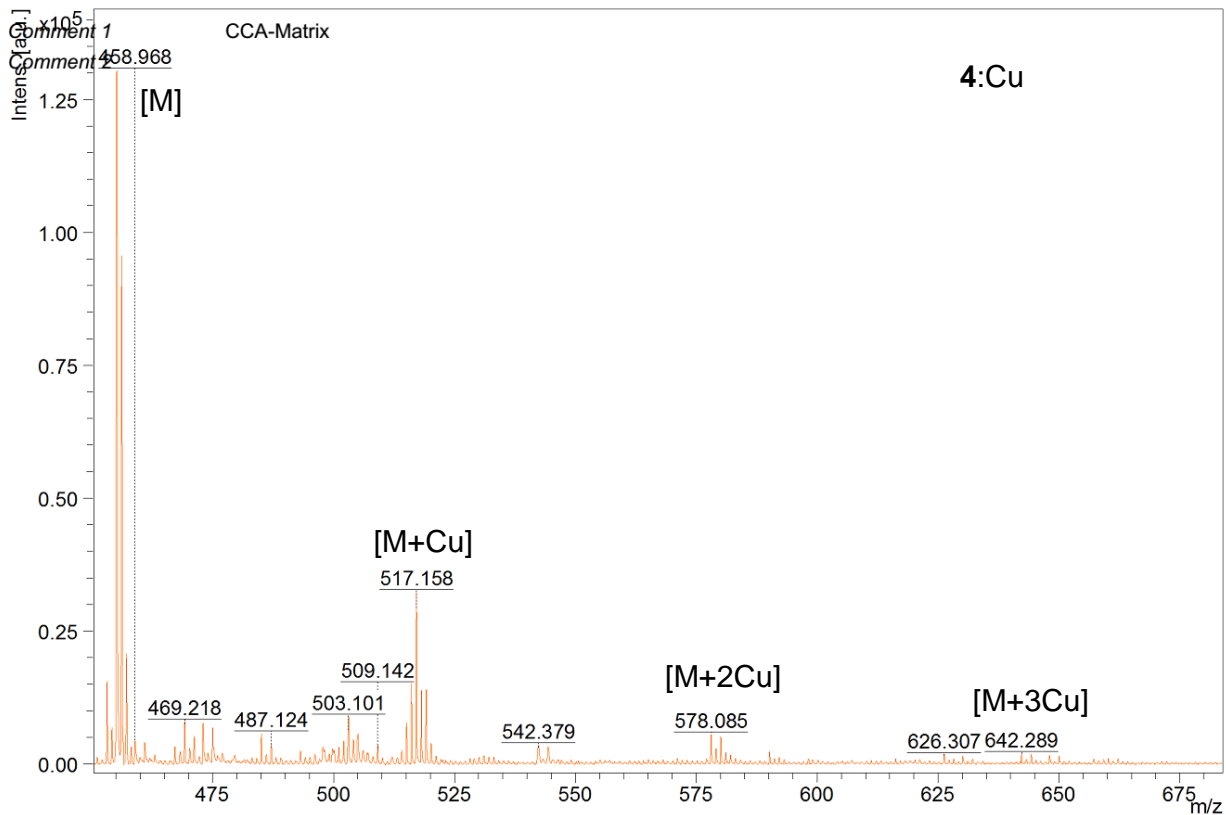
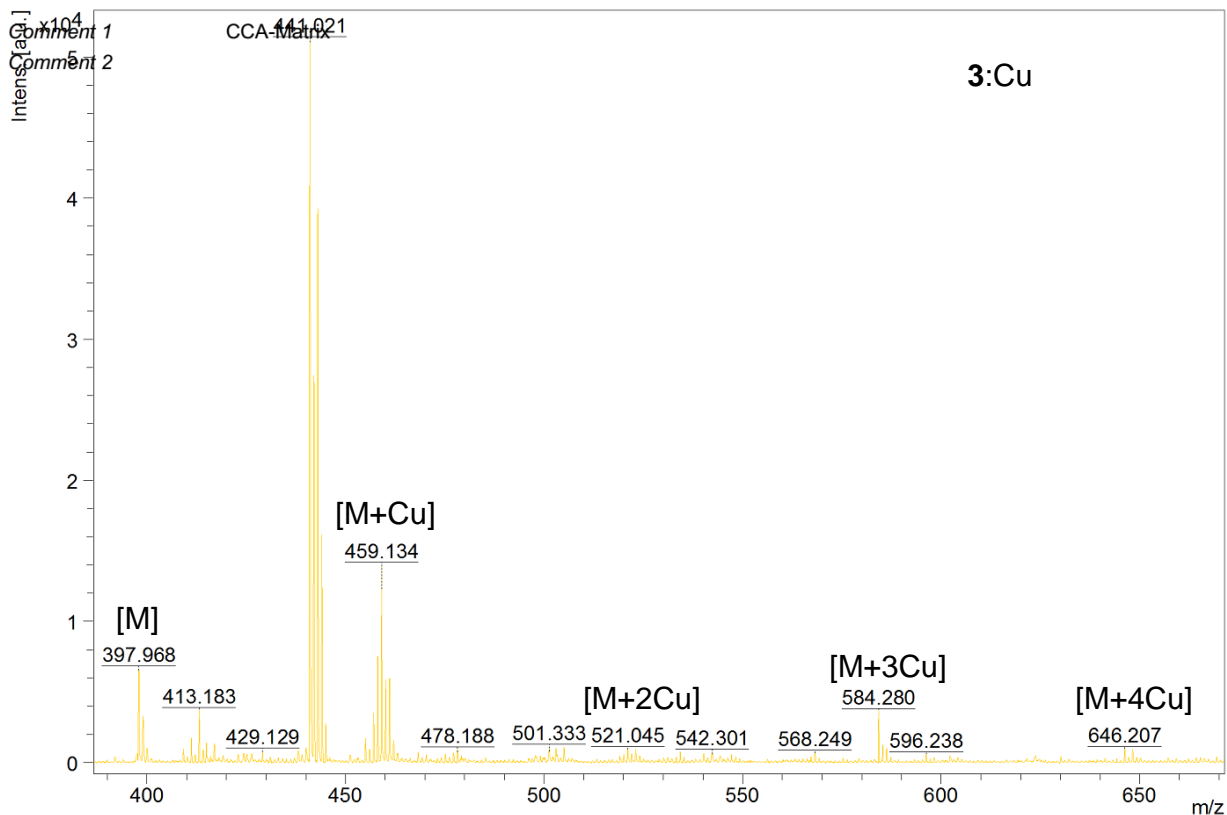
To assess the inhibition ability of our compounds against metal-independent A β fibrillar aggregates, dot blot analysis was performed. The freshly prepared metal-independent A β 42 fibrils (10 μ M) was incubated alone, and with compounds **1-4** and GHK (50 μ M) for 12 h without shaking. Then the samples were spotted onto the PVDF membrane and the membrane was blocked with 5%BSA (bovine serum albumin). The membrane was incubated with A β 42 fibrils specific

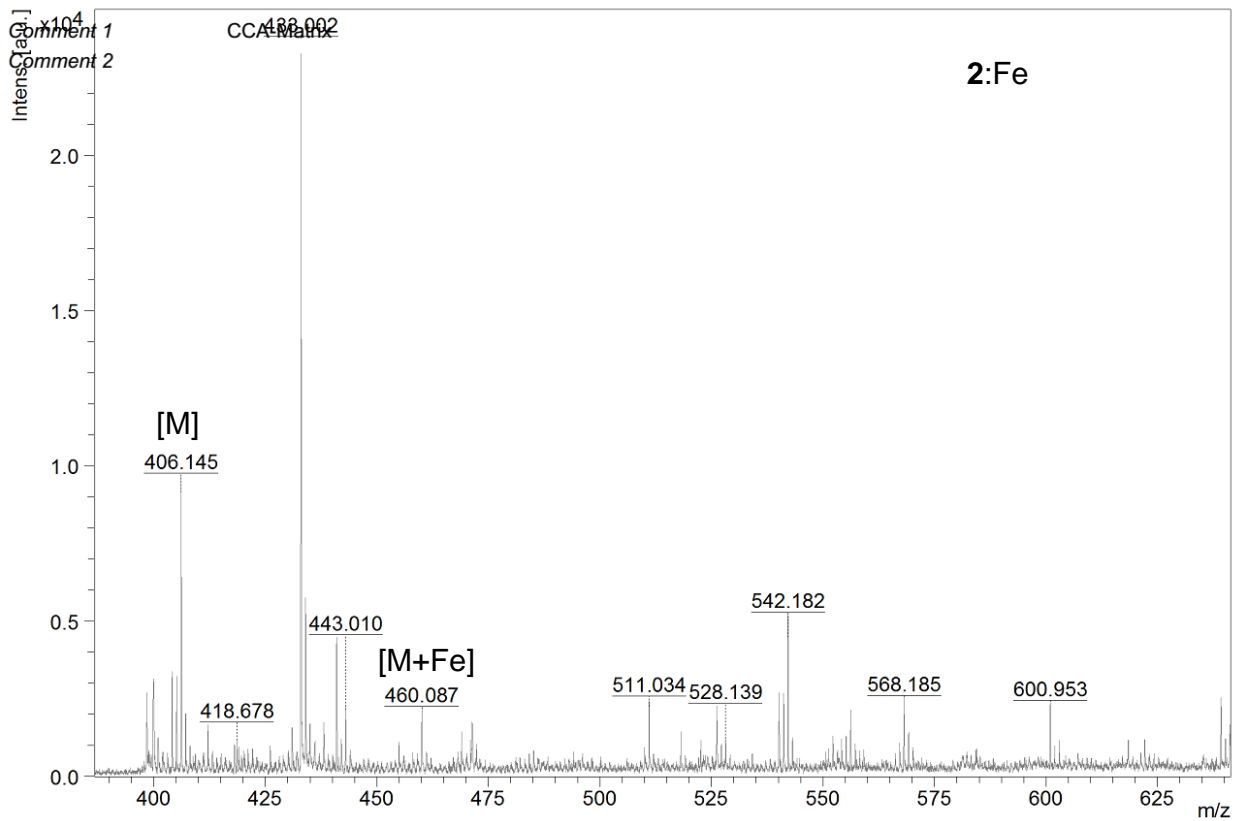
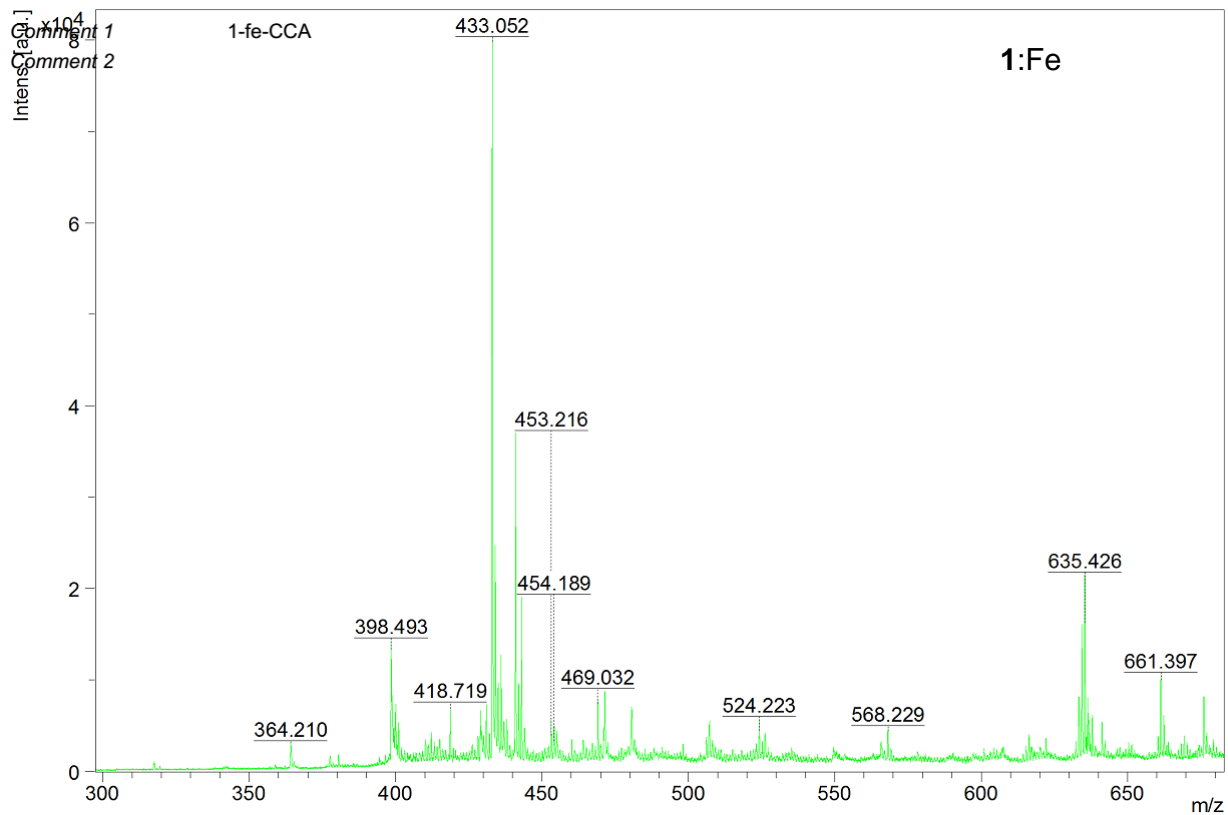
primary antibody (OC, Merck Millipore) at 4 °C for 18 h, followed by the treatment with secondary antibody (1:5000), which is conjugated with horseradish peroxidase (HRP) for 45 min. Finally, the membrane was treated with ECL reagent (Biorad) and blot image was recorded using Biorad Chemitouch imaging instrument. The blot intensity of each sample was compared with the control (A β 42 fibrils alone) using GraphPad Prism 6 software.

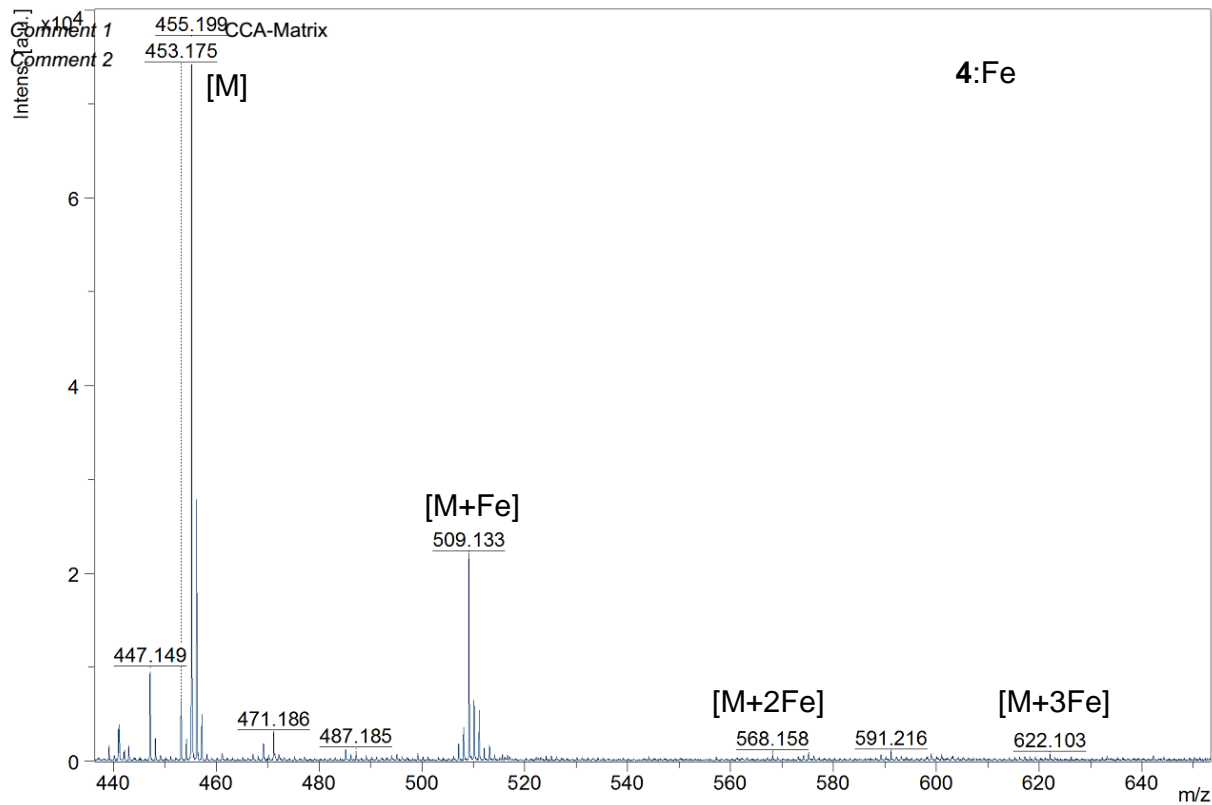
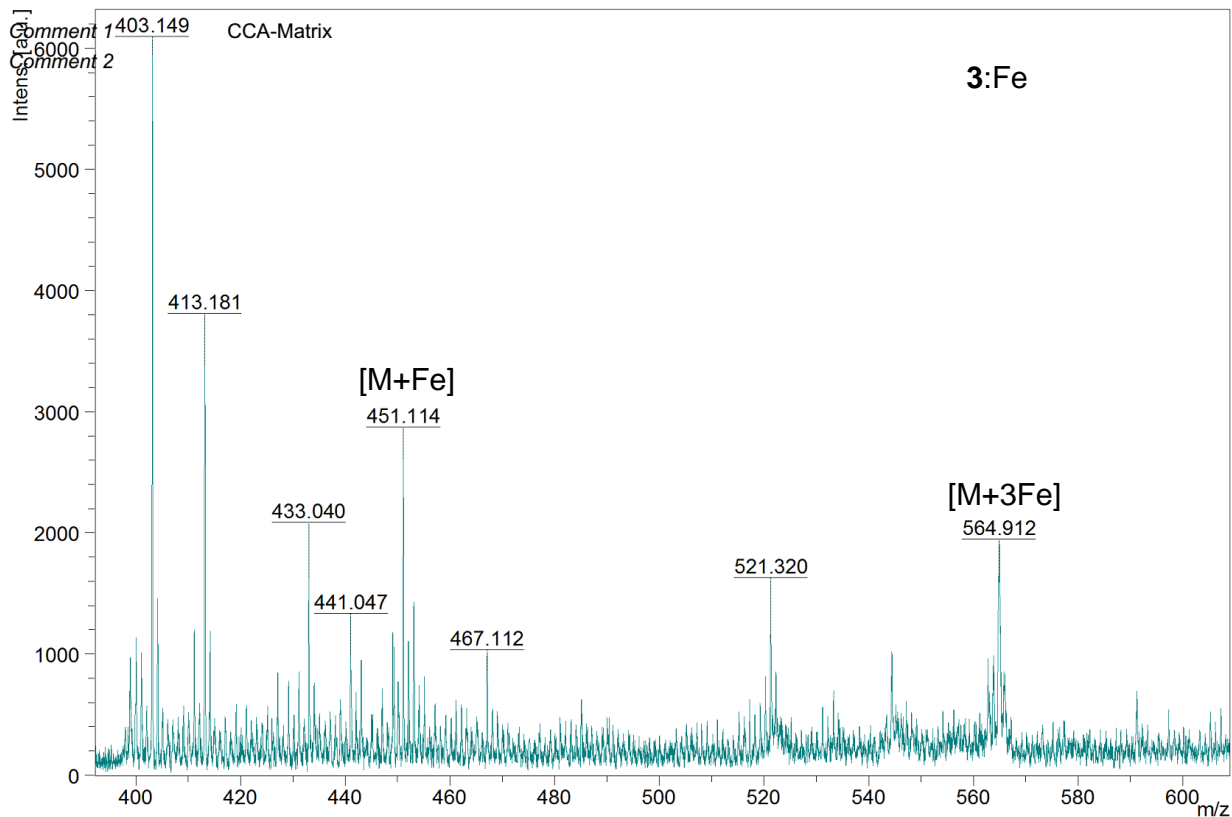
2.12 Appendix

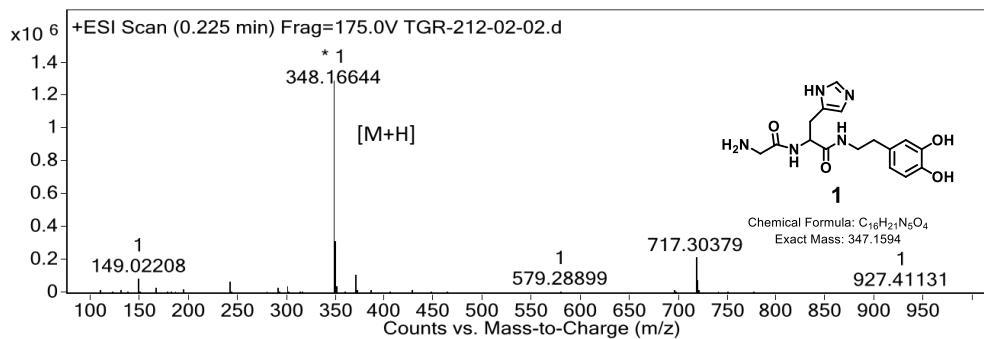
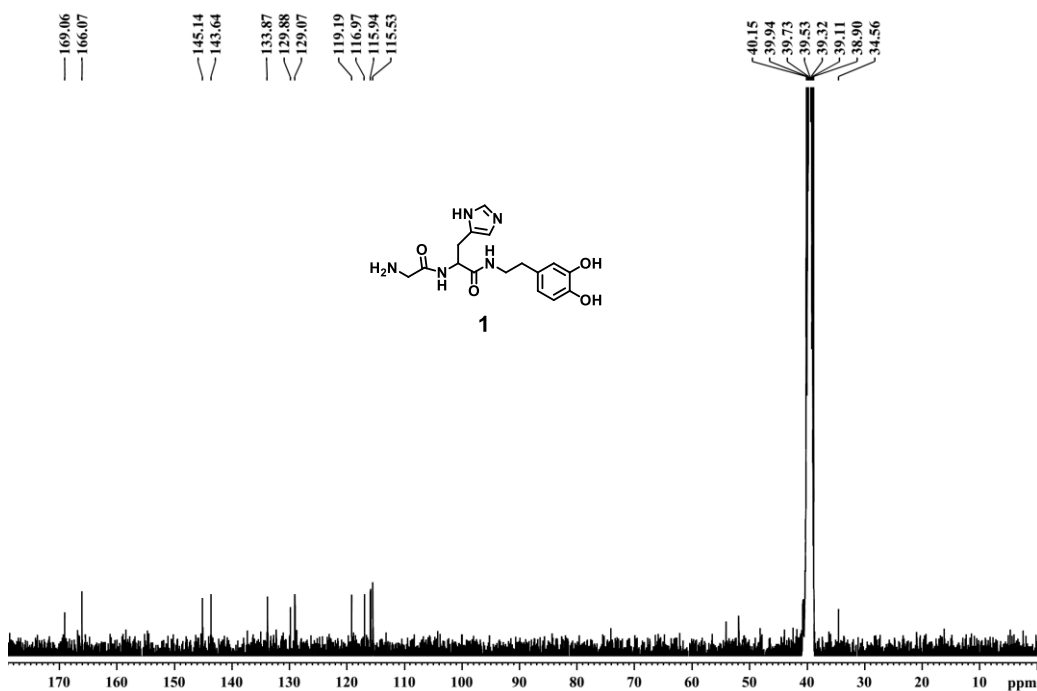
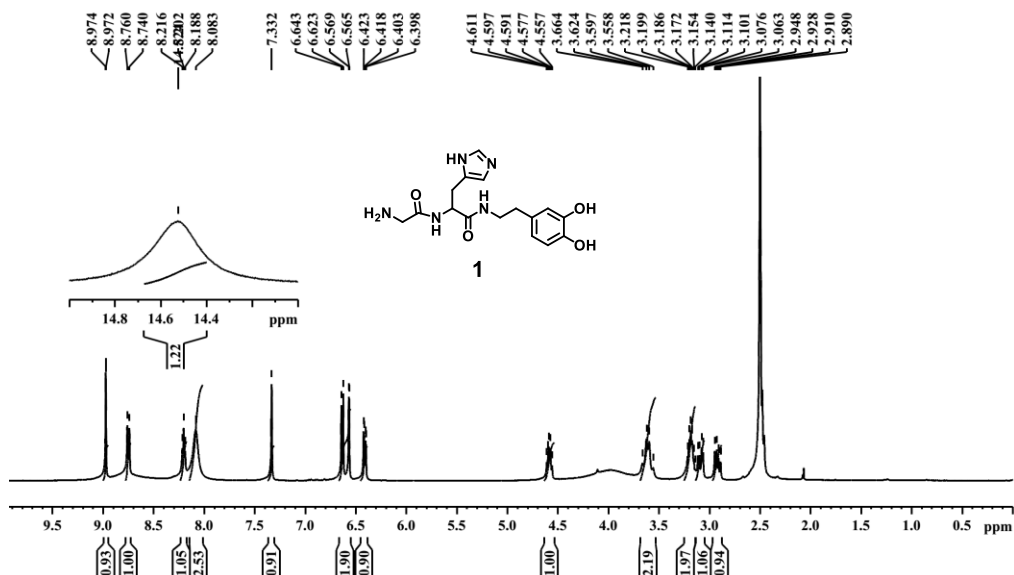
- ❖ MADLI Mass Analysis of **1**:Cu^{II}
- ❖ MADLI Mass Analysis of **2**:Cu^{II}
- ❖ MADLI Mass Analysis of **3**:Cu^{II}
- ❖ MADLI Mass Analysis of **4**:Cu^{II}
- ❖ MADLI Mass Analysis of **1**:Fe^{III}
- ❖ MADLI Mass Analysis of **2**:Fe^{III}
- ❖ MADLI Mass Analysis of **3**:Fe^{III}
- ❖ MADLI Mass Analysis of **4**:Fe^{III}
- ❖ Compound **1**: ¹H and ¹³C NMR analysis
- ❖ Compound **1**: HRMS analysis
- ❖ Compound **2**: ¹H and ¹³C NMR analysis
- ❖ Compound **1**: HRMS analysis
- ❖ Compound **3**: ¹H and ¹³C NMR analysis
- ❖ Compound **1**: HRMS analysis
- ❖ Compound **4**: ¹H and ¹³C NMR analysis
- ❖ Compound **4**: HRMS analysis
- ❖ Journal Cover Art

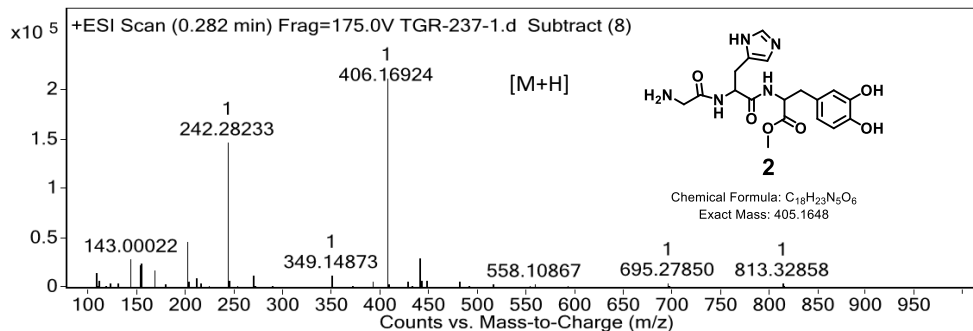
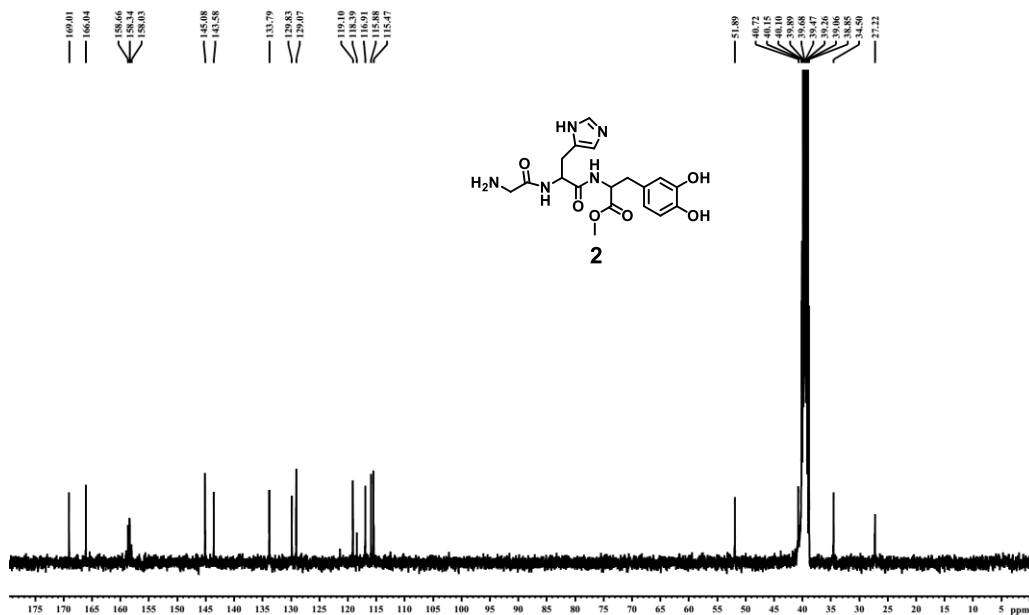
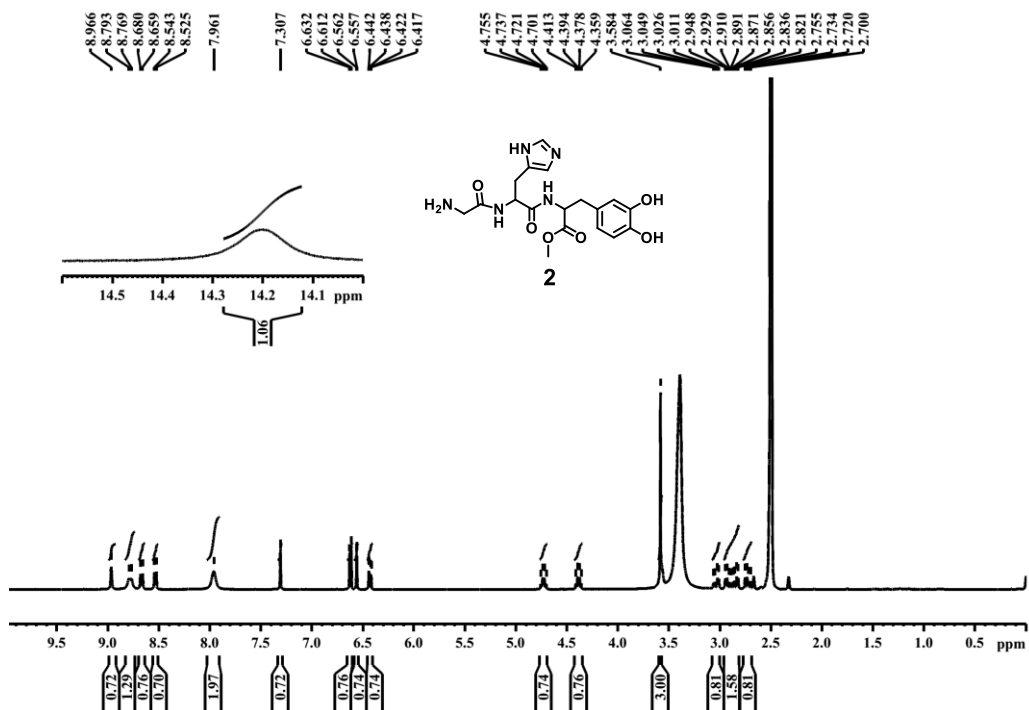


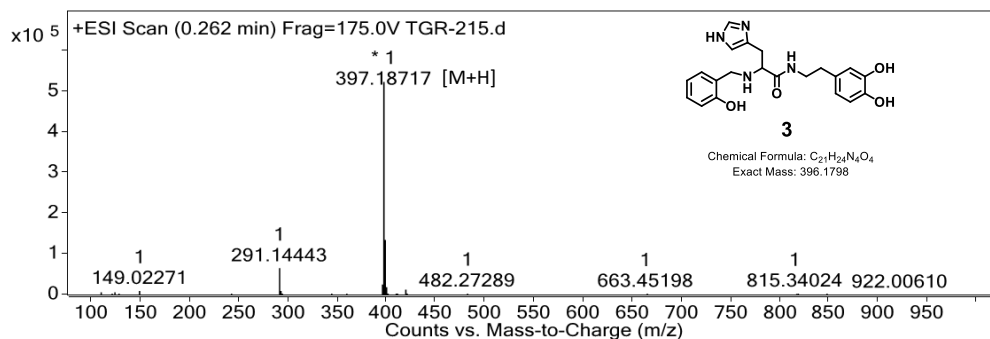
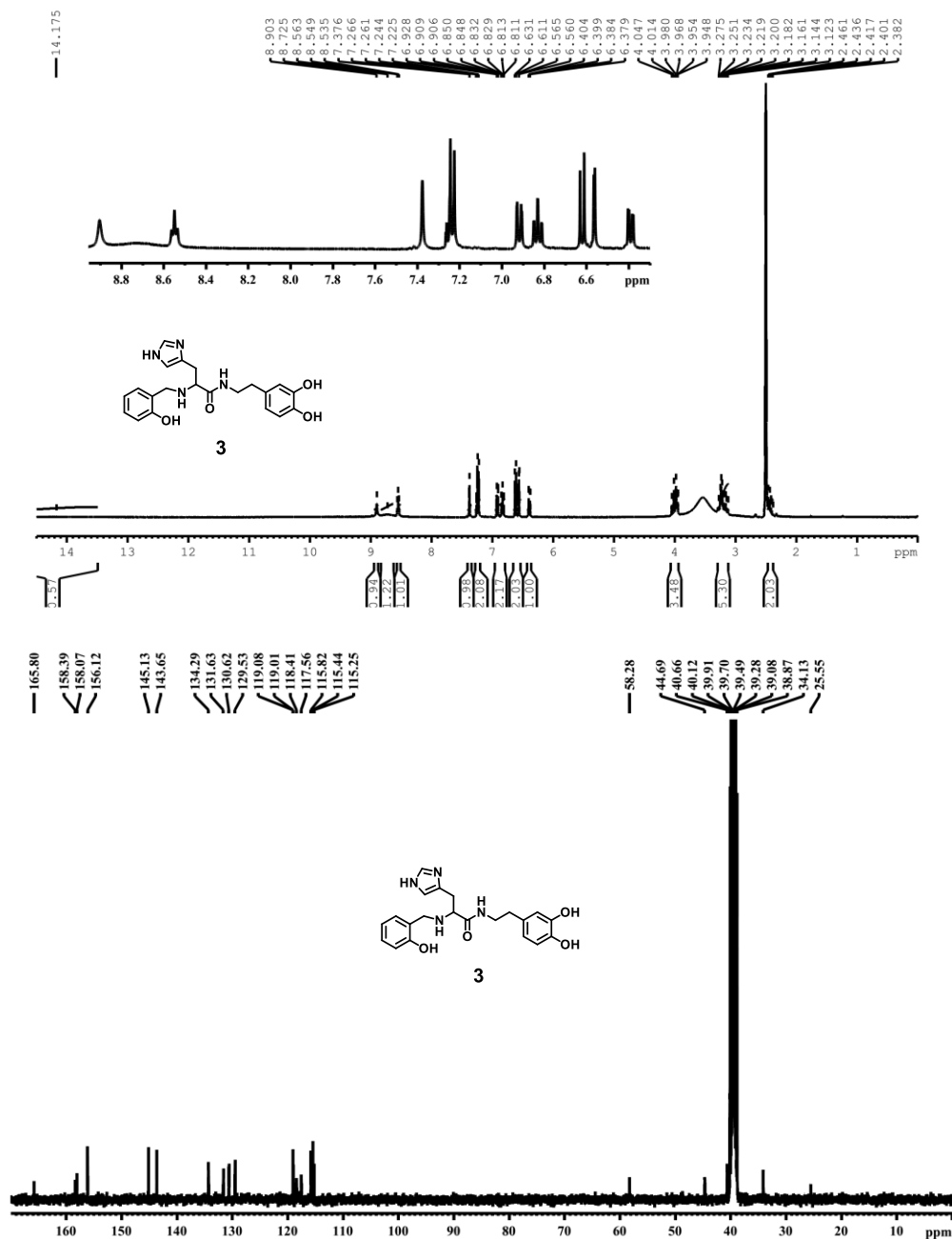


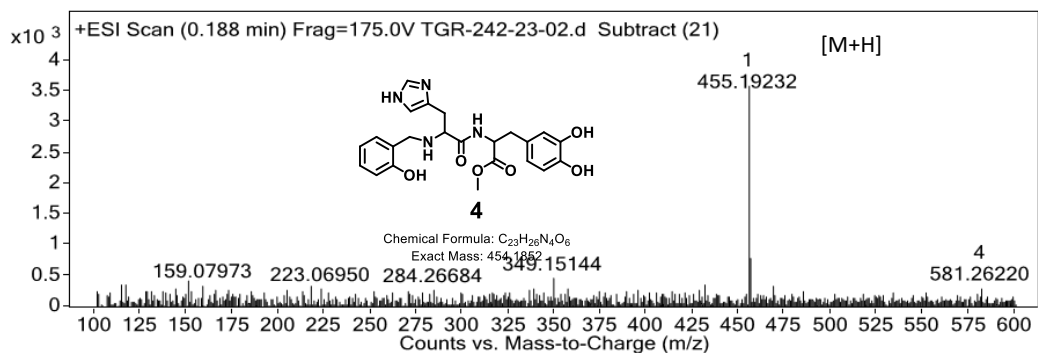
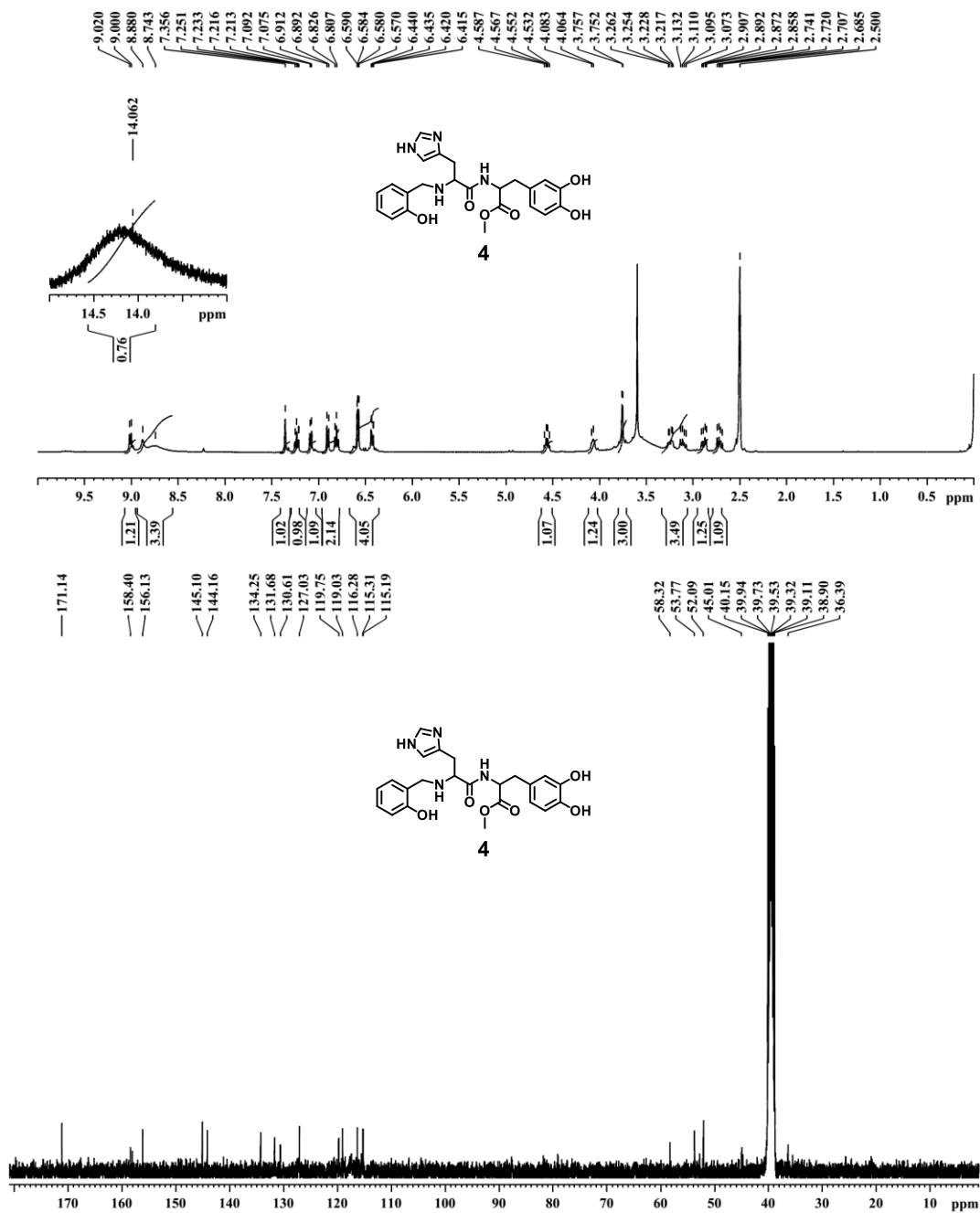


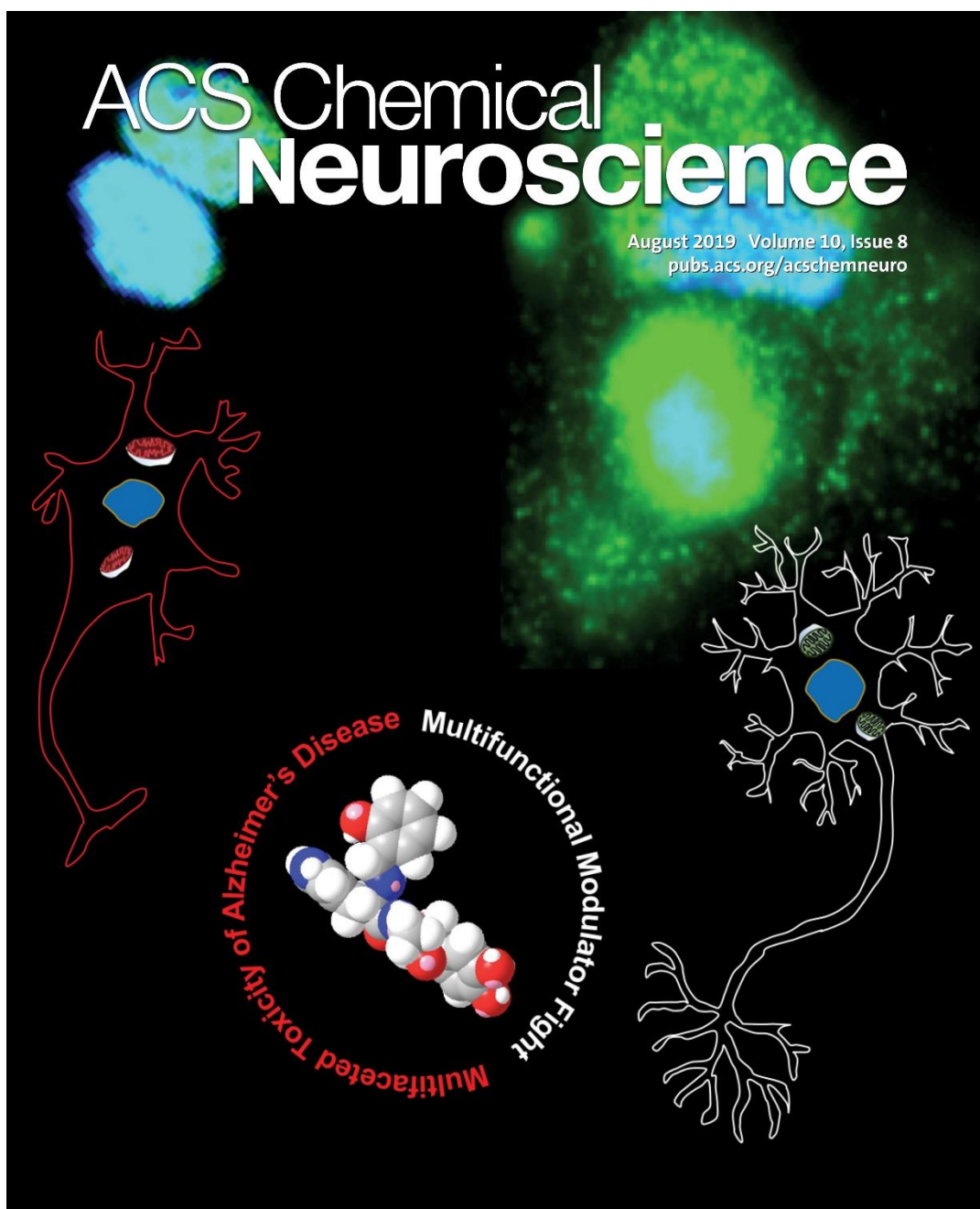












Multifunctional modulator (MFM) strategy is crucial to ameliorate multifaceted toxicity of Alzheimer's disease. This article presents design of MFMs inspired by the natural tripeptide of human origin. MFM (4) rescues neuronal cells from metal-dependent and independent amyloidogenesis, oxidative stress, redox dyshomeostasis (Nrf2 protein signaling, green color), DNA and mitochondrial damage, and inflammation.

Art designers: Sourav Samanta and Thimmaiah Govindaraju.

2.13 REFERENCES

1. Prince, M.; Bryce, R.; Albanese, E.; Wimo, A.; Ribeiro, W.; and Ferri, C. P. The global prevalence of dementia: a systematic review and metaanalysis. *Alzheimer's Dementia* **2013**, *9*, 63–75.
2. Walsh, D. M.; and Selkoe, D. J. Deciphering the molecular basis of memory failure in Alzheimer's disease. *Neuron* **2004**, *44*, 181–193.
3. Reitz, C.; Brayne, C.; and Mayeux, R. Epidemiology of Alzheimer disease. *Nat. Rev. Neurol.* **2011**, *7*, 137–152.
4. Alzheimer's Association, 2018 Alzheimer's disease facts and figures. *Alzheimers Dementia* **2018**, *14*, 701–701.
5. Rajasekhar, K.; Chakrabarti, M.; and Govindaraju, T. Function and toxicity of amyloid beta and recent therapeutic interventions targeting amyloid beta in Alzheimer's disease. *Chem. Commun.* **2015**, *51*, 13434–13450.
6. Dobson, C. M. Protein folding and misfolding. *Nature* **2003**, *426*, 884–890.
7. Ross, C. A.; and Poirier, M. A. Protein aggregation and neurodegenerative disease. *Nat. Med.* **2004**, *10*, S10–17.
8. Chiti, F.; and Dobson, C. M. Protein misfolding, amyloid formation, and human disease: a summary of progress over the last decade. *Annu. Rev. Biochem.* **2017**, *86*, 27–68.
9. Hamley, I. W. The amyloid beta peptide: a chemist's perspective. Role in Alzheimer's and fibrillization. *Chem. Rev.* **2012**, *112*, 5147–5192.
10. Hatai, J.; Motiei, L.; and Margulies, D. Analyzing amyloid beta aggregates with a combinatorial fluorescent molecular sensor. *J. Am. Chem. Soc.* **2017**, *139*, 2136–2139.
11. Sowade, R. F.; and Jahn, T. R. Seed-induced acceleration of amyloid-beta mediated neurotoxicity in vivo. *Nat. Commun.* **2017**, *8*, 512.
12. Huy, P. D.; Vuong, Q. V.; La Penna, G.; Faller, P.; and Li, M. S. Impact of Cu(II) binding on structures and dynamics of A β 42 monomer and dimer: molecular dynamics study. *ACS Chem. Neurosci.* **2016**, *7*, 1348–1363.
13. Hardy, J.; and Selkoe, D. J. The amyloid hypothesis of Alzheimer's disease: progress and problems on the road to therapeutics. *Science*, **2002**, *297*, 353–356.

14. Gaggelli, E.; Kozlowski, H.; Valensin, D.; and Valensin, G. Copper homeostasis and neurodegenerative disorders (Alzheimer's, prion, and Parkinson's diseases and amyotrophic lateral sclerosis). *Chem. Rev.* **2006**, *106*, 1995–2044.
15. Cuadrado, A.; Rojo, A. I.; Wells, G.; Hayes, J. D.; Cousin, S. P.; Rumsey, W. L.; Attucks, O. C.; Franklin, S.; Levonen, A. L.; Kensler, T. W.; and Dinkova-Kostova, A. T. Therapeutic targeting of the NRF2 and KEAP1 partnership in chronic diseases. *Nat. Rev. Drug Discovery* **2019**, *18*, 295.
16. Wyss-Coray, T. Inflammation in Alzheimer disease: driving force, bystander or beneficial response? *Nat. Med.* **2006**, *12*, 1005–1015.
17. Heneka, M. T.; McManus, R. M.; and Latz, E. Inflammasome signalling in brain function and neurodegenerative disease. *Nat. Rev. Neurosci.* **2018**, *19*, 610–621.
18. Mastroeni, D.; Khdour, O. M.; Delvaux, E.; Nolz, J.; Olsen, G.; Berchtold, N.; Cotman, C.; Hecht, S. M.; and Coleman, P. D. Nuclear but not mitochondrial-encoded oxidative phosphorylation genes are altered in aging, mild cognitive impairment, and Alzheimer's disease. *Alzheimers Dementia* **2017**, *13*, 510–519.
19. Rajasekhar, K.; Mehta, K.; and Govindaraju, T. Hybrid multifunctional modulators inhibit multifaceted Aβ toxicity and prevent mitochondrial damage. *ACS Chem. Neurosci.* **2018**, *9*, 1432–1440.
20. Rajasekhar, K.; and Govindaraju, T. Current progress, challenges and future prospects of diagnostic and therapeutic interventions in Alzheimer's disease. *RSC Adv.* **2018**, *8*, 23780–23804.
21. Karran, E.; Mercken, M.; and De Strooper, B. The amyloid cascade hypothesis for Alzheimer's disease: an appraisal for the development of therapeutics. *Nat. Rev. Drug Discovery* **2011**, *10*, 698–712.
22. Savelieff, M. G.; Nam, G.; Kang, J.; Lee, H. J.; Lee, M.; and Lim, M. H. Development of multifunctional molecules as potential therapeutic candidates for Alzheimer's disease, parkinson's disease, and amyotrophic lateral sclerosis in the last decade. *Chem. Rev.* **2019**, *119*, 1221–1322.
23. Lee, S.; Zheng, X.; Krishnamoorthy, J.; Savelieff, M. G.; Park, H. M.; Brender, J. R.; Kim, J. H.; Derrick, J. S.; Kochi, A.; Lee, H. J.; Kim, C.; Ramamoorthy, A.; Bowers, M. T.; and Lim, M. H. Rational design of a structural framework with potential use to develop

- chemical reagents that target and modulate multiple facets of Alzheimer's disease. *J. Am. Chem. Soc.* **2014**, *136*, 299–310.
24. Kumar, S.; Henning-Knechtel, A.; Magzoub, M.; and Hamilton, A. D. Peptidomimetic-based multidomain targeting offers critical evaluation of Abeta structure and toxic function. *J. Am. Chem. Soc.* **2018**, *140*, 6562–6574.
25. Beck, M. W.; Derrick, J. S.; Kerr, R. A.; Oh, S. B.; Cho, W. J.; Lee, S. J.; Ji, Y.; Han, J.; Tehrani, Z. A.; Suh, N.; Kim, S.; Larsen, S. D.; Kim, K. S.; Lee, J. Y.; Ruotolo, B. T.; and Lim, M. H. Structure-mechanism-based engineering of chemical regulators targeting distinct pathological factors in Alzheimer's disease. *Nat. Commun.* **2016**, *7*, 13115.
26. Muthuraj, B.; Layek, S.; Balaji, S. N.; Trivedi, V.; and Iyer, P. K. Multiple function fluorescein probe performs metal chelation, disaggregation, and modulation of aggregated Abeta and Abeta-Cu complex. *ACS Chem. Neurosci.* **2015**, *6*, 1880–1891.
27. Barrow, C. J.; and Zagorski, M. G. Solution structures of beta peptide and its constituent fragments: relation to amyloid deposition. *Science*, **1991**, *253*, 179–182.
28. Rajasekhar, K.; Suresh, S. N.; Manjithaya, R.; and Govindaraju, T. Rationally designed peptidomimetic modulators of abeta toxicity in Alzheimer's disease. *Sci. Rep.* **2015**, *5*, 8139.
29. Rajasekhar, K.; Narayanaswamy, N.; Mishra, P.; Suresh, S. N.; Manjithaya, R.; and Govindaraju, T. Synthesis of hybrid cyclic peptoids and identification of autophagy enhancer. *ChemPlusChem*, **2014**, *79*, 25–30.
30. Rajasekhar, K.; Madhu, C.; and Govindaraju, T. Natural tripeptide-based inhibitor of multifaceted amyloid beta toxicity. *ACS Chem. Neurosci.* **2016**, *7*, 1300–1310.
31. Pickart, L.; Vasquez-Soltero, J. M.; and Margolina, A. GHK peptide as a natural modulator of multiple cellular pathways in skin regeneration. *Bio. Med. Res. Int.* **2015**, *2015*, 648108.
32. Reybier, K.; Ayala, S.; Alies, B.; Rodrigues, J. V.; Bustos Rodriguez, S.; La Penna, G.; Collin, F.; Gomes, C. M.; Hureau, C.; and Faller, P. Free superoxide is an intermediate in the production of H_2O_2 by Copper(I)-Abeta peptide and O_2 . *Angew. Chem., Int. Ed.* **2016**, *55*, 1085–1089.
33. Cheignon, C.; Tomas, M.; Bonnefont-Rousselot, D.; Faller, P.; Hureau, C.; and Collin, F. Oxidative stress and the amyloid beta peptide in Alzheimer's disease. *Redox Biol.* **2018**, *14*, 450–464.

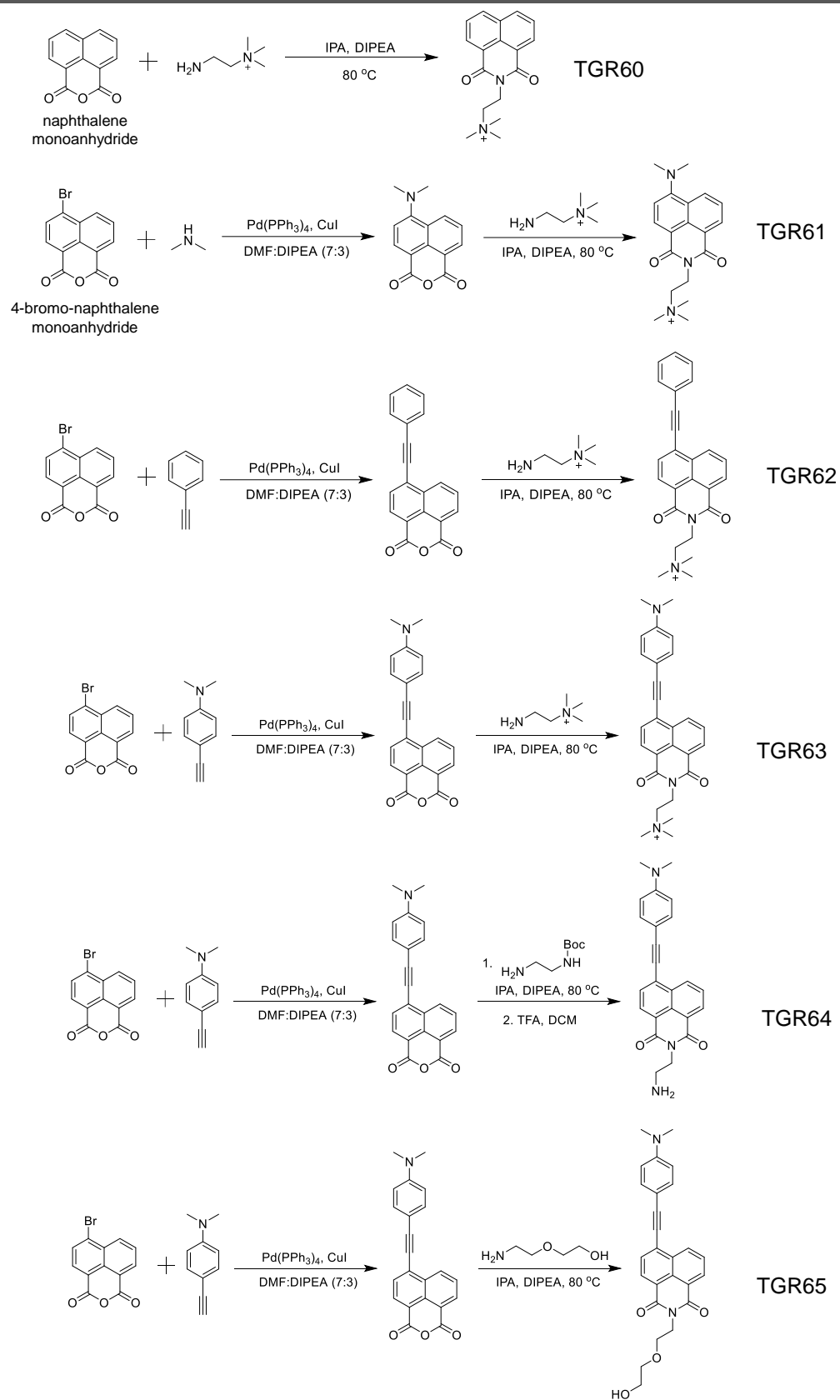
34. Barnham, K. J.; and Bush, A. I. Biological metals and metal-targeting compounds in major neurodegenerative diseases. *Chem. Soc. Rev.* **2014**, *43*, 6727–6749.
35. Kepp, K. P. Bioinorganic chemistry of Alzheimer's disease. *Chem. Rev.* **2012**, *112*, 5193–5239.
36. Caballero, A. B.; Terol-Ordaz, L.; Espargaro, A.; Vazquez, G.; Nicolas, E.; Sabate, R.; and Gamez, P. Histidine-rich oligopeptides to lessen copper-mediated amyloid-beta toxicity. *Chem. Eur. J.* **2016**, *22*, 7268–7280.
37. Whitehorne, T. J.; and Schaper, F. Square-planar Cu(II) diketiminate complexes in lactide polymerization. *Inorg. Chem.* **2013**, *52*, 13612–13622.
38. Grabo, J. E.; Chrisman, M. A.; Webb, L. M.; and Baldwin, M. J. Photochemical reactivity of the iron(III) complex of a mixeddonor, alpha-hydroxy acid-containing chelate and its biological relevance to photoactive marine siderophores. *Inorg. Chem.* **2014**, *53*, 5781–5787.
39. Mena, S.; Mirats, A.; Caballero, A. B.; Guirado, G.; Barrios, L. A.; Teat, S. J.; Rodriguez-Santiago, L.; Sodupe, M.; and Gamez, P. Drastic effect of the peptide sequence on the copper-binding properties of tripeptides and the electrochemical behaviour of their copper(II) complexes. *Chem. Eur. J.* **2018**, *24*, 5153–5162.
40. Robert, A.; Liu, Y.; Nguyen, M.; and Meunier, B. Regulation of copper and iron homeostasis by metal chelators: a possible chemotherapy for Alzheimer's disease. *Acc. Chem. Res.* **2015**, *48*, 1332–1339.
41. Liu, Z. Q. Chemical insights into ginseng as a resource for natural antioxidants. *Chem. Rev.* **2012**, *112*, 3329–3355.
42. Xie, J.; and Schaich, K. M. Re-evaluation of the 2,2-diphenyl-1-picrylhydrazyl free radical (DPPH) assay for antioxidant activity. *J. Agric. Food Chem.* **2014**, *62*, 4251–4260.
43. Biswas, A.; Kurkute, P.; Saleem, S.; Jana, B.; Mohapatra, S.; Mondal, P.; Adak, A.; Ghosh, S.; Saha, A.; Bhunia, D.; Biswas, S. C.; and Ghosh, S. Novel hexapeptide interacts with tubulin and microtubules, inhibits Abeta fibrillation, and shows significant neuroprotection. *ACS Chem. Neurosci.* **2015**, *6*, 1309–1316.
44. Pallo, S. P.; DiMaio, J.; Cook, A.; Nilsson, B.; and Johnson, G. V. W. Mechanisms of tau and Abeta-induced excitotoxicity. *Brain Res.* **2016**, *1634*, 119–1131.

45. Plascencia-Villa, G.; Ponce, A.; Collingwood, J. F.; ArellanoJimenez, M. J.; Zhu, X.; Rogers, J. T.; Betancourt, I.; Jose-Yacaman, M.; and Perry, G. High-resolution analytical imaging and electron holography of magnetite particles in amyloid cores of Alzheimer's disease. *Sci. Rep.* **2016**, *6*, 24873.
46. Collingwood, J. F.; Chandra, S.; Davidson, M.; Mikhaylova, A.; Eskin, T.; Dobson, J.; Forder, J.; and Batich, C. P2-001: Highresolution magnetic resonance imaging to quantify relaxation parameters in Alzheimer's brain tissue. *Alzheimer's Dementia* **2008**, *4*, T365.
47. Bourassa, M. W.; and Miller, L. M. Metal imaging in neurodegenerative diseases. *Metallomics*. **2012**, *24*, 721-38.
48. Barnham, K. J.; and Bush, A. I. Biological metals and metal-targeting compounds in major neurodegenerative diseases. *Chem. Soc. Rev.* **2014**, *43*, 6727-49.
49. Hunter, R. A.; Storm, W. L.; Coneski, P. N.; and Schoenfisch, M. H. Inaccuracies of nitric oxide measurement methods in biological media. *Anal. Chem.* **2013**, *85*, 1957-1963.

Chapter 3

Small Molecule with Naphthalene Monoimide Scaffold Ameliorates Amyloid Burden and Cognitive Decline in a Mouse Model of Alzheimer's Disease

AD pathophysiology is described by the phenotypic continuum, parenchymal A β plaques deposition in the brain, memory impairment, cognitive decline, and neuropsychiatric symptoms viz., agitation, irritability, hallucinations and depression in the advanced stages.¹⁻⁶ The National Institute on Aging and Alzheimer's Association research framework report (2018) proposed parenchymal A β plaques as designated pathological hallmark along with intracellular neurofibrillary tangles.⁷ The overexpression and proteolysis of amyloid precursor protein by β - and γ -secretases generate extracellular A β peptides which undergo misfolding and accumulate as senile plaques in the brain.^{2,5,8,9} Specifically, A β 42 aggregation species are extremely neurotoxic and elicit toxicity in the form of disrupting neuronal synaptic function and plasticity, impaired short-term memory, and long-term potentiation, a key process associated with learning and memory.^{10,11} The endocytosis and blocking of essential receptors such as N-methyl-D-aspartate (NMDA) and α -amino-3-hydroxy-5-methyl-4-isoxazolepropionic acid (AMPA) at synaptic cleft by A β aggregation species cause neuronal circuit disruption and cognitive decline.¹²⁻¹⁴ The clinicopathologic studies correlate cognitive decline or sequence of AD pathology to A β burden associated toxicity in the disease brain.^{8,15,16} These facts and reports have underscored the importance of clearing or reducing the A β burden from the brain as a primary target to develop therapeutic agents for the treatment of AD.¹⁷⁻¹⁹ The amyloid toxicity emphasizes the need for a novel drug design strategy to ameliorate A β burden-associated plasma membrane toxicity, cognitive decline and memory (STM and LTP) impairment under progressive AD pathogenesis.²⁰⁻²² We designed and synthesized a set of novel small molecules (TGR60-65) with naphthalene monoamide scaffold and evaluated their efficacy in ameliorating the amyloid toxicity of AD. The detailed biophysical, microscopy and cellular studies showed that 4-ethynyl-*N,N*-dimethylaniline and *N,N,N*-trimethylethylenediamine functionalized naphthalene



Scheme 1. Syntheses of small molecules with NMI scaffold (TGR60-65).

monoimide (TGR63) is a potent candidate to modulate A β 42 aggregation and associated plasma membrane toxicity. The pharmacokinetics studies revealed serum stability, blood-brain-barrier (BBB) permeability and biocompatibility of TGR63 and its suitability for long term *in vivo* administration. The *in vivo* TGR63 treatment reduces the severe cortical and hippocampal A β burden in the APP/PS1 mice brain with significant improvement of memory and cognitive functions. Molecular dynamics study of A β species in presence of TGR63 demonstrates the affinity and key interactions of TGR63 with A β peptides and provides insights on the modulation of toxic amyloidosis. *In vitro* and *in vivo* data on amelioration of amyloid burden, neuropathological hallmarks and cognitive decline are in good agreement to establish TGR63 as a potential therapeutic candidate to treat AD progression.

3.1 Design and Synthesis of Small Molecules with Naphthalene Monoimide Scaffold

The A β aggregation causes deleterious neuropathological and cognitive effects and ways to obliterate the amyloid burden and associated neurotoxicity are sought-after therapeutic strategies.^{5,22,23} We designed and synthesized a set of novel small molecules with naphthalene monoimide (NMI) scaffold to modulate the amyloid burden. The hydrophobicity of NMI core with *N,N,N*-trimethylethylenediamine as imide substituent was fine-tuned systematically by incorporating electron rich *N,N*-dimethylamine, ethynylbenzene, and 4-ethynyl-*N,N*-dimethylaniline moieties at (Scheme 1). These modifications to NMI core were undertaken to determine the required hydrophobicity-hydrophilicity to modulate A β aggregation. The structural fine-tuning of hydrophobic and hydrophilic moieties on NMI scaffold using appropriate functional groups resulted in a focused library of small molecules TGR60-65. For synthesis, 4-bromo-naphthalene monoanhydride (4-bromo NMA) was subjected to Sonogashira coupling

with *N,N*-dimethylamine, ethynylbenzene, and 4-ethynyl-*N,N*-dimethylaniline using Pd(PPh₃)₄, sodium ascorbate and copper sulfate under argon atmosphere (Scheme 1). The NMA derivatives were conjugated with *N,N*-dimethylpropan-1-amine, *N,N,N*-trimethylpropan-1-aminium and 2-propoxyethan-1-ol in isopropanol under reflux (80 °C) conditions to obtain NMI derivatives TGR60-65 in good yields. All the final compounds were thoroughly characterized by nuclear magnetic resonance (NMR) and high-resolution mass spectrometry (HRMS).

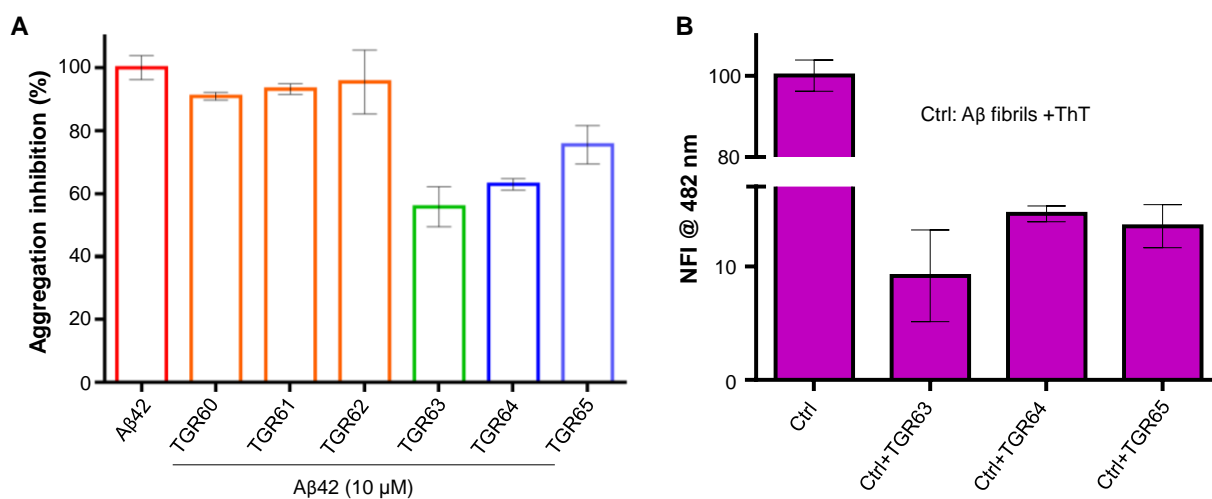


Figure 1. (A) Aggregation inhibition ability assessment: Aβ42 (10 μM) was incubated alone and with individual inhibitor (10 μM) for 72 h in PBS (10 mM, pH= 7.4) and the extent of aggregation was quantified by ThT fluorescence intensity. (B) Dissolution of Aβ42 aggregates studied by ThT assay. The data show the percentage (%) of ThT fluorescent intensity (FI) at 482 nm in presence of Aβ42 fibrils (10 μM) alone (Ctrl) and with inhibitors (30 μM). Each experiment was repeated three times (n= 3). Error bars represent the average±SEM of the fluorescence measurement.

3.2 *In Vitro* Modulation of Amyloid Aggregation and Probable Mechanism

The ability of NMI derivatives (TGR60-65) to modulate Aβ42 aggregation and associated neuronal toxicity was evaluated through inhibition and dissolution assays. Thioflavin (ThT) fluorescence assay was employed to assess the aggregation modulation efficacy of TGR60-65.

A β 42 (10 μ M) was incubated alone and with NMIs (10 μ M) individually for 72 h and the fluorescence intensity at 482 nm was measured upon treatment with ThT (10 μ M) to assess the extent of aggregation (Figure 1A). TGR60-62 treated A β 42 samples showed 90%, 93% and 95% aggregation, respectively, compare to untreated control (100%), which corresponds to nominal inhibitory effects of \sim 10%, 7% and 5%, respectively. A β 42 samples incubated with TGR63-65 showed \sim 55%, 62% and 75% aggregation suggesting significant aggregation inhibition of \sim 45%, 38% and 25%, respectively (Figure 1A). Next, fully grown A β 42 aggregates (10 μ M) was

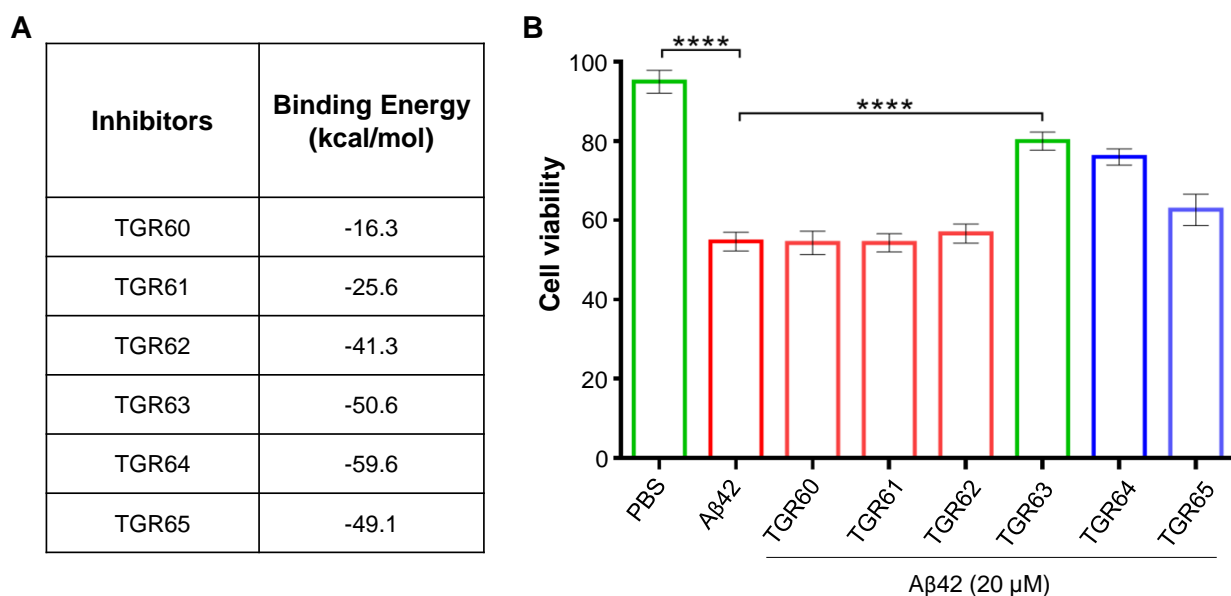


Figure 2. (A) Relative binding affinities of TGR60-65 compounds towards A β 42 fibrils. The data are based on the top high affinity binding sites within fibrils. (B) *In vitro* neuronal rescue from amyloid toxicity by TGR60-65. The observed cell viability of cultured neuronal cells (PC12) after independently incubated with PBS, A β 42 (20 μ M) alone and in the presence of TGR60-65 (40 μ M) for 24 h in cell growth media.

incubated with TGR63-65 (30 μ M) to assess their dissolution ability. The results showed decrease in ThT fluorescence to 9%, 14% and 13%, which corresponds to \sim 91%, 86% and 87% dissolution of aggregates, respectively, in presence of TGR63-65 compare to control (Figure

1B). These preliminary studies revealed that TGR63 is a promising lead aggregation modulator with pronounced inhibition and dissolution efficiency of 45% and 91%, respectively. A thorough computational study was carried out by employing molecular docking, molecular dynamics, and molecular mechanics-Generalized Born surface area (MM-GBSA) method to understand the molecular mechanism behind experimentally observed modulation of A β aggregation by TGR60-65.^{24,25} The A β 42 fibril structure reported in the protein databank (pdb id is 5OQV) based on cryogenic-electron microscopy (cryo-EM) was used for this study. The study showed

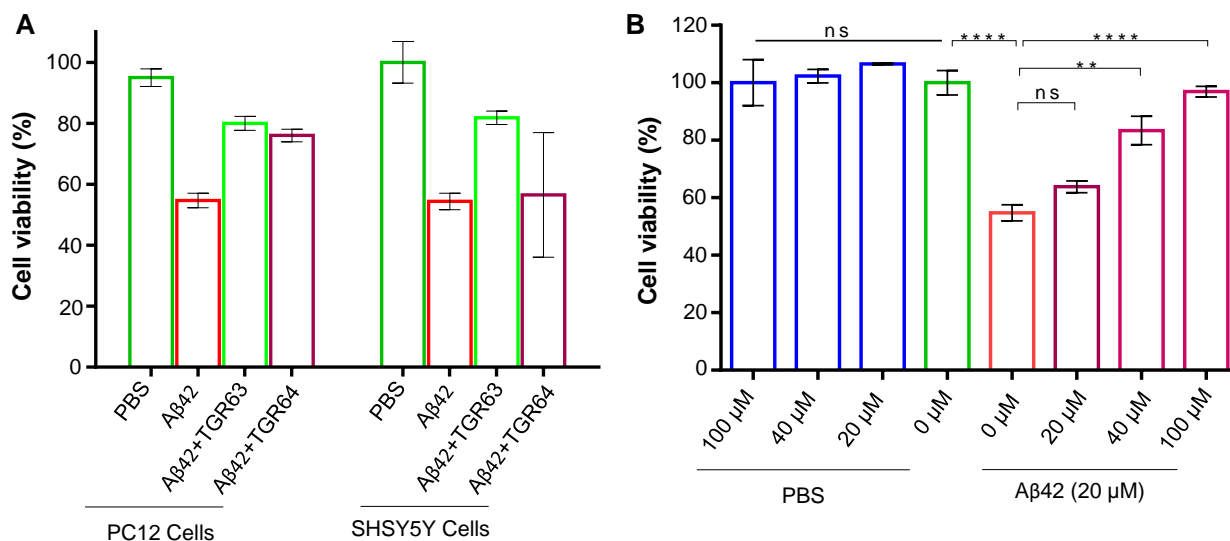


Figure 3. (A) *In vitro* neuronal rescue from A β 42 toxicity by TGR63 and TGR64. The observed cell viability of cultured neuronal cells (PC12 and SHSY5Y) after independently incubating (24 h) with A β 42 (20 μ M) peptides in absence and presence of inhibitors (TGR63 and TGR64) in the 1:2 molar stoichiometric ratio. (B) *In vitro* neuronal rescue from A β 42 toxicity by TGR63. The observed cell viability of cultured neuronal cells (SHSY5Y) after incubating (24 h) with different concentrations of TGR63 (20, 40 and 100 μ M) in absence and presence of and A β 42 (20 μ M) peptides.

that molecules have the tendency to bind to multiple binding sites in A β 42 fibril (Figure 4 refers to binding sites for TGR63). The surface sites are shown in red color and core sites are shown in green color. The binding free energies of TGR60-65 in their high affinity binding sites were

found to be -16.3, -25.6, -41.3, -50.6, -59.6, -49.1 kcal/mol, respectively (Figure 2A). The lower binding free energies for TGR63-65 indicate their better binding affinity and inhibition efficiency towards A β 42 fibrils (Figure 1A). These results encouraged us to assess the modulation of A β toxicity under cellular conditions (Figure 2B). The AD-like environment was mimicked by exposing the cultured PC12 cells to A β 42 (20 μ M), which result in the generation of cytotoxic aggregation species in the growth media. A β 42 caused mutilation to the cultured neuronal cells, as revealed by the decreased cell viability (54%) compared to untreated control

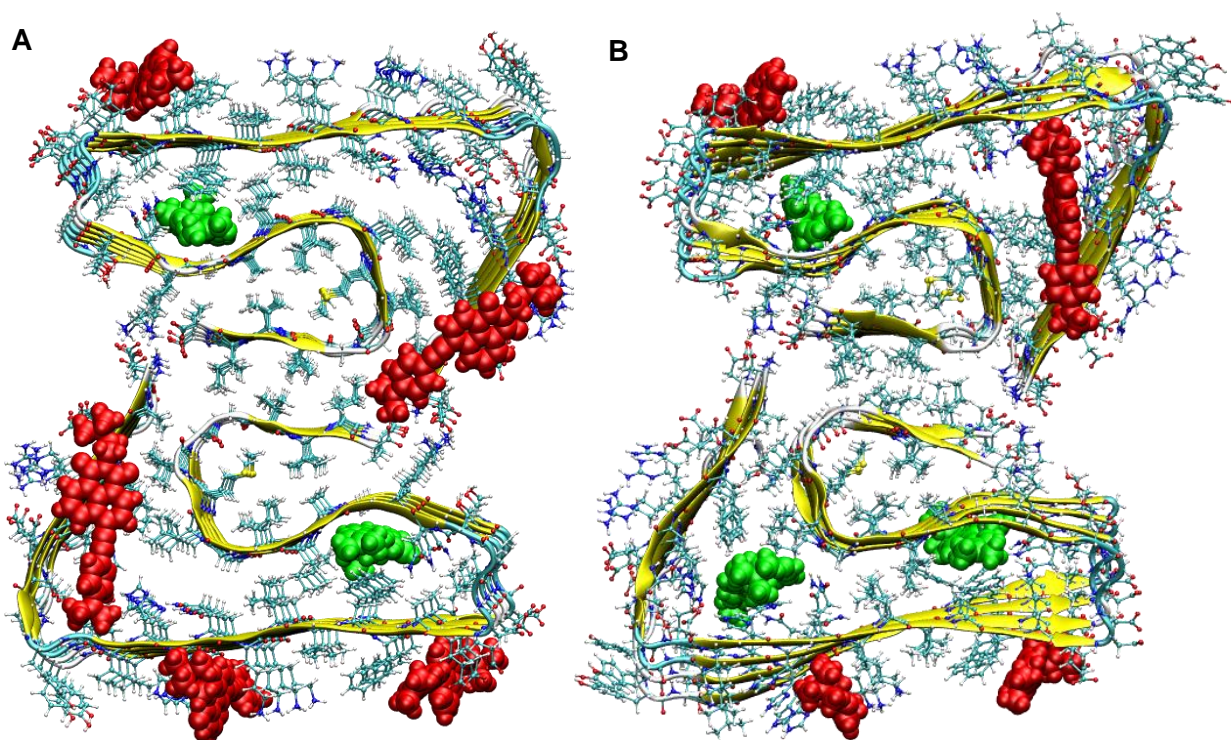


Figure 4. (A) and (B) The high affinity binding sites of TGR63 within A β 42 fibrils. A refers to the initial configuration, while B refers to a representative configuration in the production run.

cells (100%). The cells treated with A β 42 in presence of TGR60, TGR61, TGR62 and TGR65 showed cell viability of ~54%, 54%, 56% and 62%, respectively, similar to that of only A β treated cells. Interestingly, the promising aggregation modulators TGR63 and TGR64 showed 80% and 76% viability of cells treated with A β 42, respectively (Figure 2B). This corresponds to

improved cell rescue of ~26% and 22% from A β toxicity by TGR63 and TGR64, respectively, with TGR63 displaying superior neuronal rescue effect. These findings were further confirmed by the cell rescue study using SHSY5Y cells and the result are in good agreement with PC12 cells rescue data. TGR63 showed maximum cell rescue (~27%) effect on SHSY5Y cells compared to TGR64 (~3%) (Figure 3A). This neuronal rescue assessment confirmed that the 4-ethynyl-*N,N*-dimethylaniline and *N,N,N*-trimethylethylenediamine functionalization of NMI core (in TGR63) provides the best A β 42 aggregation inhibition ability compare to other functional moieties. A concentration dependent effect on the neuronal rescue was performed by treating SHSY5Y cells with varying concentrations of TGR63 (20, 40 and 100 μ M) in the absence and presence of A β 42 (20 μ M) for 24 h. The data showed concentration-dependent cellular rescue with ~63%, 83% and 95% viability of cells observed for 20, 40 and 100 μ M of TGR63, respectively, in the presence of A β 42 (Figure 3B). In addition, the cytotoxicity assay of TGR63

Table 1. Number of salt bridges and hydrogen bonds present in A β 42 fibrils in the absence and presence of inhibitors (TGR63 and TGR64).

| System | Number of salt bridges | Number of hydrogen bonds |
|------------------------------------|------------------------|--------------------------|
| A β fibrils in water | 48 | 81 |
| A β fibrils + TGR63 in water | 41 | 75 |
| A β fibrils + TGR64 in water | 54 | 74 |

in the absence of A β 42 did not show any significant cytotoxicity at 100 μ M compared to untreated control cells (100%), which demonstrates that TGR63 is nontoxic to cells at higher concentrations. *In silico* analysis was performed to understand the molecular mechanism behind the modulation of A β aggregation-induced toxicity by potential inhibitors (TGR63 and TGR64).

Interestingly, both the inhibitors interact with A β 42 fibril through multiple binding sites. In the course of molecular dynamics (MD), the inhibitors were found to bind to a “cryptic” site (a hidden site created when the ligand approaches the target) (Figure 4).^{24,25} The presence of such cryptic site in A β 42 fibril for novel inhibitor interaction is observed for the first time. The alterations in essential interactions (number of hydrogen bonds and salt bridges) of A β 42 peptides that are mainly responsible for amyloid fibril formation due to the binding of TGR63 and TGR64 were analyzed. A β 42 fibril comprises maximum number of intermolecular hydrogen bonds (81 bonds) in the absence of inhibitor and were reduced to 75 and 74 in the presence of

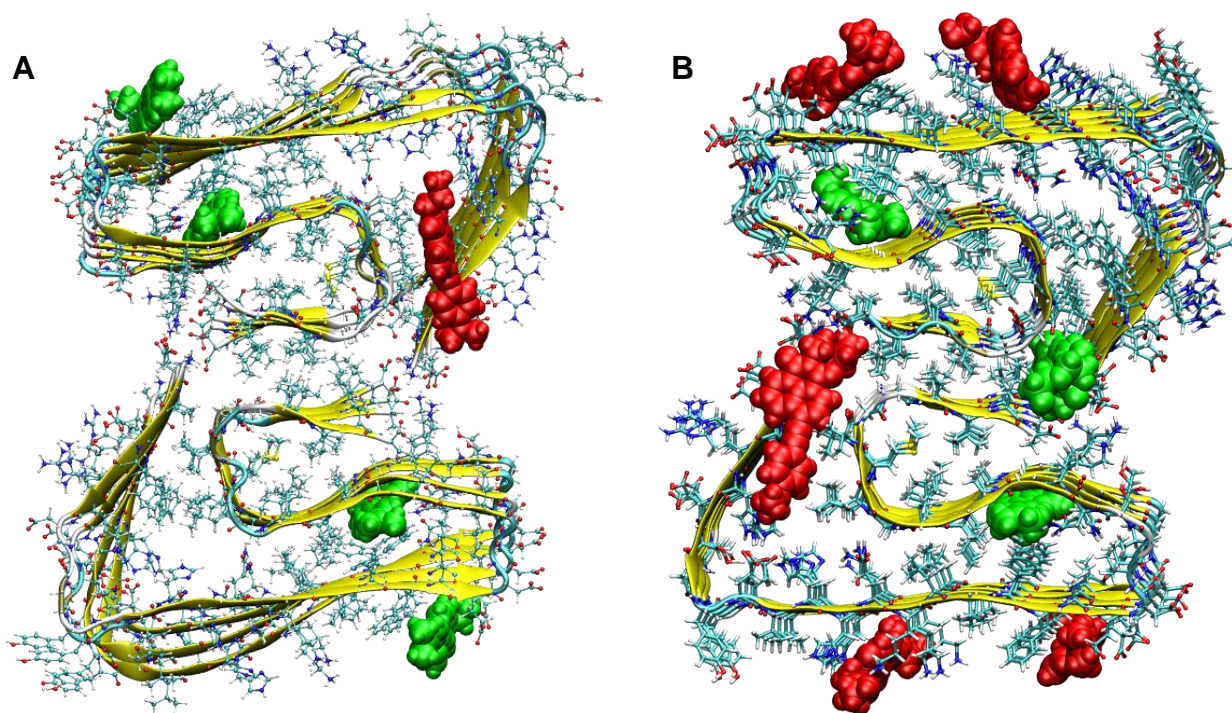


Figure 5. Different binding sites for TGR64 (A) and TGR65 (B) in A β 42 fibril.

TGR63 and TGR64, respectively (Table 1). Further, TGR63 binding significantly reduced the salt bridges in A β 42 fibrils from 48 to 41 through cation mediated disruption of electrostatic interactions (Figure 4B and Table 1). However, certain new salt bridge interactions (total 54

interactions) were formed in presence of TGR64 when compared to untreated A β 42 fibrils. The observed changes in the hydrogen bonding and salt bridge interactions clearly explain the superior amyloid aggregation inhibition and dissolution potential of TGR63 compared to TGR64 (Table 1 and Figure 5). A detailed analysis of the binding profile of TGR63 was performed due to its relatively superior disruptive interaction with A β 42 fibril. There are two modes of binding for TGR63, i) core binding and ii) surface binding (Figure 4B). The binding free energies of TGR63 in the core binding sites (as shown in green color in Figure 4A) are associated with the least binding free energies (-50.6 & -47.8 kcal/mol), while that of cryptic site is -34.9 kcal/mol (Figure 4B). The TGR63 showed slightly higher binding free energies for the surface sites (-35.4, -30.3, -24.4, and -14.5, respectively) when compared to core sites (Table 2). The total

Table 2. Binding free energies for TGR63 in different binding sites of A β 42 fibril. Different contributions to binding free energies are provided. The energies are in kcal/mol and the standard errors in binding free energies are in the range 0.12 to 0.22 kcal/mol.

| Sites | ΔE_{vdw} | ΔE_{elec} | $\Delta E_{\text{polar solvation}}$ | $\Delta E_{\text{non-polar solvation}}$ | $\Delta G_{\text{binding}}$ |
|--------|-------------------------|--------------------------|-------------------------------------|---|-----------------------------|
| Site-1 | -71.8 | -310.1 | 338.1 | -6.8 | -50.6 |
| Site-2 | -74.4 | -309.1 | 342.2 | -6.5 | -47.8 |
| Site-3 | -41.0 | -377.8 | 388.3 | -4.8 | -35.4 |
| Site-4 | -36.2 | -361.5 | 371.8 | -4.4 | -30.3 |
| Site-5 | -38.2 | -203.5 | 221.4 | -4.1 | -24.4 |
| Site-6 | -23.4 | -317.8 | 329.8 | -3.1 | -14.5 |
| Site-7 | -51.1 | -301.3 | 323.4 | -6.0 | -34.9 |

binding free energies and individual contributions from the van der Waals, electrostatic, polar and non-polar solvation free energies are shown in Table 2. The data reveal that the A β fibril-TGR63 interaction is mostly driven by electrostatic and van der Waals interactions (-310.1 and -

71.8 kcal/mol, respectively for site-1). While the electrostatic interactions appear prominent, they are largely nullified by the polar solvation free energies making the van der Waals interactions as the major driving force for the ligand-fibril association. The *in silico* study revealed that the binding of TGR63 at the surface and core sites of fibrils is responsible for modulation of A β aggregation. Overall, the *in vitro*, *in cellulo* and *in silico* studies established TGR63 as a promising candidate to modulate A β aggregation and associated toxicity in cells.

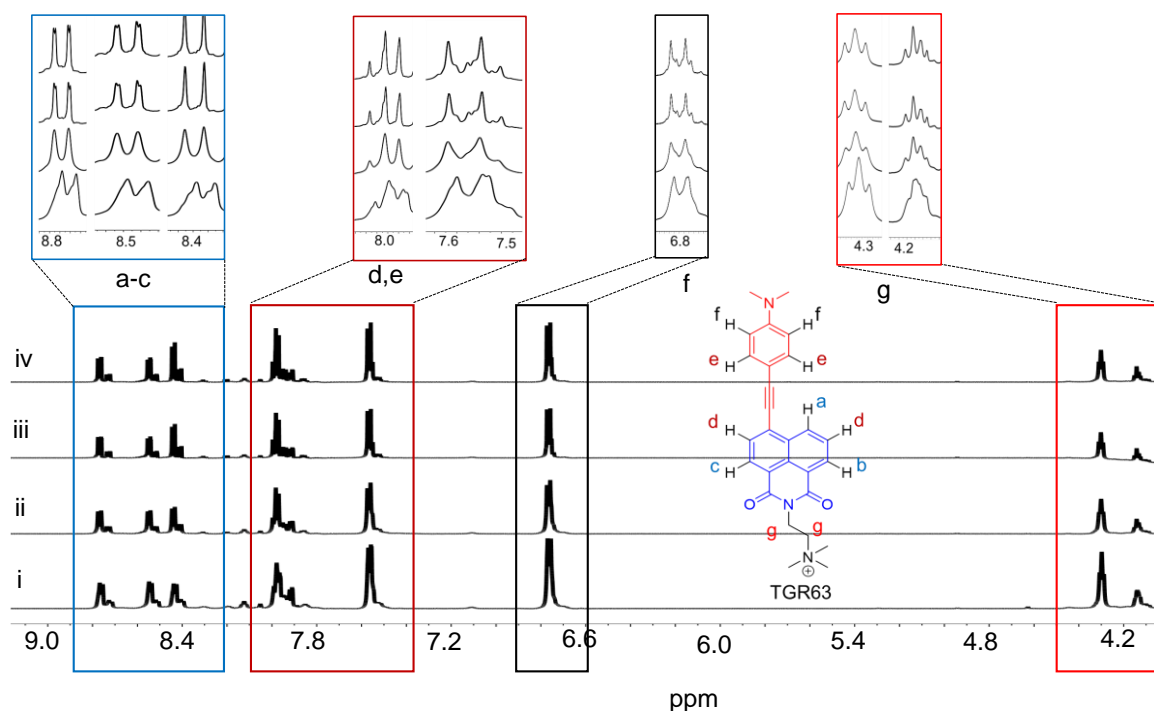


Figure 6. ¹H NMR spectra of TGR63 in the absence (i) and presence of A β 42 (10 μ M) at 6 h (ii), 24 h (iii) and 48 h (iv) of incubation at 37 $^{\circ}$ C. Selected regions were magnified to show the change in proton chemical shift values due to molecular level interactions of TGR63 with A β , which are responsible for interference and disruption of noncovalent forces that drive A β aggregation. Inset: The chemical structure of TGR63 with protons (a-g) assignment in different chemical environment.

Next, NMR spectroscopy was used to ascertain the molecular level interactions between TGR63 and A β 42 peptide (Figure 6). ¹H NMR spectra of TGR63 (1 mM) were acquired in the absence and presence of A β 42 (10 μ M) at different incubation time points (6, 24 and 48 h) using

WATERGATE sequence for solvent suppression in PBS buffer (10 mM, pH= 7.4) containing D₂O (12%).²⁰ TGR63 alone showed aromatic protons of NMI core and aniline moiety (a-f) in the chemical shift range of 6.5–8.8 ppm (Figure 6). In the presence of A β 42, the splitting pattern of these aromatic protons (7.4–8.8 ppm) were completely altered with significant downfield shift (\sim 0.05 ppm) as a function of time. This reorganization of NMR signals confirmed the interactions between the aromatic moieties of TGR63 and A β 42 peptide, and are responsible for the observed aggregation modulation. In addition, the ethyl protons (g) signals at 4.1–4.4 ppm

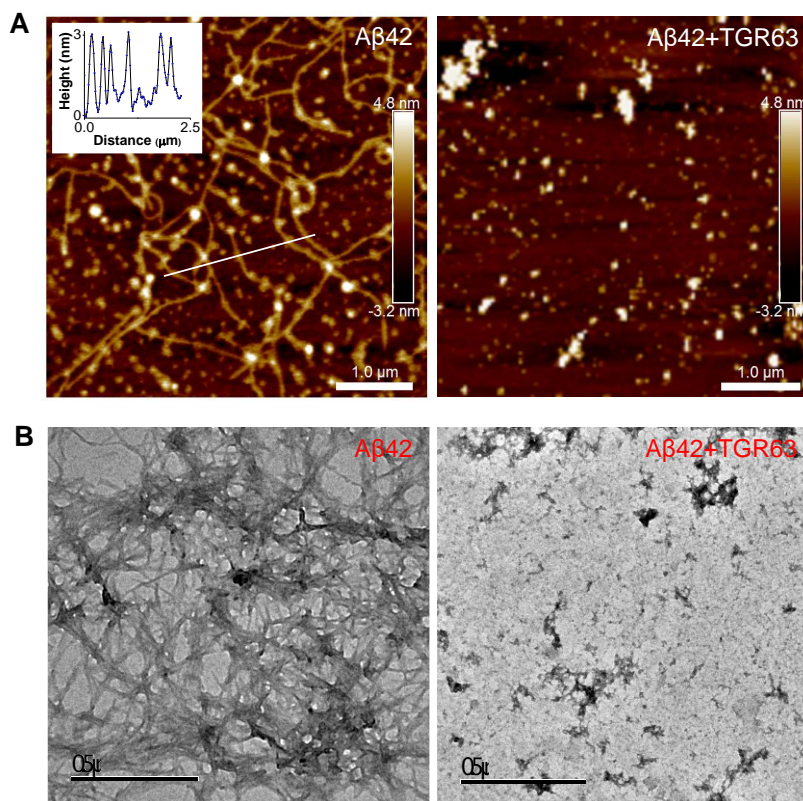


Figure 7. (A) AFM images of A β 42 in the absence (inset: height profile) and presence of TGR63. (B) TEM images of A β 42 in the absence and presence of TGR63. Scale bar: 1.0 μ m (AFM); 0.5 μ m (TEM).

became sharper with time and experienced significant down field shift, which indicate the interactions of ethyl protons of TGR63 with A β 42 peptide. As discussed (*vide supra*), the

aggregation-prone A β 42 peptides readily self-assembles into ordered β -sheet structure through noncovalent interactions.^{2,5,8} The NMR data provided insights into the molecular level interactions of TGR63 with A β 42 that possibly modulate the A β 42 aggregation by disruption of crucial noncovalent interactions.

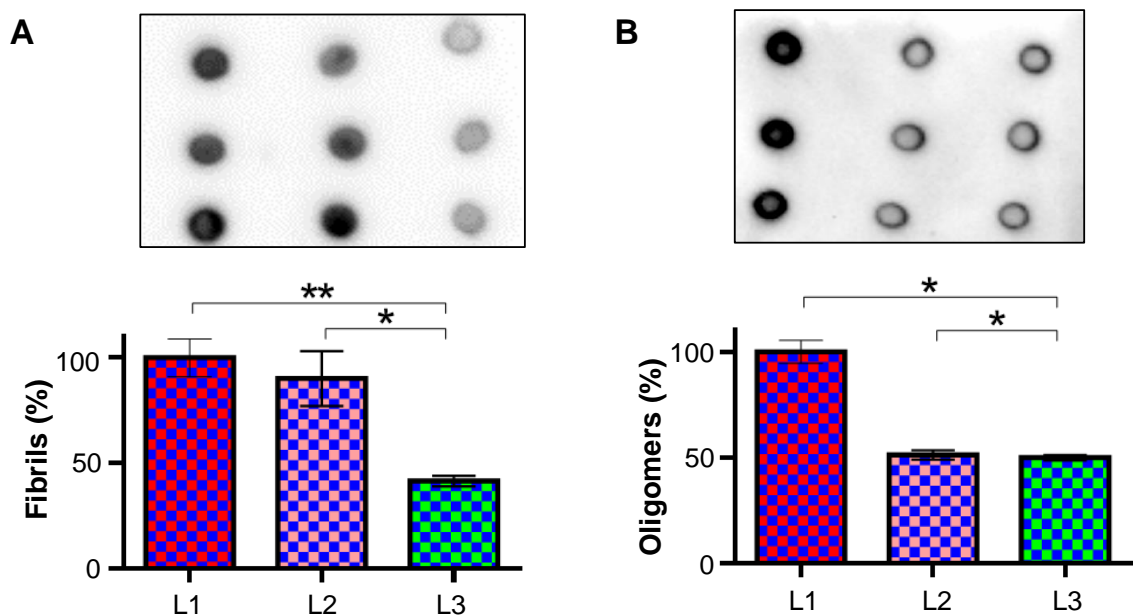


Figure 8. (A) Dot blot analysis of TGR63 treated A β 42 fibrils: The blot intensity displayed the amount of A β 42 fibrils (10 μ M) in absence (L1) and presence of TGR63 at two different molar ratios 1:1 (L2) and 1:5 (L3). A β 42 fibrils were probed using OC primary antibody (1:1000) and treated with ECL reagent to capture the image in Versa Doc instrument and the comparison of blot intensities (%) revealed the effect of TGR63 in amyloidosis. (B) Dot blot analysis of TGR63 treated A β 42 oligomers: The blot intensity displayed the amount of A β 42 oligomers (10 μ M) in the absence (L1) and presence of TGR63 at two different molar ratios 1:1 (L2) and 1:5 (L3). A β 42 oligomers were probed using A11 primary antibody (1:1000) and treated with ECL reagent to capture the blot image and the comparison of blot intensities (%) revealed the inhibition effect of TGR63 in A β 42 oligomerization.

3.3 Inhibition of A β Aggregation and Associated Toxicity: Microscopy and Dot Blot Analysis

Modulation of A β aggregation by TGR63 was evaluated through the structural and morphological analysis using atomic force microscopy (AFM) and transmission electron microscopy (TEM). A β 42 (10 μ M) was incubated alone and with TGR63 (50 μ M) for 48 h in PBS (10 mM, pH= 7.4), and the samples were spotted on mica surface and TEM grid to acquire AFM and TEM images, respectively (Figure 7). AFM image of A β 42 sample showed long fibrillar structures with \sim 3.0 nm height, while TGR63 treated A β 42 sample revealed amorphous

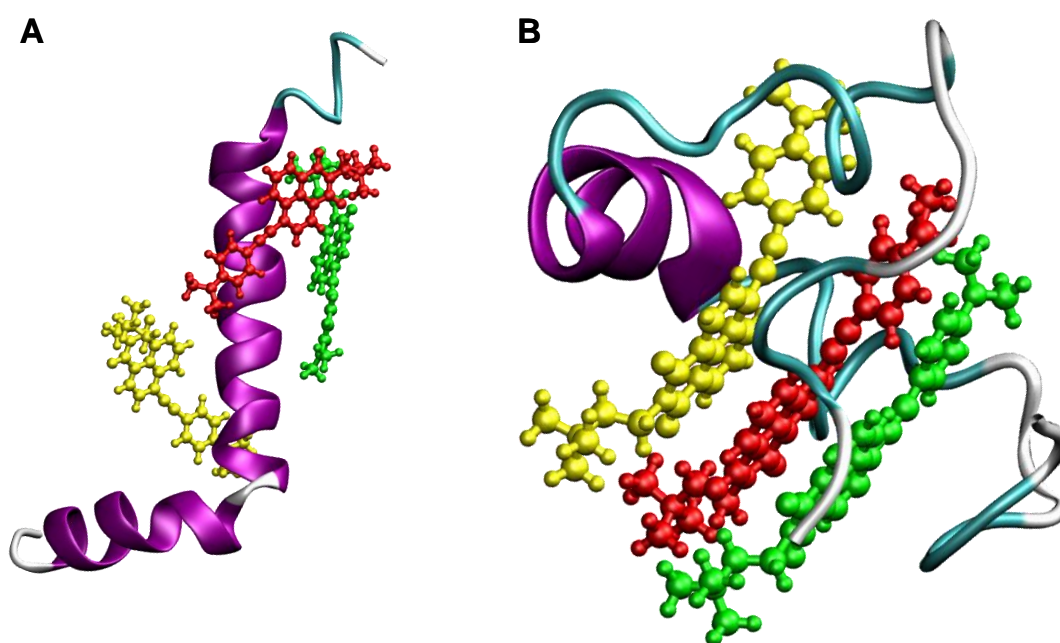


Figure 9. (A) The most stable (least energy) binding modes for TGR63 in monomeric A β 42 peptide, also refers to input MD configuration. (B) refers to a representative configuration for the TGR63-monomeric A β 42 peptide complex during the production run.

structures (Figure 7A). Similarly, TEM image displayed a highly intertwined fibrillar structures of A β 42, which are significantly disrupted by the treatment with TGR63 (Figure 7B). The modulation (inhibition and dissolution) of A β aggregation was further supported by the dot blot (immunohistochemistry) analysis (Figure 8). A β 42 (10 μ M) samples were incubated alone or

with different concentrations of TGR63 (10 and 50 μM) for 48 h at 37 $^{\circ}\text{C}$. The incubated samples were spotted on a polyvinylidene difluoride (PVDF) membrane and probed with $\text{A}\beta$ fibrils specific OC (1:1000) primary antibody followed by secondary antibody (1:10000). The spots on the PVDF membrane were further treated with enhanced chemiluminescence (ECL) reagent to image and assess the extent of inhibition of $\text{A}\beta$ aggregation using Versa Doc instrument. The blot image and their quantification data revealed maximum amount of fibrillar aggregates for $\text{A}\beta_{42}$ (L1) sample (100%), while significant reduction of fibrillar aggregates was observed in the presence of TGR63 (10% and 60% for L2: 10 μM and L3: 50 μM , respectively)

Table 3. Binding free energies for TGR63 in different binding sites of $\text{A}\beta_{42}$ monomer. The energies are in kcal/mol and the standard errors are in the range 0.1 to 0.3 kcal/mol.

| Sites | ΔE_{vdw} | ΔE_{elec} | $\Delta E_{\text{polar solvation}}$ | $\Delta E_{\text{non-polar solvation}}$ | $\Delta G_{\text{binding}}$ |
|---------|-------------------------|--------------------------|-------------------------------------|---|-----------------------------|
| Site-1m | -33.2 | -75.9 | 88.9 | -3.7 | -24.1 |
| Site-2m | -20.1 | -62.0 | 75.2 | -2.5 | -9.4 |
| Site-3m | -34.6 | -76.3 | 88.3 | -3.9 | -26.5 |

in a concentration-dependent manner (Figure 8A). These results and observations from AFM, TEM and dot blot analysis have validated the data from ThT fluorescence assay to confirm TGR63 as a potential modulator of $\text{A}\beta$ aggregation. The soluble $\text{A}\beta$ aggregation species namely oligomers are considered highly toxic and key contributors to $\text{A}\beta$ toxicity.^{5,8} $\text{A}\beta$ oligomers are known to interact and disrupt the lipid membranes (mitochondrial and plasma membranes) causing mitochondrial dysfunction and neuronal damage.¹⁸ The disruption of plasma membrane at synaptic cleft cause synaptic dysfunction followed by weakening in synaptic plasticity and LTP formation.¹⁰⁻¹⁴ Therefore, a potential modulator of $\text{A}\beta$ aggregation must effectively inhibit

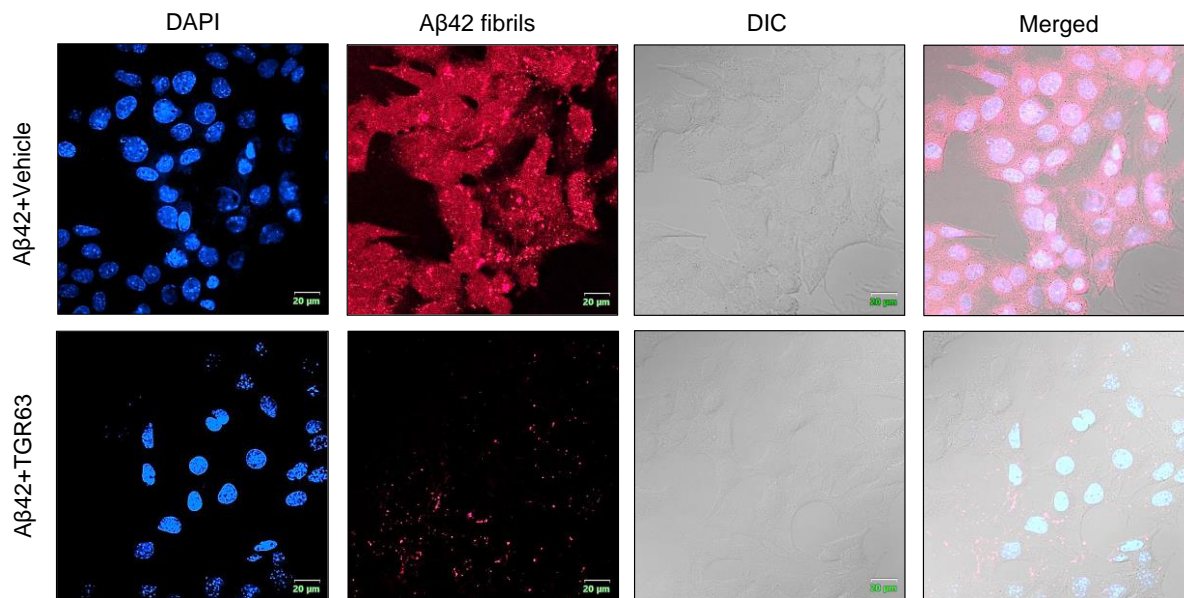


Figure 10. Protection of plasma membrane from A β toxicity: Confocal microscopy images of SHSY5Y cells after incubating (2 h) independently with only A β 42 (10 μ M) fibrils (A β 42+Vehicle) and TGR63 (50 μ M) treated A β 42 (10 μ M) fibrils (A β 42+TGR63). The SHSY5Y cells were stained with OC (1:250) primary antibody followed by fluorescently ($\lambda_{\text{ex}}=633$ nm, $\lambda_{\text{em}}=650$ nm) labeled (red) secondary antibody (1:250) and DAPI (blue). Scale bar: 20 μ m.

oligomer formation to protect neuronal cells and improve the memory impairment in AD. We assessed the inhibitory activity of TGR63 against A β 42 oligomers by immunohistochemistry assay (Figure 8B). A β 42 monomers (10 μ M) were incubated in the absence (L1) and presence of varying concentrations of TGR63 (10 and 50 μ M) for 24 h at 4 $^{\circ}$ C. The incubated samples were spotted on the PVDF membrane and treated with A β oligomer-specific primary antibody (A11) followed by ECL reagent to image and quantify the extent of inhibition of A β oligomers using Versa Doc instrument.²⁸ The quantification of spot intensities showed ~48% and 50% inhibition of oligomer by TGR63 (10 and 50 μ M, respectively) treatment compared to untreated control (100%) (Figure 8B). *In silico* analysis was performed using an integrated approach (molecular docking, molecular dynamics and binding free energy calculations) to understand the effect of

TGR63 on the conformational dynamics of monomeric A β 42 peptides. The α -helix structure of A β 42 is essential for the formation of oligomers and their interaction to disrupt the lipid membrane structure. TGR63 induced secondary structural changes play key role in the oligomer formation kinetics and membrane toxicity. The molecular docking showed three different low energy binding modes (site 1m-3m) for TGR63 in monomeric A β peptide (Figure 9). The binding free energies in 1m-3m sites were found to be -24.1, -9.4 and -26.5 kcal/mol, respectively (Table 3). It is worth noting that the binding free energies for TGR63 with monomeric A β peptide is higher compared to binding with fibril (Table 2). The considerable reduction in the van der Waals interactions in case of former is contributed to observed differences in the binding energies. Figure 9A shows A β peptide (with α -helix contents ~76%) structure similar to fusion domain of virus influenza hemagglutinin, which is responsible for making holes and cause plasma membrane damage.²⁷ Interestingly, TGR63 treatment effectively reduced the α -helix content of A β peptide which resulted in the formation of nontoxic globular structure (Figure 9B). Overall, the blot analysis and *in silico* assessments validated that TGR63 is an efficient modulator of polymorphic species of A β aggregation and a potential candidate to ameliorate the amyloid burden and associated membrane toxicity. Membrane toxicity induced A β aggregation species is one of the major toxicity routes to neuronal death.^{5,8} The deposition of A β plaques on healthy axon and dendron of mature neurons is consider as one of the possible causes of neuronal damage in the AD brain.^{13,14} In addition, soluble A β oligomers dampen smooth neuronal signaling by blocking the neuronal surface receptors (NMDA and AMPA) at synaptic cleft.^{10,12} The synaptic dysfunction impairs the synaptic plasticity and hippocampal LTP formation causing neuronal damage, memory loss and cognitive decline under AD pathogenesis.⁴ Contemporary studies have shown that A β aggregation species interact with

plasma membrane and promote the internalization of misfolded A β peptides by punch holes through the membrane.^{5,28,29} Inhibition of A β -membrane interaction and associated toxicity is anticipated to rescue neuronal cells from amyloid burden. The protective effect of TGR63 to neuronal cells from the membrane toxicity caused by A β was evaluated in SHSY5Y cells using immunocytochemistry protocols. The cells were cultured in 35 mm confocal dishes and treated independently with A β 42 and pre-incubated (24 h) A β 42-TGR63 for 2 h in the cell growth media. The experimental cells were washed and

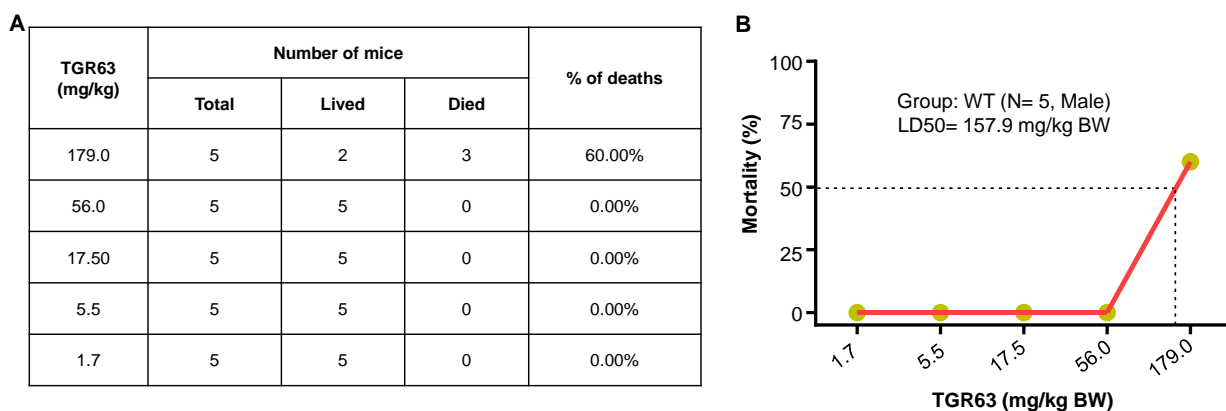


Figure 11. The calculation of lethal dose 50% (LD50) of TGR63 through intraperitoneal administration. (A) Table of experimental details and the final observation on 14th day. (B) The mortality (%) is plotted against TGR63 concentration and calculation of LD50.

fixed using 4% paraformaldehyde (PFA) and treated with OC (1:250) antibody, followed by red fluorescent-labeled (λ_{ex} = 633 nm and λ_{em} = 650 nm) secondary antibody. The unbound antibody was washed, and the cells were treated with nuclear staining dye DAPI for confocal imaging. The red fluorescence signal was significantly high and mostly localized on the plasma membrane for cells treated with A β 42 (A β 42+Vehicle), which correlates to levels of A β 42 fibrillar aggregates (Figure 10). The cells treated with A β 42-TGR63 sample showed significant reduction in the red fluorescence signals on the plasma membrane. This observation clearly supports the

inhibition of toxic A β aggregation species by TGR63 to protect plasma membrane. Collectively, the *in vitro* and *in cellulo* results showed the importance of simple structure-function relationship study and the balanced hydrophobicity and hydrophilicity of TGR63 attained by means of meticulously chosen substituents (4-ethynyl-*N,N*-dimethylaniline and *N,N,N*-trimethylethylenediamine) to successfully modulate the A β aggregation as per the design strategy. These results motivated us to evaluate the anti-AD properties of TGR63 in an APP/PS1 double transgenic AD mouse model.

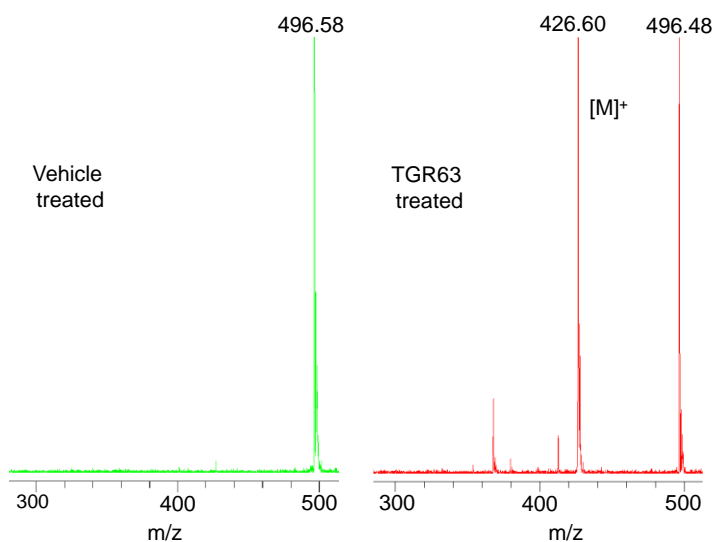


Figure 12. Serum stability of TGR63. MALDI mass analysis of vehicle and TGR63 treated mice blood serum after 1 h of administration. The presence of TGR63 mass peak at 426.60 ([M]⁺) confirmed the serum stability of TGR63.

3.4 Pharmacokinetics study of TGR63

We performed pharmacokinetics of TGR63 in WT mice to assess its *in vivo* efficacy (Figure 12A). The lethal dose 50 (LD50) of TGR63 was determined in WT mice through intraperitoneal (IP) injection following the Organisation for Economic Co-operation and Development (OECD)

guidelines. Twenty five WT mice were segregated in five different groups (G1-5, N= 5 per group) and administered with different doses of TGR63 (1.7, 5.5, 17.5, 56.0 and 179.0 mg/kg body weight, respectively) through IP injection and their survival was monitored for 14 days (Figure 11A). The survival of the experimental mice showed that TGR63 is mostly nontoxic in the experimental period due to high LD50 value of ~157.9 mg/kg body weight (Figure 11B). The serum stability and blood-brain barrier (BBB) crossing ability of TGR63 were assessed through matrix-assisted laser desorption ionization (MALDI) mass spectrometry analysis of blood and

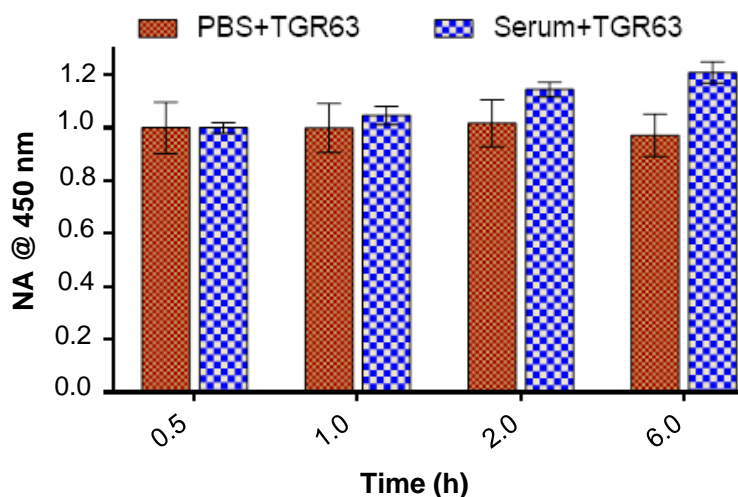


Figure 13. Serum stability of TGR63 under *in vitro* conditions: TGR63 was incubated in PBS (10 mM, pH= 7.4) and blood serum (WT mouse) for different time (0.5, 1, 2 and 6 h) at 37 °C. Data show the normalized absorbance (NA) of TGR63 at 450 nm recorded at different time intervals, which confirmed the stability of TGR63 in blood serum.

brain samples of vehicle and TGR63 treated mice. TGR63 and vehicle were administered in WT mice and sacrificed after 1 and 24 h to collect the blood for MALDI mass analysis (Figure 12). Mass analysis confirmed the presence of TGR63 in blood after 24 h of administration. TGR63 was incubated in PBS (10 mM, pH= 7.4) and blood serum (WT mouse) for different time intervals (0.5, 1, 2 and 6 h) at 37 °C to evaluate the serum stability under *in vitro* conditions. The spectrometric analysis (absorbance) confirmed the stability of TGR63 in blood serum (Figure

13). Next, we calculated partition coefficient (P), a valuable physical property to predict the BBB permeability. TGR63 (20 μM) was added to an immiscible solution of water (10 mL) and octanol (10 mL), followed by thorough mixing, the solution was allowed to segregate into two layers. The absorption of the octanol layer at 450 nm was measured and the amount of TGR63 was determined from the standard concentration curve (Figure 14). The concentrations of

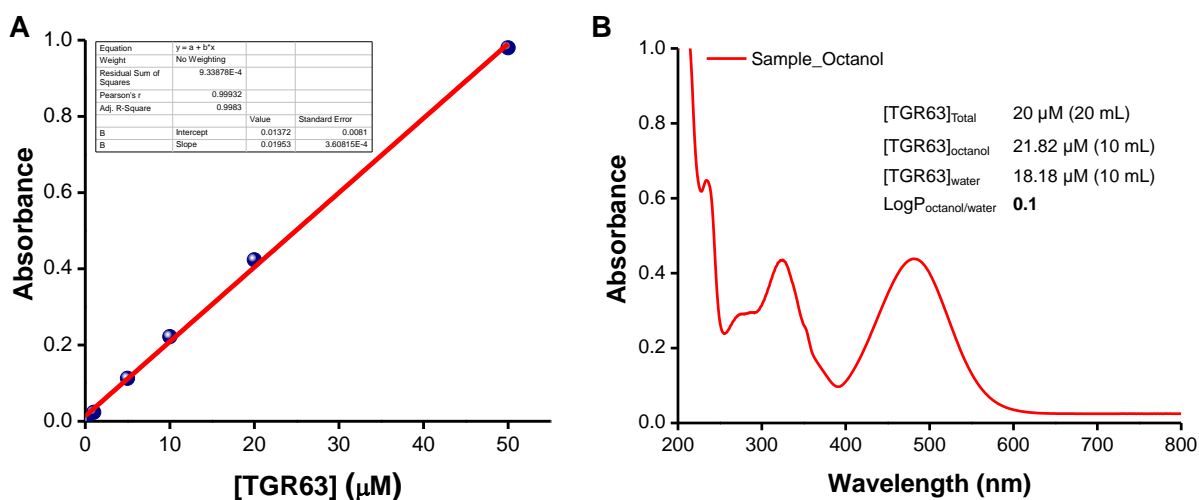


Figure 14. Calculation of LogP. (A) Standard concentration curve obtained by measuring absorbance at 480 nm for 1, 5, 10, 20 and 50 μM of TGR63 in octanol. (B) Absorbance of octanol layer (Sample_Octanol) and calculation of LogP.

TGR63 in octanol and water layer were found to be 21.82 and 18.18 μM , respectively and logP value was calculated to be 0.1 (Figure 14). The calculated positive logP value predicts the possible BBB crossing ability for TGR63.¹⁴ For *in vivo* assessment, TGR63 and vehicle administrated WT mice were sacrificed after 1 h to collect the brains for MALDI mass analysis. TGR63 treated mouse brain sample showed a mass peak at 426.04 (m/z), which was absent in the vehicle-treated sample and confirmed BBB crossing ability of TGR63 (Figure 15). Further,

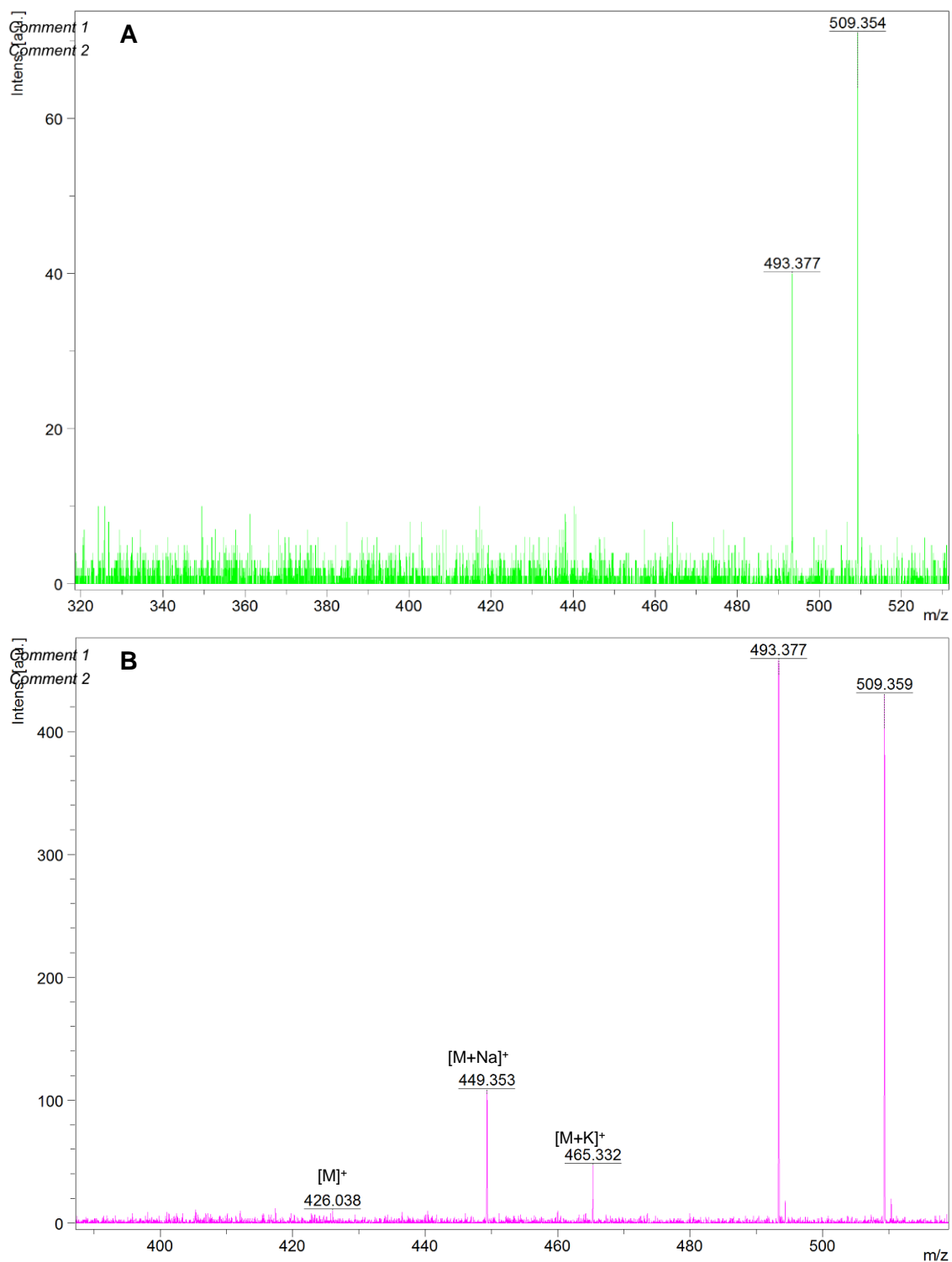


Figure 15. MALDI mass analysis of vehicle (A) and TGR63 (B) treated mouse brain lysate after 1 h. The absence of any characteristic mass peaks in vehicle treated control sample confirm the presence of TGR63 in treated mice brain.

TGR63 (5 mg/kg body weight) and vehicle (control) were administered in age (6 months old) matched APP/PS1 and WT mice on daily basis for 8 months to examine the organ toxicity upon prolonged TGR63 administration. The experimental mice were sacrificed at 14 months of age and critical organs *viz.*, liver, heart, spleen and kidney were harvested to perform gold standard hematoxylin and eosin (H&E) staining (stain nucleus and cytoplasm, respectively). The H&E staining of TGR63 treated mice (WT and AD) tissue samples exhibited nucleus and cytoplasm staining similar to healthy tissue (vehicle treated WT mice). The healthy or TGR63 treated tissue samples did not show any abnormal scar, disorganization, inflammatory infiltrate, hepatotoxicity or necrosis (Figure 16), which confirmed the excellent *in vivo* biocompatibility and nontoxic nature of TGR63. The pharmacokinetics study of TGR63 revealed serum stability, BBB permeability and biocompatibility underscoring its suitability for the long-term treatment in APP/PS1 AD phenotypic mice. These studies have encouraged us to evaluate the efficacy of the lead candidate to ameliorate the cognitive impairment, for which APP/PS1 AD and WT mice were administered (IP) with TGR63 (daily dose of 5 mg/kg body weight) starting from the age of 6 months to 14 months (Figure 16).

3.5 *In Vivo* Amelioration of Amyloid Burden

We sought to evaluate the activity of TGR63 to ameliorate amyloid burden in *in vivo* AD model. APP/PS1 mice were bred, maintained and characterized (WT: wild type; AD: APP/PS1 positive) according to provider's protocols.¹⁶ The double transgenic APP/PS1 mice (B6C3-Tg (APP^{swe}, PSEN 1dE9)85Dbo/J; stock number 004462) which express human transgenes APP and presenilin 1 (PS1) in the central nervous system (CNS) contain the Swedish and L166P mutations, respectively.³⁰ The K595N/M596L (Swedish) mutation favors the amyloidogenic

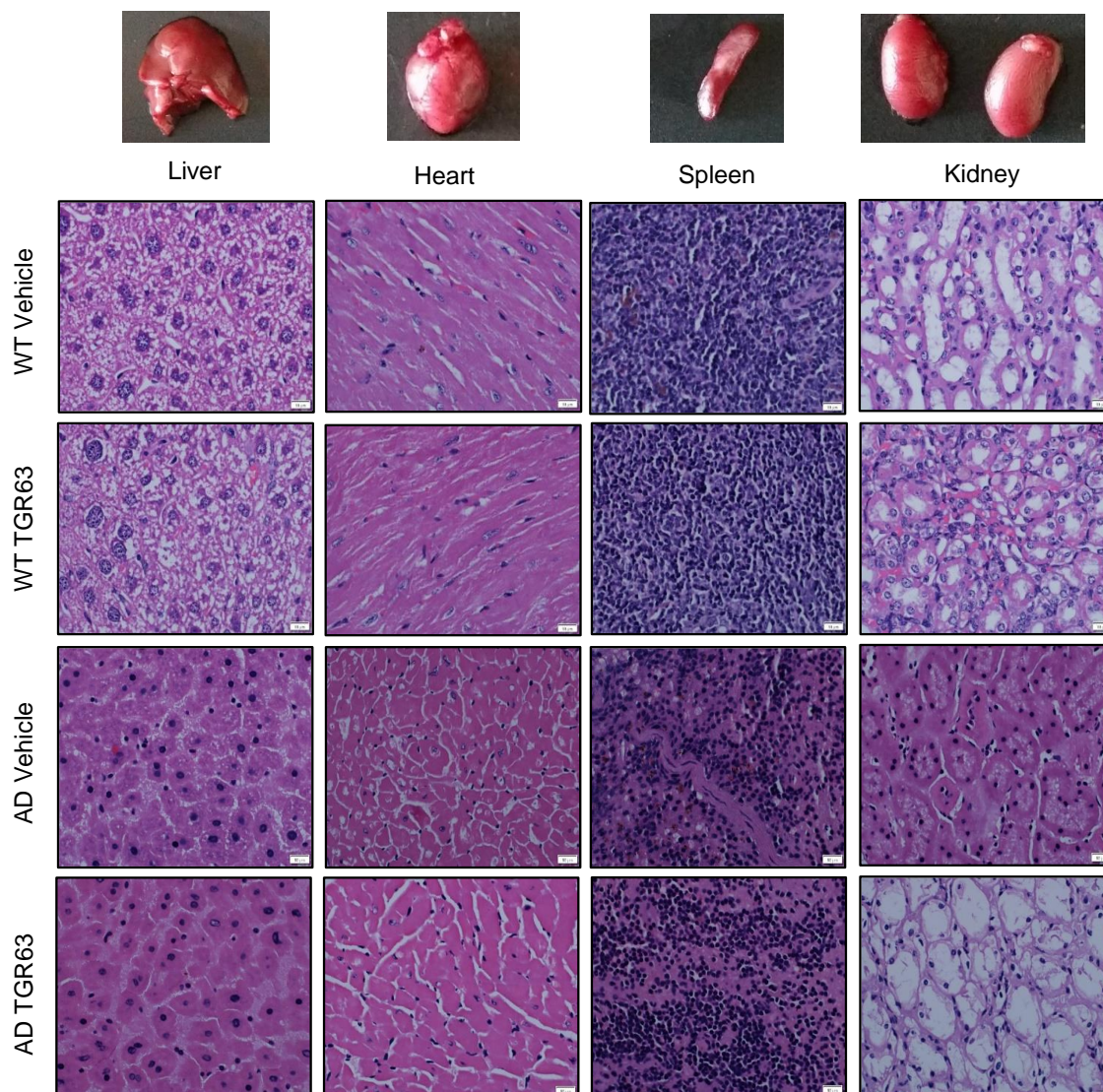


Figure 16. Evaluation of organ toxicity of TGR63: Bright field images of vehicle and TGR63 treated mice (WT and AD) organs (liver, heart, spleen and kidney) stained with hematoxylin and eosin (H&E), which confirmed the biocompatibility and nontoxic nature of TGR63. Scale bar: 10 μ m.

processing of APP protein and PS1 mutation (L166P) elevates the production of A β peptides through modifying the intra-membrane γ -complex. Consequently, deposition of A β plaque starts appearing in the neocortex at the age of ~45 days and can be found in thalamus, brainstem, striatum and hippocampus regions at the age of 5-6 months. The deposition of A β plaque in the

cortex and hippocampus regions initiate cognitive dysfunction and memory impairment at the age of ~7 months. The presence of A β plaques in the APP/PS1 AD phenotypic mouse brain was confirmed and compared with the healthy brain by A β plaques-specific staining protocols (Figure 17A). The brains were harvested from the age matched WT and AD mice and treated

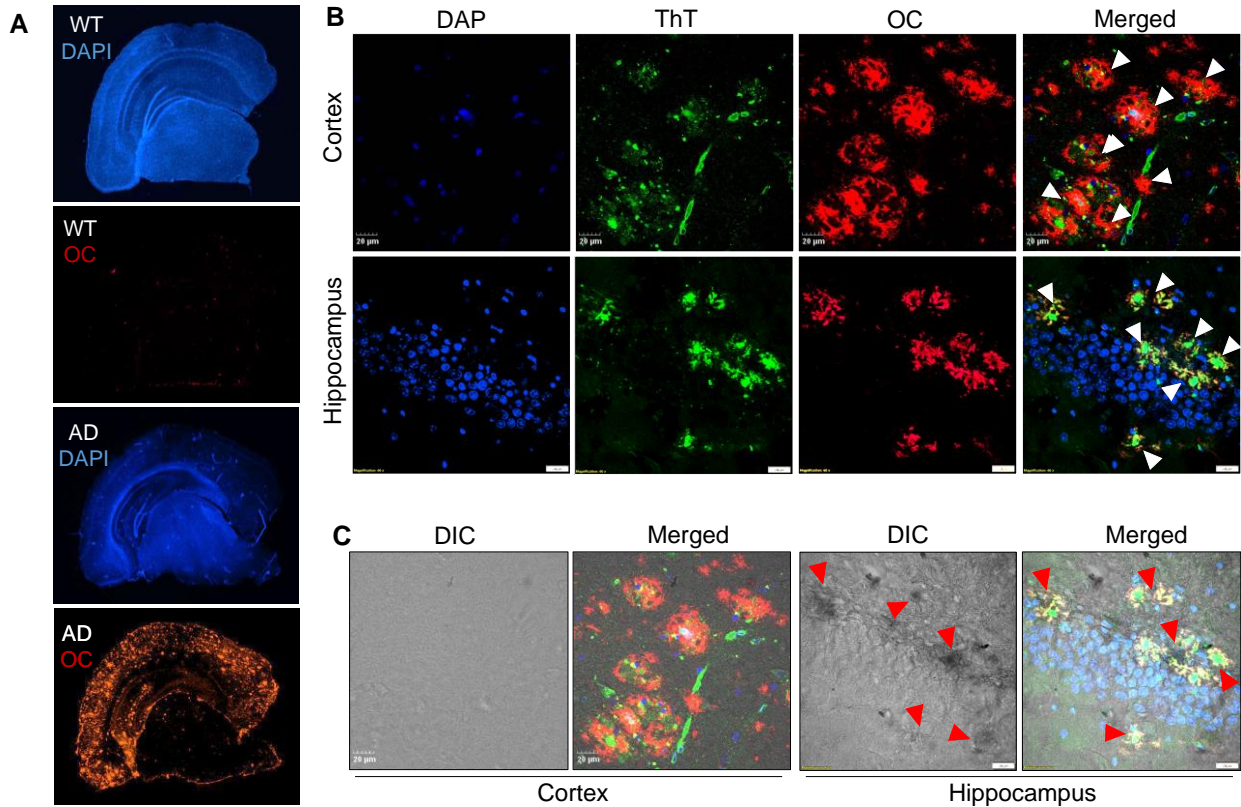


Figure 17. (A) Visualization of amyloid plaques in half hemisphere: Confocal microscopy images of coronal section of WT and AD mice brains immunostained with amyloid fibrils specific OC primary antibody followed by fluorescently (λ_{ex} = 633 nm, λ_{em} = 650 nm) labeled (red) and DAPI (blue) (B) Staining of amyloid plaques with OC primary antibody and ThT or CQ probe: The high-resolution confocal microscopy images of cortex and hippocampus regions of the AD mouse brain, immunostained with OC antibody (red), DAPI (blue) and ThT (green). The merged images display significant overlap between ThT and OC staining to confirm the amyloid deposition (pointed with white arrows). (C) Visualization of amyloid deposits associated neuronal damage: The DIC images of different regions of AD. The merged images of DIC and confocal microscopy images show amyloid plaques associated brain damage (pointed out with red arrows). Scale bar: 20 μ m.

with PFA (4%) and sucrose solution (30%) for the sagittal brain sectioning (40 μm sections). The brain sections were co-stained with ThT ($\lambda_{\text{ex}}= 442 \text{ nm}$, $\lambda_{\text{em}}= 482 \text{ nm}$) and OC primary antibody followed by fluorescently labeled secondary antibody ($\lambda_{\text{ex}}= 633 \text{ nm}$, $\lambda_{\text{em}}= 650 \text{ nm}$) or CQ to visualize and confirm the amyloid plaques deposition.³¹ The confocal images acquired from different regions of the brain (cortex and hippocampus) showed localized bright green and red fluorescence signals confirming the deposits of amyloid plaques in the APP/PS1 mice brain. Similar fluorescence signals (green and red) were absent in the age-matched WT brain section confirming the amyloid plaques-free healthy brain (Figure 17B). The hippocampal damage, a hallmark of advanced AD condition was partially observed in 14 month old APP/PS1 mice (Figure 17C). Age matched AD and WT cohorts were administered with TGR63 (5 mg/kg body weight/day) and vehicle starting from the age of 6 months following our treatment protocols (Figure 18A). The experimental mice were sacrificed after completing the behavioral studies (14 months) to investigate amyloid deposits in the brain using immunohistochemistry.¹⁶ The sagittal brain sections were permeabilized and blocked with PBTx (0.1M PBS and 0.1% TritonX-100) and goat serum (1%) containing BSA (2%) at room temperature, respectively. The processed sections were incubated with amyloid fibrils specific primary antibody (OC, 1:250) at 4 °C for 48 h to stain the dense-core of amyloid plaques. The processed brain sections were further treated with red fluorescent-labeled ($\lambda_{\text{ex}}= 633 \text{ nm}$ and $\lambda_{\text{em}}= 650 \text{ nm}$) secondary antibody (1:1000) and DAPI to perform confocal imaging (Figure 18B). The confocal images of WT cohort brain tissue sections did not show any deposits of A β plaques in both cortex and hippocampus regions. The age matched AD cohort brain tissue sections prominently displayed deposits of A β plaques in different parts of the brain *viz.*, neocortex, striatum, primary sensory-motor areas, hippocampus, temporobasal and frontomedial areas (Figure 18C). These results provided strong

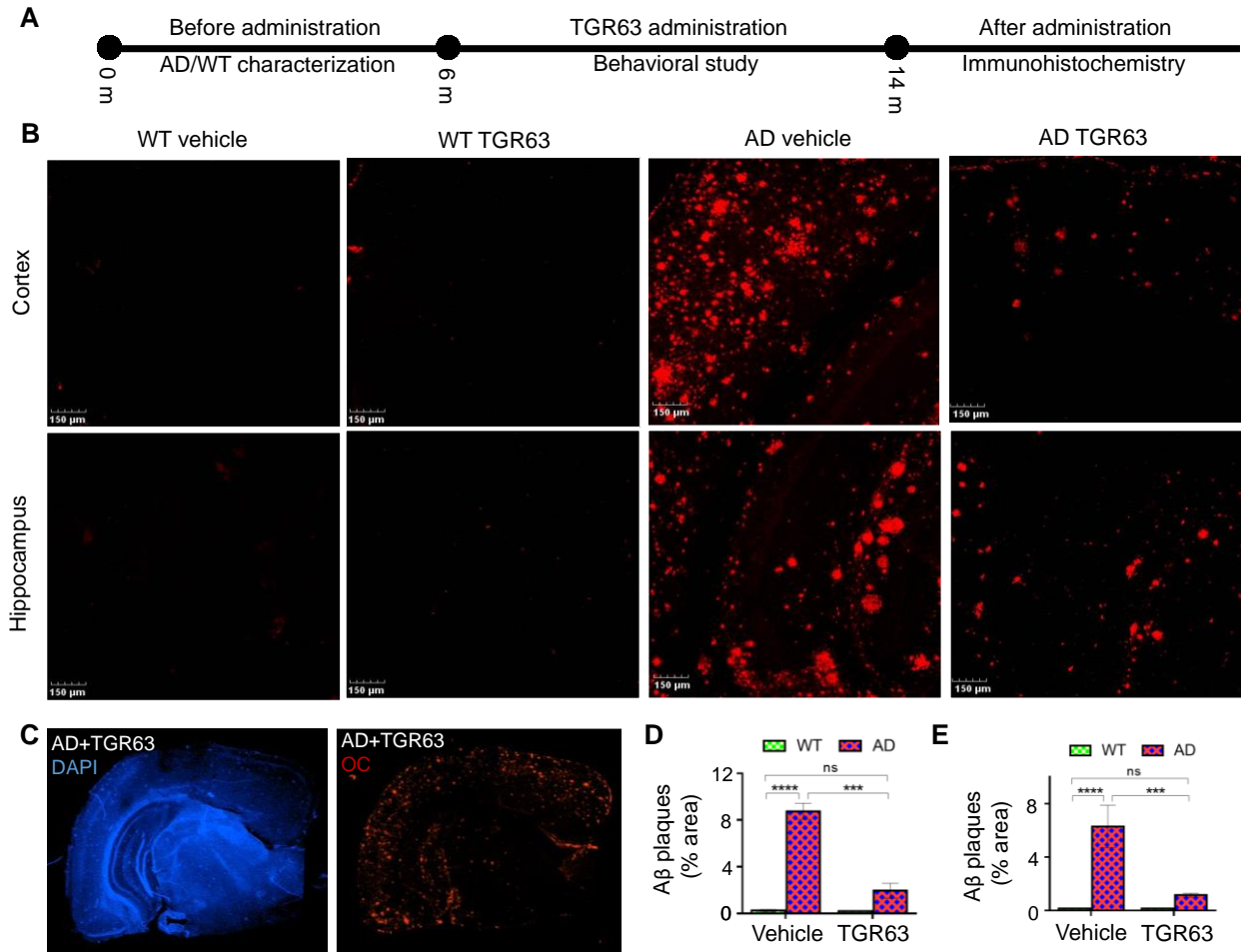


Figure 18. (A) Experimental planning and TGR63 administration in APP/PS1 mice (age in month, m). (B) Reduction of cortical and hippocampal amyloid burden by TGR63 treatment: Higher magnification images of vehicle and TGR63 treated mice (WT and AD) brain sections to visualize and compare the A β plaques deposition in the cortex and hippocampus areas. The brain tissue sections were immunostained with amyloid fibrils specific primary antibody (OC) and red fluorescent-labeled (λ_{ex} = 633 nm and λ_{em} = 650 nm) secondary antibody. (C) Visualization of amyloid plaques in half hemisphere: Confocal microscopy images of coronal section of TGR63 treated AD mouse brain immunostained with amyloid fibrils specific OC primary antibody followed by fluorescently (λ_{ex} = 633 nm, λ_{em} = 650 nm) labeled (red) secondary antibody and DAPI (blue). (D and E) Quantification of A β plaques: Amount of A β plaques (% area) deposited in different regions (cortex and hippocampus) of vehicle and TGR63 treated mice (WT and AD) brain was analyzed. Data represent mean \pm SEM, n= 3 per group. Scale bar: 20 μ m.

evidence of chronic accumulation of A β plaques in the brain associated with AD progression. Predictably, the vehicle-treated AD cohort's (N= 3) brain tissue images showed accumulation of A β plaques 8.87% and 6.28% area of the cortex and hippocampus, respectively. Remarkably, TGR63 treatment (N= 3) significantly reduced the A β plaques deposits to 1.94% and 0.94% area of the cortex and hippocampus, respectively (Figure 18D and E). In other words, TGR63 treatment reduced A β deposits by 78% and 85% in cortex and hippocampus, respectively. The immunostaining of A β deposits in TGR63 treated AD brain tissue displayed an appreciable reduction in the amyloid load and encouraged corresponding improvement of memory and cognitive functions.

3.6 Recovery of Cognitive Functions

AD is characterized by the progressive deterioration in cognitive functions, which generally include learning and memory impairment leading to neuropsychiatric symptoms viz., aggression, agitation, anxiety and depression.^{2,4,8} APP/PS1 mice show age-related AD-like phenotypes linked to A β plaques deposition in the brain.³² We set out to assess the recovery of cognitive functions in TGR63 treated APP/PS1 mice (<https://www.biorxiv.org/content/10.1101/2020.08.20.260166v1.supplementary-material>). First, open-field (OF) test was performed to assess the effect of TGR63 on hippocampal lesions induced behavioral disability and neurochemical abnormalities. Next, the amelioration of learning disability and memory impairment by TGR63 treatment was evaluated through novel object identification (NOI) and Morris water maze (MWM) behavioral tests. In OF test, all the experimental mice were individually allowed to explore a novel platform (45 × 45 cm) and their locomotion activity was monitored through top camera for 5 min and analyzed by the smart 3

software (Figure 19). The trajectories of vehicle-treated AD mice (AD vehicle) showed higher activity (travel average 2698.25 cm) compared to vehicle-treated WT mice (travel average 1403.80 cm), which indicates the AD-like phenotype of APP/PS1 mice model (Figure 19B). Interestingly, TGR63 treated AD (AD TGR63) mice showed significantly shorter travel paths (average 1515.33 cm) compared to AD vehicle cohort suggesting improved cognitive functions similar to vehicle-treated WT mice (WT vehicle). However, TGR63 treated WT (WT TGR63) mice were marginally more active than WT vehicle mice and showed average travel of 2027.25

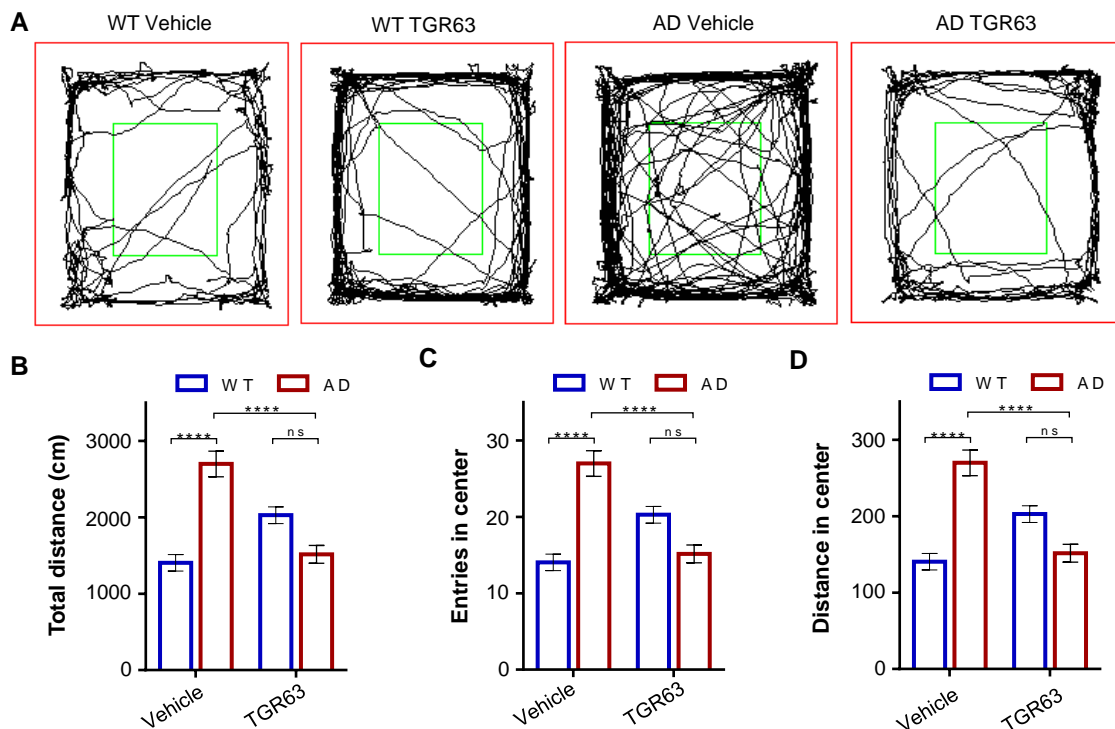


Figure 19. (A) Tracing of vehicle and TGR63 treated mice (WT and AD) locomotion during open field (OF) test (test period: 5 min). (B) Total distance traveled by experimental mice cohorts. (C) Average number of entries into the center zone. (D) Distance traveled by experimental mice cohorts in the center zone. Data are presented as mean \pm SEM, WT vehicle group N= 10, WT TGR63 group N= 8, AD vehicle group N= 8 and AD TGR63 group N= 9. * $p < 0.05$, analyzed by two-way ANOVA followed by Bonferroni test. (video 1: <https://www.biorxiv.org/content/10.1101/2020.08.20.260166v1.supplementary-material>).

cm. The aggression and anxiety behaviors of TGR63 treated mice were assessed by the activity in the center zone (20 X 20 cm) of OF arena. The total exploration and number of entries in the center zone was analyzed for all the experimental mice. As expected, AD vehicle showed maximum number of entries (~20) and travel path (average 243.0 cm) among other cohorts in the center zone, which confirmed the characteristic aggression and anxiety under AD conditions (Figure 19C and D). Remarkably, TGR63 treated AD mice showed behaviors similar to healthy WT vehicle cohorts with ~9 entries and travel average of 98.14 cm exploration in the center

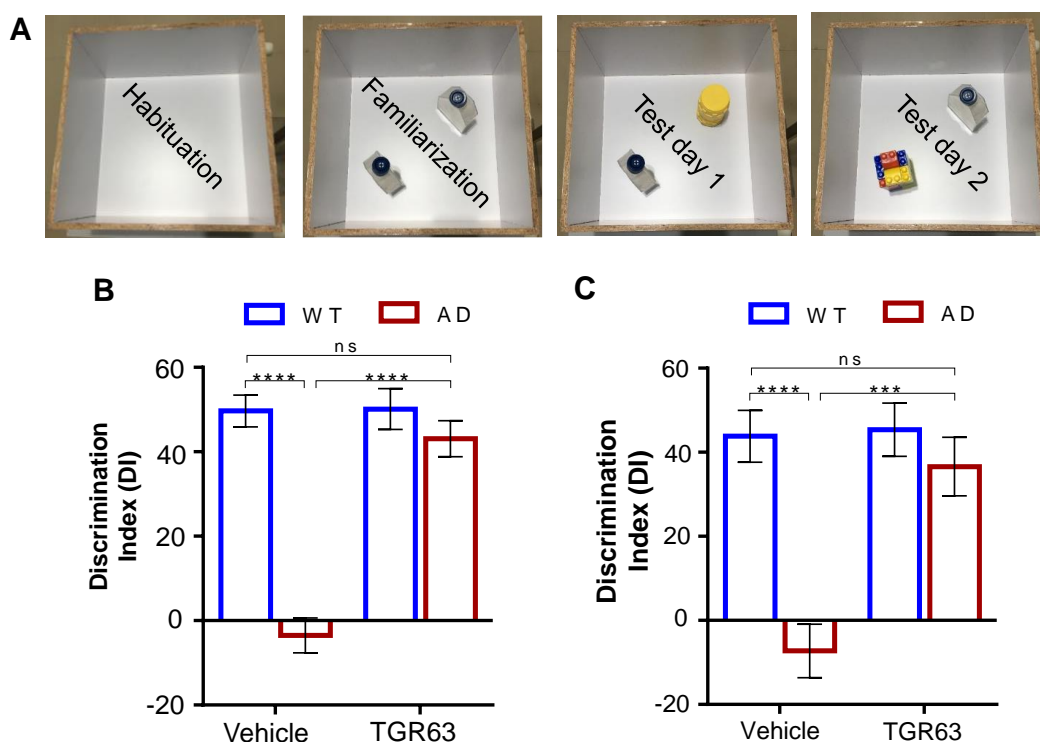


Figure 20. (A) The novel object identification (NOI) test protocol: Image of experimental arenas during habituation, familiarization and test days. (B and C) The recognition of novel objects compared to old object on test day 1 and 2, respectively. Data are presented as discrimination index (DI) [DI= (time exploring the novel object – time exploring the familiar) / (time exploring novel + familiar) * 100], WT vehicle group N= 8, WT TGR63 group N= 8, AD vehicle group N= 8 and AD TGR63 group N= 8. * p < 0.05, analyzed by two-way ANOVA followed by Bonferroni test. (video 2: <https://www.biorxiv.org/content/10.1101/2020.08.20.260166v1.supplementary-material>)

zone. The OF test data revealed that TGR63 ameliorate the amyloid stress induced behavioral disability and neuropsychiatric symptoms, viz. aggression, agitation and anxiety under AD conditions. Next, the effect of acquisition, consolidation and retrieval were evaluated through NOI test. NOI test has been widely used as a tool to study the neurobiology of memory using the natural tendency of rodents to explore novel objects more than the familiar objects.¹⁹ All the experimental mice were familiarized with two identical objects (familiar objects) in a known habituated arena and allowed to explore a novel and familiar object after 24 and 48 h of familiarization (Figure 20A). The exploration time with each object was recorded using stopwatch for individual experimental mouse and the discrimination index (DI) was determined using the formula, (time exploring the novel object – time exploring the familiar) / (time exploring novel + familiar) * 100.²⁷ The test result after 24 h showed significantly lower DI (-3) for AD vehicle cohort compared to WT vehicle cohort (+49), which affirmed the disability of LTP formation under progressive AD conditions (Figure 20B). On the other hand, calculated DI of WT TGR63 cohort (+50) is similar to the WT vehicle cohort confirming TGR63 did not affect the LTP formation in normal psychological condition. Remarkably, AD TGR63 cohort exhibited an improved DI (+43) compare to AD vehicle cohort (-3) confirming the therapeutic efficacy of TGR63 in memory processing (acquisition, consolidation and retrieval) under AD condition. Similarly, the calculated DI after 48 h was lowest (-7) for AD vehicle cohort compared to both vehicle and TGR63 treated WT cohorts (+43 and +45, respectively) (Figure 20C). AD TGR63 cohort showed DI of +38, which indicate healthy LTP formation and successful retrieval of memory. The DI of TGR63 treated WT and AD cohorts at 48 h have marginally reduced (~ 5 units of DI) compare to 24 h, reveal the natural long-term depression of healthy animals. The blocking of essential synaptic receptors (NMDA and AMPA) by A β aggregation species leading

to synaptic dysfunction followed by impairment in hippocampal LTP formation. The NOI test result demonstrated that AD positive mice (APP/PS1) exhibit the memory impaired phenotypes compare to WT mice. TGR63 treatment ameliorates the memory impairment in APP/PS1 mice by reducing the toxic amyloid burden from the brain under progressive AD conditions. The spatial and episodic memory formation under AD conditions were investigated through spatial

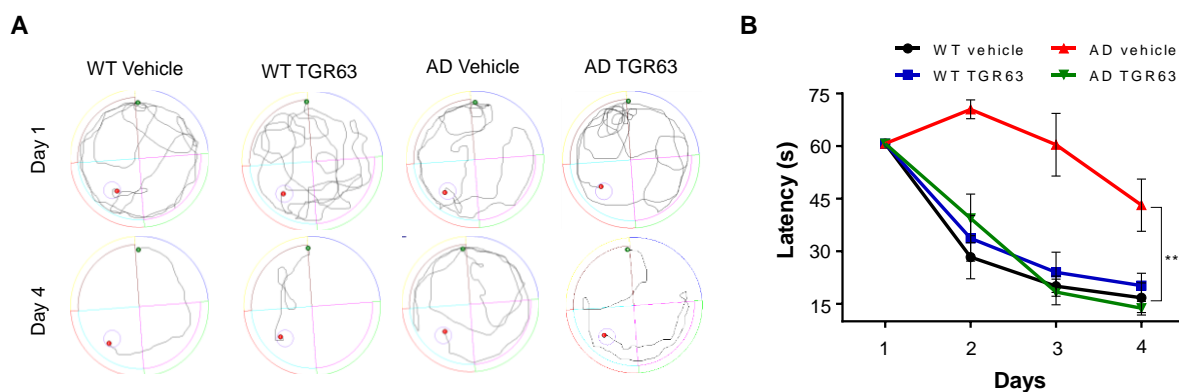


Figure 21. (A) The Morris water maze (MWM) test analysis: Trajectory of experimental (vehicle and TGR63 treated) WT and AD mice in training period (day 1 and 4). (B) Latency time (second) of each cohort for searching the hidden platform during training. (video 3: <https://www.biorxiv.org/content/10.1101/2020.08.20.260166v1.supplementary-material>). WT vehicle group N= 8, WT TGR63 group N= 8, AD vehicle group N= 8 and AD TGR63 group N= 8. * $p < 0.05$, analyzed by two-way ANOVA followed by Bonferroni test.

learning and memory development tasks in MWM test.³⁴ MWM test was performed in a water pool (radius: 70 cm) and experimental mice were trained four times in a day to find a hidden platform, which was removed in probe trial to assess the spatial memory. The latency time to reach the hidden platform during the training period was recorded to determine spatial learning (Figure 21A). As anticipated, AD vehicle cohort required more time (~ 70, 60 and 43 s) to reach the platform during training days (2nd, 3rd and 4th, respectively), while other cohorts showed a

smooth spatial memory formation with time (Figure 21B). AD TGR63 cohort behaved like a healthy WT mouse and exhibited significant improvement in spatial memory formation compared to AD vehicle cohort. In the probe trial, AD vehicle cohort spent most of the time (~87% of total time) in other quadrants (without platform), while other cohorts (WT vehicle, WT TGR63 and AD TGR63) spent only ~67%, 58% and 66% of total time in without platform quadrants, respectively. The AD vehicle cohort spent minimum time (~13% of total time) in

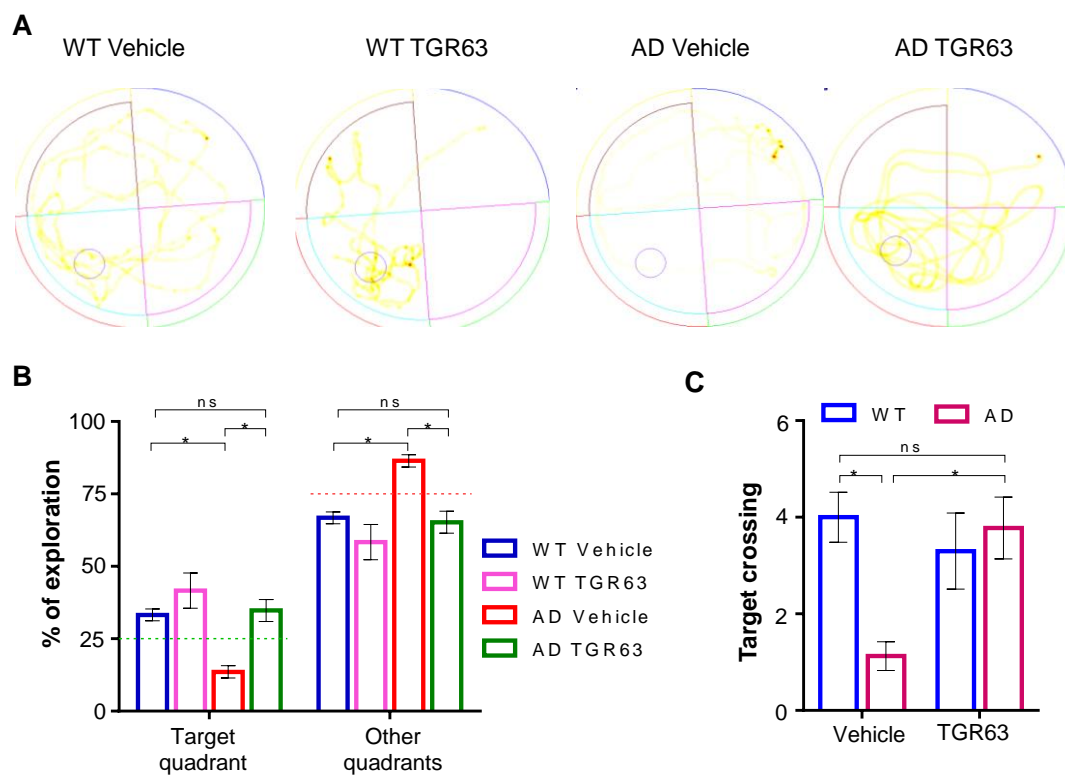


Figure 22. (A) The representative trace of experimental mouse in probe trail (no platform). (B) Percentage of total exploration by each cohort in target quadrant (platform was placed during training) and other quadrants in probe trial. (C) Average number of target (platform) crossing by each cohort during probe trail (no platform). Data are presented as mean \pm SEM, WT vehicle group N= 10, WT TGR63 group N= 10, AD vehicle group N= 8 and AD TGR63 group N= 10. * $p < 0.05$, analyzed by two-way ANOVA followed by Bonferroni test. (video 3: <https://www.biorxiv.org/content/10.1101/2020.08.20.260166v1.supplementary-material>)

target quadrant (with platform) compared to WT vehicle cohort (~33% of total time). TGR63 does not affect the spatial memory formation and retrieval in the healthy brain, as the WT TGR63 cohort showed similar exploration (<35% of total time) tendency like WT vehicle cohort. Interestingly, AD TGR63 cohort explored <20% (~34% of total time) in the target quadrant than AD vehicle cohort, which is similar to that of healthy mice (Figure 22A). Further, we determined the spatio-temporal memory by analyzing their activity in the platform region, which revealed AD vehicle cohort crossed the platform for minimum times (~1 time) compared to the WT vehicle cohort (~4 times) (Figure 22B). Remarkably, AD TGR63 cohort crossed the platform region ~4 times, which is greater than the AD vehicle cohort. MWM study demonstrated significant effect of TGR63 treatment on the medial entorhinal cortex and hippocampus in the AD brain, the key areas for the development of spatial learning and memory. Overall, the significant enhancement of memory and cognitive performance in the behavioral studies is in excellent agreement with the amelioration of amyloid burden and associated neuronal toxicity in the AD (APP/PS1) mice validated the anti-AD credentials of TGR63.

3.7 Discussion

Several therapeutic candidates have been developed to modulate AD progression with A β burden as a therapeutic target.^{5,8,35-37} Identification of potent small molecules to ameliorate A β burden and associated cognitive deficits eluded researchers and clinicians to find an effective treatment for AD.⁸ Targeting A β burden includes the modulating production, misfolding and parenchymal plaques deposition of A β , promotion of plaques clearance and amelioration of neuropathological hallmarks and cognitive decline.^{9,18,37} Inhibition of β or γ -secretases is a promising approach to reduce the A β production, albeit their expression and functional relevance in others part of the

body resulted in the failure of large number of clinical candidates due to severe side effects and off-target interactions.³⁸ The immunotherapy or acceleration of A β clearance strategies have shown significant enhancement in the brain inflammatory response besides reduction in the cerebral amyloid burden and associated cognitive impairment. These observations and findings have reiterated the fact that targeting parenchymal plaques deposition and associated neurotoxicity through meticulous design of small molecule inhibitors is a promising approach to develop a potential therapeutic candidate for the treatment of AD.^{2,8,9,39} We designed focused set of small molecules to identify a lead candidate to ameliorate A β burden and related neuropathological hallmarks to improve cognitive functions in AD mice model.

The sequential proteolytic cleavages of APP by β and γ -secretases produce A β peptides of variable lengths (37-43 amino acids).^{2,40} Among these A β peptides, A β 42 is highly aggregation prone and undergoes misfolding and ordered assembly to form neurotoxic amyloid plaques which contribute to multifaceted toxicity including plasma membrane disruption, synaptic dysfunction, memory impairment, cognitive decline and neuronal loss in the AD brain.⁴¹⁻⁴⁷ The modulation of severe amyloid burden and associated neurotoxicity to improve cognitive functions is a gigantic challenge to research and clinical community. There is an unmet need to develop new class of efficient modulators of A β aggregation and related neurotoxicity through unique and robust drug design strategy.⁹ Here, we discuss a simple yet eloquent design of focused set of NMI-based small molecules and their structure-function relationship study to identify a lead candidate (TGR63) as *in vitro* and *in vivo* modulator of A β aggregation to tackle amyloid burden associated neuropathological hallmarks to ameliorate cognitive deterioration.

NMI-based small molecules (TGR60-65) were designed through systematic variation of substituents to fine tune the hydrophobicity and hydrophilicity balance required to interact and

effectively modulate A β aggregation. A detailed *in vitro* biophysical and screening assays revealed NMI-core with of *N,N*-dimethylamine and *N,N,N*-trimethylpropan-1-aminium substituents (TGR63) emerged as an efficient inhibitor of A β aggregation. TGR63 was obtained by functionalizing 4-bromo-NMA with *N,N*-dimethylamine using Sonogashira coupling protocols followed by the conjugation of *N,N,N*-trimethylpropan-1-aminium as imide substituent (Scheme 1). The detailed evaluation by ThT fluorescence, dot blot, AFM and TEM analysis validated effective *in vitro* modulation of A β 42 aggregation by TGR63. NMR study revealed molecular level interactions of TGR63 with A β 42. A clear splitting pattern and downfield shift of aromatic protons (6.45–6.65 and 6.85–7.15 to 6.50–6.70 and 6.90–7.20, respectively) in ¹H NMR spectra in the presence of A β 42 revealed molecular interactions of TGR63 with A β 42, which provided as possible molecular mechanism of aggregation modulation. In addition, *in silico* results are in good agreements with experimental results and established the superiority of TGR63 in A β aggregation modulation. TGR63 efficiently binds with existing sites (core and surface binding) and an additional cryptic site (core binding site) of amyloid fibril, and generates stable TGR63-A β complex through the strong van der Waals and electrostatic interactions. Interestingly, this stable complex formation significantly decreases the crucial interactions (salt bridge and hydrogen bonding) within amyloid fibrils, and is proposed as a plausible mechanism behind its effective aggregation modulation. A recent study revealed that A β aggregation process promotes misfolded A β -membrane interactions and internalization of A β , which initiates various cell signaling cascades and interrupt physiological neuronal functions.⁸ We have shown the interaction of A β aggregation species on the plasma membrane and associated neuronal loss in cultured cells.²⁹ Interestingly, modulation (inhibition and dissolution) of A β 42 aggregation in presence of TGR63 reduced the membrane toxicity and rescued cultured neuronal cells.

As discussed (*vide supra*), the chronic A β plaques deposition induced dendritic and axonal atrophy in the AD brain contributing to loss of mature neurons and neuronal circuit disruption.^{10,11,48} The soluble A β aggregation species interact with synaptic receptors (NMDA and AMPA) at the synaptic cleft hampering the neuronal signaling cascade, memory formation and cognitive functions.^{12,14,49} Double transgenic APP/PS1 AD mice show AD phenotypes viz., accumulation of chronic A β plaques, memory impairments, cognitive decline and neuronal loss with age.^{4,50} Human transgenes APP and PS1 with Swedish and L166P mutations, respectively, are overexpressed in the APP/PS1 mouse brain and promote amyloidogenic APP cleavage to generate excess A β in CNS.^{2,30} Accumulation of A β plaques has been supported by the postmortem report of the AD brains and our immunohistochemistry data of the APP/PS1 mouse brain tissue fully supported A β plaque deposits in abundance. Deposition of A β plaques in the brain is the characteristic neuropathological hallmark of AD which subsequently cause neuropsychiatric dysfunction, as validated by the behavioral (OF) assay. The downstream effects of A β burden associated cognitive dysfunction include interruption of neuronal circuits, synapse and synaptic plasticity, which result in deterioration of recognition ability, learning ability and spatiotemporal memory formation. Our NOR and MWM behavioral tests validated cognitive decline in APP/PS1 mouse and AD phenotype to evaluate the efficacy of our lead candidate.

The *in vivo* efficacy of TGR63 was evaluated in APP/PS1 mice model and the results showed global improvement of cognitive and memory functions under progressive AD conditions. The trajectory of TGR63 treated AD mice in an unexplored arena (OF test) revealed improved neuropsychiatric symptoms similar to that of vehicle-treated WT cohort. The OF test confirmed the recovery of neuropsychiatric functions by the exclusive TGR63 treatment. Acquisition, consolidation and retrieval of memory was assessed by the ability of TGR63 treated AD mice to

identify novel object at different time intervals of memory formation. TGR63 treated AD mice showed significantly improved novel object identification (NOI) ability identical to that of vehicle-treated WT cohort and the NOI ability declined with time. The NOI test confirmed the partial recovery in LTP formation under progressive AD conditions by TGR63 treatment. The learning ability and the formation of working and spatiotemporal memory of TGR63 treated AD mice was evaluated using standard MWM test. The MWM test results showed recovery of the learning, and spatiotemporal and working memory formation in TGR63 treated AD mice. The improved physiological brain functions of TGR63 treated AD mice are similar to healthy mice indicated rescue of synapse and stable synaptic plasticity upon TGR63 administration. The cognitive improvement was supported by the reduction in amyloid deposits in the AD mice brain as revealed by immunohistochemical studies. AD positive transgenic mice showed a significant deposition of A β plaques in different regions of the brain including cortex and hippocampus. The observed amyloid deposits and associated cognitive decline directly correlates with AD phenotypes.⁴ The histochemical studies of TGR63 treated APP/PS1 AD mice showed significant reduction of A β plaques throughout the brain including hippocampal and cortical regions. The reduced neuropathological hallmark in the AD brain diminish the amyloid toxicity such as, membrane disruption, synaptic dysfunction and neuronal loss, thereby improve the physiological brain functions. Further, the pharmacokinetics study established serum stability, BBB permeability and biocompatibility of TGR63. The gold standard H&E staining of organs from TGR63 treated AD and WT mice revealed biocompatible and wholesome nature and established TGR63 as a suitable candidate for prolonged administration through IP injection.

In conclusion, the misfolding and aggregation of A β peptides into toxic soluble and insoluble aggregation species are hallmarks of AD progression and associated multifaceted toxicity.

Accumulation of A β plaques in the brain directly correlates with AD phenotypes such as neuropsychiatric symptoms, learning deficiency, memory impairment, and cognitive decline. Modulation of A β burden and amelioration of associated neuropsychiatric symptoms are considered as the major therapeutic routes to treat AD. In this context, we designed, synthesized and identified a small molecule modulator of A β aggregation to ameliorate *in vitro* and *in vivo* A β induced neuronal toxicity and associated neuropsychiatric symptoms. The *in vitro* and *in cellulo* studies demonstrated that NMI derivative TGR63 with 4-ethynyl-*N,N*-dimethylaniline and *N,N,N*-trimethylethylenediamine functionalities bestowed right hydrophobicity-hydrophilicity balance to inhibit A β 42 aggregation and associated neuronal toxicity. The detailed NMR and *in silico* study provided valuable insights on the molecular level interactions between TGR63 and A β species (monomers and fibrils), which revealed the plausible mechanism of aggregation inhibition and justified our design strategy. The *in vivo* pharmacokinetics study established serum stability, BBB permeability, *in cellulo* and *in vivo* biocompatibility and suitability of TGR63 for prolonged treatment through IP injection. TGR63 treated APP/PS1 mice brain tissue revealed significant reduction of A β deposits validating its therapeutic efficacy as *in vivo* modulator of amyloid burden under progressive AD conditions. The treatment of APP/PS1 mice with TGR63 showed amelioration of learning deficiency, memory impairment, cognitive decline and neuropsychiatric symptoms, as revealed by distinct OF, NOI and MWM behavioral tests. Remarkably, the improvement in brain functions (learning efficiency, memory formations and cognitive functions) under progressive disease conditions is in excellent correlation with the reduced cortical and hippocampal A β load following the TGR63 treatment. These key attributes have validated the potential of TGR63 as a promising candidate for the treatment of AD.

3.8 Limitations

Our study focused on the design, synthesis and validation of small molecule inhibitor to ameliorate multifaceted amyloid burden and associated neurotoxicity in a double transgenic AD mouse model. The *in vitro* and *in vivo* experimental results have demonstrated efficacy of TGR63 to ameliorate amyloid burden associated cognitive decline, memory impairment and neuropathological hallmarks under progressive AD conditions. Further studies are required to explore the detailed mechanism of action of TGR63 by gene and protein analyses besides modulation of amyloid burden in the AD brain. The NFT of tau also plays an important role in AD progression, which necessitates *in vitro* and *in vivo* evolution of TGR63 for NFT modulation. The amelioration of memory impairment and cognitive decline could be further supported by detailed electrophysiological analysis. Assessment of modulation of inflammatory response by TGR63 treatment will be an interesting study, as inflammation is a key contributor to multifaceted AD toxicity.

3.9 Experimental Methods

3.9.1 General Methods

All solvents and reagents were obtained from Spectrochem or Merck and used without any further purification unless mentioned. Dulbecco's Modified Eagle Medium/Nutrient Mixture F 12 (DMEM F12), Roswell Park Memorial Institute (RPMI), fetal bovine serum (FBS) and horse serum (HS) was obtained from Invitrogen. Argon or nitrogen atmosphere was maintained for all the reactions. Agilent Cary series UV-Vis-NIR absorption, Agilent Cary eclipse fluorescence spectrophotometers and microplate reader (SpectraMax i3x) were used to perform absorption and fluorescence assay. ^1H and ^{13}C NMR spectra were recorded in Bruker AV-400 and JEOL-600

MHz spectrometers, and tetramethylsilane (TMS) was used as an internal standard. All the raw data was processed and analyzed using Prism 6 or Origin 8.5 software. HRMS spectra were acquired using Agilent 6538 UHD HRMS/Q-TOF high-resolution spectrometer. The calculated amount of inhibitors were dissolved in deionized water (Milli Q) (contain 5% dimethyl sulfoxide) to store (-20 °C) and diluted in phosphate buffered saline (pH= 7.4) for the experiments. Amyloid beta peptide was obtained from Merck (PP69-0.05 MG). The anti-amyloid fibrils (OC) and oligomers (A11) specific primary antibodies were obtained from Merck and ThermoFisher, respectively, to performed immunohistochemistry. Thioflavine T (ThT) was obtained from Sigma-Aldrich (T3516) and CQ probe was obtained from VNIR Biotech. Sodium citrate buffer was obtained from Fisher Scientific, India (6132-4-3,) and DAPI (4',6-diamidino-2-phenylindole) was obtain from Vector Laboratories, CA, USA (H-1200). Blue Star micro slides were used to mount the brain sections. The tissue homogenizer (D9938) and primers were obtained from Sigma-Aldrich. We got the mice ear tagging set from Jaxson laboratory, USA. The experimental brains were sectioned using Leica Vibratome (VT1200). All the images (cells and the brain) were captured using confocal fluorescence microscope (Olympus FV3000).

3.9.2 Synthesis of 4-((4-*N,N* dimethylaniline) ethynyl)-1,8-naphthalic anhydride

To a solution of 4-bromo-1,8-naphthalic anhydride (200 mg, 0.72 mmol) in dimethyl formamide (DMF)/triethylamine (Et₃N) (1 : 1) under argon atmosphere, Pd(PPh₃)₄ (27 mg, 23 μmol), sodium ascorbate (10 mg, 50 μmol), copper (II) sulfate (2 mg, 8 μmol) and 4-ethynylanisole (93.6 μL, 0.72 mmol) were added. The reaction mixture was stirred for 4 h at 80 °C and completion of the reaction was monitored by thin layer chromatography (TLC). The reaction mixture was extracted into ethyl acetate, washed with NH₄Cl and brine, dried over Na₂SO₄ and evaporated under vacuo to obtain the

crude product. The product was re-dissolved in ethyl acetate, precipitated with diethyl ether and the pure product (1) was collected by filtration. The product was obtained as dark red coloured solid in good yield (68%).

^1H NMR (CDCl_3 , 400 MHz) δ 8.65 (d, 2H, $J = 6.4$), 8.64 (d, 2H, $J = 4.2$), 8.55 (d, 2H, $J = 8$), 7.92 (d, 2H, $J = 7.6$), 7.89 (t, 2H, $J = 15$), 7.55 (d, 2H, $J = 4.2$), 6.73 (d, 2H, $J = 6.4$), 3.06 (s, 6H); ^{13}C NMR (CDCl_3 , 100 MHz) δ 163.8, 151, 134.2, 133.6, 132.7, 131.5, 130.7, 130.4, 130, 127.4, 116.5, 111.7, 108, 40.1; HRMS (ESI-MS): found 342.1145, calcd. for $\text{C}_{22}\text{H}_{16}\text{NO}_3$ $[\text{M}+\text{H}]^+$ $m/z = 342.1112$.

3.9.3 Synthesis of TGR60

To a solution of naphthalic anhydride (114 mg, 0.58 mmol) dispersed in isopropanol, *N,N*-diisopropylethylamine (DIPEA; 31 μL , 1.7 mmol) and 2-amino-*N,N,N*-trimethylethanaminium (60 mg, 0.58 mmol) were added and refluxed at 80 °C for 6 h. The reaction mixture was extracted with chloroform (CHCl_3), washed with brine, dried over Na_2SO_4 and evaporated under vacuo to obtain the crude product. The crude product was purified by column chromatography on silica gel using 2% methanol (MeOH) in CHCl_3 as an eluent to afford a white solid in excellent yield (88%).

^1H NMR ($\text{DMSO } d_6$, 400 MHz) δ 8.54-8.50 (m, 4H), 7.93-7.89 (m, 2H), 4.49 (t, 2H, $J = 14.4$), 3.66 (t, 2H, $J = 14.4$), 3.23 (s, 9H); ^{13}C NMR ($\text{DMSO } d_6$, 100 MHz) δ 163.4, 134.7, 131.3, 130.9, 127.4, 127.3, 121, 89, 61.9, 52.5, 33.6; HRMS (ESI-MS): found 283.1439, calcd. for $\text{C}_{17}\text{H}_{19}\text{N}_2\text{O}_2$ $[\text{M}]^+$ $m/z = 283.1441$.

3.9.4 Synthesis of TGR61

To a solution of 4-dimethylamine-1,8-naphthalic anhydride (139 mg, 0.58 mmol) dispersed in isopropanol, DIPEA (31 μ L, 1.7 mmol) and 2-amino-*N,N*-trimethylethanaminium (60 mg, 0.58 mmol) were added and refluxed at 80 °C for 6 h. The reaction mixture was extracted with CHCl_3 , washed with brine, dried over Na_2SO_4 and organic layer was evaporated to obtain the crude product. The crude product was purified by column chromatography on silica gel using 3.5% MeOH in CHCl_3 as an eluent to afford a yellow solid in good yield (54%).

^1H NMR (DMSO d_6 , 400 MHz) δ 8.50 (d, 1H, $J = 6.4$), 8.49 (d, 1H, $J = 4.2$), 8.38 (d, 1H, $J = 8.4$), 7.80 (d, 1H, $J = 7.2$), 7.78 (d, 1H, $J = 7.2$), 7.24 (d, 1H, $J = 4.2$), 4.96 (t, 2H, $J = 14$), 3.64 (t, 2H, $J = 14$), 3.20 (s, 9H), 3.12 (s, 6H); ^{13}C NMR (DMSO d_6 , 100 MHz) 163.7, 162.9, 156.9, 132.6, 132.1, 130.8, 124.9, 124, 122, 112.8, 112.5, 52.4, 44.3, 33.4; HRMS (ESI-MS): found 326.1864, calcd. for $\text{C}_{19}\text{H}_{24}\text{N}_3\text{O}_2$ $[\text{M}]^+$ $m/z = 326.1863$.

3.9.5 Synthesis of TGR62

To a solution of 4-(benzylethynyl)-1,8-naphthalic anhydride (172 mg, 0.58 mmol) dispersed in isopropanol, DIPEA (31 μ L, 1.7 mmol) and 2-amino-*N,N,N*-trimethylethanaminium (60 mg, 0.58 mmol) were added and refluxed at 80 °C for 6 h. The reaction mixture was extracted with CHCl_3 , washed with brine, dried over Na_2SO_4 and evaporated under vacuo to obtain the crude product. The crude product was purified by column chromatography on silica gel using in CHCl_3 as an eluent to afford a yellow solid in good yield (74%).

^1H NMR (DMSO d_6 , 400 MHz) δ 8.83 (d, 1H, $J = 8.4$), 8.61 (d, 1H, $J = 7.2$), 8.51 (d, 1H, $J = 7.6$), 8.13 (d, 1H, $J = 7.6$), 8.05 (t, 1H, $J = 15.6$), 7.81-7.78 (m, 2H), 7.54-7.52 (m, 3H), 4.49 (t, 2H, $J = 14.4$), 3.67 (t, 2H, $J = 14.4$), 3.24 (s, 9H); ^{13}C NMR (DMSO d_6 , 100 MHz) 163.2, 162.9, 132.3, 131.9, 131.4, 131, 130.9, 130.2, 129.9, 128.9, 128.4, 127.4,5, 126.5, 122.5, 121.8,

121.2, 99, 86.0, 61.9, 54.8, 52.4, 33.7; HRMS (ESI-MS): found 384.1693, calcd. for C₂₅H₂₃N₂O₂ [M]⁺ m/z = 384.1854.

3.9.6 Synthesis of TGR63

To a solution of 4-((4-*N,N* dimethylaniline) ethynyl)-1,8-naphthalic anhydride (200 mg, 0.58 mmol) dispersed in isopropanol, DIPEA (31 mL, 1.7 mmol) and 2-amino-*N,N,N*-trimethylethanaminium (60 mg, 0.58 mmol) were added and refluxed at 80 °C for 6 h. The reaction mixture was extracted with ethyl acetate, washed with brine, dried over Na₂SO₄ and evaporated to obtain the crude product. The crude product was purified by column chromatography on silica gel using 1% MeOH in CHCl₃ as an eluent to afford a red coloured solid in good yield (75%).

¹H NMR (DMSO *d*₆, 400 MHz) δ 8.60 (d, 1H, *J* = 0.8), 8.58 (d, 1H, *J* = 1.2), 8.48 (d, 1H, *J* = 7.6), 8.03 (d, 2H, *J* = 4.4), 8.01 (t, 2H, *J* = 4.8), 7.61 (d, 2H, *J* = 2), 6.80 (d, 2H, *J* = 8.8), 4.48 (t, 2H, *J* = 13.6), 3.65 (t, 2H, *J* = 14.8), 3.21 (s, 9H), 3.01 (s, 6H); ¹³C NMR (DMSO *d*₆, 100 MHz) δ 163.3, 163, 158, 150.9, 133.2, 132.5, 131.3, 130.6, 130.4, 129.7, 128, 127.6, 122.4, 120.5, 111.8, 106.9, 102.3, 85.9, 52.4, 33.6; HRMS (ESI-MS): found 426.2176, calcd. for C₂₇H₂₈N₃O₂ [M]⁺ m/z = 426.2176.

3.9.7 Synthesis of TGR64

To a solution of 4-((4-*N,N* dimethylaniline) ethynyl)-1,8-naphthalic anhydride (200 mg, 0.58 mmol) dispersed in isopropanol, DIPEA (31 μL, 1.7 mmol) and tert-butyl 2-aminoethylcarbamate (39 mg, 0.58 mmol) were added and refluxed at 80 °C for 6 h. The reaction mixture was extracted with ethyl acetate, washed with brine, and dried over Na₂SO₄. The crude

product was purified using column chromatography on silica gel using 0.25% MeOH in CHCl₃ as an eluent to afford a red coloured solid. Then the compound was deprotected using TFA (95% TFA, 4.5% DCM and 0.5% TIPS) and the product was precipitated to obtain pure product in good yield (68%).

¹H NMR (DMSO *d*₆, 400 MHz) δ 8.77 (d, 1H, *J* = 1.8), 8.56 (d, 1H, *J* = 3.6), 8.45 (d, 1H, *J* = 3.8), 8.00 (d, 2H, *J* = 3), 7.97 (d, 2H, *J* = 8.8), 7.59 (d, 2H, *J* = 3.3), 6.74 (d, 2H, *J* = 3.8), 4.33 (t, 2H, *J* = 11.6), 3.17 (s, 2H), 3.01 (s, 6H); ¹³C NMR (DMSO *d*₆, 100 MHz) δ 163.8, 163.5, 150.8, 133.2, 132.2, 131.1, 130.5, 130.1, 129.7, 127.9, 127.7, 122.7, 120.8, 111.8, 107, 102, 85, 37.6, 37.5; HRMS (ESI-MS): found 383.1767, calcd. for C₂₄H₂₁N₃O₂ [M]⁺ *m/z* = 383.1634.

3.9.8 Synthesis of TGR65

To a solution of 4-((4-*N,N* dimethylaniline) ethynyl)-1,8-naphthalic anhydride (200 mg, 0.58 mmol) dispersed in isopropanol, DIPEA (31 μL, 1.7 mmol) and 2-(2-aminoethoxy)ethanol (22 mL, 0.58 mmol) were added and refluxed at 80 °C for 6 h. The reaction mixture was extracted with ethyl acetate, washed with brine, and dried over Na₂SO₄ and evaporated under vacuo to obtain the crude product. The crude product was purified by column chromatography on silica gel CHCl₃ as an eluent to afford a red coloured solid in good yield (72%).

¹H NMR (DMSO *d*₆, 400 MHz) δ 8.76 (d, 1H, *J* = 8.4), 8.55 (d, 1H, *J* = 7.2), 8.43 (d, 1H, *J* = 7.6), 7.98 (d, 2H, *J* = 8), 7.95 (t, 2H, *J* = 1.6), 7.59 (d, 2H, *J* = 8.8), 6.79 (d, 2H, *J* = 8.8), 4.25 (t, 2H, *J* = 12.8), 3.67 (t, 2H, *J* = 12.8), 3.47 (s, 4H), 3.31 (s, 4H), 3.00 (s, 6H); ¹³C NMR (DMSO *d*₆, 100 MHz) 163.2, 162.9, 133.2, 132.1, 131.1, 130.5, 130.2, 129.7, 127.9, 127.6, 127.5, 122.4, 120.6, 111.8, 107, 101.8, 85, 72, 66.8, 60.1, 28.9; HRMS (ESI-MS): found 429.1803, calcd. for C₂₆H₂₅N₂O₄ [M+H]⁺ *m/z* = 429.1814.

3.9.9 Preparation of A β 42 Aggregation Species

A β 42 peptide was dissolved in hexafluoro-2-propanol (HFIP, 250 μ L) and incubated for 1 h at room temperature, and HFIP was removed by nitrogen gas flow. The processed A β 42 peptide was dissolved in 2% DMSO or NaOH solution (100 mM) containing PBS buffer (pH = 7.4) to prepare the monomeric A β 42 solution and the peptide concentration was calculated by UV-visible absorbance study ($\epsilon = 1450 \text{ cm}^{-1} \text{ M}^{-1}$). Oligomers were prepared by incubating A β 42 monomers for 24 h at 4 °C. Similarly, A β 42 monomers were incubated for 2 days in PBS buffer (pH = 7.4) at 37 °C to prepare fully grown fibrillar aggregates and the presence of A β 42 fibrils was confirmed by ThT assay.

3.9.10 Dot Blot Analysis

To demonstrate the A β 42 aggregation modulation ability of TGR63, we performed dot blot analysis. The freshly prepared A β 42 (10 μ M) sample was incubated (at 4 and 37 °C) with TGR63 and alone independently for 24 h (oligomers) and 48 h (fibrils) without shaking, respectively. The incubated samples were dotted on the PVDF membrane and allowed to dry. The PVDF membranes was blocked using 5% skimmed milk (HIMEDIA, GRM 1254) in PBS for 1 h at room temperature. The blots were washed (3 times) with 1% of Tween 20 (HIMEDIA GRM156) containing PBS (PBST) for 10 min and incubated with A11 (1:1000) and OC (1:1000) primary antibody, specific to A β 42 oligomers and fibrils, respectively, at 4 °C for 16 h. Then the unbound primary antibody was removed by PBST wash (3 times) and incubated with HRP conjugated anti-mouse (for A11) anti-rabbit (for OC) secondary antibody (Biorad, 1706515),

which was diluted 10000 times. The blots were developed with the treatment of enhanced chemiluminescence (ECL) reagent in Versa Doc (Biorad) instrument.

3.9.11 Cell Culture

SHSY5Y and PC12 cells were cultured using DMEM/F-12 (Dulbecco's Modified Eagle Medium/Nutrient Mixture F 12) medium (Gibco, Invitrogen) containing 10% of FBS (fetal bovine serum) and 1% PS (pen-strep) and RPMI (Roswell Park Memorial Institute) medium (Gibco, Invitrogen) with fetal bovine serum (FBS, 10%), horse serum (HS, 5%), and pen-strep (1%), respectively, under the cell growing condition (37 °C temperature and 5% CO₂ atmosphere).

3.9.12 Imaging of A β 42 Fibrils in Cellular Milieu

We performed A β 42 fibrils imaging in SHSY5Y cells to study the plasma membrane toxicity of A β 42 fibrils in absence and presence of TGR63. For imaging experiment, cells were cultured in petri dishes (35 mm) and treated with TGR63 treated and untreated A β 42 fibrils for 2 h. The experimental cells were washed and fixed with PBS and 4% PFA, respectively. Then, the cells were treated with red fluorescent-labeled (λ_{ex} = 633 nm and λ_{em} = 650 nm) secondary antibody or CQ followed by A β 42 fibrils specific primary antibody, OC (1:250) and DAPI to capture images under the confocal fluorescence microscope.

3.9.13 Neuronal Cell Rescue

To demonstrate the neuronal cells rescue ability of inhibitors (TGR60-65) from A β 42 peptide toxicity, we performed MTT assay. The cells were (15,000 cells/well) cultured in a 96-well plate

using cell growing media and incubated with for A β 42 peptide and inhibitors for 24 h at 37 °C temperature within 5% CO₂ atmosphere. Further MTT (5 mg/mL) solution was added into the experimental cell media and incubated for 2.5 h. Finally, the experimental medium was removed and 100 μ L of DMSO:MeOH (1:1) mixture was added, and the absorbance (570 nm) was monitored using microplate reader.

3.9.14 *In Silico* Assessment

The molecular level interaction of compounds TGR60-65 with A β monomer and fibrils was studied using an integrated approach involving molecular docking, molecular dynamics and binding free energy calculations. The molecular docking approach was employed to identify all the low energy binding sites and modes for TGR63 with monomeric and fibril forms of A β . The target structure for A β monomer is based on the NMR structure deposited in the protein databank (pdb id is 1IYT). The A β monomer structure reported corresponds to aqueous solvent environment and has two helical regions (involving residues in the range 8-25 and 28-38) with a type I β -turn. There are 10 different models reported for A β monomer and the docking was carried out for all the models using auto dock software. Since the binding modes are not known, a blind docking procedure was adopted by incorporating the entire peptide within a sufficiently larger grid box having grid points 110, 90, 160 along x, y and z directions. The grid point spacing was chosen to the default value of 0.375 Å. The Lamarckian genetic algorithm was adopted to find out the least energy binding sites and binding modes for TGP63 within the A β peptide. The model with the least energy has been adopted for the subsequent molecular dynamics (MD) simulations. At least three independent least energy binding sites were observed. A complex structure of A β monomer with three molecules of TGR63 bound in the lowest energy

binding modes was prepared as the input structure for MD. The simulation box was solvated with approximately 13350 water molecules. The MD simulations followed a routine protocol and involved minimization, simulation in constant volume ensemble and simulation in isothermal isobaric ensemble. A short time scale equilibration run was carried out to allow the system to evolve to the ambient temperature and pressure. Followed by the equilibration run for a time scale of 5 ns, final production run was carried out for a time scale of 40 ns. All MD simulations were performed using Amber16 software. The time step for solving the Newton's equation of motion was set to 2 fs. 500 configurations from last 5 ns were used for carrying out ensemble average of binding free energies using molecular mechanics-generalized Born surface area (MM-GBSA) approach. This approach involves calculations of free energies of complex and subsystems namely ligands and target. The binding free energies were computed as the difference between the complex and subsystem free energies. The solvents and ions were stripped from the simulation trajectories and only the receptor-ligand coordinates were used for the free energy calculations. To account for the solvent effect, the approach employs generalized Born approach and polar and non-polar solvation energies together account for the free energy changes associated with binding due to aqueous environment. A similar approach described above for A β monomer was adopted for A β fibril. The A β fibril structure reported in protein databank (pdb id is 5OQV) based on cryo-EM was used for molecular docking. This structure constitutes of 9 A β peptides organized with LS topology and the c-terminal regions are protected from exposure to solvents. Grid box chosen for docking includes entire fibril structure such that all possible surface sites can be identified. The number of grid points along x, y and z directions were chosen as 220, 200 and 130 with a default grid spacing. The molecular docking study showed that TGR63 can bind to 6 different binding sites in A β fibril. The binding modes in the

initial configuration for TGR63 are shown in Figure 4. The binding modes for TGR64 and TGR65 are shown in Figure 5. The MD simulation for complex of A β fibril with TGR63 in different binding sites was carried out following the procedure described for A β monomer. The total time for the production run was 40 ns. The binding free energies for TGR63 in different binding sites of A β fibril were computed using MM-GBSA approach. The binding free energies for other molecules TGR60, TGR61, TGR62, TGR64, TGR65 were also computed following the protocols described above.

3.9.15 Animal Maintenance

Double transgenic mice [B6.Cg-Tg(APP^{swe},PSEN1^{dE9})85Dbo/Mmjax] were obtained from the Jackson Laboratory (MMRRC stock no 34832 jax) and maintained them in JNCASR Animal Facility, maintained 12 h light and dark cycle. Then these mice were bred with WT mice (C57/BL6) to increase the mice number and maintain its colony. All the animal maintenances and studies were performed according to the protocols of the Institutional Animal Ethics Committee (IAEC), JNCASR. The protocol (TG001) was approved by the IAEC and Committee for purpose of Control and Supervision of Experiments on Animals (CPCSEA), New Delhi.

3.9.16 Genotyping of Mice

All the cultured mice were genotyped after at 4-6 weeks of age. Genomic DNA was collected from each and every mouse tail and processed with NaOH and Tris-HCl buffer. The Jackson Laboratory's protocol was followed to confirm the Alzheimer's positive mice. The primer sequences used for genotyping: APP: 5'-GACTGACCACTCAGCCAGGTTCTG-3'; 5'-CTTGTAAGTTGGATTCTCATATCCG-3'; PSEN1: 5'-ATTAGAGAACGGCAGGAGCA-

3';5'-GCCATGAGGGCACTAATCAT-3'.

3.9.17 Blood Brain Barrier (BBB) Crossing and Serum Stability Experiment

Vehicle (PBS) and TGR63 were administrated to WT mice and sacrificed at different time points to collect the blood and brain samples. Collected blood and brain samples were processed to obtain blood serum and brain lysate, which were analyzed through MALDI mass using α -cyano-4-hydroxycinnamic acid (CCA) matrix for identifying TGR63 in blood serum and brain.

3.9.18 Immunohistochemistry

After all the behavioral studies, experimental AD positive and WT mice were sacrificed (cervical dislocation) and their brains were dissected out. The collected brains were fixed with paraformaldehyde (4%) for 48 h and then rehydrated with 30% sucrose solution. The experimental brains were sectioned (40 μ m) using vibratome, and stored at -20 °C. The brain sections were treated 10 mM sodium citrate buffer to remove the antigen. The sections were blocked with Bovine Serum Albumin (BSA, 2%) and goat serum (1%) for 4 h followed by permeabilization with 0.1% Triton-X-100 containing 0.1 M PBS (PBTx). After blocking, the sections were incubated with primary antibodies for 24 h at 4 °C with gentle sacking. The unbound primary antibody was washed out and the sections were incubated with fluorescently (green and red) labeled secondary antibodies for 4 h at room temperature in dark with gentle sacking. Finally, these brain sections were incubated with DAPI for 10 min and taken on glass slide for mounting with vecta-sheild, and imaged using confocal fluorescence microscope.

3.9.19 Open Field Test

The open-field locomotion of experimental mice in a novel environment was assessed to confirm the recovery of cognitive function by TGR63 treatment. This experiment was conducted in a 45 × 45 cm OF apparatus made of grey plywood with 45 cm walls high. All the mice were placed in a same position (corner) of the open field and the movement of the mouse was recorded for 5 min using a video camera fix on the top of the apparatus and analyzed using smart 3.0 software. 70% ethanol was used to clean the test apparatus after each and every experiment.

3.9.20 NOI Test

The improvement of recognizing memory by TGR63 treatment were assessed using the NOI test as previously described. The experiment was performed using a 33 × 33 cm OF platform with 20 cm of walls high. All the experimental mice were habituated for 1 day in the platform and two diagonally located identical objects were familiarized in 1st day. During testing (after 24 and 48 h) one novel object was introduce in place of one familiar object, respectively and the mice were allowed to explore for 10 min. The exploration time of familiar and novel objects was recorded using stopwatch. The discrimination index (DI) [DI= (time exploring the novel object – time exploring the familiar) / (time exploring novel + familiar) * 100] was calculated to analyze the exploration tendency. After each and every experiment the test apparatus and objects were cleaned with 70% ethanol and wiped out with tissue paper.

3.9.21 MWM Test

Morris water maze experiment was performed with our experimental mice, which is extensively used to analyze the spatial memory and learning as previously described. This experiment was conducted in a water of pool 122 cm in diameter and 90 cm in depth and the pool was filled up to

60 cm. Non-toxic paint was used to make the water opaque and pool temperature was maintained at 26 ± 0.5 °C. A 14 cm² platform was placed in the center of South-West (SW) quadrant of the pool, which is submerged 1 cm under the water surface. During all the training days the platform remained in the same position and removed from the pool in the probe test. Mice were placed into the pool facing the wall and allow 60 s to find the hidden platform. If the mouse did not able to find the hidden platform in given time, it was guided towards the platform and allow to stay on it for 60 s before returning to its home cage. This procedure was repeated for four time in a day, each time starting position was different. After each and every trail the mouse was dried off with tissue paper and clean towel. On 5th day the probe test was performed by removing the hidden platform. Mice were placed into the pool in a novel position of opposite quadrant (NE) where the platform used to be (SW). All tested mice were allowed 60 s to find the platform in the entire pool. Videos were recorded using Nikon coolPex camera and analyzed using smart 3.0 software.

3.9.22 Statistical Analysis

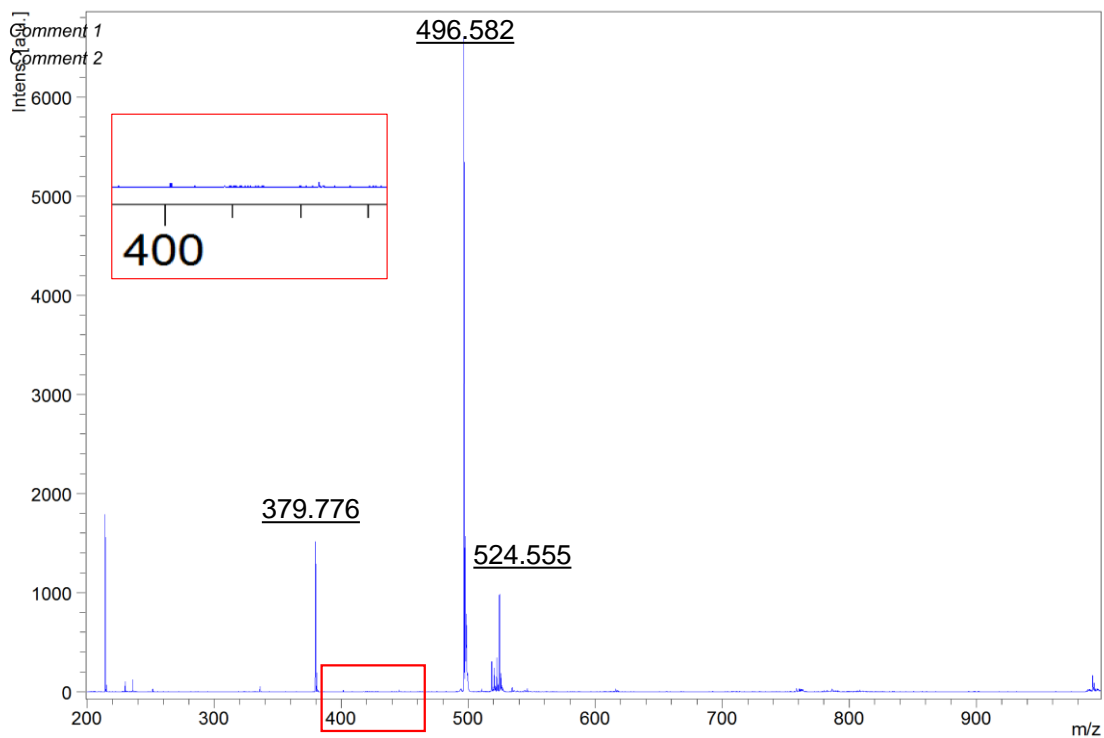
All the behavioral results and brain images were analyzed using GraphPad Prism 6 and ImageJ software, respectively. Significance level between different groups were assessed using Two-way ANOVA with more than one independent variable. Further, significant difference was determined using Bonferroni's multiple comparisons Post hoc test (* $p < 0.05$).

3.10 Appendix

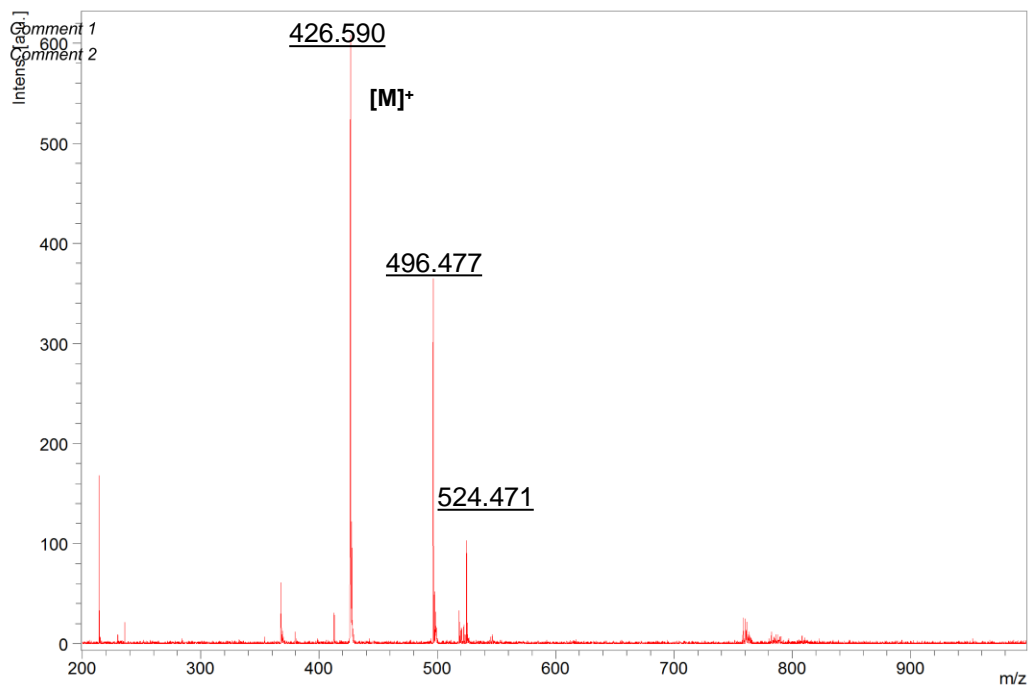
- ❖ MALDI analysis of vehicle and TGR63 treated mice blood samples
- ❖ The locomotion of vehicle and TGR63 treated WT mice cohort during OF test.

- ❖ The locomotion of vehicle and TGR63 treated AD mice cohort during OF test.
- ❖ The trajectory of vehicle and TGR63 treated WT mice cohort during MWM probe trail
- ❖ The trajectory of vehicle and TGR63 treated AD mice cohort during MWM probe trail
- ❖ TGR60: ^1H , ^{13}C NMR and HRMS analysis
- ❖ TGR61: ^1H , ^{13}C NMR and HRMS analysis
- ❖ TGR62: ^1H , ^{13}C NMR and HRMS analysis
- ❖ TGR63: ^1H , ^{13}C NMR and HRMS analysis
- ❖ TGR64: ^1H , ^{13}C NMR and HRMS analysis
- ❖ TGR65: ^1H , ^{13}C NMR and HRMS analysis
- ❖ Statically analysis of behavioural test result

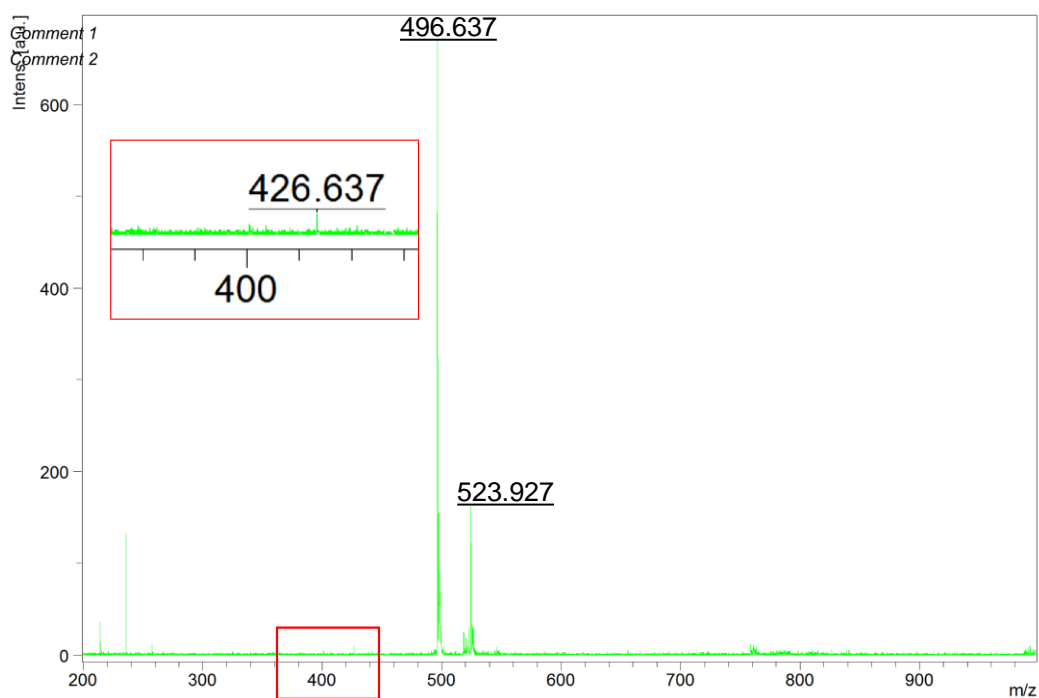
MALDI analysis of vehicle treated mouse blood sample



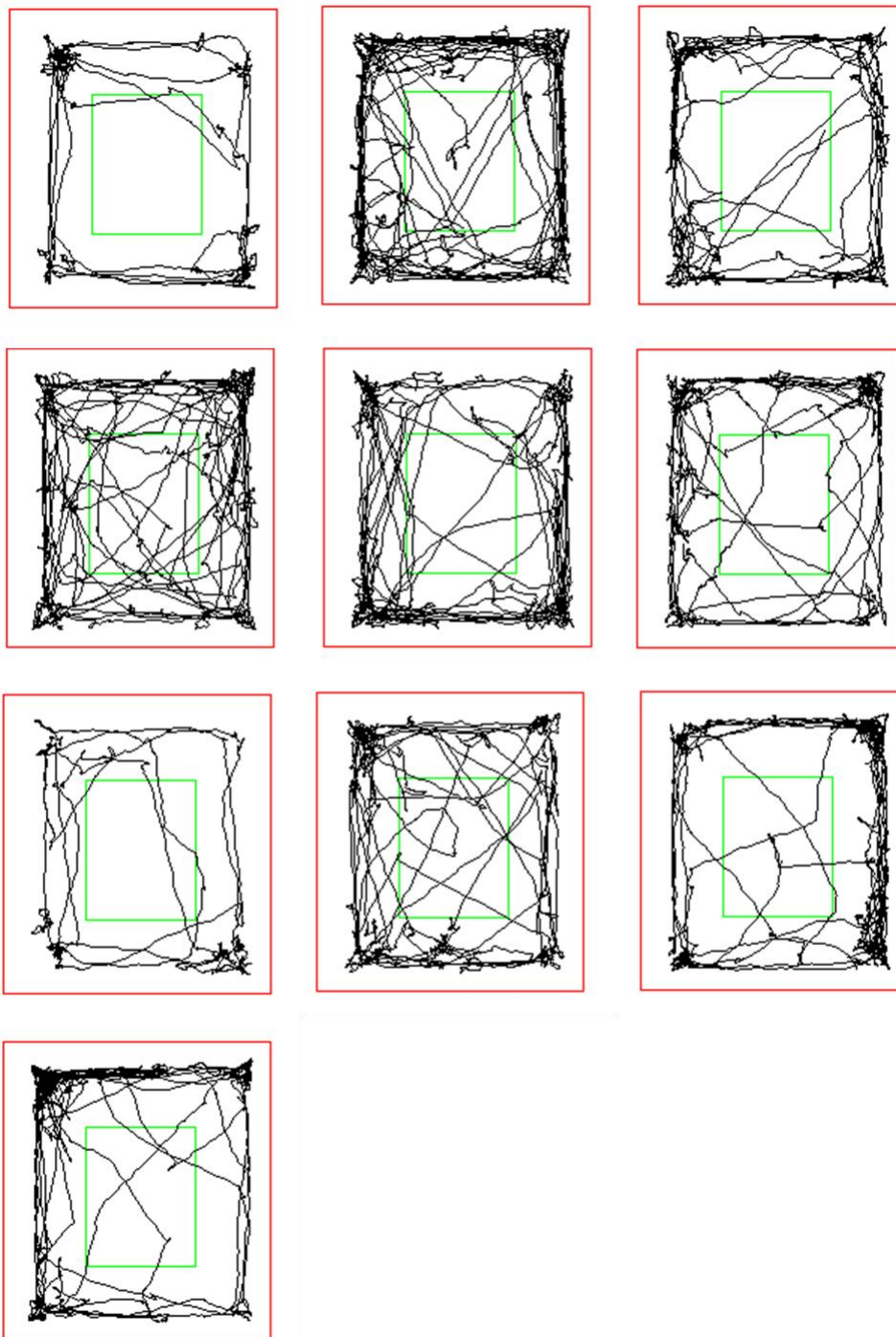
MALDI analysis of TGR63 treated mouse blood sample after 1 h of administration



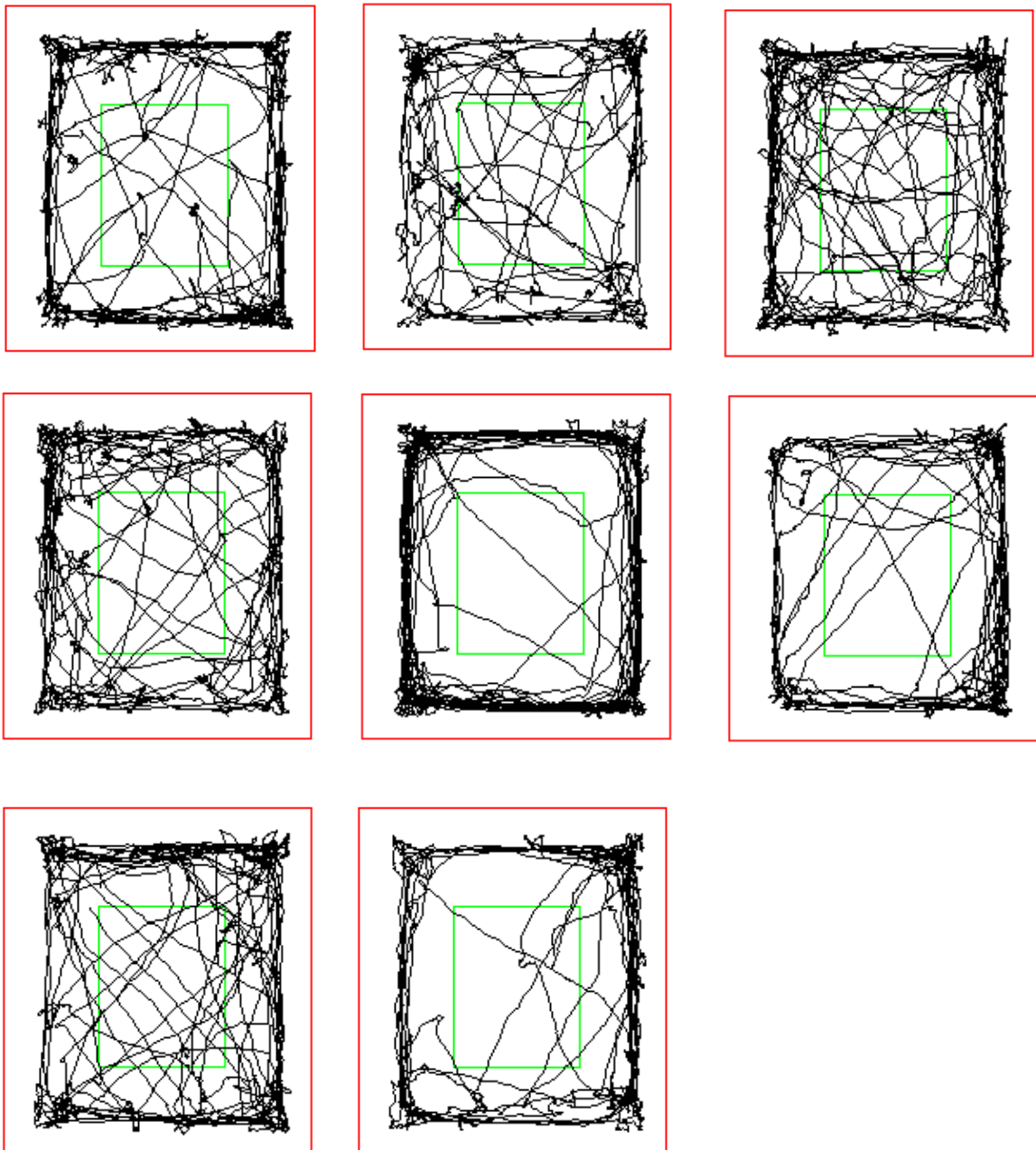
MALDI analysis of TGR63 treated mouse blood sample after 24 h of administration



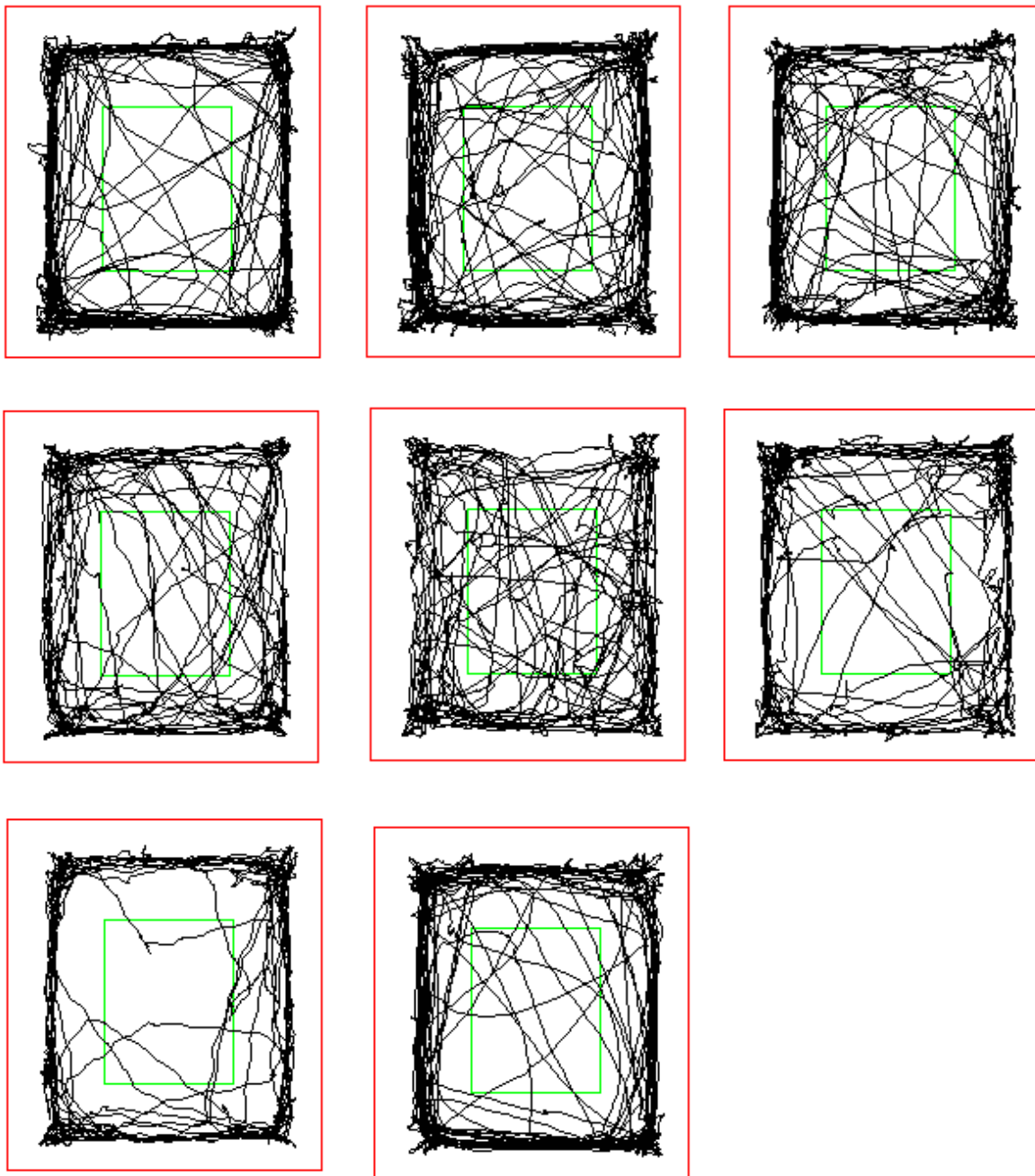
The locomotion of vehicle treated WT mice cohort during OF test



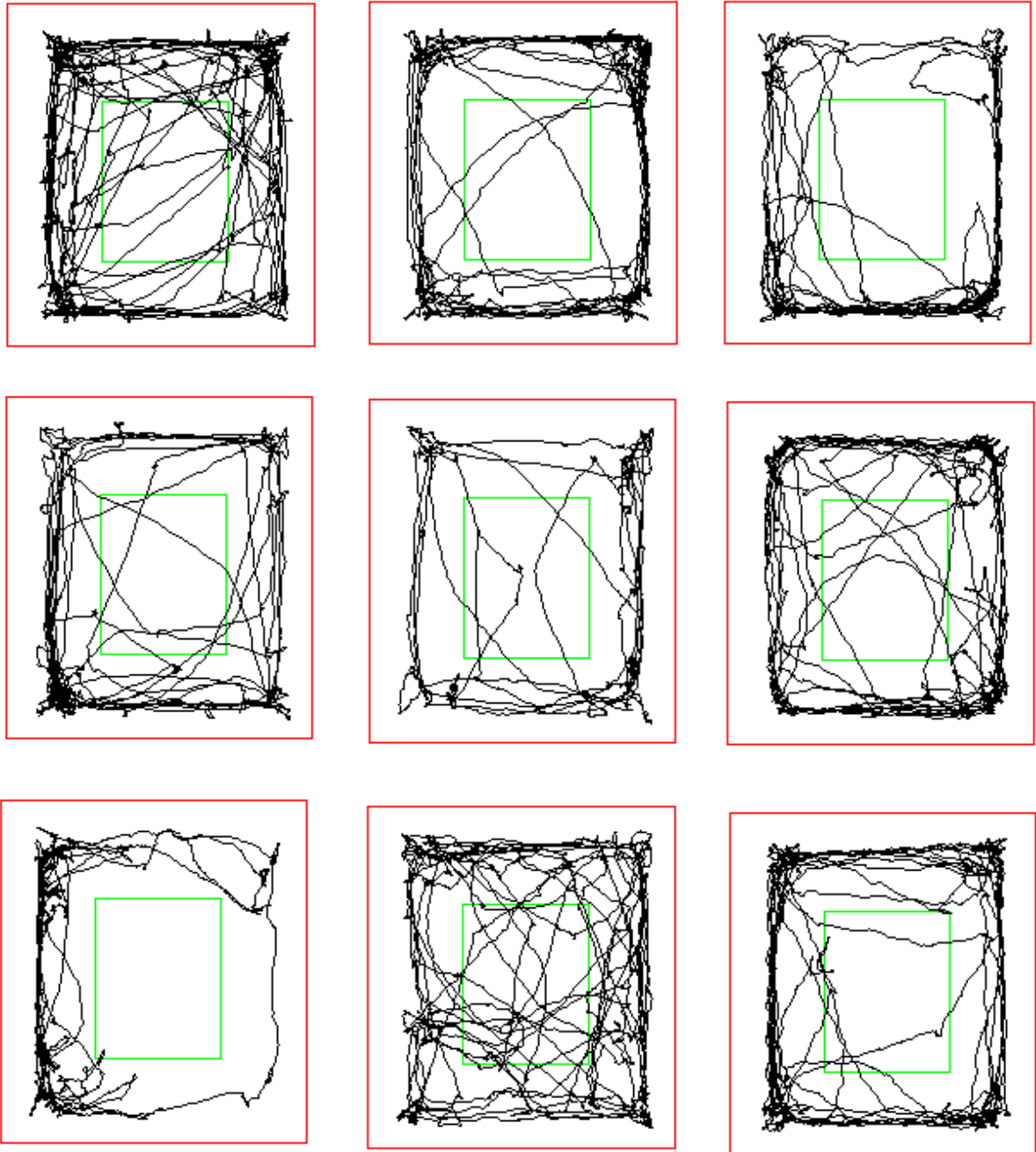
The locomotion of TGR63 treated WT mice cohort during OF test



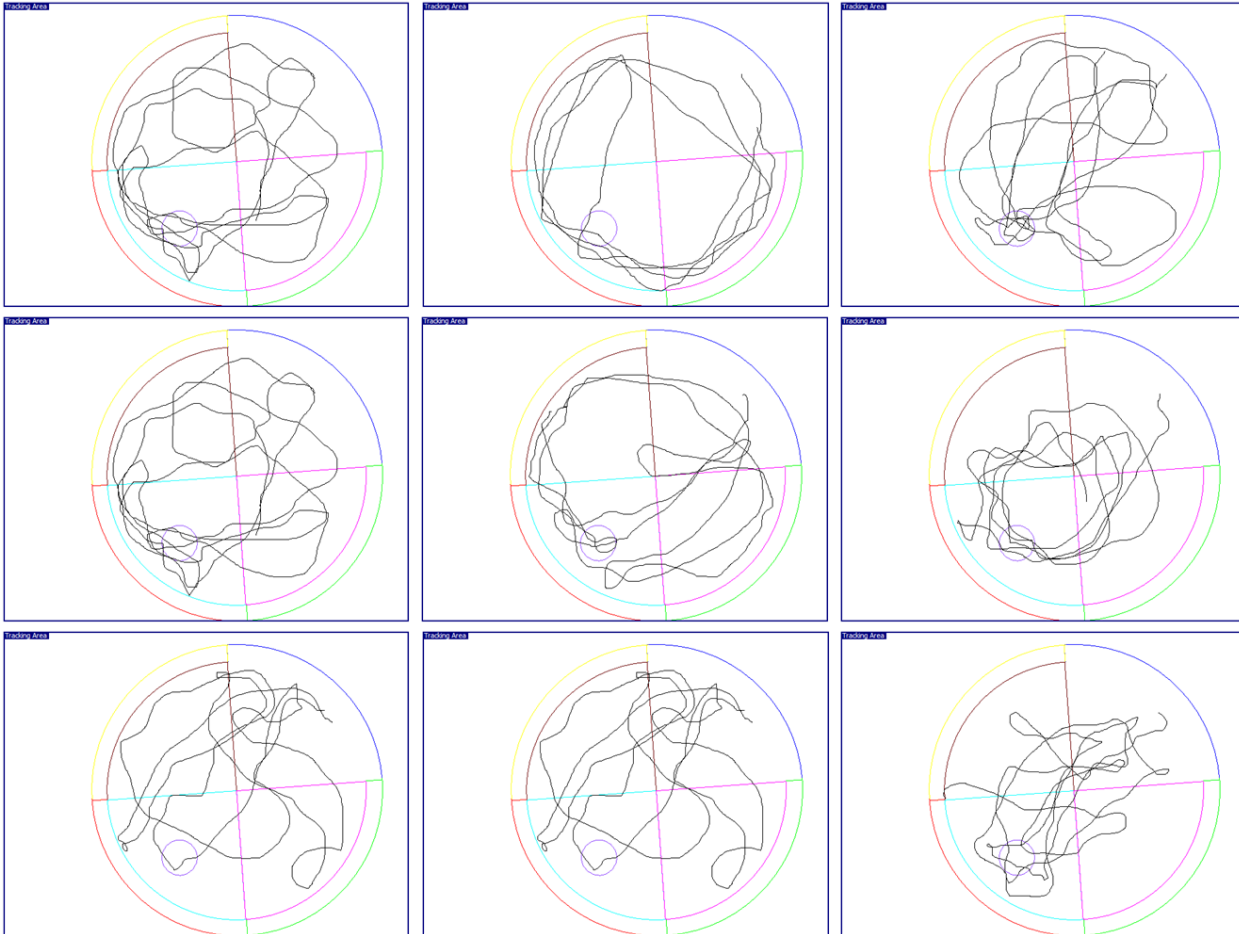
The locomotion of vehicle treated AD mice cohort during OF test



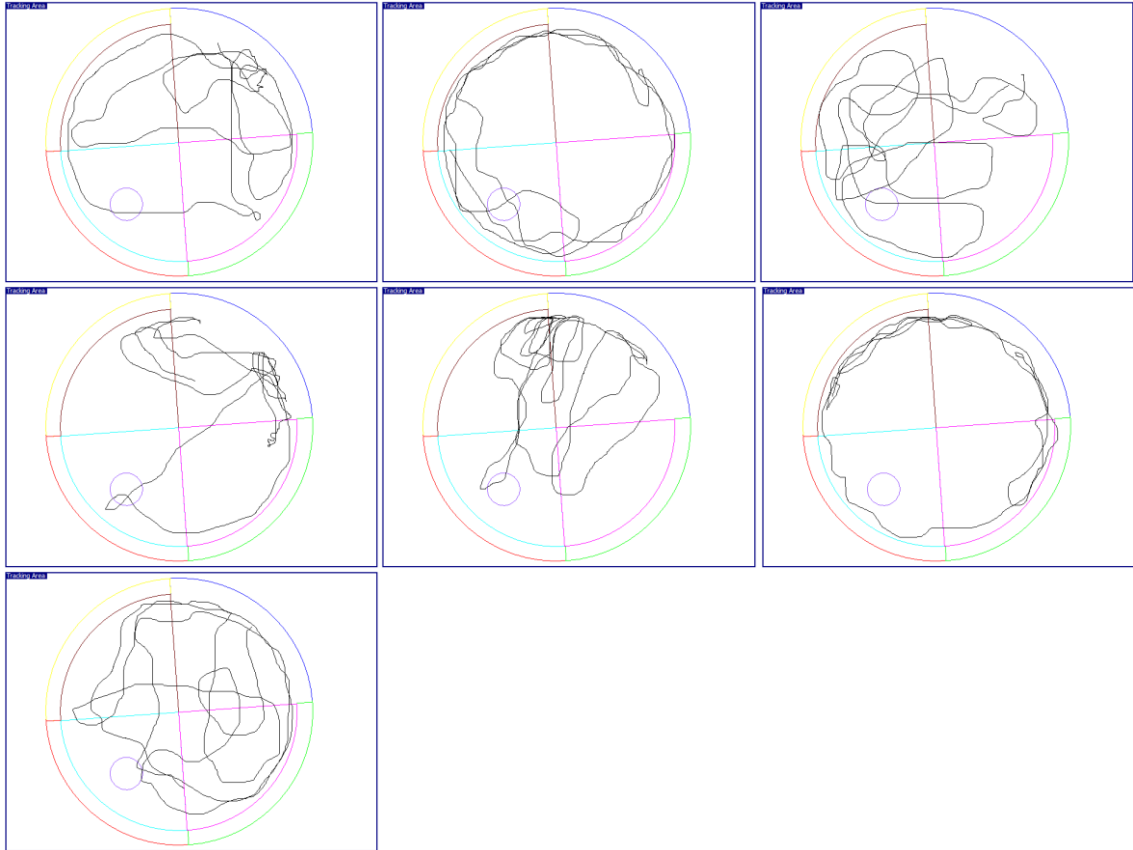
The locomotion of TGR63 treated AD mice cohort during OF test



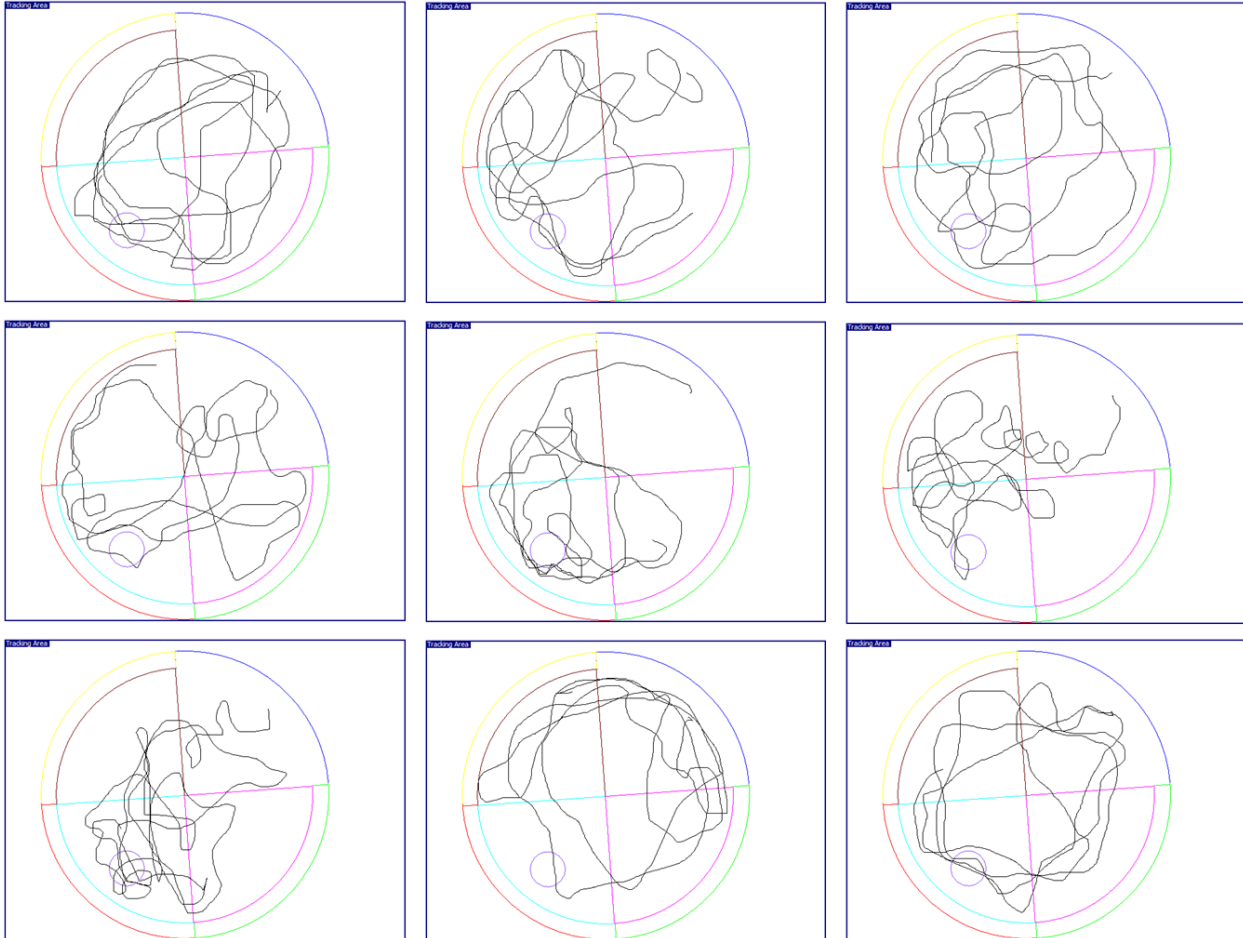
The trajectory of vehicle treated WT mice cohort during MWM probe trial (without platform)



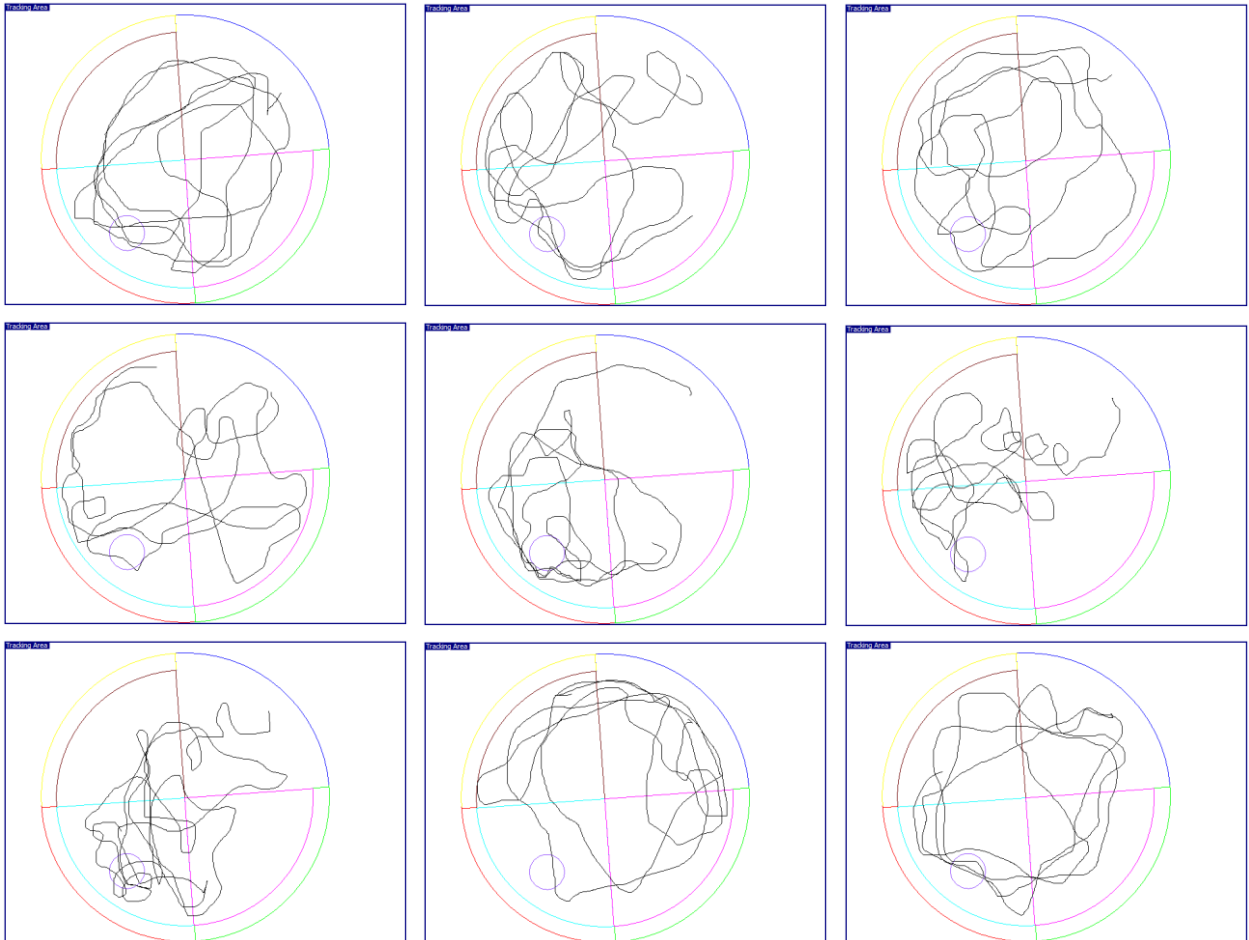
The trajectory of TGR63 treated WT mice cohort during MWM probe trial (without platform)



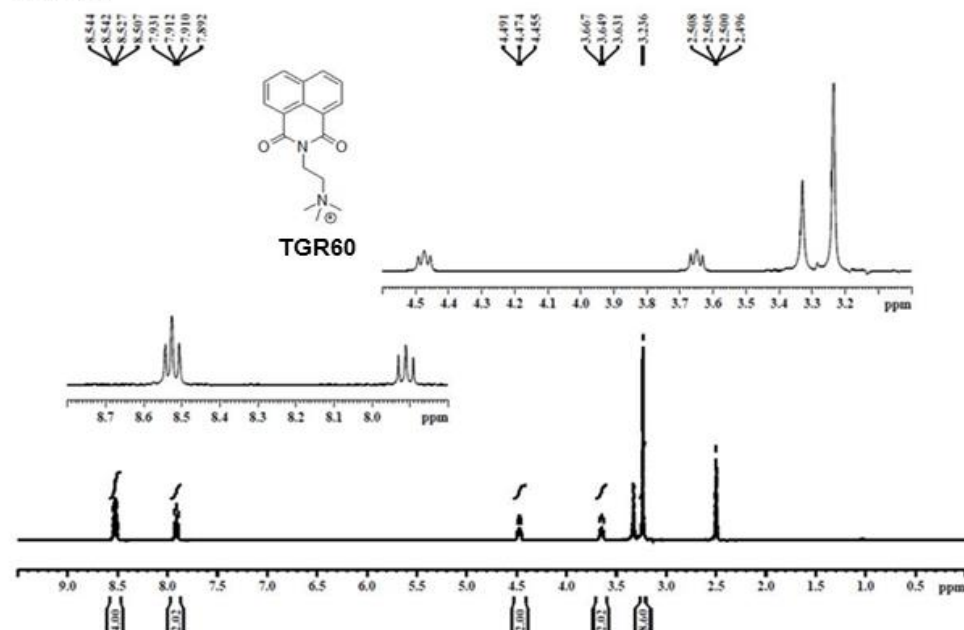
The trajectory of vehicle treated AD mice cohort during MWM probe trial (without platform)



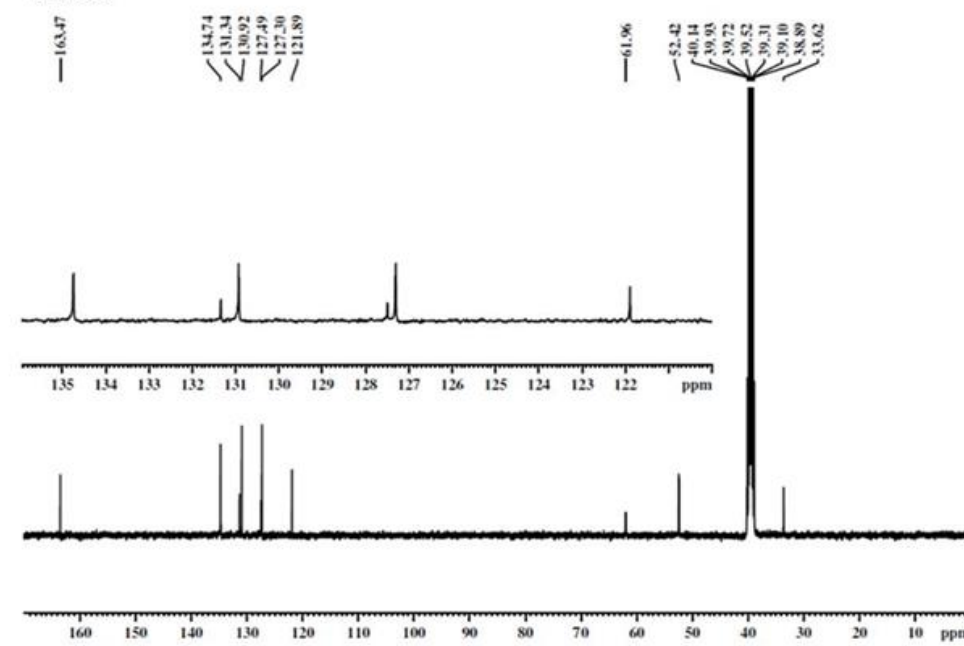
The trajectory of TGR63 treated AD mice cohort during MWM probe trial (without platform)



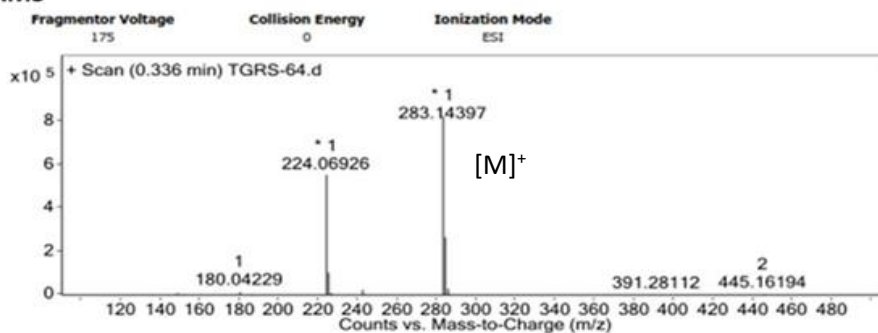
¹H NMR

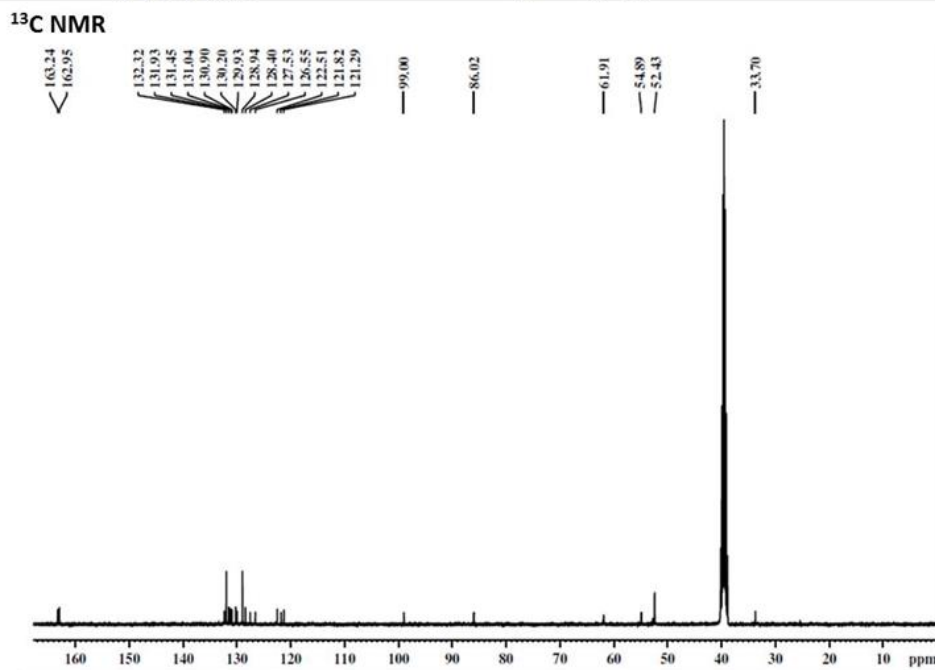
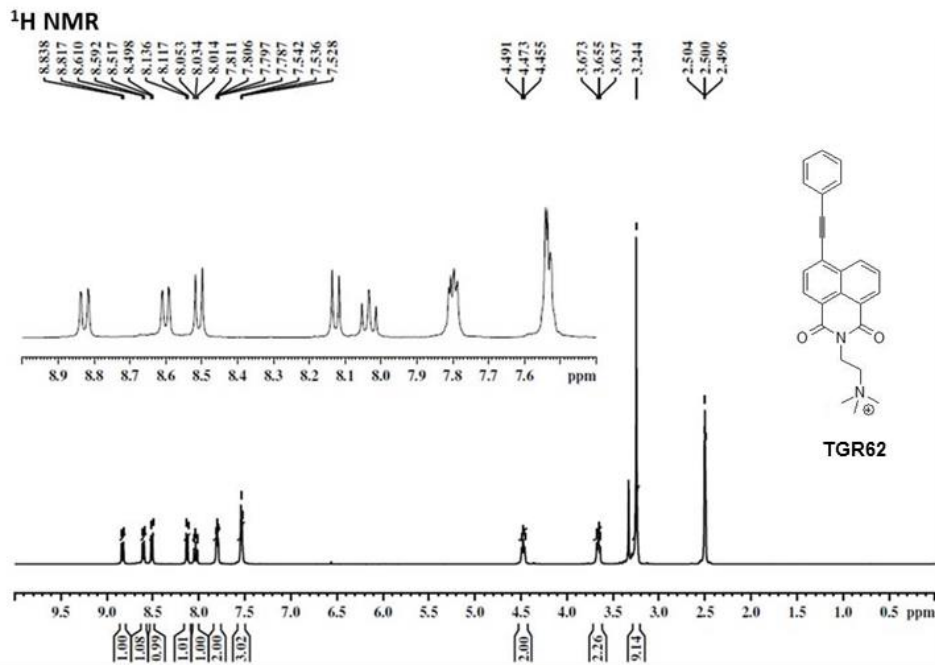
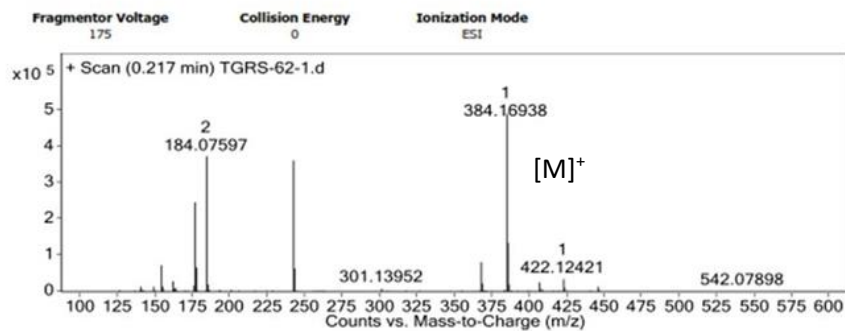


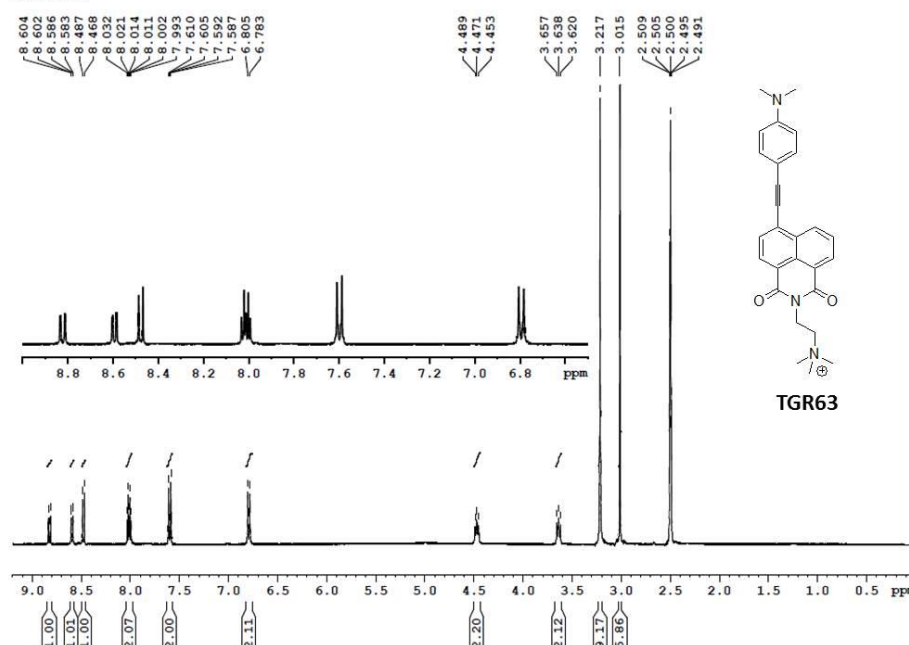
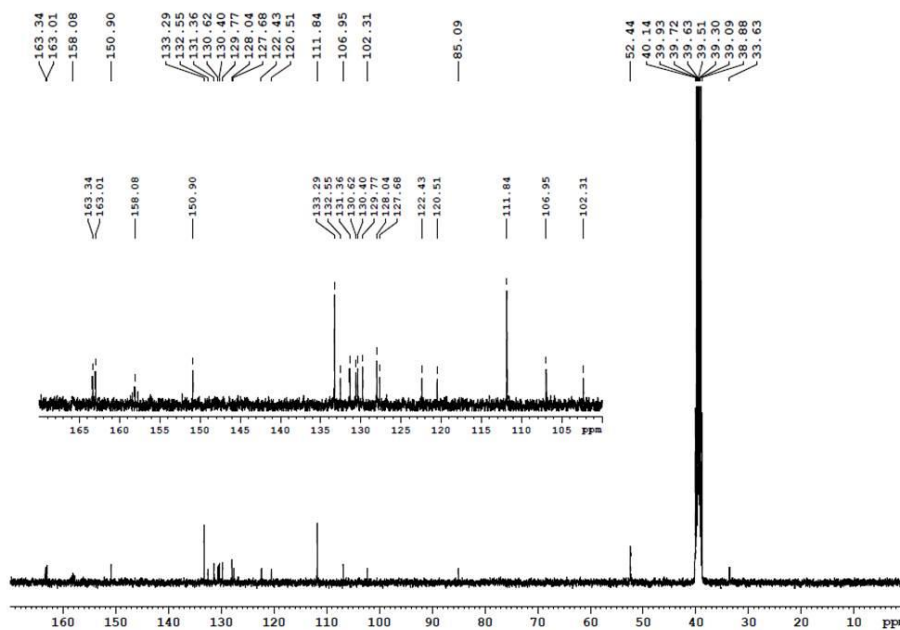
¹³C NMR



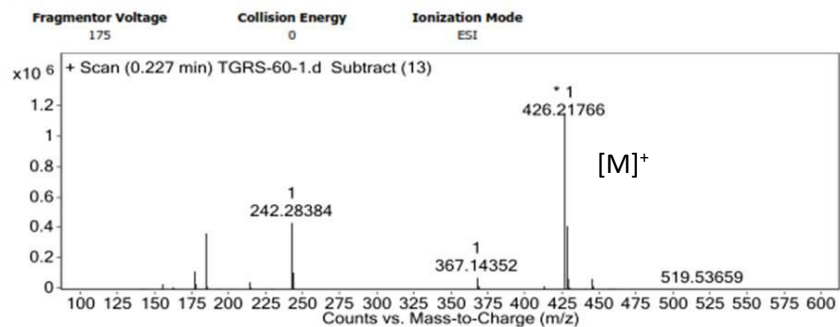
HRMS

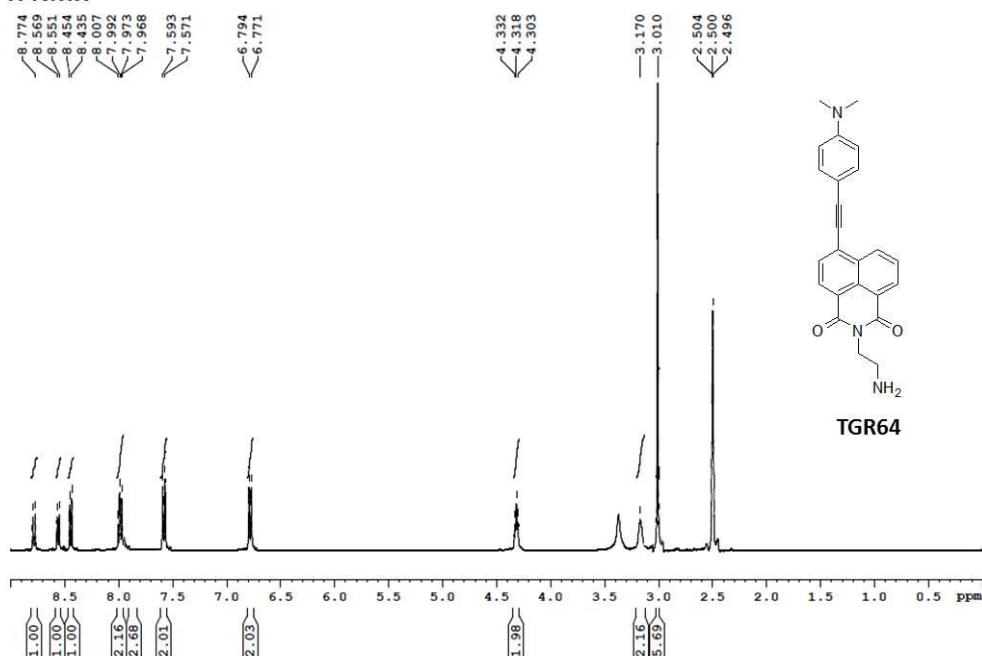
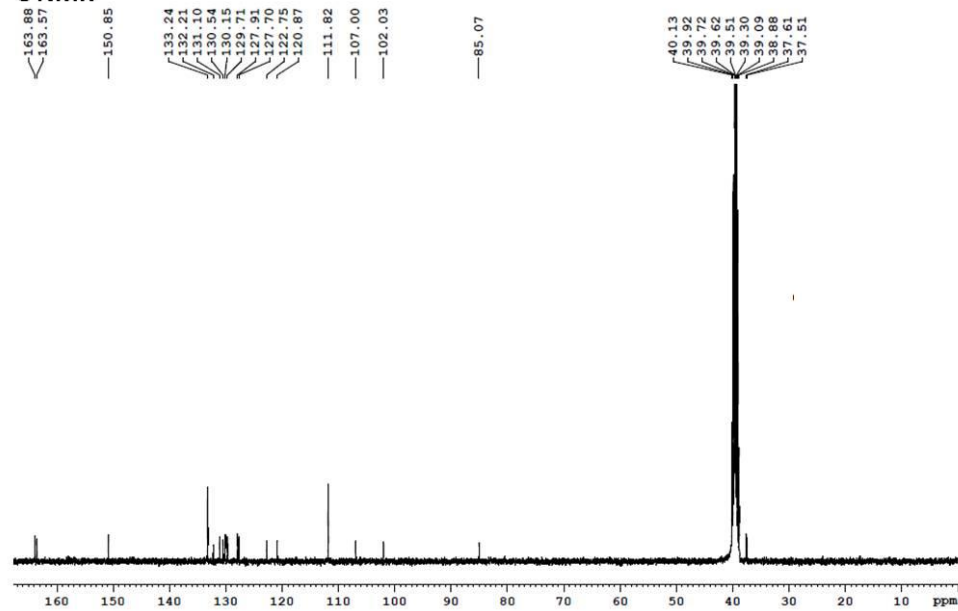


**HRMS**

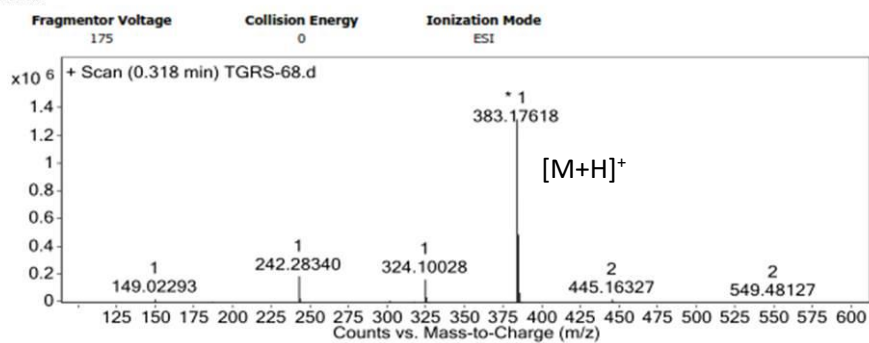
^1H NMR ^{13}C NMR

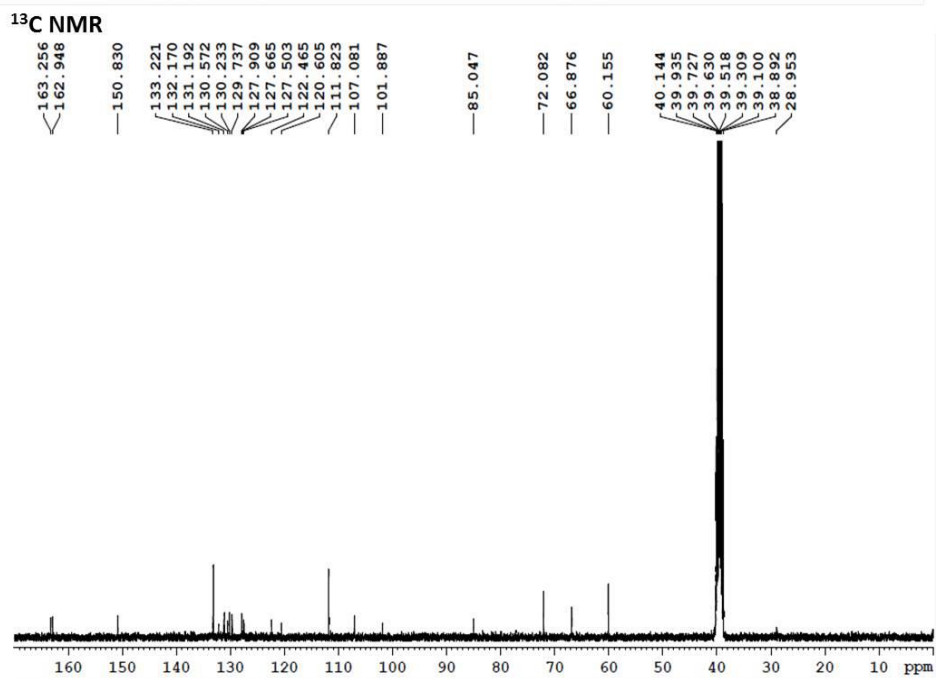
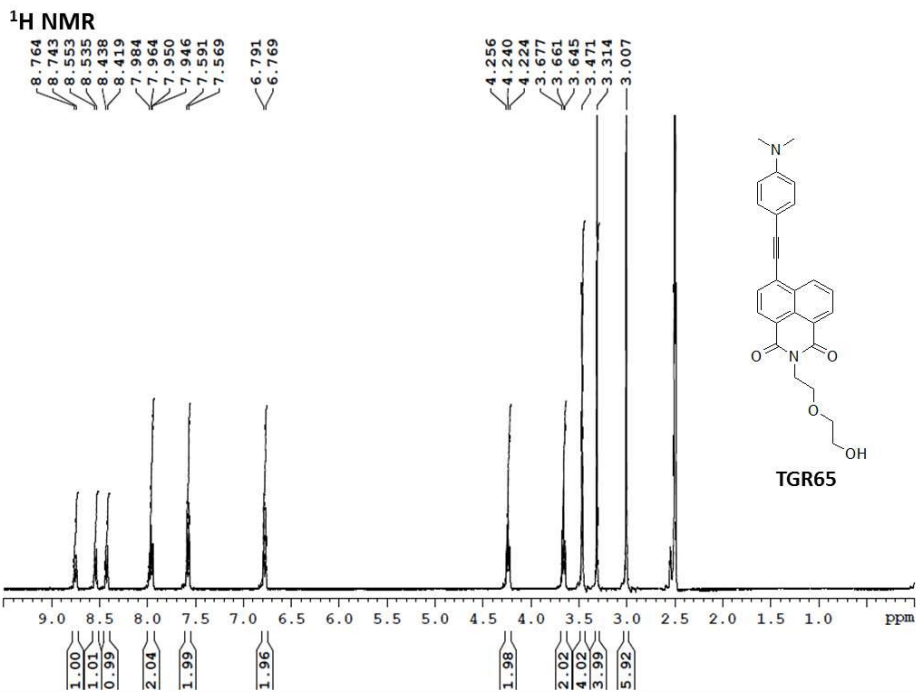
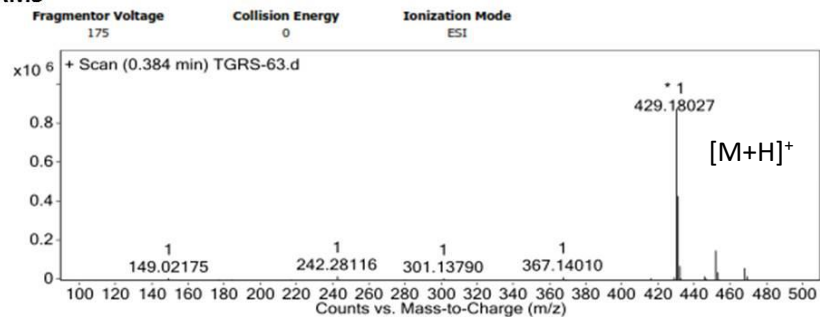
HRMS



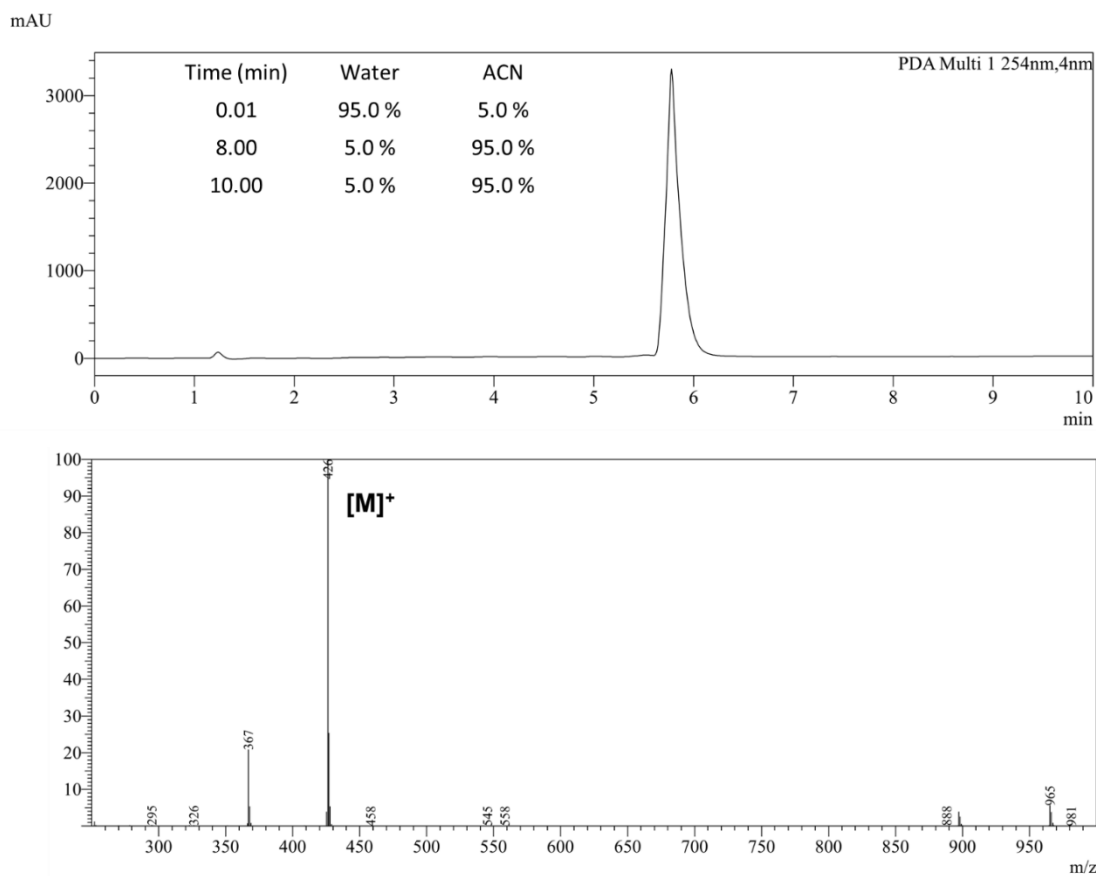
^1H NMR ^{13}C NMR

HRMS



**HRMS**

LCMS Characterization of TGR63



Statistical Analysis of Figure 19B

| 2way ANOVA | | A | B | C | D | E |
|------------|---------------------|----------------------|------------|-----------------|-------------------|------------|
| | | Data Set-A | Data Set-B | Data Set-C | Data Set-D | Data Set-E |
| | | Y | Y | Y | Y | Y |
| 1 | Table Analyzed | Data 1 | | | | |
| 2 | | | | | | |
| 3 | Two-way ANOVA | Ordinary | | | | |
| 4 | Alpha | 0.05 | | | | |
| 5 | | | | | | |
| 6 | Source of Variation | % of total variation | P value | P value summary | Significant? | |
| 7 | Interaction | 53.38 | < 0.0001 | **** | Yes | |
| 8 | Treatment | 5.121 | 0.0338 | * | Yes | |
| 9 | Group | 10.02 | 0.0040 | ** | Yes | |
| 10 | | | | | | |
| 11 | ANOVA table | SS | DF | MS | F (DFn, DFd) | P value |
| 12 | Interaction | 7.076e+006 | 1 | 7.076e+006 | F (1, 31) = 51.43 | P < 0.0001 |
| 13 | Treatment | 678802 | 1 | 678802 | F (1, 31) = 4.934 | P = 0.0338 |
| 14 | Group | 1.328e+006 | 1 | 1.328e+006 | F (1, 31) = 9.652 | P = 0.0040 |
| 15 | Residual | 4.265e+006 | 31 | 137588 | | |

Statically Analysis of Figure 19C

| 2way ANOVA Tabular results | | A | B | C | D | E |
|-------------------------------|---------------------|----------------------|------------|-----------------|--------------------|------------|
| | | Data Set-A | Data Set-B | Data Set-C | Data Set-D | Data Set-E |
| | | Y | Y | Y | Y | Y |
| 1 | Table Analyzed | Data 1 | | | | |
| 2 | | | | | | |
| 3 | Two-way ANOVA | Ordinary | | | | |
| 4 | Alpha | 0.05 | | | | |
| 5 | | | | | | |
| 6 | Source of Variation | % of total variation | P value | P value summary | Significant? | |
| 7 | Interaction | 25.83 | 0.0016 | ** | Yes | |
| 8 | Treatment | 2.623 | 0.2810 | ns | No | |
| 9 | Group | 1.756 | 0.3763 | ns | No | |
| 10 | | | | | | |
| 11 | ANOVA table | SS | DF | MS | F (DFn, DFd) | P value |
| 12 | Interaction | 662.0 | 1 | 662.0 | F (1, 32) = 11.84 | P = 0.0016 |
| 13 | Treatment | 67.22 | 1 | 67.22 | F (1, 32) = 1.203 | P = 0.2810 |
| 14 | Group | 45.00 | 1 | 45.00 | F (1, 32) = 0.8050 | P = 0.3763 |
| 15 | Residual | 1789 | 32 | 55.90 | | |

Statically Analysis of Figure 19D

| 2way ANOVA Tabular results | | A | B | C | D | E |
|-------------------------------|---------------------|----------------------|------------|-----------------|--------------------|------------|
| | | Data Set-A | Data Set-B | Data Set-C | Data Set-D | Data Set-E |
| | | Y | Y | Y | Y | Y |
| 1 | Table Analyzed | Data 1 | | | | |
| 2 | | | | | | |
| 3 | Two-way ANOVA | Ordinary | | | | |
| 4 | Alpha | 0.05 | | | | |
| 5 | | | | | | |
| 6 | Source of Variation | % of total variation | P value | P value summary | Significant? | |
| 7 | Interaction | 31.50 | 0.0004 | *** | Yes | |
| 8 | Row Factor | 2.167 | 0.3091 | ns | No | |
| 9 | Column Factor | 1.430 | 0.4074 | ns | No | |
| 10 | | | | | | |
| 11 | ANOVA table | SS | DF | MS | F (DFn, DFd) | P value |
| 12 | Interaction | 117065 | 1 | 117065 | F (1, 32) = 15.53 | P = 0.0004 |
| 13 | Row Factor | 8053 | 1 | 8053 | F (1, 32) = 1.068 | P = 0.3091 |
| 14 | Column Factor | 5314 | 1 | 5314 | F (1, 32) = 0.7049 | P = 0.4074 |
| 15 | Residual | 241219 | 32 | 7538 | | |

Statically Analysis of Figure 20B

| 2way ANOVA Tabular results | | A | B | C | D | E |
|-------------------------------|---------------------|----------------------|------------|-----------------|-------------------|------------|
| | | Data Set-A | Data Set-B | Data Set-C | Data Set-D | Data Set-E |
| | | Y | Y | Y | Y | Y |
| 1 | Table Analyzed | Data 1 | | | | |
| 2 | | | | | | |
| 3 | Two-way ANOVA | Ordinary | | | | |
| 4 | Alpha | 0.05 | | | | |
| 5 | | | | | | |
| 6 | Source of Variation | % of total variation | P value | P value summary | Significant? | |
| 7 | Interaction | 21.66 | < 0.0001 | **** | Yes | |
| 8 | Treatment | 22.53 | < 0.0001 | **** | Yes | |
| 9 | Group | 36.85 | < 0.0001 | **** | Yes | |
| 10 | | | | | | |
| 11 | ANOVA table | SS | DF | MS | F (DFn, DFd) | P value |
| 12 | Interaction | 4509 | 1 | 4509 | F (1, 30) = 29.34 | P < 0.0001 |
| 13 | Treatment | 4690 | 1 | 4690 | F (1, 30) = 30.52 | P < 0.0001 |
| 14 | Group | 7671 | 1 | 7671 | F (1, 30) = 49.92 | P < 0.0001 |
| 15 | Residual | 4610 | 30 | 153.7 | | |

Statically Analysis of Figure 20C

| 2way ANOVA Tabular results | | A | B | C | D | E |
|-------------------------------|---------------------|----------------------|------------|-----------------|-------------------|------------|
| | | Data Set-A | Data Set-B | Data Set-C | Data Set-D | Data Set-E |
| | | Y | Y | Y | Y | Y |
| 1 | Table Analyzed | Data 1 | | | | |
| 2 | | | | | | |
| 3 | Two-way ANOVA | Ordinary | | | | |
| 4 | Alpha | 0.05 | | | | |
| 5 | | | | | | |
| 6 | Source of Variation | % of total variation | P value | P value summary | Significant? | |
| 7 | Interaction | 14.67 | 0.0028 | ** | Yes | |
| 8 | Treatment | 16.94 | 0.0015 | ** | Yes | |
| 9 | Group | 29.43 | < 0.0001 | **** | Yes | |
| 10 | | | | | | |
| 11 | ANOVA table | SS | DF | MS | F (DFn, DFd) | P value |
| 12 | Interaction | 3672 | 1 | 3672 | F (1, 29) = 10.67 | P = 0.0028 |
| 13 | Treatment | 4240 | 1 | 4240 | F (1, 29) = 12.32 | P = 0.0015 |
| 14 | Group | 7368 | 1 | 7368 | F (1, 29) = 21.40 | P < 0.0001 |
| 15 | Residual | 9983 | 29 | 344.2 | | |

Statically Analysis of Figure 21B

| 2way ANOVA Tabular results | | A | B | C | D | E |
|-------------------------------|---------------------|----------------------|------------|-----------------|------------------------|------------|
| | | Data Set-A | Data Set-B | Data Set-C | Data Set-D | Data Set-E |
| | | Y | Y | Y | Y | Y |
| 1 | Table Analyzed | Data 1 | | | | |
| 2 | | | | | | |
| 3 | Two-way ANOVA | Ordinary | | | | |
| 4 | Alpha | 0.05 | | | | |
| 5 | | | | | | |
| 6 | Source of Variation | % of total variation | P value | P value summary | Significant? | |
| 7 | Interaction | 17.19 | < 0.0001 | **** | Yes | |
| 8 | Quadrant | 64.04 | < 0.0001 | **** | Yes | |
| 9 | Group | 8.490e-009 | > 0.9999 | ns | No | |
| 10 | | | | | | |
| 11 | ANOVA table | SS | DF | MS | F (DFn, DFd) | P value |
| 12 | Interaction | 7462 | 3 | 2487 | F (3, 68) = 16.15 | P < 0.0001 |
| 13 | Quadrant | 27799 | 1 | 27799 | F (1, 68) = 180.4 | P < 0.0001 |
| 14 | Group | 3.686e-006 | 3 | 1.229e-006 | F (3, 68) = 7.974e-009 | P > 0.9999 |
| 15 | Residual | 10476 | 68 | 154.1 | | |

Statically Analysis of Figure 22B

| 2way ANOVA Tabular results | | A | B | C | D | E |
|-------------------------------|---------------------|----------------------|------------|-----------------|-------------------|------------|
| | | Data Set-A | Data Set-B | Data Set-C | Data Set-D | Data Set-E |
| | | Y | Y | Y | Y | Y |
| 1 | Table Analyzed | Data 1 | | | | |
| 2 | | | | | | |
| 3 | Two-way ANOVA | Ordinary | | | | |
| 4 | Alpha | 0.05 | | | | |
| 5 | | | | | | |
| 6 | Source of Variation | % of total variation | P value | P value summary | Significant? | |
| 7 | Interaction | 16.28 | 0.0102 | * | Yes | |
| 8 | Treatment | 5.523 | 0.1220 | ns | No | |
| 9 | Group | 8.323 | 0.0599 | ns | No | |
| 10 | | | | | | |
| 11 | ANOVA table | SS | DF | MS | F (DFn, DFd) | P value |
| 12 | Interaction | 25.78 | 1 | 25.78 | F (1, 33) = 7.427 | P = 0.0102 |
| 13 | Treatment | 8.744 | 1 | 8.744 | F (1, 33) = 2.519 | P = 0.1220 |
| 14 | Group | 13.18 | 1 | 13.18 | F (1, 33) = 3.797 | P = 0.0599 |
| 15 | Residual | 114.5 | 33 | 3.471 | | |

3.11 REFERENCES

1. Alzheimer's Association, 2020 Alzheimer's disease facts and figures. *Alzheimers Dement* **2020**, doi: 10.1002/alz.12068.
2. Hardy, J.; Selkoe, D. J., The amyloid hypothesis of Alzheimer's disease: progress and problems on the road to therapeutics. *Science* **2002**, *297*, 353-356.
3. Knowles, T. P.; Vendruscolo, M.; Dobson, C. M., The amyloid state and its association with protein misfolding diseases. *Nat. Rev. Mol. Cell Biol.* **2014**, *15*, 384-396.
4. Sweet, R. A.; Nimgaonkar, V. L.; Devlin, B.; Jeste, D. V., Psychotic symptoms in Alzheimer disease: evidence for a distinct phenotype. *Mol. Psychiatry* **2003**, *8*, 383-392.
5. Rajasekhar, K.; Chakrabarti, M.; Govindaraju, T., Function and toxicity of amyloid beta and recent therapeutic interventions targeting amyloid beta in Alzheimer's disease. *Chem. Commun.* **2015**, *51*, 13434-13450.
6. Alzheimer's Association, 2018 Alzheimer's Disease Facts and Figures. *Alzheimers Dementia* **2018**, *14*, 701-701.
7. Jack, C. R., Jr.; Bennett, D. A.; Blennow, K.; Carrillo, M. C.; Dunn, B.; Haeberlein, S. B.; Holtzman, D. M.; Jagust, W.; Jessen, F.; Karlawish, J.; Liu, E.; Molinuevo, J. L.; Montine, T.; Phelps, C.; Rankin, K. P.; Rowe, C. C.; Scheltens, P.; Siemers, E.; Snyder, H. M.; Sperling, R.; Contributors, NIA-AA research framework: toward a biological definition of Alzheimer's disease. *Alzheimers Dement* **2018**, *14*, 535-562.
8. Rajasekhar, K.; Govindaraju, T., Current progress, challenges and future prospects of diagnostic and therapeutic interventions in Alzheimer's disease. *RSC Adv* **2018**, *8*, 23780-23804.
9. Huang, Y.; Mucke, L., Alzheimer mechanisms and therapeutic strategies. *Cell* **2012**, *148*, 1204-1222.
10. Yan, S. D.; Zhu, H.; Zhu, A.; Golabek, A.; Du, H.; Roher, A.; Yu, J.; Soto, C.; Schmidt, A. M.; Stern, D.; Kindy, M., Receptor-dependent cell stress and amyloid accumulation in systemic amyloidosis. *Nat. Med.* **2000**, *6*, 643-651.
11. Walsh, D. M.; Selkoe, D. J., Deciphering the molecular basis of memory failure in Alzheimer's disease. *Neuron* **2004**, *44*, 181-193.

12. Snyder, E. M.; Nong, Y.; Almeida, C. G.; Paul, S.; Moran, T.; Choi, E. Y.; Nairn, A. C.; Salter, M. W.; Lombroso, P. J.; Gouras, G. K.; Greengard, P., Regulation of NMDA receptor trafficking by amyloid-beta. *Nat. Neurosci.* **2005**, *8*, 1051-1058.
13. Bero, A. W.; Yan, P.; Roh, J. H.; Cirrito, J. R.; Stewart, F. R.; Raichle, M. E.; Lee, J. M.; Holtzman, D. M., Neuronal activity regulates the regional vulnerability to amyloid-beta deposition. *Nat. Neurosci.* **2011**, *14*, 750-756.
14. Selkoe, D. J., Early network dysfunction in Alzheimer's disease. *Science* **2019**, *365*, 540-541.
15. Watt, A. D.; Villemagne, V. L.; Barnham, K. J., Metals, membranes, and amyloid-beta oligomers: key pieces in the Alzheimer's disease puzzle? *J Alzheimers Dis.* **2013**, *33*, S283-93.
16. Samanta, S.; Govindaraju, T., Unambiguous detection of elevated levels of hypochlorous acid in double transgenic ad mouse brain. *ACS Chem. Neurosci.* **2019**, *10*, 4847-4853.
17. Laor, D.; Sade, D.; Shaham-Niv, S.; Zaguri, D.; Gartner, M.; Basavalingappa, V.; Raveh, A.; Pichinuk, E.; Engel, H.; Iwasaki, K.; Yamamoto, T.; Noothalapati, H.; Gazit, E., Fibril formation and therapeutic targeting of amyloid-like structures in a yeast model of adenine accumulation. *Nat. Commun.* **2019**, *10*, 62.
18. Rajasekhar, K.; Samanta, S.; Bagoband, V.; Murugan, N. A.; Govindaraju, T., Antioxidant berberine-derivative inhibits multifaceted amyloid toxicity. *iScience* **2020**, *23*, 101005.
19. Savelieff, M. G.; Nam, G.; Kang, J.; Lee, H. J.; Lee, M.; Lim, M. H., Development of multifunctional molecules as potential therapeutic candidates for Alzheimer's disease, Parkinson's disease, and amyotrophic lateral sclerosis in the last decade. *Chem. Rev.* **2019**, *119*, 1221-1322.
20. Samanta, S.; Rajasekhar, K.; Babagond, V.; Govindaraju, T., Small molecule inhibits metal-dependent and -independent multifaceted toxicity of Alzheimer's disease. *ACS Chem. Neurosci.* **2019**, *10*, 3611-3621.
21. Rajasekhar, K.; Madhu, C.; Govindaraju, T., Natural tripeptide-based inhibitor of multifaceted amyloid beta toxicity. *ACS Chem. Neurosci.* **2016**, *7*, 1300-1310.
22. Rajasekhar, K.; Mehta, K.; Govindaraju, T., Hybrid multifunctional modulators inhibit multifaceted abeta toxicity and prevent mitochondrial damage. *ACS Chem. Neurosci.* **2018**, *9*, 1432-1440.

23. Rajasekhar, K.; Suresh, S. N.; Manjithaya, R.; Govindaraju, T., Rationally designed peptidomimetic modulators of abeta toxicity in Alzheimer's disease. *Sci Rep* **2015**, *5*, 8139.
24. Crescenzi, O.; Tomaselli, S.; Guerrini, R.; Salvadori, S.; D'Ursi, A. M.; Temussi, P. A.; Picone, D., Solution structure of the Alzheimer amyloid beta-peptide (1-42) in an apolar microenvironment. Similarity with a virus fusion domain. *Eur. J. Biochem.* **2002**, *269* (22), 5642-5648.
25. Kuang, G.; Murugan, N. A.; Zhou, Y.; Nordberg, A.; Agren, H., Computational insight into the binding profile of the second-generation PET tracer PI2620 with tau fibrils. *ACS Chem. Neurosci.* **2020**, *11*, 900-908.
26. Liu, P.; Reed, M. N.; Kotilinek, L. A.; Grant, M. K.; Forster, C. L.; Qiang, W.; Shapiro, S. L.; Reichl, J. H.; Chiang, A. C.; Jankowsky, J. L.; Wilmot, C. M.; Cleary, J. P.; Zahs, K. R.; Ashe, K. H., Quaternary structure defines a large class of amyloid-beta oligomers neutralized by sequestration. *Cell Rep.* **2015**, *11*, 1760-1771.
27. Rushworth, J. V.; Hooper, N. M., Lipid Rafts: Linking Alzheimer's amyloid-beta production, aggregation, and toxicity at neuronal membranes. *Int. J Alzheimers Dis* **2010**, *2011*, 603052.
28. Cleary, J. P.; Walsh, D. M.; Hofmeister, J. J.; Shankar, G. M.; Kuskowski, M. A.; Selkoe, D. J.; Ashe, K. H., Natural oligomers of the amyloid-beta protein specifically disrupt cognitive function. *Nat. Neurosci.* **2005**, *8*, 79-84.
29. Sun, H.; Liu, J.; Li, S.; Zhou, L.; Wang, J.; Liu, L.; Lv, F.; Gu, Q.; Hu, B.; Ma, Y.; Wang, S., Reactive Amphiphilic conjugated polymers for inhibiting amyloid beta assembly. *Angew. Chem. Int. Ed. Engl.* **2019**, *58*, 5988-5993.
30. Li, L.; Cheung, T.; Chen, J.; Herrup, K., A comparative study of five mouse models of Alzheimer's disease: cell cycle events reveal new insights into neurons at risk for death. *Int J Alzheimers Dis* **2011**, *2011*, 171464.
31. Rajasekhar, K.; Narayanaswamy, N.; Murugan, N. A.; Viccaro, K.; Lee, H. G.; Shah, K.; Govindaraju, T., Abeta plaque-selective NIR fluorescence probe to differentiate Alzheimer's disease from tauopathies. *Biosens. Bioelectron.* **2017**, *98*, 54-61.

32. Reddy, P. H., Amyloid beta-induced glycogen synthase kinase 3beta phosphorylated VDAC1 in Alzheimer's disease: implications for synaptic dysfunction and neuronal damage. *Biochim. Biophys. Acta* **2013**, *1832*, 1913-1921.
33. Leger, M.; Quideville, A.; Bouet, V.; Haelewyn, B.; Boulouard, M.; Schumann-Bard, P.; Freret, T., Object recognition test in mice. *Nat. Protoc.* **2013**, *8*, 2531-2537.
34. Vorhees, C. V.; Williams, M. T., Morris water maze: procedures for assessing spatial and related forms of learning and memory. *Nat. Protoc.* **2006**, *1*, 848-858.
35. DeMattos, R. B.; Bales, K. R.; Cummins, D. J.; Dodart, J. C.; Paul, S. M.; Holtzman, D. M., Peripheral anti-A beta antibody alters CNS and plasma A beta clearance and decreases brain A beta burden in a mouse model of Alzheimer's disease. *Proc. Natl. Acad. Sci. U S A* **2001**, *98*, 8850-8855.
36. Rajasekhar, K.; Narayanaswamy, N.; Mishra, P.; Suresh, S. N.; Manjithaya, R.; Govindaraju, T., Synthesis of hybrid cyclic peptoids and identification of autophagy enhancer. *ChemPlusChem* **2014**, *79*, 25-30.
37. Kalita, S.; Kalita, S.; Paul, A.; Sarkar, A.; Mandal, B., Peptidomimetics prepared by tail-to-side chain one component peptide stapling inhibit Alzheimer's amyloid- β fibrillogenesis. *Chem. Sci.* **2020**, *11*, 4171-4179.
38. Vassar, R., BACE1 inhibitor drugs in clinical trials for Alzheimer's disease. *Alzheimers Res. Ther.* **2014**, *6*, 89.
39. Kumar, S.; Henning-Knechtel, A.; Magzoub, M.; Hamilton, A. D., Peptidomimetic-based multidomain targeting offers critical evaluation of A β structure and toxic function. *J. Am. Chem. Soc.* **2018**, *140*, 6562-6574.
40. Bourassa, M. W.; Miller, L. M., Metal imaging in neurodegenerative diseases. *Metallomics* **2012**, *4*, 721-738.
41. Li, S.; Hong, S.; Shepardson, N. E.; Walsh, D. M.; Shankar, G. M.; Selkoe, D., Soluble oligomers of amyloid Beta protein facilitate hippocampal long-term depression by disrupting neuronal glutamate uptake. *Neuron* **2009**, *62*, 788-801.
42. Hatai, J.; Motiei, L.; Margulies, D., Analyzing amyloid beta aggregates with a combinatorial fluorescent molecular sensor. *J. Am. Chem. Soc.* **2017**, *139*, 2136-2139.
43. Resnick, S. M.; Bilgel, M.; Moghekar, A.; An, Y.; Cai, Q.; Wang, M. C.; Thambisetty, M.; Prince, J. L.; Zhou, Y.; Soldan, A.; Wong, D. F.; O'Brien, R. J.; Ferrucci, L.; Albert,

- M. S., Changes in Abeta biomarkers and associations with APOE genotype in 2 longitudinal cohorts. *Neurobiol. Aging* **2015**, *36*, 2333-2339.
44. Svenningsson, A. L.; Stomrud, E.; Insel, P. S.; Mattsson, N.; Palmqvist, S.; Hansson, O., beta-amyloid pathology and hippocampal atrophy are independently associated with memory function in cognitively healthy elderly. *Sci Rep* **2019**, *9*, 11180.
45. Barnham, K. J.; Kenche, V. B.; Ciccotosto, G. D.; Smith, D. P.; Tew, D. J.; Liu, X.; Perez, K.; Cranston, G. A.; Johanssen, T. J.; Volitakis, I.; Bush, A. I.; Masters, C. L.; White, A. R.; Smith, J. P.; Cherny, R. A.; Cappai, R., Platinum-based inhibitors of amyloid-beta as therapeutic agents for Alzheimer's disease. *Proc. Natl. Acad. Sci U S A* **2008**, *105*, 6813-6818.
46. Kommaddi, R. P.; Das, D.; Karunakaran, S.; Nanguneri, S.; Bapat, D.; Ray, A.; Shaw, E.; Bennett, D. A.; Nair, D.; Ravindranath, V., Abeta mediates F-actin disassembly in dendritic spines leading to cognitive deficits in Alzheimer's disease. *J. Neurosci.* **2018**, *38*, 1085-1099.
47. Javed, I.; Peng, G.; Xing, Y.; Yu, T.; Zhao, M.; Kakinen, A.; Faridi, A.; Parish, C. L.; Ding, F.; Davis, T. P.; Ke, P. C.; Lin, S., Inhibition of amyloid beta toxicity in zebrafish with a chaperone-gold nanoparticle dual strategy. *Nat. Commun.* **2019**, *10*, 3780.
48. Nortley, R.; Korte, N.; Izquierdo, P.; Hirunpattarasilp, C.; Mishra, A.; Jaunmuktane, Z.; Kyrargyri, V.; Pfeiffer, T.; Khennouf, L.; Madry, C.; Gong, H.; Richard-Loendt, A.; Huang, W.; Saito, T.; Saido, T. C.; Brandner, S.; Sethi, H.; Attwell, D., Amyloid beta oligomers constrict human capillaries in Alzheimer's disease via signaling to pericytes. *Science* **2019**, *365*, 6450.
49. Zhang, F.; Gannon, M.; Chen, Y.; Yan, S.; Zhang, S.; Feng, W.; Tao, J.; Sha, B.; Liu, Z.; Saito, T.; Saido, T.; Keene, C. D.; Jiao, K.; Roberson, E. D.; Xu, H.; Wang, Q., beta-amyloid redirects norepinephrine signaling to activate the pathogenic GSK3beta/tau cascade. *Sci. Transl. Med.* **2020**, *12*, 526.
50. Bassil, F.; Brown, H. J.; Pattabhiraman, S.; Iwasyk, J. E.; Maghames, C. M.; Meymand, E. S.; Cox, T. O.; Riddle, D. M.; Zhang, B.; Trojanowski, J. Q.; Lee, V. M., Amyloid-beta (Abeta) plaques promote seeding and spreading of alpha-synuclein and tau in a mouse model of lewy body disorders with abeta pathology. *Neuron* **2020**, *105*, 260-275.

Chapter 4

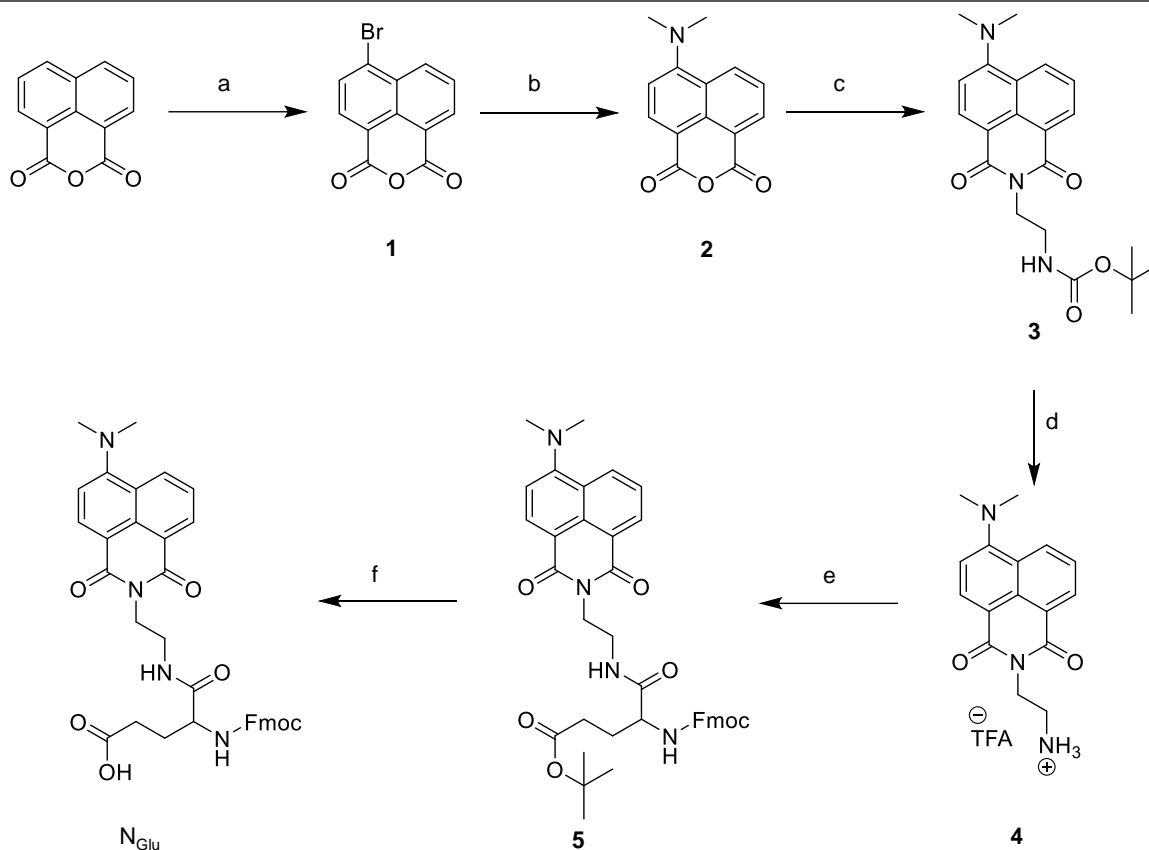
**Fluorescent Tripeptide to Probe Cu^{II}-induced
Amyloid Toxicity in Alzheimer's Disease**

Peptides and proteins are the most abundant biomacromolecules and perform most of functions in the living organisms. Undesirable aggregation of peptides/proteins exhibit cytotoxicity to cells.^{1,2} Especially, accumulation of toxic aggregates in the brain results in the progressive structural and functional loss of neurons leading to neurodegeneration.^{3,4} Many neurological diseases such as prion, AD, PD, and HD are associate with protein aggregation.⁵ Besides, the dyshomeostasis of biological metal ions is one of the detrimental factors to aggravate the protein aggregation and associated toxicity in various neurodegenerative disorders.^{2,6} The physiological metal ions are essential for the healthy functioning and survival of cells. However, the accumulation of excess metal ions and inclusion with peptides or proteins in the brain aggravates the disease progression.⁷ The preclinical and clinical results pointed to the possible involvement of copper (Cu), iron (Fe), zinc (Zn), and aluminum (Al) in the multifactorial AD development.^{8,9} In the brain, APP is cleaved by secretase enzymes (β and γ), which leads to the production of pathogenic A β peptides.¹⁰⁻¹² Cu^{II} plays a vital role in the expression and processing of the APP protein in the AD brain. The elevated level of copper in ATP-7A defective fibroblast cells derived from mouse/human has shown enhanced APP transcription, which triggers the A β production. A β misfolds into an ordered β -sheet structure that self-aggregates to form toxic oligomers, protofibrils and fibrils.¹³⁻¹⁵ The pathogenic A β contains unstructured N-terminal (D₁AEFRHDSGYEVHHQK₁₆), which does not participate in the β -sheet formation. This unstructured N-terminal interacts with the physiological metal ions, including Cu^{II}. Various studies have shown the involvement of histidine (His-6, His-13, and His-14), tyrosine (Tyr-10), and aspartic acid (Asp-1) residues in the formation of A β -Cu^{II} complex.¹⁶ The metal complexation accelerate the A β aggregation to produce highly toxic and stable polymorphic A β -metal species.^{2,16,17} These stable metal (Cu)-A β species are associated with membrane toxicity,

mitochondrial dysfunction and trigger various neurotoxic cascade processes.^{18,19} Specifically, the inclusion of redox-active Cu^{II} in A β species triggers the Fenton-type reaction to generate reactive intermediate species (RIS), which induce oxidative stress and inflammation.^{20,21} The generation of excessive RIS under AD conditions damage essential biomolecules like DNA and lipid, protein, contributing to additional level of toxicity and neuronal death.²²⁻²⁶ Under the oxidative stress conditions, Nrf, a nuclear transcription factor that governs the cellular process to adjust the redox imbalance by activating an array of genes associated with antioxidant proteins.²⁷ Besides lethal oxidative stress, the excess RIS promotes the neuroinflammation, a key contributor to the multifactorial AD toxicity.²⁵⁻²⁹ A detailed understanding of Cu-dependent and -independent A β aggregation species is essential to target amyloid toxicity. Recent evidences have revealed the distinction between the toxic nature of Cu-mediated and -free A β aggregation species. Here, we report our efforts in understanding the structural and functional (toxicity) variance of A β aggregation species in the absence and presence of Cu ions. We designed and synthesized a Cu-binding tripeptide based fluorescent probe (NTP), which sequesters Cu^{II} from the different A β -Cu^{II} species (oligomers and fibrils). This study established the suitability of NTP in sequestering Cu^{II} from A β species that demonstrates the distinct features of Cu-induced aggregation species including oligomers and fibrils with implication for the development of metal chelator-based therapeutic agents.^{27,30-35}

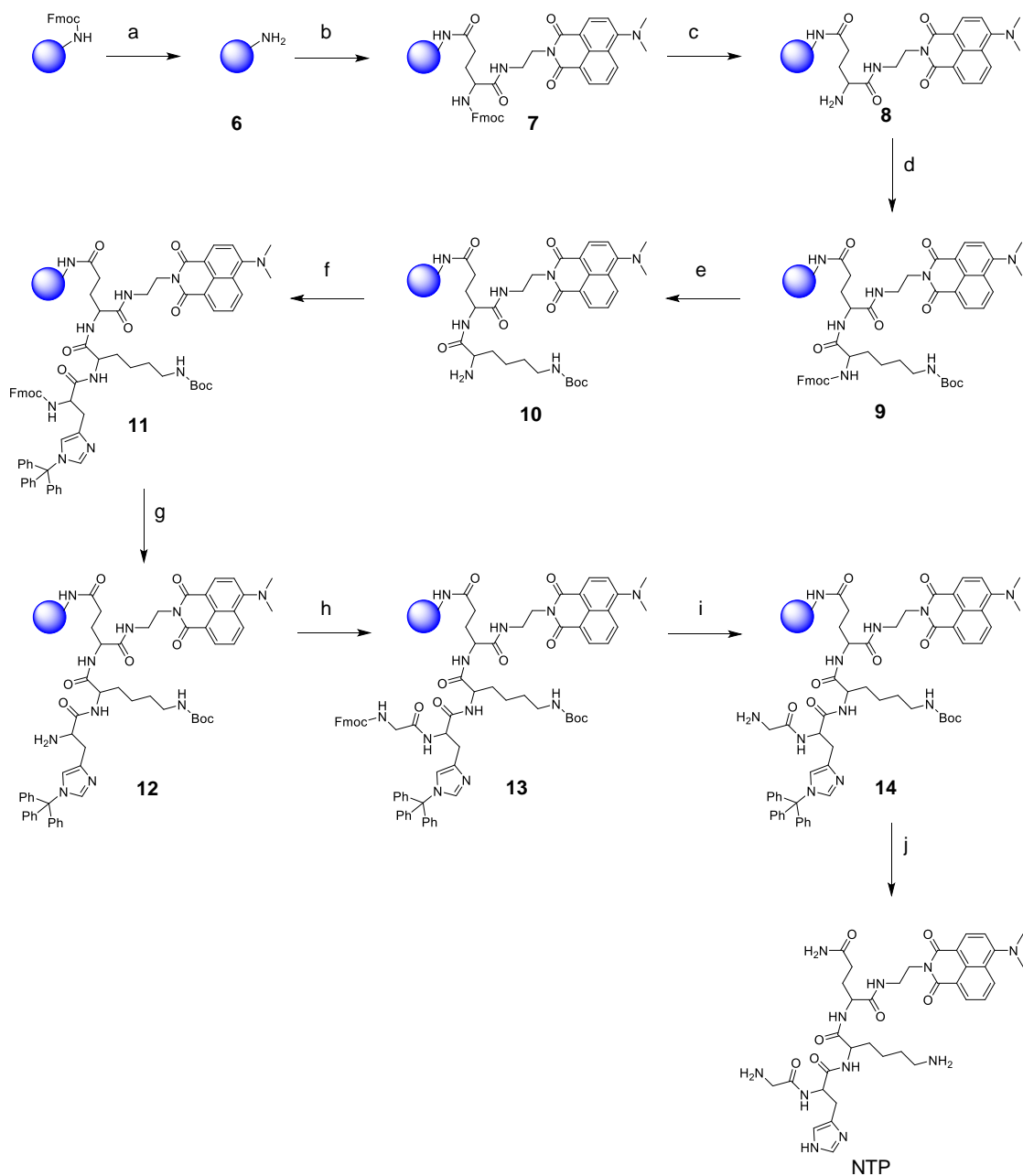
4.1 Design Strategy

The accumulation of Cu^{II} around the amyloid plaques demonstrates its possible role in exacerbating the plaques in the AD brain. The sequestration of Cu^{II} from the A β -Cu^{II} inclusion complex is one of the promising approaches to analyze the involvement of Cu^{II} in aggravating



Scheme 1. Synthesis of the fluorescent amino acid (N_{Glu}). a: Br_2 , KOH , heat (0-70 °C); b: $\text{HN}(\text{CH}_3)_2$, CuSO_4 , isopropanol, heat; c: Et_3N , $\text{Boc-NHCH}_2\text{CH}_2\text{NH}_2$, isopropanol, 90 °C; d: TFA , DCM ; e: $\text{Fmoc-Glu}(\text{O}^t\text{Bu})\text{-OH}$, HBTU , HOBt , DIPEA , DMF ; and f: TFA , DCM .

the $\text{A}\beta$ toxicity. We designed and synthesized a tripeptide based fluorescent probe (NTP) using solution- and solid-phase reactions starting from the easily available starting material, 1,8-naphthalene anhydride. Naphthalene anhydride was chemically modified into a fluorescent amino acid (N_{Glu}) and coupled to a well-known Cu binding glycine-histidine-lysine (GHK) tripeptide. The N-terminal glycine and histidine residues of GHK are mostly involved in Cu chelation, while C-terminal lysine remains free in the Cu-GHK complex. We conjugated N_{Glu} at the C-terminal of GHK to avoid any direct interference in Cu chelation (Scheme 1 and 2).



Scheme 2. Synthesis of fluorescent-labelled tripeptide (NTP). a: DCM, DMF, Pip (20%); b: NTP, HBTU, HOBT, DIPEA, DMF; c: DMF, Pip (20%); d: Fmoc-Lys(Boc)-OH, HBTU, HOBT, DIPEA, DMF; e: DMF, Pip (20%); f: Fmoc-His(trt)-OH, HBTU, HOBT, DIPEA, DMF; g: DMF, Pip (20%); h: Fmoc-Gly-OH, HBTU, HOBT, DIPEA, DMF; i: DMF, Pip (20%); and j: DCM, TFA.

4.2 Synthesis of NTP

NTP was synthesized in two parts (i) synthesis of N_{Glu} in the solution phase and (ii) synthesis of Cu binding peptide through the solid phase protocols (Scheme 2). Naphthalene anhydride was heated (0-70 °C) with bromine and potassium hydroxide for 20 h to obtain bromo- substituted naphthalene anhydride (**1**). The non-fluorescent intermediate **1** was converted to a fluorescent intermediate (**2**) by substituting bromine atom with dimethylamine (HN(CH₃)₂) in the presence of copper sulfate (CuSO₄). The intermediate **2** was reacted with Boc-protected ethylenediamine (Boc-NHCH₂CH₂NH₂) under basic conditions (triethylamine; Et₃N) in isopropanol (IPA) at 90 °C for 15 h to obtain naphthalene monoimide derivative (**3**). The Boc group was deprotected using trifluoroacetic acid (TFA) to obtain **4**, which further coupled with Fmoc-Glu(O^tBu)-OH in the presence of diisopropylethylamine (DIPEA), tetramethyl-O-(1H-benzotriazol-1-yl)uronium hexafluorophosphate (HBTU), and hydroxy benzotriazole (HOBt) in dimethylformamide (DMF) to obtain **5**. Finally, intermediate **5** was treated with TFA in dichloromethane (DCM) to obtain N_{Glu}, ready for the solid-phase synthesis of NTP.

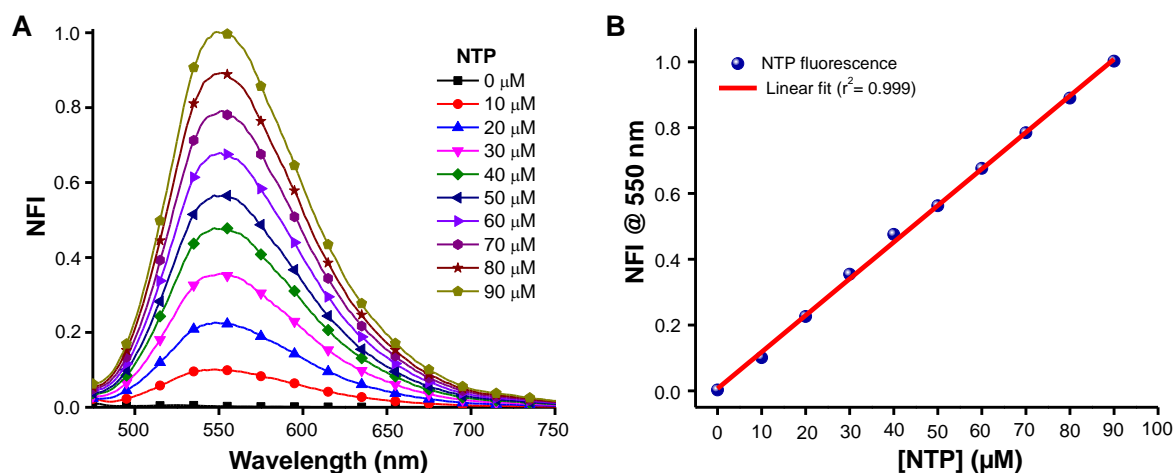


Figure 1. The fluorescence emission study of NTP in PBS buffer (10 mM, pH= 7.4). (A) The fluorescence spectra of NTP upon excitation at 450 nm. (B) The plot of fluorescent intensity at 550 nm ($\lambda_{\text{ex}}= 450$ nm) with increasing concentrations of NTP. NFI: Normalized fluorescence intensity.

In the solid phase synthesis, resin beads were washed (DCM and DMF) and treated with piperidine (20 % in DMF) to deprotect the surface amine group (**6**). N_{Glu} was coupled to the resin using HBTU, HOBt, and DIPEA in DMF to obtain intermediate **7**. The formation of **7** was confirmed using the Kaiser test and treated with piperidine (20 % in DMF) to obtain the free amine of N_{Glu} unit (**8**). Next, intermediate **8** was coupled with Fmoc-Lys(Boc)-OH to obtain **9**, which was further deprotected (**10**) and coupled with Fmoc-His(trt)-OH to obtain intermediate **11**. Finally, Fmoc-Gly-OH was coupled to **11** to yield **12**, which was treated with piperidine followed by TFA to obtain NTP. The synthesized NTP was purified and characterized using NMR, HPLC and HRMS.

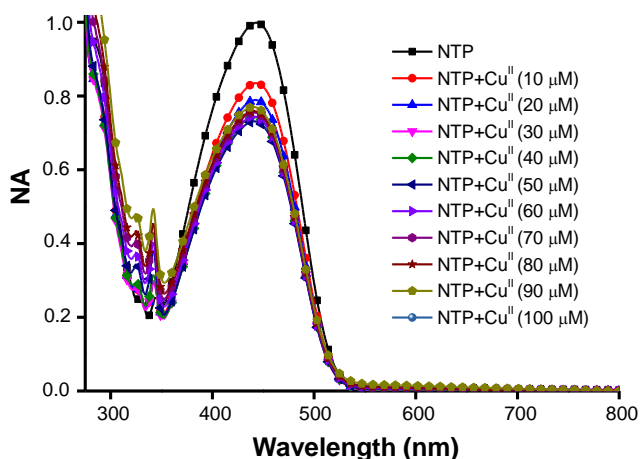


Figure 2. The absorbance spectra of NTP (50 μM) and increasing concentrations of Cu^{II} (10-100 μM). NA: Normalized absorbance.

4.3 Cu^{II} Chelation by NTP

We evaluated the Cu^{II} chelation ability of NTP through spectroscopy and MALDI mass analysis. The absorption study showed that NTP has a strong absorption band in the visible region ($\lambda_{\text{max}}=445$ nm) that indicates the presence of N_{Glu} moiety (Figure 1). The addition of increasing concentration of Cu^{II} (10-100 μM) to a homogeneous solution of NTP (50 μM) decreased the

absorbance maxima of NTP at 445 nm (Figure 2), which indicates the interacts among Cu^{II} and NTP. As designed, NTP shows a strong emission band in the green region with the $\lambda_{\text{max}} = 550$ nm upon excitation at 445 nm. Interestingly, the addition of Cu^{II} to the homogeneous solution of NTP significantly decreased NTP emission intensity in a concentration-dependent manner (Figure 3). The change in the fluorescent intensity of NTP in the presence of Cu^{II} displayed the formation of the NTP- Cu^{II} complex in a 1:1 stoichiometric ratio. The MALDI mass analysis further validated the Cu^{II} chelation by NTP. NTP was incubated with Cu^{II} in a 1:5 stoichiometric ratio for 2 h at 37 °C, and MALDI mass analysis was performed using the α -cyano-4-hydroxycinnamic acid (CCA) matrix (Figure 4). The MALDI analysis of NTP using the CCA matrix showed the presence of $[\text{M}+\text{H}]^+$ and $[\text{M}+\text{Na}]^+$ peaks at 734.55 and 756.56, respectively, confirmed the presence of NTP (Figure 4A). The presence of $[\text{M}+\text{Cu}]^+$ peak at 797.55 confirmed

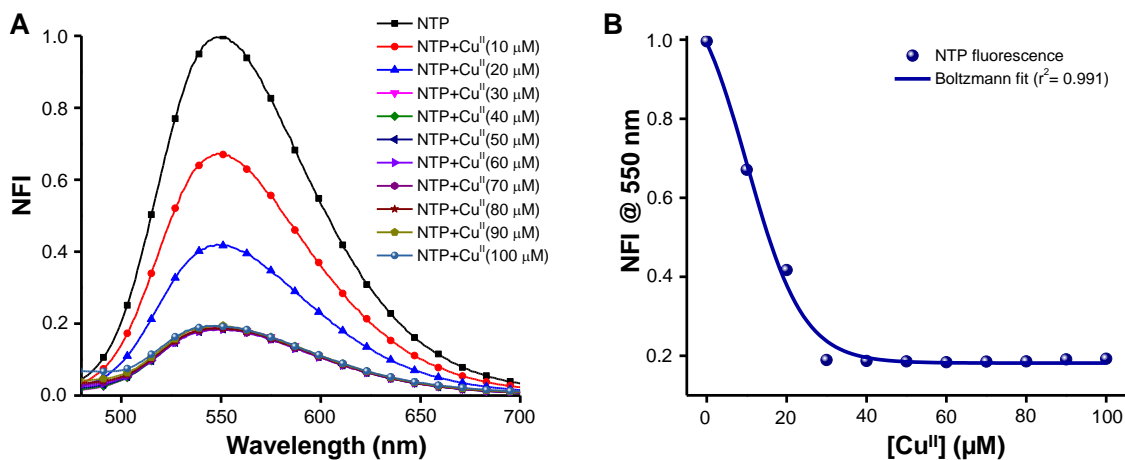


Figure 3. (A) The fluorescence spectra of NTP (50 μM) and with the increasing concentrations of Cu^{II} (10-100 μM) upon excitation at 450 nm. (B) The plot of the fluorescent intensity of NTP (50 μM) at 550 nm ($\lambda_{\text{ex}} = 450$ nm) with increasing concentrations of Cu^{II} .

the NTP- Cu^{II} complex formation in a 1:1 stoichiometric ratio. However, a trace amount of NTP- Cu^{II} complex in a 1:2 stoichiometric ratio was also observed in the MALDI analysis, as

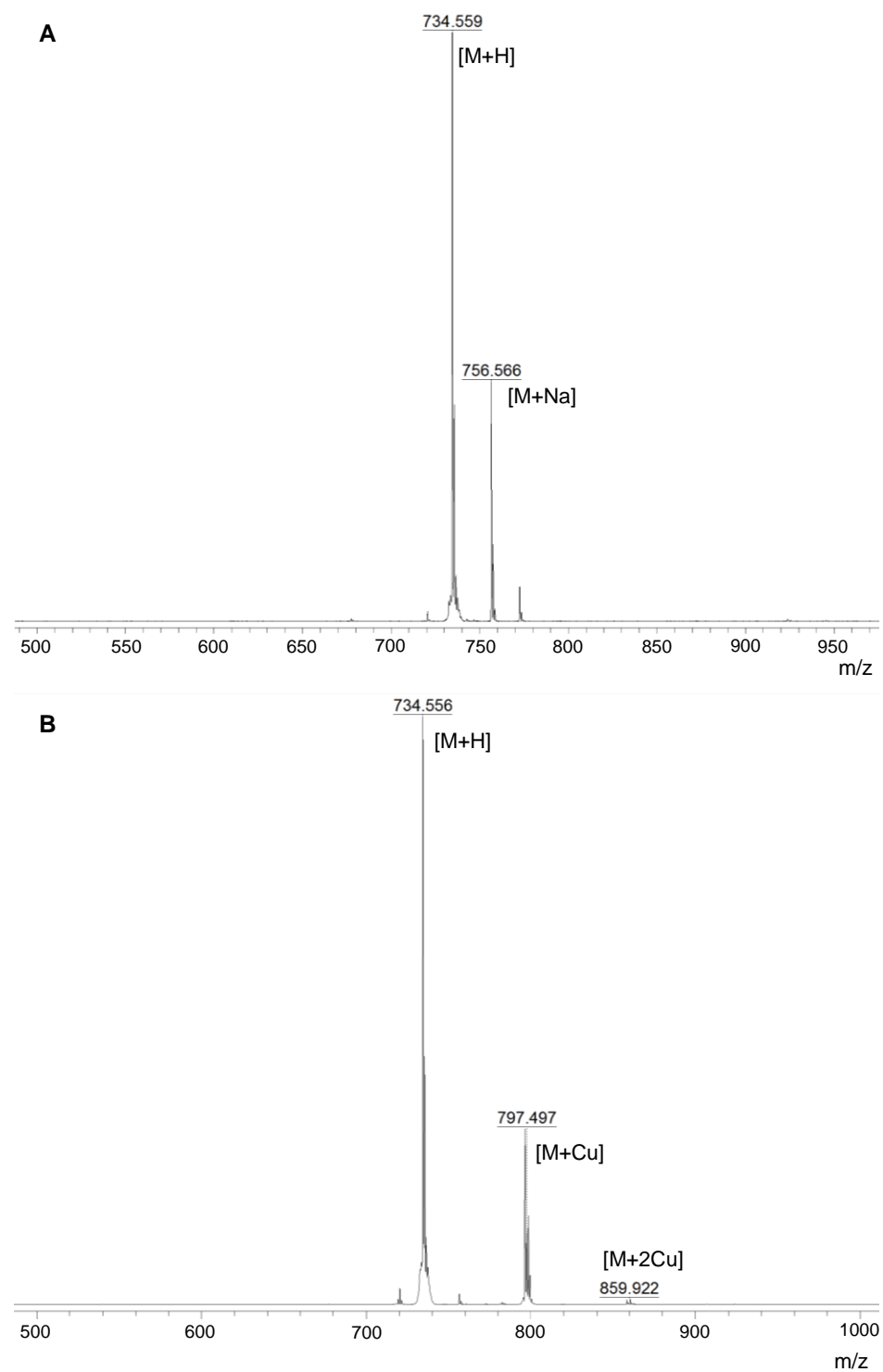


Figure 4. MALDI analysis of NTP and NTP-Cu complexation. **(A)** The presence of $[M]^+$ and $[M+Na]^+$ mass peaks at 734.55 and 756.56, respectively, confirmed the presence of NTP. **(B)** The presence of $[M]^+$ mass peaks at 797.49 and 859.92 confirmed the formation of the NTP-Cu complex in 1:1 and 1:2 stoichiometric ratio, respectively.

confirmed by the presence of $[M+2Cu]^+$ mass peak at 859.92 (Figure 4B). Next, we performed the fluorescent study of N_{Glu} in the presence of Cu^{II} to understand the NTP- Cu^{II} complex formation. The fluorescent emission spectra in Figure 5 demonstrated that Cu^{II} does not affect the fluorescent property of N_{Glu} moiety. These results from various spectroscopy and mass analysis are in good agreement to establish NTP as an excellent fluorescence probe for Cu^{II} chelation.

4.4 The Selectivity of NTP Towards Cu^{II}

Experimental evidences have shown the role of various metal ions (Cu^{II} , Zn^{II} , Fe^{III} , and Al^{III}) in AD pathogenesis. These metal ions interact and complex with $A\beta$ that modulate the amyloid toxicity.^{16,22-25,36} Therefore, the selective sequestration of metal ions from the $A\beta$ -Cu inclusion species is anticipated to help in assessing their role in amyloid toxicity. The detailed photophysical investigation demonstrated the selective Cu^{II} sequestration by NTP in the presence of other metal ions. In this context, the homogeneous solution of NTP (50 μ M) was treated with Cu^{II} , Zn^{II} , Fe^{III} , and Al^{III} , independently, in a 1:1 stoichiometric ratio, and the fluorescent emission at $\lambda_{ex}= 445$ nm (NTP) was recorded. As shown in Figure 5B, NTP fluorescence reduced selectively in the presence of Cu^{II} , while other metal ions do not affect the NTP fluorescence at 550 nm. This result confirmed our design strategy, the selective complexation of Cu^{II} by NTP in the presence of other metal ions. Next, we evaluate the formation of NTP- Cu^{II} complex in the presence of other metal ions (Figure 6). For this assessment, we prepared a homogeneous solution (25 μ M) of four metal ions (Cu^{II} , Zn^{II} , Fe^{III} , and Al^{III}) and NTP was added in increasing concentrations (0-100 μ M). The fluorescence intensity linearly increased with the increasing concentration of NTP in the absence of Cu^{II} . As expected, the increase of fluorescence at 545 nm in the presence of Cu^{II} is significantly low with the increasing concentrations of NTP, which

indicates the NTP-Cu^{II} complex formation. Interestingly, a similar NTP fluorescence encasement pattern was observed when NTP was added to the homogeneous solution containing a mixture of Cu^{II}, Zn^{II}, Fe^{III}, and Al^{III}. Overall, the spectroscopy results are in excellent agreement and establish the suitability of NTP for assessing Cu^{II}-mediated amyloid toxicity.

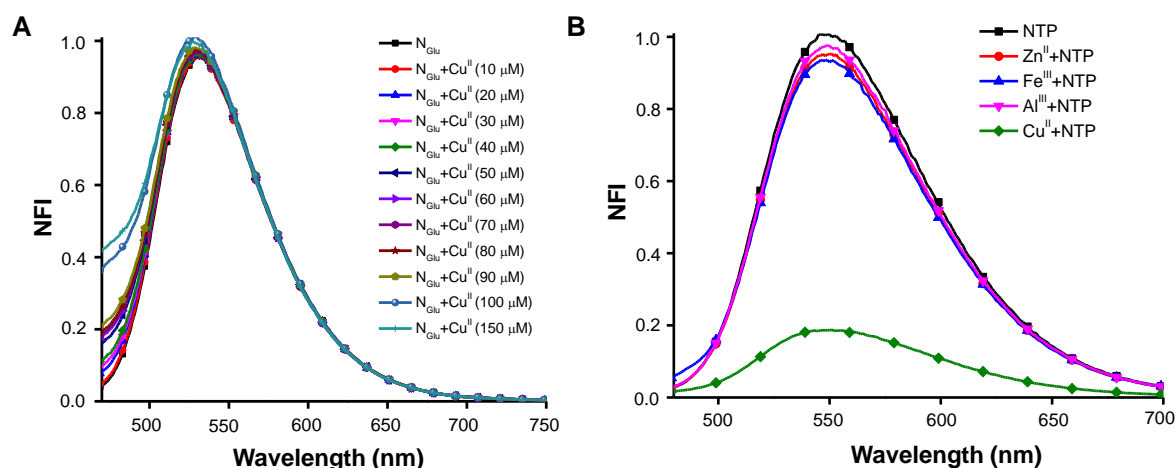


Figure 5. (A) The fluorescence spectra of N_{Glu} (50 μM) and with the increasing concentrations of Cu^{II} (10-100 μM). (B) The fluorescence spectra of only NTP (50 μM) and in the presence of Zn^{II}, Fe^{III}, Al^{III}, and Cu^{II} (50 μM) upon excitation in 450 nm.

4.5 Structural Assessment of Amyloid Species

Before performing the Cu^{II} sequestration study from Cu^{II}-mediated aggregation species, we have confirmed the formation of Aβ oligomers and fibrils using atomic force microscopy (AFM) analysis (Figure 7). Aβ aggregation species were freshly prepared for the AFM analysis. Aβ₄₂ (25 μM) was incubated (48 h) in PBS buffer (pH= 7.4, 10 mM) at 4 °C and 37 °C to form oligomers and fibrils, respectively. The samples were then spotted and air-dried on the mica surface, and the AFM images were acquired using scan assisted mode. The obtained AFM images displayed the uniformly distributed spherical oligomeric species and highly intertwined fibrillar assembly, respectively. Similarly, Aβ₄₂ (10 μM) and Cu^{II} (10 μM) was incubated (48 h)

in PBS (pH= 7.4, 10 mM) at 4 °C and 37 °C to prepare oligomers and fibrils, respectively, and the images were acquired. Cu^{II}-mediated A β 42 oligomers sample showed random small aggregates, which are completely different from Cu-free oligomers. However, it was also observed that the Cu^{II}-mediated A β 42 fibrillar sample exhibit a more complex fibrillar network than Cu-free fibrils. We believe this structural difference has a direct impact on their neuronal toxicity. Next, we performed Cu^{II} sequestration assay using NTP to understand the differential toxicity of various amyloid aggregation species.

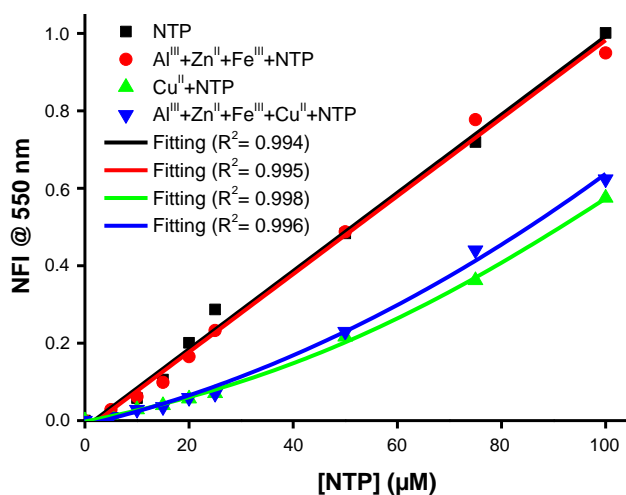


Figure 6. The plot of fluorescent intensity of NTP at 550 nm ($\lambda_{\text{ex}}= 450$ nm) with increasing concentrations in PBS buffer (black), in the presence of Zn^{II}, Fe^{III}, and Al^{III} (red), Cu^{II} (green), and Zn^{II}, Fe^{III}, Al^{III}, and Cu^{II}, respectively.

4.6 Sequestration of Cu^{II} from A β Aggregation Species

As discussed earlier, amyloid toxicity is aggravated in the presence of Cu^{II}. It has been established that the Cu^{II}-mediated aggregation of pathogenic amyloid peptides (mainly A β 42) follows different kinetics compare to Cu^{II} free conditions.^{2,6} The sequestration of Cu^{II} from A β -Cu^{II} aggregation species (oligomers and fibrils) could help assess the role of Cu^{II} in amyloid

toxicity.³⁷⁻³⁹ We evaluated the Cu^{II} sequestering ability of NTP from Cu^{II}-dependent A β oligomers and fibrils through fluorescence assay. For the experiment, we prepared A β oligomers and fibrils in the absence and presence of Cu^{II} with a 1:1 stoichiometric ratio. The freshly prepared Cu^{II}-dependent A β aggregation species (25 μ M) were treated with NTP (25 μ M), and its fluorescence (λ_{ex} = 445 nm, λ_{em} = 545 nm) was measured. The NTP fluorescence intensity significantly decreased in the sample containing Cu^{II}, which validates the NTP-Cu^{II} complex formation (Figure 8A). A detailed analysis established that the hydrophobic environment

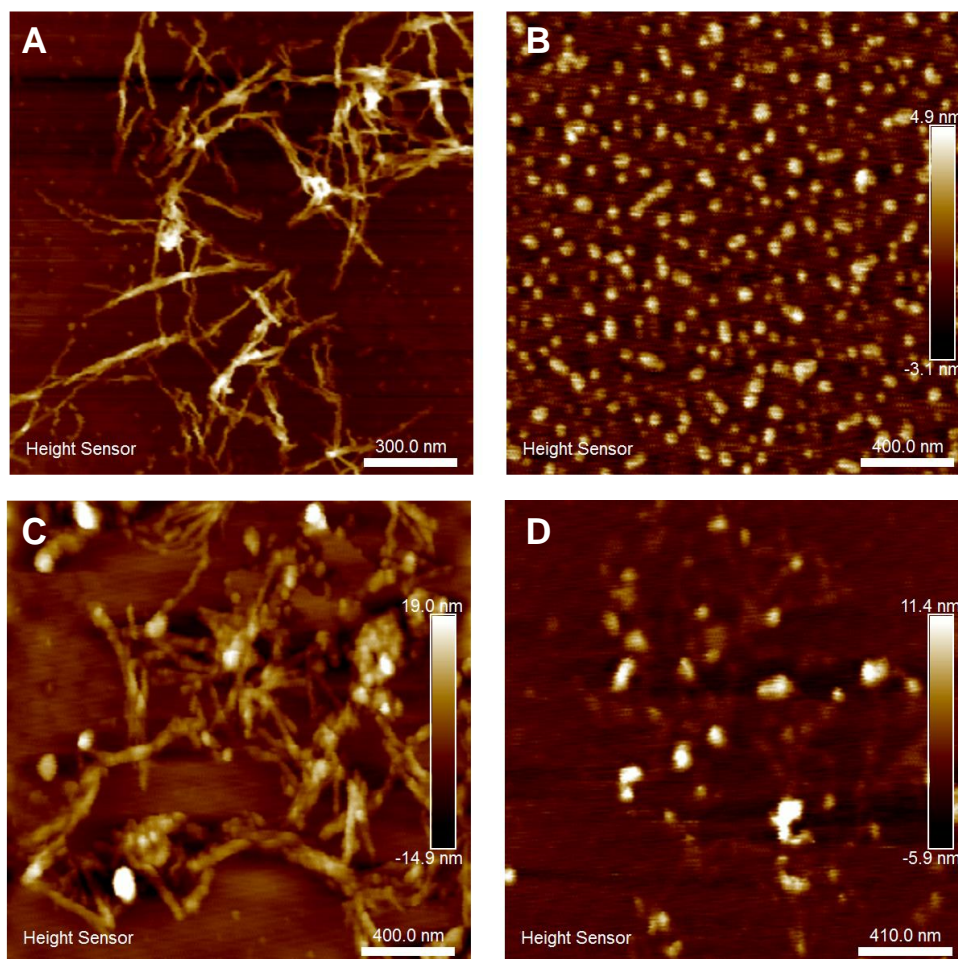


Figure 7. The visualization A β 42 (10 μ M) aggregation species using atomic force microscopy (AFM) in the absence and presence of Cu^{II} (10 μ M). **A:** A β 42 fibrils, **B:** A β 42 oligomers, **C:** A β 42-Cu^{II} fibrils, and **D:** A β 42-Cu^{II} oligomers.

enhances the fluorescence of the probe.^{37,39} Interestingly, NTP treated A β aggregation species exhibited a significant increase in fluorescence emission at 545 nm compared to the control sample (only NTP). Interestingly, the fluorescence signal of Cu^{II}-mediated oligomer and fibril samples displayed differential features, of which NTP efficiently sequester Cu^{II} from A β fibrils than oligomers (Figure 8A). This result suggested the fact that the association constant and

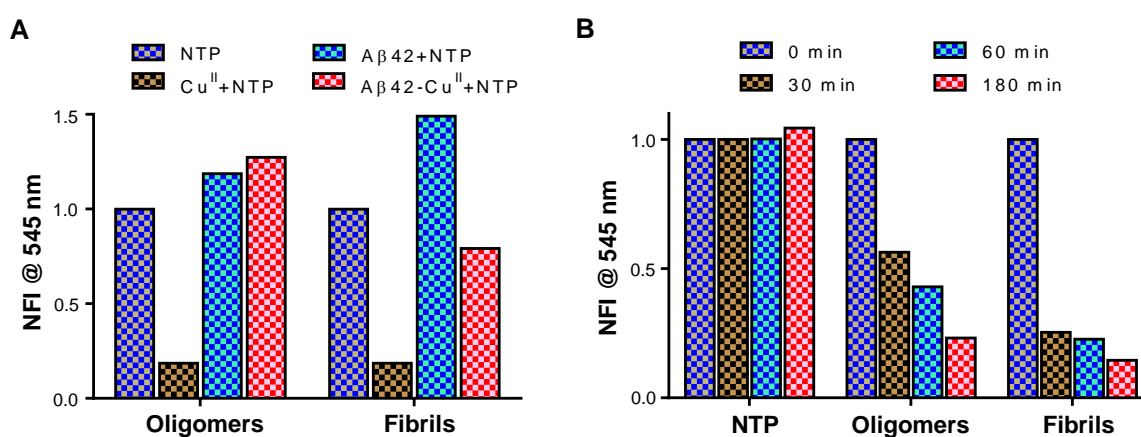


Figure 8. (A) The plot of the fluorescent intensity of NTP (25 μ M) at 545 nm (λ_{ex} = 450 nm) upon instant addition of Cu^{II} (25 μ M), A β 42 oligomers (25 μ M), A β 42-Cu^{II} oligomers (1:1, 25 μ M), A β 42 fibrils (25 μ M), and A β 42-Cu^{II} fibrils (1:1, 25 μ M). (B) The plot of the fluorescent intensity of NTP (25 μ M) at 545 nm (λ_{ex} = 450 nm) in the presence of Cu^{II} (25 μ M), A β 42 oligomers (25 μ M), A β 42-Cu^{II} oligomers (1:1, 25 μ M), A β 42 fibrils (25 μ M), and A β 42-Cu^{II} fibrils (1:1, 25 μ M) at different time points (0, 30, 60, and 180 min).

microenvironment of Cu^{II} in various aggregation species might be different. Next, we performed kinetics of Cu^{II} sequestration by NTP from Cu^{II}-dependent A β oligomers and fibrils for strengthening our observation (Figure 8B). NTP was allowed to sequester Cu^{II} from A β -Cu^{II} inclusion complex for 3 h, and NTP fluorescence was measured at different time points (0, 30, 60, and 180 min). As shown in Figure 8B, NTP fluorescence emission at 545 nm remains

unaffected in the control sample (PBS). As expected, NTP fluorescence emission at 545 nm decreases with time for A β -Cu^{II} oligomers and fibrillar samples (Figure 8B). Interestingly, the sequestration kinetics revealed that NTP can sequester Cu^{II} faster from A β -Cu^{II} fibrils than A β -Cu^{II} oligomers. This distinct nature of A β -Cu^{II} species is a key player for the differential A β -Cu^{II} toxicity, which needs to be further validated using cellular AD models.

4.7 Conclusion

The misfolding and aggregation of A β plays an important role in AD development. The presence of Cu with A β accelerates amyloid aggregation and aggravates the associated toxicity that leads to multifactorial AD. Cu has a significant influence on A β aggregation kinetics, which is responsible for producing stable oligomers. Moreover, the redox-active nature of Cu remains intact in the A β -Cu complex, which is the leading cause of excess ROS production, followed by oxidative stress and inflammation. Herein, we attempted to understand the differential toxicity of A β aggregation species in the presence and absence of Cu. We designed and synthesized tripeptide based fluorescent probe, NTP, which sequester Cu^{II} from A β -Cu^{II} species. Our results demonstrated the differential microenvironment of Cu^{II} in A β oligomers and matured fibrils. The detailed structural analyses of all A β aggregation species in the presence and absence of Cu are in good agreement with their toxicity profiles.

4.8 Experimental Methods

4.9.1 General Methods

All the chemicals and solvents were obtained from Merck. Ar/N₂ atmosphere was maintained for moisture-sensitive solution-phase reactions. The absorption and fluorescence measurements are

performed using Agilent Cary series UV–Vis-NIR absorption, Agilent Cary eclipse fluorescence spectrophotometers or microplate reader, respectively. NMR (^1H and ^{13}C) experiments were performed using Bruker AV–400 spectrometer with tetramethylsilane as an internal standard. HRMS data were recorded on Agilent 6538 UHD HRMS/Q-TOF high-resolution spectrometer. The stock solutions of NTP was prepared by dissolving the calculated amount of corresponding solids in deionized Milli-Q water and stored at $-20\text{ }^\circ\text{C}$. The stock sample was diluted in the same deionized Milli-Q water for the experiments. Cu^{II} , Zn^{II} , Al^{III} and Fe^{III} samples were obtained by dissolving the calculated amount of copper sulfate (CuSO_4), zinc chloride (ZnCl_2), aluminum sulfate ($\text{Al}_2(\text{SO}_4)_3$), and ferric chloride (FeCl_3) in deionized Milli Q water, respectively. A β 42 (Cat: PP69- 0.25 MG) peptide was obtained from Merck, and a freshly prepared amyloid peptide solution was used for all the experiments.

4.8.2 Synthesis of N_{Glu}

To a stirred solution of 1,8-naphthalene anhydride (10.0 g, 50.5 mmol) in KOH solution (4 mM, 15 mL) at $0\text{ }^\circ\text{C}$, liquid bromine (5.2 mL, 101.0 mmol) were added. The reaction mixture was stirred for 1 h under nitrogen atmosphere at $0\text{ }^\circ\text{C}$ and further heated at $70\text{ }^\circ\text{C}$ for 20 h. The reaction was monitored by thin-layer chromatography (TLC). After completing the reaction, the precipitated was collected and washed with cold water (200 mL). The product was purified by column chromatography using ethyl acetate (EtOAc) and hexane as eluent. Next, 4-bromo-1,8-naphthene anhydride (**1**) (1.0 g, 3.61 mmol) was dissolved in DMF (10 mL). The reaction mixture was taken into a pressure tube, and copper sulfate (CuSO_4 , catalytic amount) and dimethylamine (2 mL, 15 % solution) were added and heated at $90\text{ }^\circ\text{C}$ for 6 h under stirring conditions. After completion of the reaction, the excess solvent was removed under reduced

pressure, and the crude product was precipitated in cold ethanol (25 mL). The product was purified by column chromatography using EtOAc and hexane as eluent. Next, **2** (200 mg, 0.83 mmole) was dissolved in isopropanol (IPA, 15 mL) and Boc-protected ethylene diamine (172.5 mg, 1.1 mmole) and triethylamine (0.23 mL, 1.66 mmole) were added. The reaction mixture was refluxed for 12 h under the nitrogen atmosphere. After the completion of the reaction (monitored by TLC), the excess solvent was removed, the crude was diluted with water (20 mL), and the residue was extracted into EtOAc (3 × 20 mL). The combined organic phase (EtOAc) was washed with water (1 × 25 mL) and brine (1 × 30 mL). The organic layers were combined and dried on anhydrous Na₂SO₄ and evaporated. The product (**3**) was purified by column chromatography using EtOAc and hexane as eluent. Next, the intermediated **3** (0.5 g, 1.5 mmole) was dissolved in DCM (5 mL) and TFA (2 mL) was added, and the reaction mixture was stirred for 3h at room temperature. The solvent was removed, and the product was precipitated with cold diethyl ether (25 mL). Next, to a stirred solution of **4** (215 mg, 0.51 mmol) in DMF (10 mL) at 0 °C, DIPEA (0.17 mL, 1.02 mmol), HBTU (232.1 mg, 0.61 mmol), and HOBt (83.0 mg, 0.61 mmol) were added. The reaction mixture was kept for stirring about 20 min under a nitrogen atmosphere, and Fmoc-Glu(OtBu)-OH (2.15 mg, 0.51 mmol) was added to the solution; the reaction was left to stir for 5–6 h at room temperature. After completing the reaction (monitored by TLC), the DMF was removed. The crude was diluted with water (25 mL), and the residue was extracted into EtOAc (3 × 20 mL). The combined organic layers (EtOAc) was washed with water (1 × 25 mL) and brine (1 × 25 mL), dried over anhydrous Na₂SO₄ and evaporated under vacuum to afford the crude peptide. The intermediate **5** was purified by column chromatography using DCM and methanol as eluent. Finally, **5** (0.3 g, 0.43 mmole) was dissolved in DCM (10 mL), and TFA (2 mL) was added, and the reaction mixture was stirred for 3h at room temperature.

The DCM was removed under vacuum, and the crude N_{Glu} was precipitated in cold diethyl ether, which was used for solid-phase synthesis of NTP.

¹H-NMR (600 MHz, DMSO-D₆) δ 12.07 (s, 1H), 8.42-8.48 (m, 2H), 8.30 (d, J = 8.5 Hz, 1H), 8.03 (t, J = 5.9 Hz, 1H), 7.87 (d, J = 7.5 Hz, 2H), 7.71 (dd, J = 13.6, 7.6 Hz, 3H), 7.40 (t, J = 8.2 Hz, 3H), 7.30 (dd, J = 11.9, 7.3 Hz, 2H), 7.16 (d, J = 8.3 Hz, 1H), 4.10-4.22 (m, 5H), 3.85 (td, J = 8.4, 5.2 Hz, 1H), 3.29 (dd, J = 13.2, 6.0 Hz, 1H), 3.05 (s, 6H), 2.19 (dd, J = 15.4, 9.0 Hz, 2H), 1.83 (td, J = 14.4, 5.9 Hz, 1H), 1.59-1.66 (m, 1H), 1.14-1.32 (m, 1H). ¹³C-NMR (150 MHz, DMSO-D₆) δ 173.9, 171.4, 163.8, 163.2, 156.4, 155.8, 143.8, 143.7, 140.6, 132.2, 131.2, 130.5, 129.7, 127.6, 127.0, 125.3, 125.3, 124.9, 124.2, 122.5, 120.0, 115.6, 113.6, 112.9, 79.1, 78.9, 78.7, 65.6, 54.0, 46.6, 44.3, 36.7, 34.3, 30.2, 28.9, 26.9. HRMS (ESI-MS): found 635.2525, calcd. For C₃₆H₃₄N₄O₇ [M+H]⁺ m/z= 635.2506.

4.8.3 Synthesis of NTP

Rink amide resin (100 mg) was washed with DCM (3 × 3 mL) and DMF (3 × 3 mL), and the resin was kept in DCM (3 mL) for 30 min under shaking condition. The DCM was removed, and again DMF (5 mL) containing piperidine (Pip, 20 %) was added; the reaction mixture was subjected to vigorous shaking for 30 min at room temperature. The DMF was removed, and the resin was washed with DCM (3 × 3 mL) and DMF (3 × 3 mL). The **6** was dispersed in DMF (4 mL), and N_{Glu} (98.5 mg, 2 equivalent), DIPEA (0.8 mL, 4 equivalent), HBTU (118.0 mg, 4 equivalent), and HOBt (42.0 mg, 4 equivalent) were added, and the reaction mixture has been subjected to vigorous shaking for 4 h at room temperature. The completion of the reaction was monitored by the Kaiser test. After the completion of the reaction, the solvent was removed, and DMF (5 mL) containing Pip (20 %) was added to intermediate **7**, and allowed to react for 30 min

at room temperature. Next, **8** was dispersed in DMF (5 mL) and Fmoc-Lys(Boc)-OH (146.2 mg, 4 equivalent), DIPEA (0.8 mL, 4 equivalent), HBTU (118.0 mg, 4 equivalent), and HOBt (42.0 mg, 4 equivalent) were added; and the reaction mixture was again subjected to vigorous shaking for 2 h at room temperature. After the completion of the reaction, the solvent was removed, and DMF (5 mL) containing Pip (20 %) was added in intermediate **9**, and allowed to react for 30 min at room temperature. Next, **10** was dispersed in DMF (5 mL) and Fmoc-His(trt)-OH (193.4 mg, 4 equivalent), DIPEA (0.8 mL, 4 equivalent), HBTU (118.0 mg, 4 equivalent), and HOBt (42.0 mg, 4 equivalent) were added; and the coupling reaction was carried out for 5 h at room temperature. After the completion of the reaction, the solvent was removed, and DMF (5 mL) containing Pip (20 %) was added in intermediate **11** to obtain intermediate **12**. Next, **12** was dispersed in DMF (5 mL) and Fmoc-Gly-OH (92.7 mg, 4 equivalent), DIPEA (0.8 mL, 4 equivalent), HBTU (118.0 mg, 4 equivalent), and HOBt (42.0 mg, 4 equivalent) were added; and the reaction mixture again allowed to vigorous shaking for 3 h at room temperature. After the completion of the reaction, the solvent was removed, and DMF (5 mL) containing Pip (20 %) was added in intermediate **13** to obtain intermediate **14**. Finally, the **14** was dispersed in DCM (3 mL), and TFA (1 mL) was added to the solution to obtain crude peptide, which was purified using a reverse-phase (RP) semipreparative HPLC on the C18 column at 40 °C and the integrity of the product (NTP) was ascertained by analytical liquid chromatography-mass spectrometry (LCMS) analysis.

4.8.4 Spectroscopy Analysis

To confirm the metal (Cu) chelating ability of NTP, we performed spectroscopy analysis (absorbance and fluorescence) in the absence and presence of Cu^{II}. UV-Visible spectroscopy

measurements were carried out using the single beam Agilent 8453 UV-Vis spectrophotometer at room temperature. 1 cm path length quartz cuvette (1 mL) was used for the absorbance measurement (200-800 nm). The fluorescence study was performed using quartz cuvette and well plate in Agilent Cary eclipse fluorescence spectrophotometers and microplate reader, respectively. The raw data was processed and analyzed using Origin 8.5 software or Prism 6.

4.8.5 Preparation of A β 42 Monomer, Oligomers and Fibrils

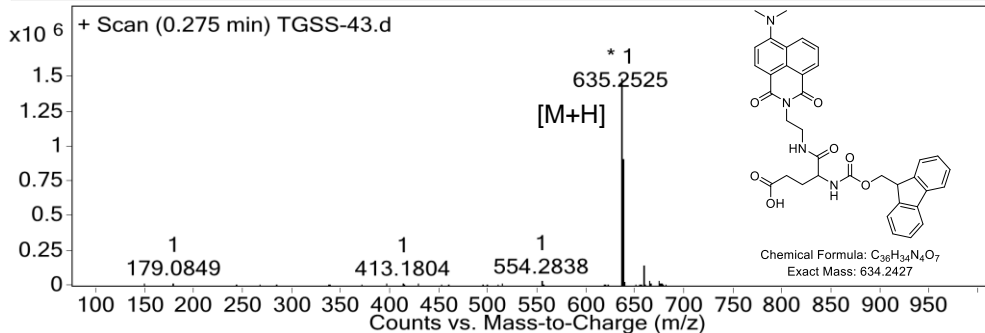
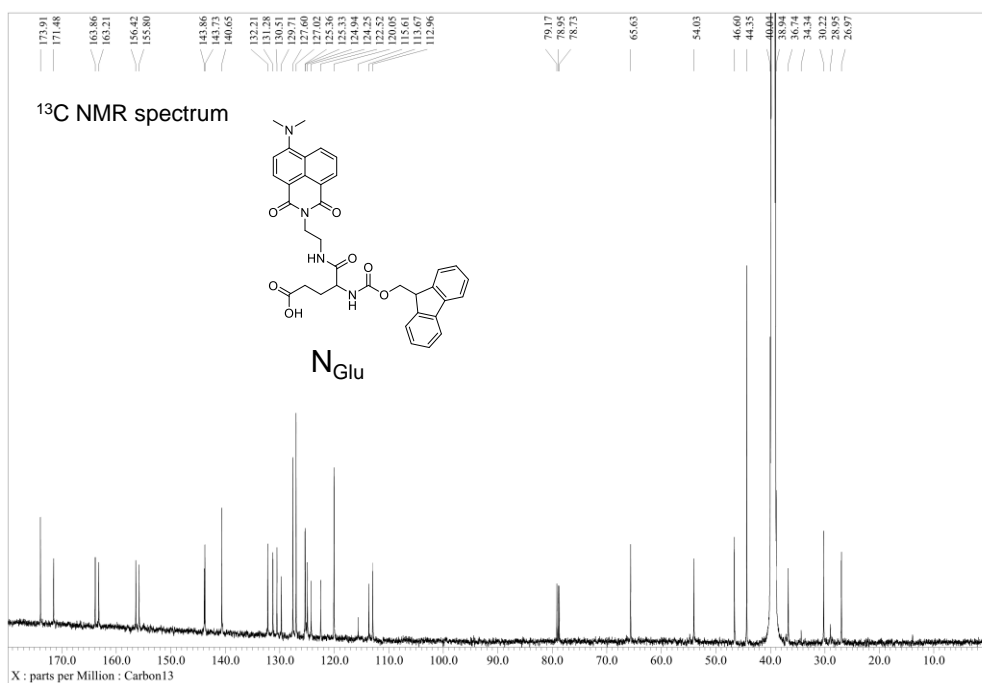
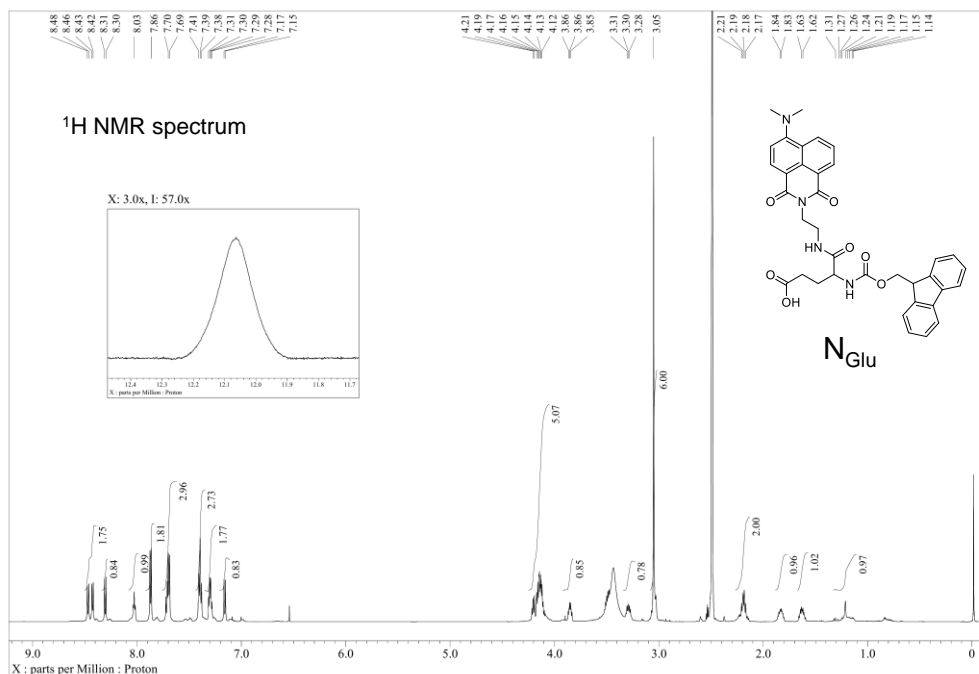
A β 42 peptide was dissolved in 250 μ L of hexafluoro-2-propanol (HFIP) and incubated for 1 h at room temperature. Then, HFIP was first removed by nitrogen gas flow. Again, A β 42 peptide was dissolved in PBS buffer (10 mM, pH= 7.4) containing 2% DMSO or NaOH solution (100 mM). The concentration of A β 42 peptide was calculated by the UV-Visible absorbance study using the molar extinction coefficient $1450 \text{ cm}^{-1} \text{ M}^{-1}$. The A β 42 oligomers and fibrils were prepared by incubating a calculated amount of A β 42 monomers for 48 h at 4 °C and 37 °C, respectively. For metal-induced amyloid aggregates, the A β 42 monomers were incubated with Cu^{II} for 48 h in PBS (10 mM, pH = 7.4). ThT fluorescence measurement confirmed the formation of A β 42 oligomers and fibrils.

4.8.6 Atomic Force Microscopy (AFM) Imaging

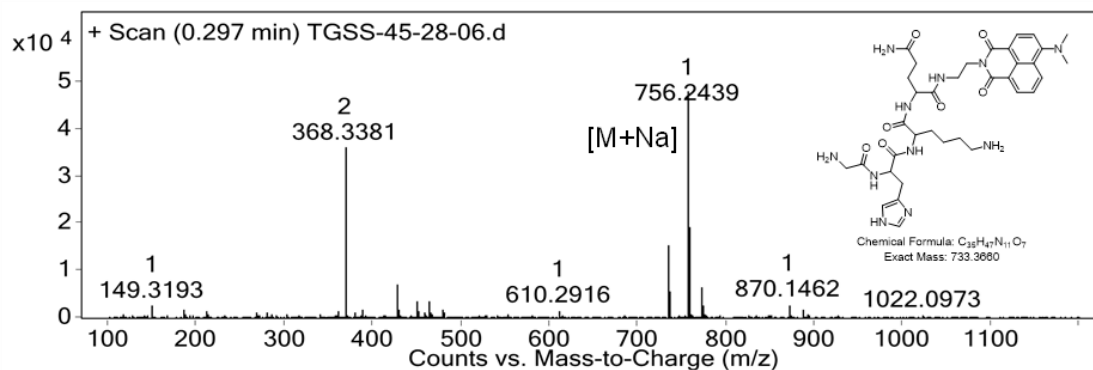
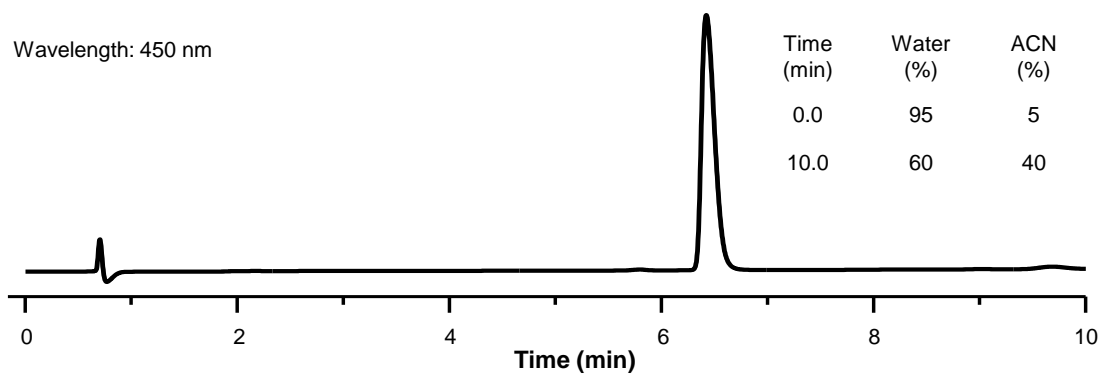
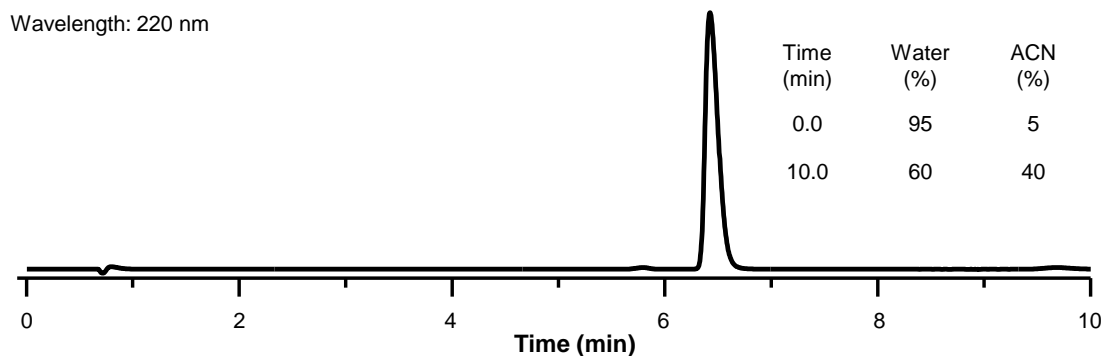
To visualize Cu-mediated and -free A β 42 aggregation species, we performed AFM imaging using Bruker Bioscope Resolve AFM microscope. Freshly reconstituted A β 42 (10 μ M) was incubated alone and with Cu^{II} (10 μ M) for 48 h at 4 °C and 37 °C. The incubated samples were spotted and air-dried on the Micra surface, and the sample was washed with Milli-Q water to remove excess salt and imaged.

4.9 Appendix

- ❖ ^1H NMR spectrum of N_{Glu}
- ❖ ^{13}C NMR spectrum of N_{Glu}
- ❖ HRMS of N_{Glu}
- ❖ HPLC characterization of NTP
- ❖ HRMS of NTP



LCMS characterization of NTP



4.10 References

1. Dobson, C. M., Protein folding and misfolding. *Nature* **2003**, 426 (6968), 884-890.

2. Rajasekhar, K.; Chakrabarti, M.; Govindaraju, T., Function and toxicity of amyloid beta and recent therapeutic interventions targeting amyloid beta in Alzheimer's disease. *Chem. Commun. (Camb)* **2015**, *51* (70), 13434-13450.
3. Ross, C. A.; Poirier, M. A., Protein aggregation and neurodegenerative disease. *Nat. Med.* **2004**, *10*, S10-7.
4. Rajasekhar, K.; Govindaraju, T., Current progress, challenges and future prospects of diagnostic and therapeutic interventions in Alzheimer's disease. *RSC Adv.* **2018**, *8* (42), 23780-23804.
5. Chiti, F.; Dobson, C. M., Protein misfolding, amyloid formation, and human disease: a summary of progress over the last decade. *Annu. Rev. Biochem.* **2017**, *86*, 27-68.
6. Watt, A. D.; Villemagne, V. L.; Barnham, K. J., Metals, membranes, and amyloid-beta oligomers: key pieces in the Alzheimer's disease puzzle? *J Alzheimers Dis.* **2013**, *33* (1), S283-293.
7. Bourassa, M. W.; Miller, L. M., Metal imaging in neurodegenerative diseases. *Metallomics* **2012**, *4* (8), 721-738.
8. Gaggelli, E.; Kozlowski, H.; Valensin, D.; Valensin, G., Copper homeostasis and neurodegenerative disorders (Alzheimer's, prion, and Parkinson's diseases and amyotrophic lateral sclerosis). *Chem. Rev.* **2006**, *106* (6), 1995-2044.
9. Hamley, I. W., The amyloid beta peptide: a chemist's perspective. Role in Alzheimer's and fibrillization. *Chem. Rev.* **2012**, *112* (10), 5147-5192.
10. Barrow, C. J.; Zagorski, M. G., Solution structures of beta peptide and its constituent fragments: relation to amyloid deposition. *Science* **1991**, *253* (5016), 179-1182.
11. Hardy, J. A.; Higgins, G. A., Alzheimer's disease: the amyloid cascade hypothesis. *Science* **1992**, *256* (5054), 184-85.
12. Schnabel, J., Amyloid: little proteins, big clues. *Nature* **2011**, *475* (7355), S12-4.
13. Huy, P. D.; Vuong, Q. V.; La Penna, G.; Faller, P.; Li, M. S., Impact of Cu(II) binding on structures and dynamics of Aβ₄₂ monomer and dimer: molecular dynamics study. *ACS Chem. Neurosci.* **2016**, *7* (10), 1348-1363.

14. Alzheimer's Association, 2018 Alzheimer's disease facts and figures. *Alzheimers Dement* **2018**, *14* (5), 701-701.
15. Alzheimer's Association, 2020 Alzheimer's disease facts and figures. *Alzheimers dementia* **2020**. doi: 10.1002/alz.12068.
16. Alies, B.; Hureau, C.; Faller, P., The role of metal ions in amyloid formation: general principles from model peptides. *Metallomics* **2013**, *5* (3), 183-192.
17. Liu, Y.; Nguyen, M.; Robert, A.; Meunier, B., Metal ions in alzheimer's disease: a key role or not? *Acc. Chem. Res.* **2019**, *52* (7), 2026-2035.
18. Drago, D.; Bolognin, S.; Zatta, P., Role of metal ions in the Abeta oligomerization in Alzheimer's disease and in other neurological disorders. *Curr. Alzheimer Res.* **2008**, *5* (6), 500-507.
19. Huang, X.; Atwood, C. S.; Moir, R. D.; Hartshorn, M. A.; Tanzi, R. E.; Bush, A. I., Trace metal contamination initiates the apparent auto-aggregation, amyloidosis, and oligomerization of Alzheimer's Abeta peptides. *J Biol. Inorg. Chem.* **2004**, *9* (8), 954-960.
20. Cioffi, F.; Adam, R. H. I.; Broersen, K., Molecular mechanisms and genetics of oxidative stress in Alzheimer's disease. *J Alzheimers Dis.* **2019**, *72* (4), 981-1017.
21. Butterfield, D. A.; Boyd-Kimball, D., Oxidative stress, amyloid-beta peptide, and altered key molecular pathways in the pathogenesis and progression of Alzheimer's disease. *J Alzheimers Dis.* **2018**, *62* (3), 1345-1367.
22. Neely, M. D.; Sidell, K. R.; Graham, D. G.; Montine, T. J., The lipid peroxidation product 4-hydroxynonenal inhibits neurite outgrowth, disrupts neuronal microtubules, and modifies cellular tubulin. *J Neurochem.* **1999**, *72* (6), 2323-2333.
23. Nunomura, A.; Perry, G.; Pappolla, M. A.; Wade, R.; Hirai, K.; Chiba, S.; Smith, M. A., RNA oxidation is a prominent feature of vulnerable neurons in Alzheimer's disease. *J Neurosci.* **1999**, *19* (6), 1959-1964.
24. Zhu, X.; Rottkamp, C. A.; Boux, H.; Takeda, A.; Perry, G.; Smith, M. A., Activation of p38 kinase links tau phosphorylation, oxidative stress, and cell cycle-related events in Alzheimer disease. *J Neuropathol. Exp. Neurol.* **2000**, *59* (10), 880-88.

25. Wyss-Coray, T., Inflammation in Alzheimer disease: driving force, bystander or beneficial response? *Nat. Med.* **2006**, *12* (9), 1005-1015.
26. Go, Y. M.; Jones, D. P., Redox control systems in the nucleus: mechanisms and functions. *Antioxid. Redox. Signal.* **2010**, *13* (4), 489-509.
27. Samanta, S.; Rajasekhar, K.; Babagond, V.; Govindaraju, T., Small molecule inhibits metal-dependent and -independent multifaceted toxicity of Alzheimer's disease. *ACS Chem. Neurosci.* **2019**, *10* (8), 3611-3621.
28. Torres, L. L.; Quaglio, N. B.; de Souza, G. T.; Garcia, R. T.; Dati, L. M.; Moreira, W. L.; Loureiro, A. P.; de Souza-Talarico, J. N.; Smid, J.; Porto, C. S.; Bottino, C. M.; Nitrini, R.; Barros, S. B.; Camarini, R.; Marcourakis, T., Peripheral oxidative stress biomarkers in mild cognitive impairment and Alzheimer's disease. *J Alzheimers Dis.* **2011**, *26* (1), 59-68.
29. Kinney, J. W.; Bemiller, S. M.; Murtishaw, A. S.; Leisgang, A. M.; Salazar, A. M.; Lamb, B. T., Inflammation as a central mechanism in Alzheimer's disease. *Alzheimers Dement* **2018**, *4*, 575-590.
30. Huang, Y.; Mucke, L., Alzheimer mechanisms and therapeutic strategies. *Cell* **2012**, *148* (6), 1204-1222.
31. Savelieff, M. G.; Nam, G.; Kang, J.; Lee, H. J.; Lee, M.; Lim, M. H., Development of multifunctional molecules as potential therapeutic candidates for Alzheimer's disease, parkinson's disease, and amyotrophic lateral sclerosis in the last decade. *Chem. Rev.* **2019**, *119* (2), 1221-1322.
32. Rajasekhar, K.; Madhu, C.; Govindaraju, T., Natural tripeptide-based inhibitor of multifaceted amyloid beta toxicity. *ACS Chem. Neurosci.* **2016**, *7* (9), 1300-1310.
33. Rajasekhar, K.; Mehta, K.; Govindaraju, T., Hybrid multifunctional modulators inhibit multifaceted Abeta toxicity and prevent mitochondrial damage. *ACS Chem. Neurosci.* **2018**, *9* (6), 1432-1440.
34. Datta, L. P.; Samanta, S.; Govindaraju, T., Polyampholyte-based synthetic chaperone modulate amyloid aggregation and lithium delivery. *ACS Chem. Neurosci.* **2020**, *11* (18), 2812-2826.

35. Rajasekhar, K.; Samanta, S.; Bagoband, V.; Murugan, N. A.; Govindaraju, T., Antioxidant berberine-derivative inhibits multifaceted amyloid toxicity. *iScience* **2020**, *23* (4), 101005.
36. Bush, A. I.; Pettingell, W. H.; Multhaup, G.; d Paradis, M.; Vonsattel, J. P.; Gusella, J. F.; Beyreuther, K.; Masters, C. L.; Tanzi, R. E., Rapid induction of Alzheimer Abeta amyloid formation by zinc. *Science* **1994**, *265* (5177), 1464-1467.
37. Rajasekhar, K.; Narayanaswamy, N.; Murugan, N. A.; Viccaro, K.; Lee, H. G.; Shah, K.; Govindaraju, T., Abeta plaque-selective NIR fluorescence probe to differentiate Alzheimer's disease from tauopathies. *Biosens. Bioelectron.* **2017**, *98*, 54-61.
38. Samanta, S.; Govindaraju, T., Unambiguous detection of elevated levels of hypochlorous acid in double transgenic AD mouse brain. *ACS Chem. Neurosci.* **2019**, *10* (12), 4847-4853.
39. Arora, H.; Ramesh, M.; Rajasekhar, K.; Govindaraju, T., Molecular tools to detect alloforms of A β and tau: implications for multiplexing and multimodal diagnosis of Alzheimer's disease. *Bull. Chem. Soc. Jpn.* **2020**, *93* (4), 507-546.

Chapter 5

**Unambiguous Detection of Elevated Levels of
HOCl and Its Proximal Localization with A β
Plaques in Double Transgenic AD Mouse Brain**

AD pathology is characterized by the presence of toxic A β plaques and NFTs in the brain.¹⁻⁶ Currently, AD is detected only in the advanced stage at which there are no treatment options available.⁷⁻⁹ AD is characterized by multifaceted toxicity that involves multiple biomarkers, and all these biomarkers must be effectively addressed individually as well as collectively through reliable analytical tools.¹⁰⁻¹³ Therefore, the development of analytical tools for biomarkers that have a direct or indirect role in AD pathogenesis demands immediate attention to aid multiplexing and multimodal analysis.⁶ The National Institute on Aging and Alzheimer's Association (NIA-AA) Research Framework report (2018) recommended the use of definite biomarkers instead of cognitive tests to diagnose AD and proposed A β , tau, and related neurodegeneration as core biomarkers.¹⁴ The NIA-AA Research Framework has consciously left the biomarkers list open ended to add newly validated biomarkers that are reliable and quantifiable. This encourages researchers to validate newer biomarkers to improve the accuracy of diagnosis, as core biomarkers are not completely successful in delivering an accurate diagnostic platform for multifaceted AD.¹⁵⁻
²¹ The weak inorganic acid HOCl (pKa= 7.5) plays a detrimental role in the process leading to oxidative stress and neuroinflammation and hence is a potential candidate as AD biomarker.²² The redox active transition metal ions (Cu^{II} and Fe^{III}) chelate with A β and stabilize highly toxic metal-dependent A β -aggregation species which create severe imbalance in the physiological redox homeostasis in the AD brain.^{6,21,23} The bound metal ions (Cu^{II} or Fe^{III}) undergo two electron reduction in the presence of the host A β peptide or other biological reducing agents to generate excessive hydrogen peroxide (H₂O₂) from molecular oxygen.^{6,24} In the subsequent transformation, myeloperoxidase enzyme in the presence of chloride ions converts H₂O₂ to HOCl.²⁵ HOCl is a strong oxidizing agent and helps in an array of essential biological processes such as fighting against external pathogens, regulation of growth factors, stimulation of healing, modulation of

inflammation, and posttranslational modifications (PTMs).²⁶ Several HOCl sensors have been reported in the literature for HOCl sensing,^{27–33} while the detection or imaging of HOCl and its relation to A β (production and localization) under *in vitro* and *in vivo* AD-like conditions is yet to be established to validate HOCl as a potential biomarker. A simple, accurate, and reliable method for the detection and imaging of HOCl in the AD brain is useful for the effective diagnosis of AD pathology. In this Chapter, we report a blood-brain barrier (BBB) permeable thioamide probe CM2 for highly specific and sensitive detection, imaging, and quantification of HOCl under *in vitro* and *in vivo* AD-like conditions to validate it as one of the prospective biomarkers for the diagnosis of AD (Figure 1).

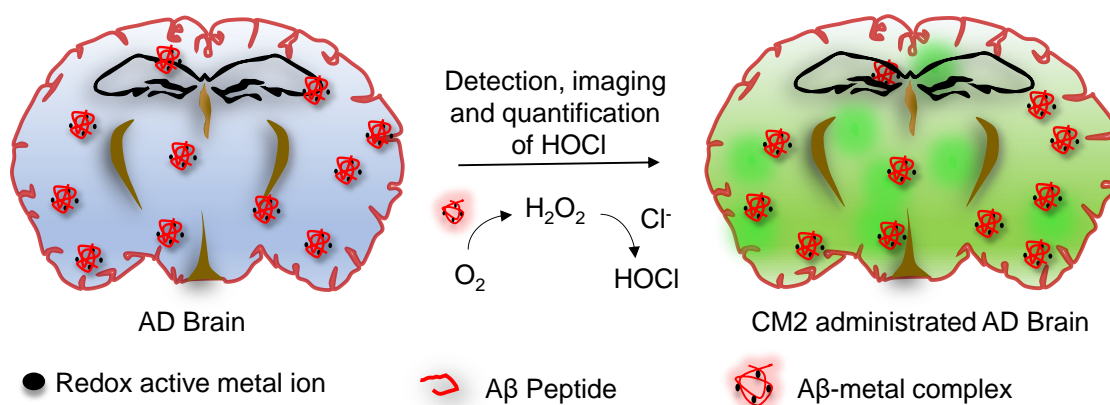


Figure 1. Schematic diagram shows the AD brain with A β deposition, A β -metal complex catalyzed production of elevated levels of HOCl and its *in vivo* detection using BBB permeable CM2.

5.1 Design and Synthesis of CM Probes

The design strategy of CM probes was to conjugate coumarin and morpholine units through amide (CM1) and thioamide (CM2) linkages. We anticipated that the thioamide bond (fluorescence quencher) makes CM2 nonfluorescent and upon transformation to CM1 with an amide bond in the presence of HOCl restores the fluorescence of the coumarin moiety.^{16,34–38} The synthetic route

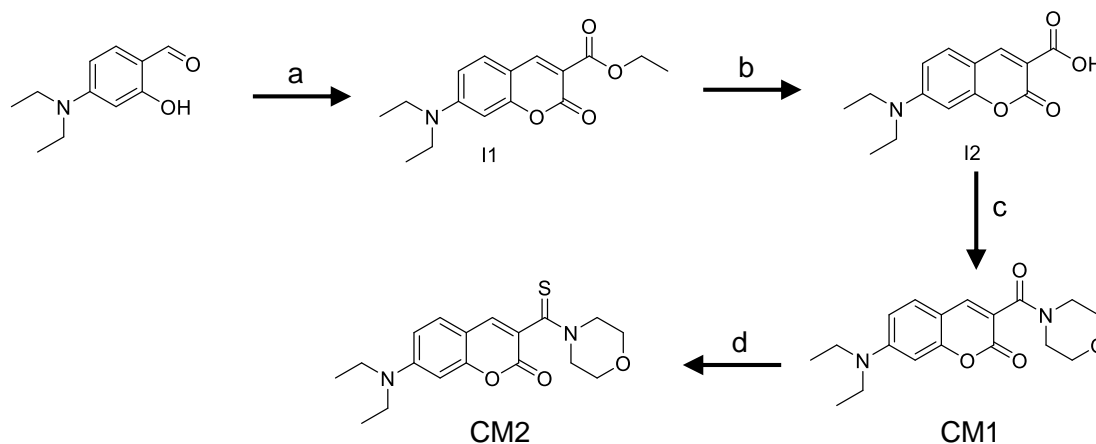


Figure 2. Synthesis of CM probes. (a) diethylmalonate, piperidine, EtOH; (b) conc. HCl; (c) morpholine, HBTU, HOBt, DIPEA, DMF; (d) Lawesson's reagents, THF.

for the preparation of CM2 is shown in Figure 2. 4-(Diethylamino)-2-hydroxybenzaldehyde was condensed with diethyl malonate using piperidine as a base under reflux conditions to obtain intermediate I1. The intermediate I1 was hydrolyzed in acidic conditions to obtain 7-(diethylamino)-2-oxo-2H-chromene-3-carboxylic acid (I2). The carboxylic acid I2 was condensed with morpholine using HBTU [(2-(1Hbenzotriazol-1-yl)-1,1,3,3-tetramethyluronium hexafluorophosphate)] and HOBt (1-hydroxybenzotriazole) in dimethylformamide (DMF) to obtain CM1 (7-(diethylamino)-3-(morpholine-4-carbonyl)-2H-chromen-2-one). The amide carbonyl oxygen atom in CM1 was substituted with sulfur atom using

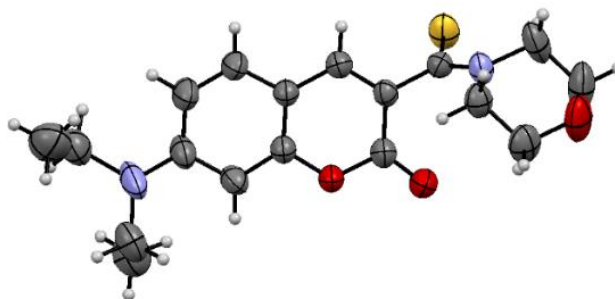


Figure 3. ORTEP diagram of single crystal X-ray diffraction of CM2.

Lawesson's reagent to obtain CM2. The integrity of all the intermediates and probes (CM1 and CM2) was confirmed by NMR, HPLC, and high-resolution mass spectrometry (HRMS) techniques. The structure of the probe CM2 was confirmed by single crystal X-ray diffraction analysis, which revealed planar and chair conformations of coumarin and morpholine units, respectively (Figure 3). The single crystal XRD structure confirmed the regioselective amide (CM1) to thioamide (CM2) conversion without affecting the lactone carbonyl of the coumarin moiety.

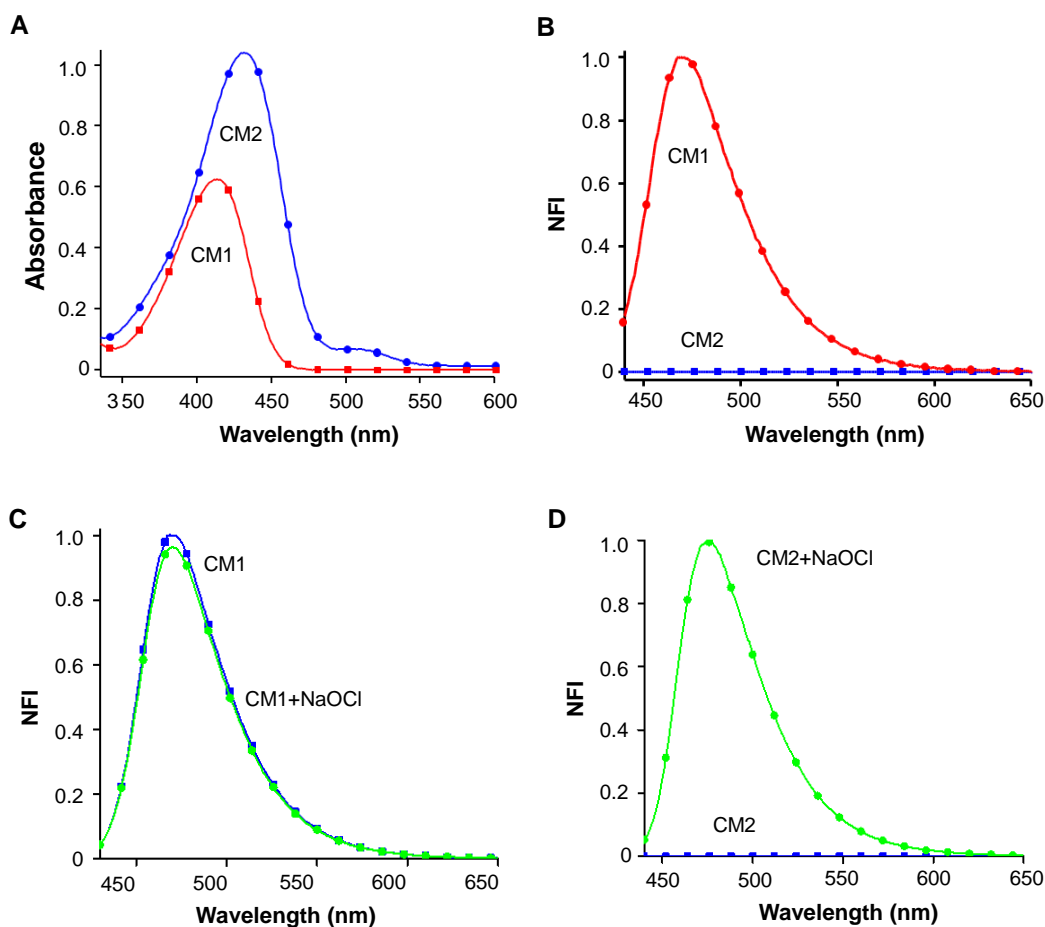


Figure 4. The absorbance (A) and fluorescence (B) spectra of CM1 and CM2. (C) Fluorescence emission spectra of CM1 in the absence (blue) and presence (green) of ClO⁻. (D) Fluorescence emission spectra of CM2 in the absence (blue) and presence (green) of ClO⁻. NFI: Normalized fluorescence intensity.

5.2 Regioselective Oxidation of CM2 and HOCl Detection

As anticipated, CM2 rapidly reacted with HOCl in solution and showed bright green fluorescence ($\lambda_{\text{ex}}=417\text{ nm}$, $\lambda_{\text{em}}=485\text{ nm}$), while CM1 did not show any significant changes and remained unresponsive under similar conditions (Figure 4). These initial findings validated our chemical design and indicated the probable transformation of nonfluorescent thioamide (CM2) to fluorescent amide (CM1). The ClO^- oxidize the sulfur atom of the thiocarbonyl group of CM2 and transformed into a good leaving group which is subsequently removed by the hydrolysis to generate the carbonyl group as in fluorescent CM1. The oxidative transformation of CM2 to CM1 was thoroughly characterized by HPLC and HRMS analysis (Figure 5). The HPLC chromatograms monitored at 420 nm showed the retention time (t_{R}) of 5.38 and 6.65 min for CM1 and CM2,

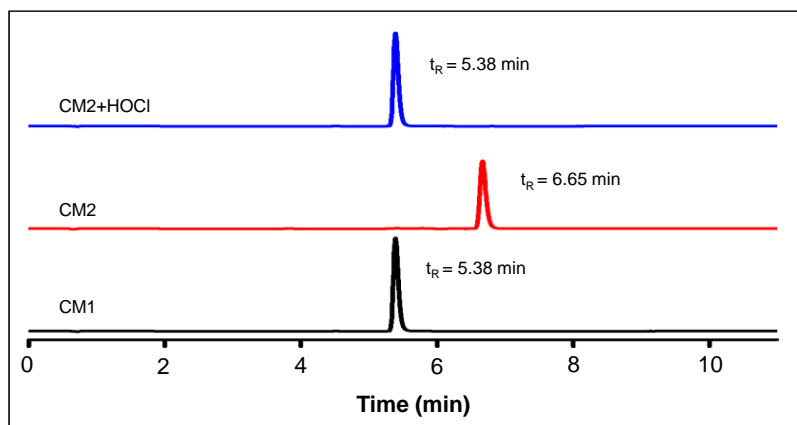


Figure 5. HPLC analysis of CM2 before (red) and after treating with HOCl (blue) treated CM2, and characteristic retention time (t_{R}) is indicated.

respectively. The dichloromethane extract of the HOCl treated CM2 sample under similar conditions showed $t_{\text{R}} = 5.38\text{ min}$, which confirmed the formation of CM1 (Figure 5). HRMS analysis of the CM2 sample treated with HOCl revealed the absence of a mass peak at 347.1434 $[\text{CM2} + \text{H}]^+$ and showed new mass peaks at 331.1641 and 353.1455 corresponding to $[\text{CM1} + \text{H}]^+$ and $[\text{CM1} + \text{Na}]^+$, respectively (Figure 6). These results confirmed the regioselective oxidation of CM2 at the thiocarbonyl in the presence of HOCl to generate green fluorescent amide CM1, and the suitability of this transformation for the detection and imaging of HOCl.

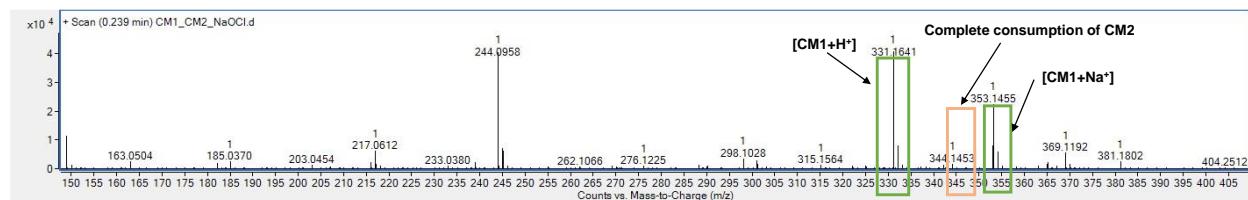


Figure 6. High resolution mass spectrometry (HRMS) analysis of CM2 in the presence of NaOCl.

5.3 Specific Detection of HOCl Over Other ROS

The selectivity of the probe CM2 was assessed against various ROS including HO \cdot , H $_2$ O $_2$, NO $_2^-$, NO, 1 O $_2$, NO $_3^-$, tBuOOH, and ClO $^-$ in phosphate buffer saline (PBS) containing ethanol (1:1) solution. Strong green emission was observed in the presence of HOCl, while other ROS did not show significant fluorescence under similar conditions (Figure 7). CM2 was evaluated in the presence of different cations and anions to further ascertain its selectivity to HOCl. The data confirmed the selectivity of CM2 toward OCl $^-$ over other biological species tested to generate fluorescent CM1 (Figure 7). Besides, we evaluated the response of CM2 in the presence of freshly prepared monomers, oligomers, and fibrils of A β 42 under *in vitro* conditions. The fluorescence response monitored at 485 nm did not show significant changes compared to the strong signal from the positive control with exogenously added HOCl (Figure S8). This study demonstrated that the probe has no interference from the A β 42 or peptide species. However, in cellulo study shows a strong response of the probe in the presence of the A β 42-Cu II complex, which is attributed to the redox process and *in situ* generation of excessive HOCl (vide infra). The hypsochromic shift (15 nm) and hypochromic effect of absorbance maxima at 417 nm in the presence of NaOCl resulted in a colorimetric change from yellowish to colorless solution (Figure 9A). The fluorescence emission of CM2 enhanced gradually (up to 90 folds) as a function of NaOCl concentration and reached saturation at 1 mM (Figure 9B). The data showed that a submicromolar concentration of

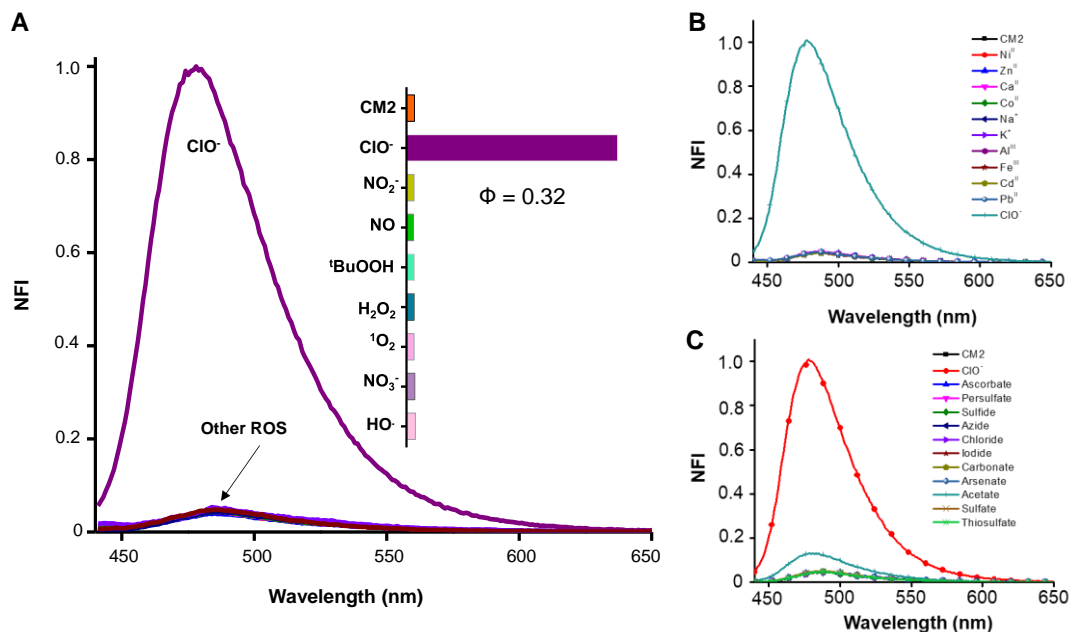


Figure 7. (A) Fluorescence response measured upon treatment of CM2 with ClO⁻ and various other ROS (HO[•], H₂O₂, NO₂⁻, NO, ¹O₂, NO₃⁻, and ^tBuOOH) in phosphate buffer saline containing ethanol (1:1). (B) The fluorescence spectra of CM2 in presence of ClO⁻ and various metal ions. (C) The fluorescence spectra of CM2 in presence of ClO⁻ and various anions. NFI: Normalized fluorescence intensity.

ClO⁻ could be detected using CM2 with the detection limit of 0.17 μ M (Figure 10A). The presence of the sulfur atom (thioamide) acts as an intramolecular fluorescence quencher of the coumarin moiety in CM2 (quantum yield, $\Phi = \text{null}$). The oxidative transformation of thioamide to generate CM1 in the presence of ClO⁻ restores the bright green fluorescence ($\Phi = 0.32$). Interestingly, CM2 selectively detects HOCl over a wide pH range from 3.0 to 12.0, confirming the possible utility for *in vitro* and *in vivo* detection and imaging of HOCl in physiological conditions without interference from other chemical species (Figure 10B and C).

5.4 Detection of HOCl in SHSY5Y Cells Using CM2

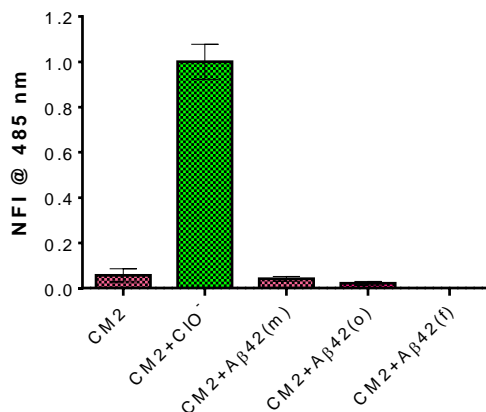


Figure 8. Fluorescence intensity of CM2 in presence of monomers (m), oligomers (o), and fibrils (f) of A β 42. External NaOCl was used as a positive control. NFI: Normalized fluorescence intensity.

We evaluated the utility of CM2 to detect HOCl under complex physiological conditions in neuronal cells (SHSY5Y). The assessment of cytotoxicity showed that CM2 is nontoxic to cells in the working concentration (500 nM) and exhibited cell viability of >95% for the concentration

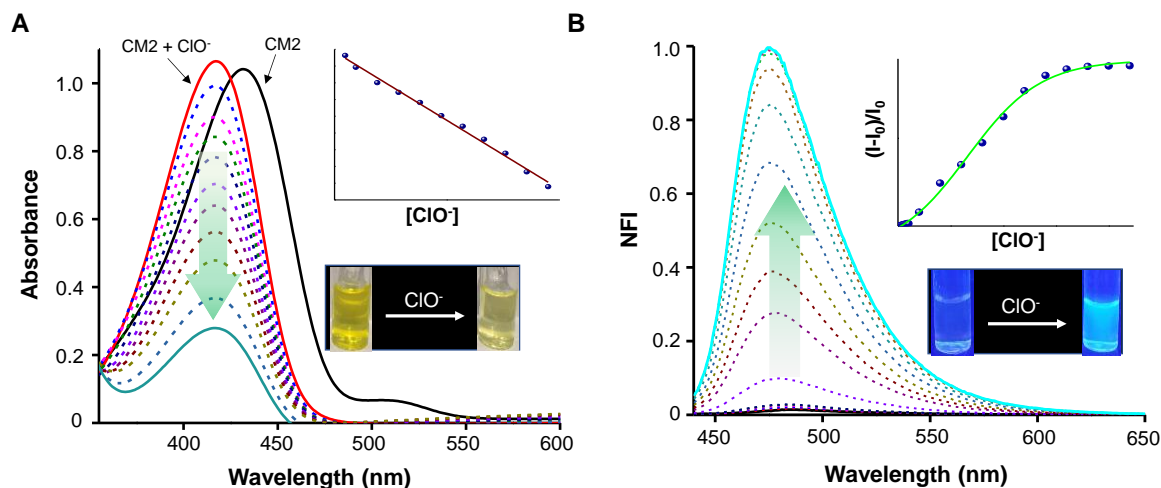


Figure 9. (A) The absorption spectra of CM2 with increasing concentrations of ClO⁻ (Insets: change in absorbance maxima (λ_{\max} = 417 nm) with ClO⁻ concentrations and colorimetric change of CM2 solution from yellowish to colorless). (B) Fluorescence response was recorded upon the treatment of CM2 with an increasing concentration of ClO⁻. Insets show a plot of fluorescence intensity at 485 nm as a function of [ClO⁻] and visible color change of CM2 solution on treatment with OCl⁻ visualized under UV light (λ_{ex} = 365 nm). NFI: Normalized fluorescence intensity.

of 10 μM , after 24 h of incubation (Figure 11). SHSY5Y cells were cultured in confocal (35 mm) dishes and incubated with CM2 and 4',6 diamidino-2-phenylindole (DAPI) for 30 min under 5% CO_2 at 37 $^\circ\text{C}$. The cells were washed, and images were captured under the fluorescence microscope in the absence and presence of exogenous NaOCl (Figure 12). The green fluorescence signal with the FITC channel confirmed the cellular uptake of CM2 and its regioselective transformation to generate fluorescent CM1. Next, SHSY5Y cells were incubated with the A β 42-Cu II (20 μM) complex for 2 h to create in vitro AD-like conditions and visualize the production of HOCl under metal-dependent amyloid stress. The experimental cells were fixed with 4% paraformaldehyde (PFA) followed by the incubation with CM2 for 30 min, and DAPI was used

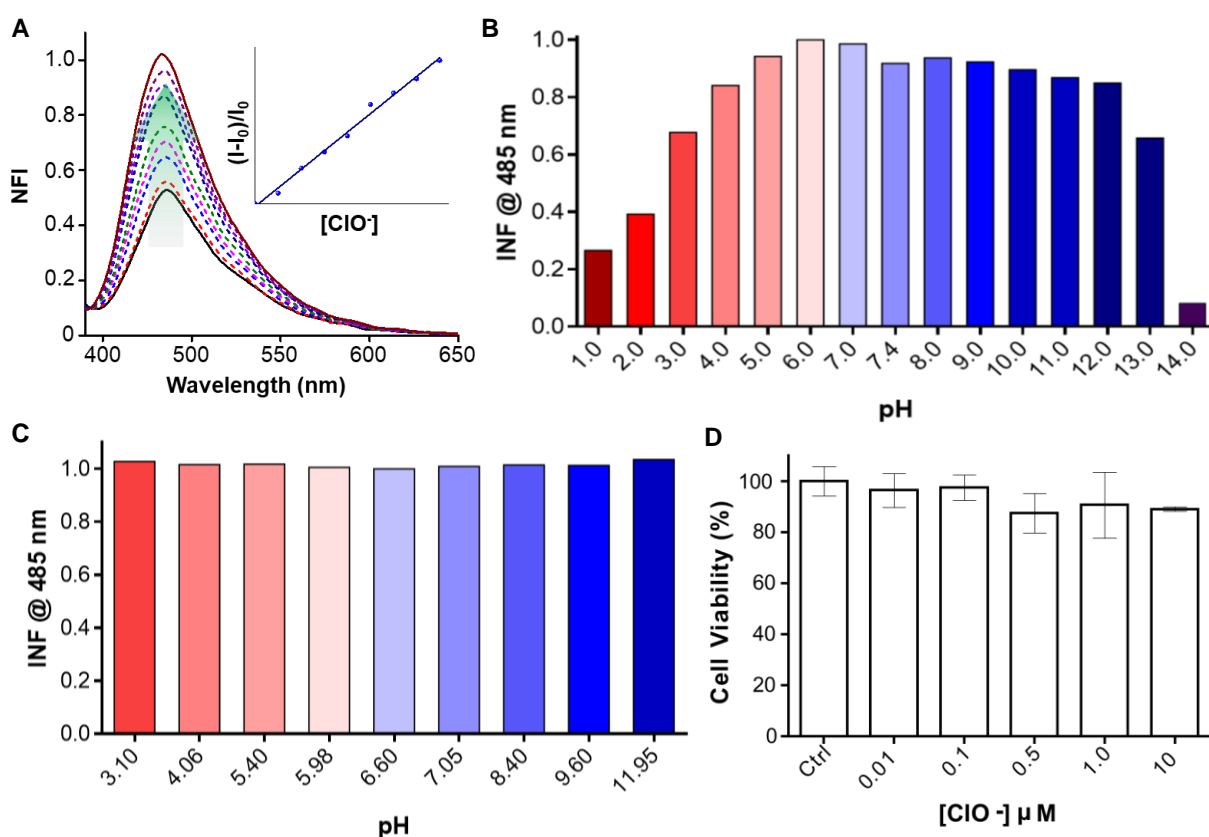


Figure 10. (A) The fluorescence spectra of CM2 in presence of very low concentration (5-40 μM) of NaOCl. Normalized fluorescence intensity (NFI) of CM2 with NaOCl at different pH in PBS (B) and Milli Q water (C). (D) Cytotoxicity study of CM2 at different concentrations in SHSY5Y cells.

to stain the nucleus. The green fluorescence signal from the cells revealed regioselective transformation of CM2 to CM1 and *in situ* generation of HOCl as a consequence of metal-

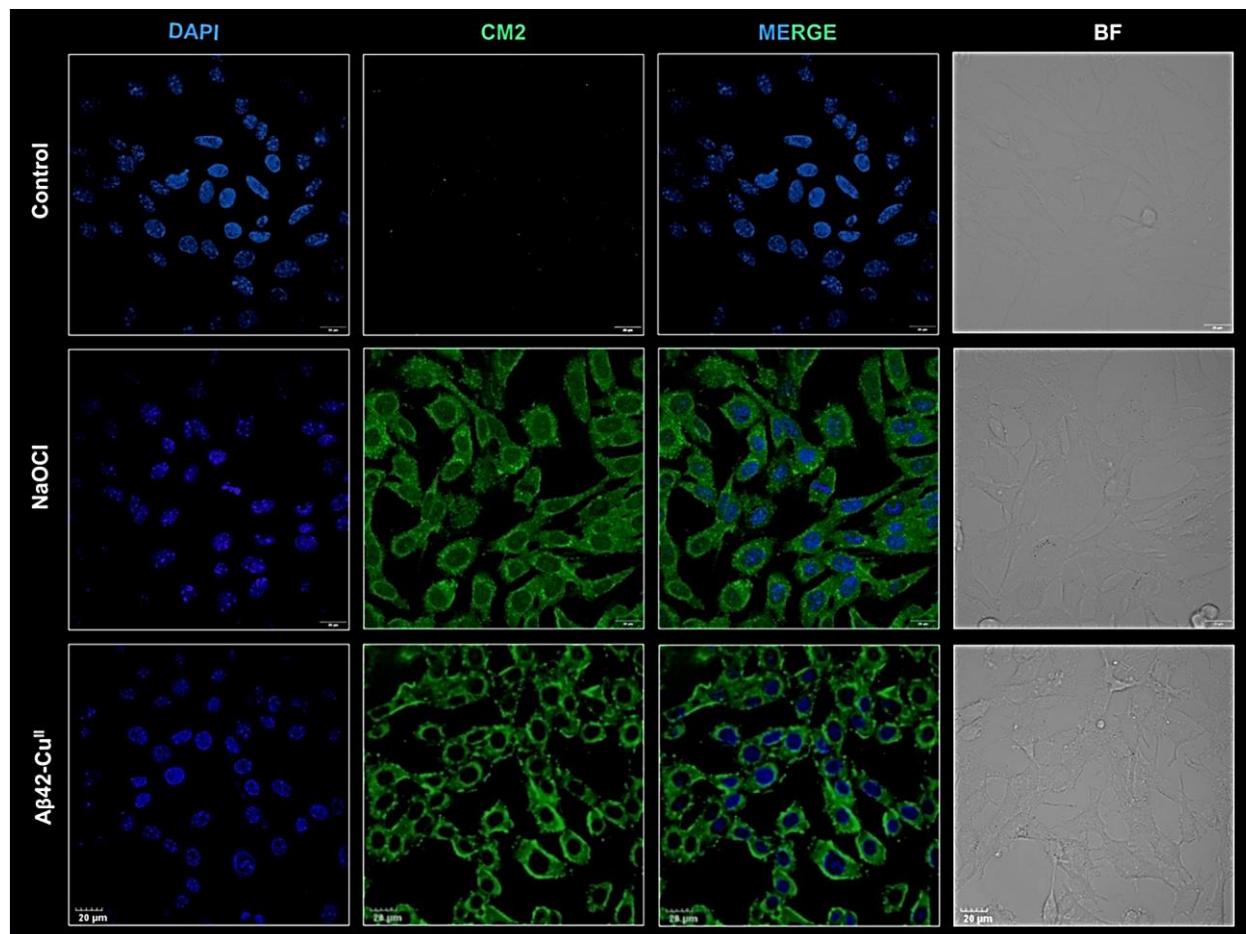


Figure 11. Detection of HOCl in SHSY5Y cells using the CM2 probe. PBS (control), NaOCl, and A β 42-Cu^{II} complex (2 h) treated cells were imaged under the confocal microscope upon staining with CM2 (green) and DAPI (blue). BF: bright field; scale bar: 20 μ m.

dependent amyloid toxicity (Figure 11). The strong in cellulo fluorescence confirmed excess production of HOCl in AD-like conditions, which motivated us to explore the utility of CM2 for *in vivo* detection and imaging of HOCl. The BBB crossing ability of CM2 was evaluated by administering the probe in wild type (WT) C57BL/6 mice and analyzing the brain tissue at

different time points (45 and 90 min). The mass spectrometry analysis of the CM2 administered mouse brain samples showed molecular peaks corresponding to [CM2]⁺ (346.44) and partially transformed [CM1+2H]⁺ (332.17) due to the presence of physiological HOCl (Figure 12, 13 and 14). Further, absorption and emission spectroscopy analysis were carried out to reconfirm the presence of unreacted CM2 in the probe administered mouse brain samples. The absorption spectrum showed absorbance maxima at $\lambda = 430$ nm which revealed the presence of unreacted CM2. However, CM2 present in the sample reacted rapidly upon addition of exogenous ClO⁻ and showed a significant fluorescence enhancement at 485 nm ($\lambda_{ex} = 417$ nm). On the other hand, the PBS administered (control) brain sample did not show any fluorescence enhancement under

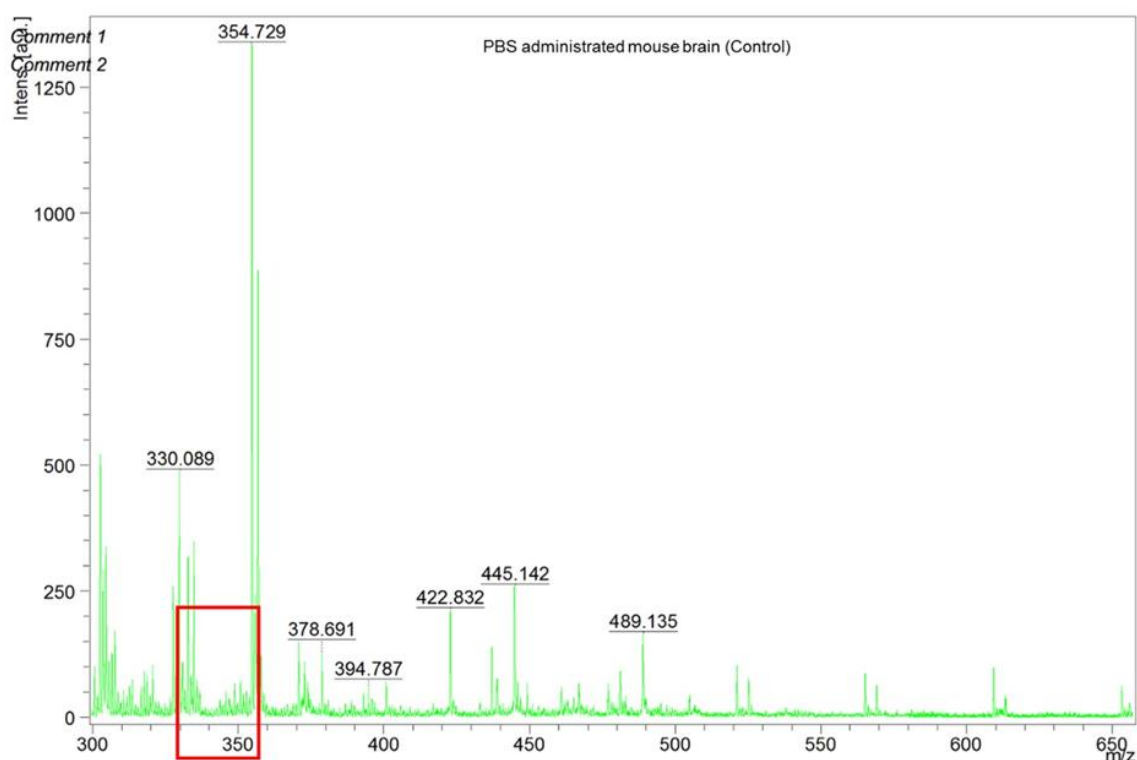


Figure 12. The MALDI mass analysis of vehicle treated mouse brain samples after 45 min of administration.

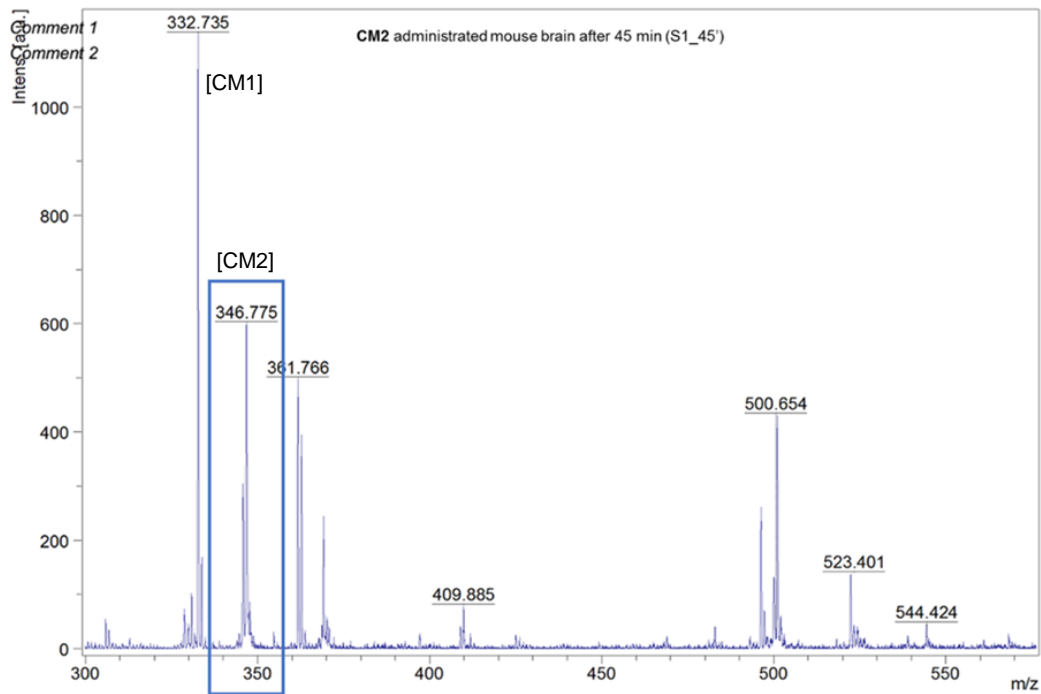


Figure 13. The MALDI mass analysis of CM2 treated mouse brain samples after 45 min of administration.

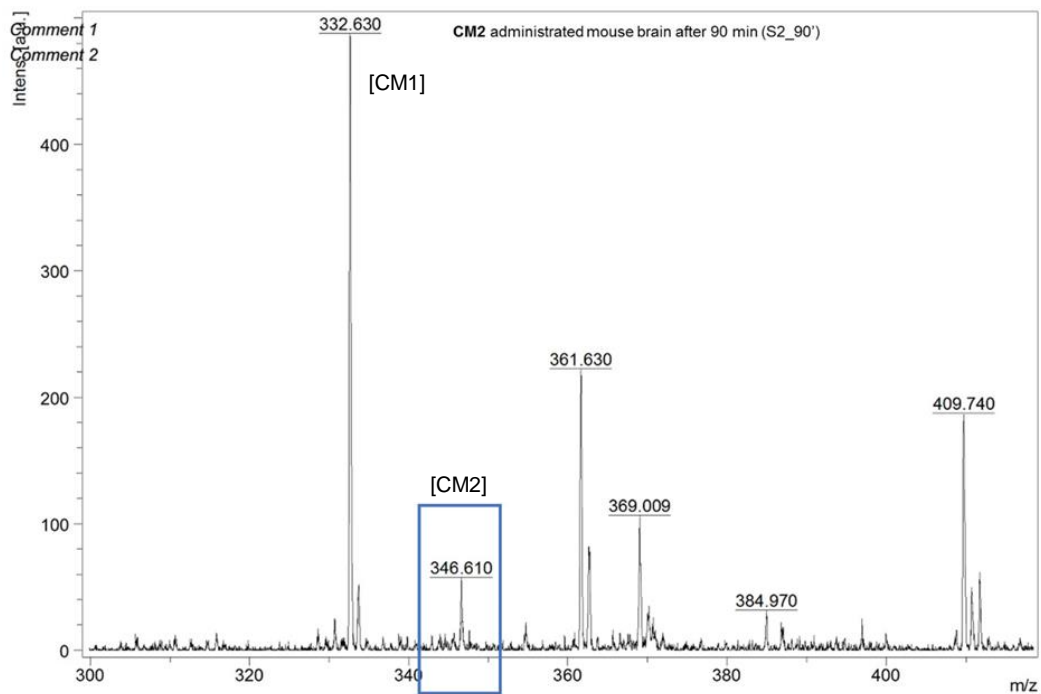


Figure 14. The MALDI mass analysis of CM2 treated mouse brain sample after 90 min of administration.

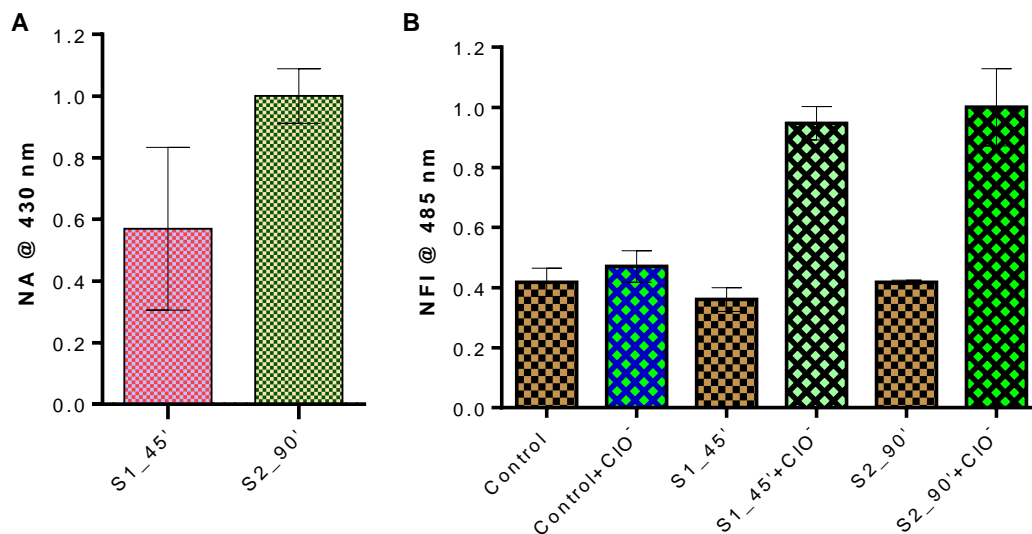


Figure 15. (A) The normalized absorbance (NA) of CM2 administrated brain samples collected after 45 (S1_45') and 90 (S2_90') min of probe administration. The presented data is baseline corrected with PBS administrated brain sample (control). (B) Normalized fluorescence intensity (NFI) of PBS (control) and CM2 administrated brain samples in the absence and presence of OCl (λ_{ex} = 417 nm).

similar conditions (Figure 15). These studies have established that CM2 effectively crosses the BBB and is a potential *in vivo* probe to detect and image HOCl in the brain.

5.5 Detection, Imaging, and Quantification of HOCl in APP/PS1 Mouse Model

We proceeded with the detection and imaging of HOCl employing CM2 in the brains of 12 month old APP/PS1 male AD mice and age matched control (WT mice). The APP/PS1 double transgenic AD mouse model (B6C3-Tg (APP^{swe}, PSEN1^{1dE9}) 85Dbo/J; stock number 004462) with mutations in amyloid precursor protein (APP) and γ -secretase (PSEN1) results in the production and deposition of A β plaques in the brain. The deposition of amyloid plaques accompanied by the accumulation of redox active metal ions in the AD brain produce excess ROS causing oxidative stress and neuroinflammation.^{6,8} To detect and image HOCl in the mouse brain, CM2 was

administered twice (12 h interval) in AD and WT mice and the mice were sacrificed after 6 h of a second administration to collect the brains. The collected brains were fixed with 4% PFA and rehydrated with 30% sucrose solution to obtain the sagittal brain sections (40 μ m). The brain

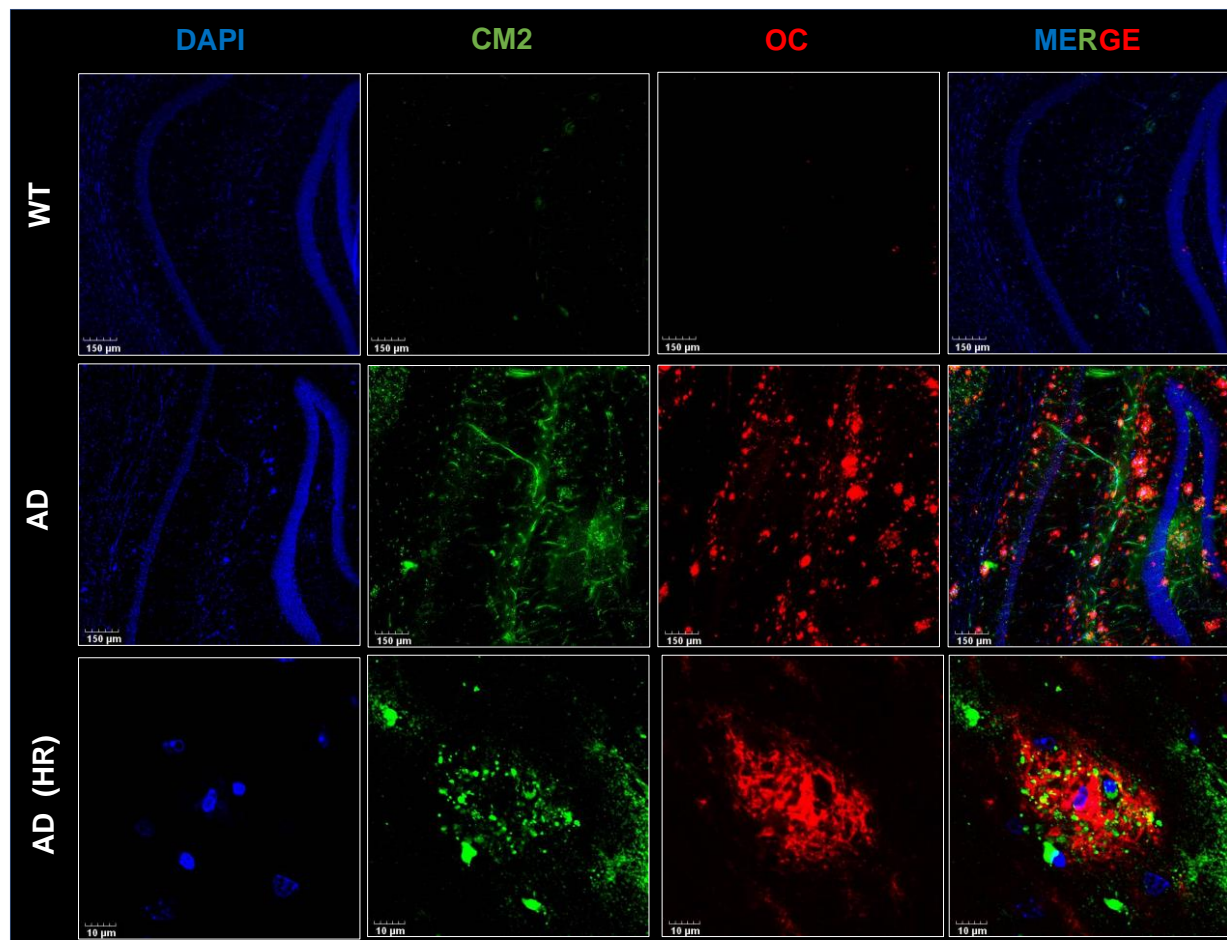


Figure 16. Confocal microscopy images of hippocampus region of the CM2 administered WT and AD mouse brain, which are immunostained with amyloid fibril specific antibody (OC) followed by fluorescent labeled ($\lambda_{\text{ex}}= 633 \text{ nm}$, $\lambda_{\text{em}}= 650 \text{ nm}$) secondary antibody (red) and DAPI (blue). Scale bar: 20 μ m (HR) and 150 μ m (HR); HR: high resolution.

sections were immunostained with DAPI and amyloid fibril specific antibody (OC) followed by the treatment with fluorescently ($\lambda_{\text{ex}}= 633 \text{ nm}$, $\lambda_{\text{em}}= 650 \text{ nm}$) labeled secondary antibody, and the images were captured under the confocal microscope (Figure 16 and 17). The images obtained

from two different regions of the brain viz., hippocampus and cortex showed green fluorescence signal, which confirmed the presence of CM1 in the CM2 administered mouse brain compare to age-matched control. The images under red fluorescence channel displayed the deposition of

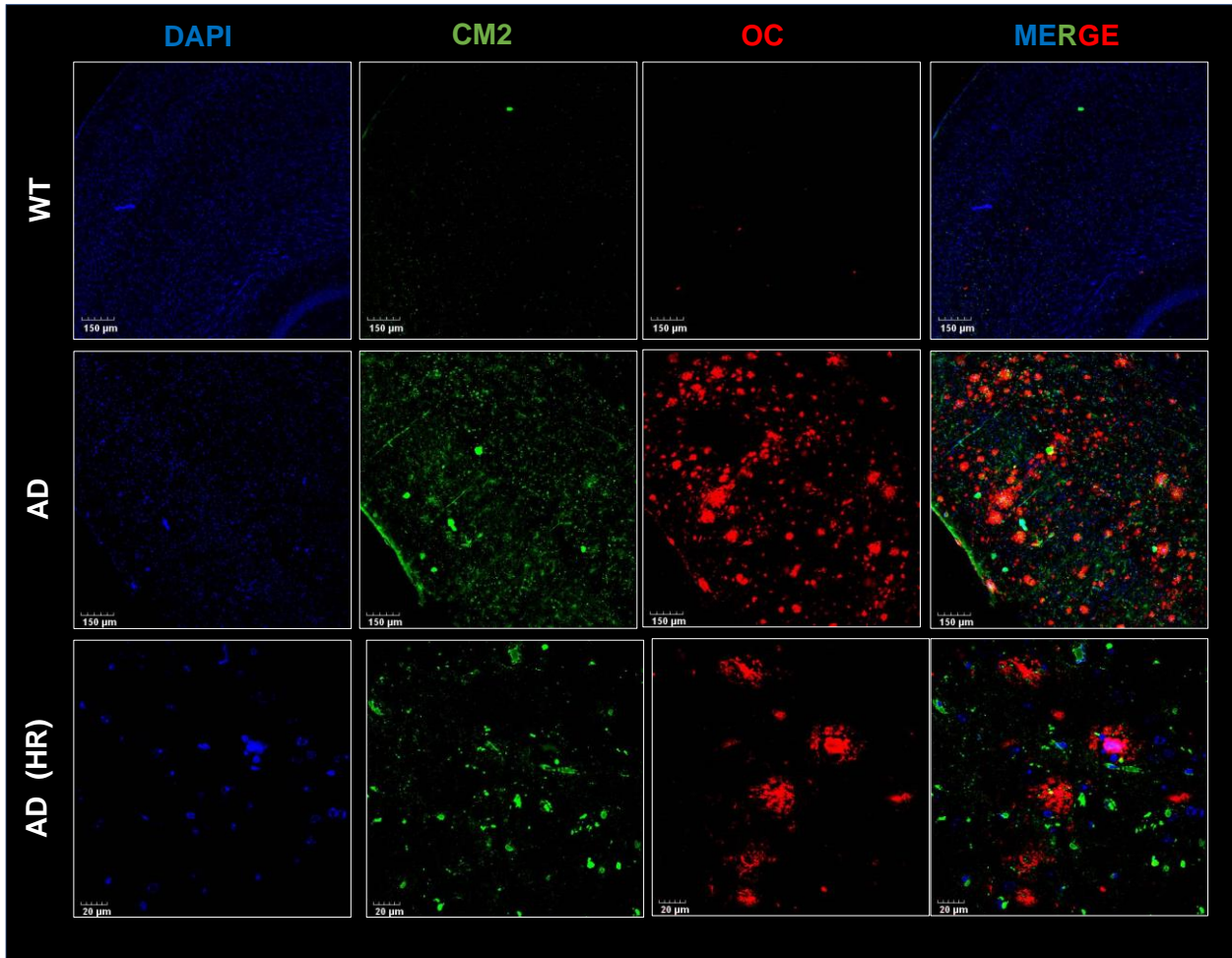


Figure 17. Confocal microscopy images of the cortex region of the CM2 administered WT and AD mouse brain, which are immunostained with amyloid fibril specific antibody (OC) followed by fluorescent-labeled ($\lambda_{\text{ex}}= 633 \text{ nm}$, $\lambda_{\text{em}}= 650 \text{ nm}$) secondary antibody (red) and DAPI (blue). Scale bar: 20 μm (HR) and 150 μm (HR); HR: high resolution.

amyloid plaques in the AD brain sections. Remarkably, high resolution images showed the localization of green fluorescence (CM1) around red fluorescence (OC) stains in both

hippocampus and cortex regions of the AD brain (Figure 16). The localization of CM1 and OC in close proximity reveals a higher local concentration of HOCl around A β aggregates and its possible involvement in the production of excessive HOCl under AD conditions. The CM2 administered AD mouse brain (hippocampus and cortex) showed significantly greater green fluorescence (~4- and 7-fold, respectively) than that of WT mouse brain, which indicates higher levels of HOCl in AD conditions (Figure 17). Furthermore, the image of A β plaques displayed an uneven amyloid burden in the cortex (~7-fold) and hippocampus (~5-fold) region of AD brain. Interestingly, the HOCl levels correlate with the amyloid burden in the cortex (~7-fold) as well as hippocampus (~4-fold) regions under AD conditions (Figure 17B and C). These proximal localization and quantification results confirm the link between A β and elevated levels of HOCl in the AD brain and qualify HOCl as a potential biomarker for AD pathogenesis along with amyloid plaques. These remarkable observations convincingly demonstrate that the elevated level of HOCl in the brain is possibly one of the definite causative factors for the oxidative stress and

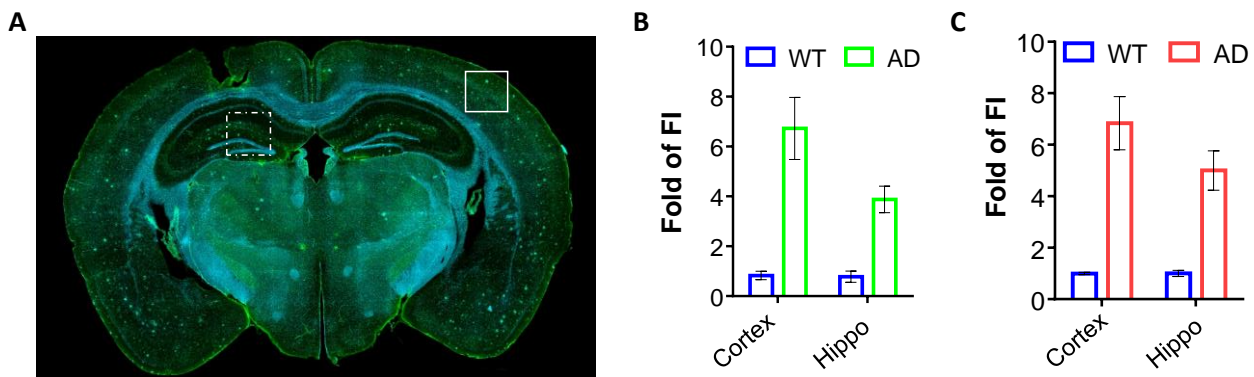


Figure 18. (A) Full view of the coronal section of the AD brain; high resolution confocal images of the specific locations of the hippocampus (broken line) and cortex (thick line) are shown in Figure 15 and 16. (B, C) Quantification of green-FI (HOCl levels) and red-FI (amyloid plaques) in different regions (cortex and hippocampus) of WT and AD mouse brain. Data represent mean intensity \pm SEM, n = 3 per group. FI: fluorescence increment; Hippo: hippocampus.

neuroinflammation in AD pathogenesis. These studies have established the selective detection, imaging, and quantification of HOCl levels in the AD brain employing the thioamide to amide transformation of CM probes.

5.6 CONCLUSIONS

In conclusion, we demonstrated the design, synthesis, and regioselective transformation of thioamide (CM2) to amide (CM1) to serve as fluorescence off- and on-states for the *in vitro* and *in vivo* detection and imaging of HOCl. The BBB crossing ability of CM2 allowed unambiguous and differential detection, imaging, and quantification of HOCl in the mouse brain, which revealed elevated levels of HOCl in the AD mice compared to age-matched control. The proximal localization of HOCl possibly suggests its generation in the downstream cascade of ROS production pathways of metal-amyloid plaques. Our study established and validated that the elevated levels of HOCl in the AD brain correlate well with the amyloid plaques and that HOCl is a reliable biomarker to expand the repertoire of NIA-AA biomarkers for the diagnosis of AD.

5.7 EXPERIMENTAL METHODS

5.7.1 General Methods

All reagents and solvents were obtained from Merck or Spectrochem and used without further purification unless it is mentioned. The amyloid specific antibody (OC) for immunostaining was obtained from Merck (AB2286). All the moisture sensitive reactions were performed under nitrogen or argon atmosphere. Agilent Cary series UV-Vis-NIR absorption and Agilent Cary eclipse fluorescence spectrophotometers were used to perform absorption and fluorescence measurements, respectively. Origin 8.5 or Prism 6 software was used to process and analyze the raw data. NMR spectra (^1H and ^{13}C NMR) of all synthesized compounds were recorded by a

Bruker AV-400 spectrometer (tetramethylsilane used as internal standard). HRMS spectra of all synthesized compounds were acquired on Agilent 6538 UHD HRMS/Q-TOF high-resolution spectrometer. The calculated amount of CM probes was dissolved in deionized water (Milli Q) (contain 5% dimethyl sulfoxide) and stored at -20 °C. Further, the stock solutions were diluted in phosphate buffered saline (PBS, pH= 7.4) for the experiments. The cells and the brain images were captured using confocal fluorescence microscope (Olympus FV3000).

5.7.2 Synthesis of ethyl-7-(diethylamino)-2-oxo-2H-chromene-3-carboxylate (I1).

To a solution of diethylsalicylaldehyde (2.5 g, 12.94 mmol) in EtOH (35 mL), diethylmalonate (2.36 mL, 15.52 mmol) and piperidine (1.5 mL) were added. The reaction mixture was refluxed at 85 °C for 12 h and monitored by thin layer chromatography (TLC). After completion of the reaction, solvent was evaporated under vacuum and the crude was diluted with water (30 mL) and the compound was extracted into dichloromethane (DCM) (3 X 50 mL). The DCM extract was washed with water (1 X 25 mL), brine (1 X 30 mL), dried over Na₂SO₄ (anhydrous) and evaporated under vacuum. The crude product was purified by column chromatography using hexane : ethyl acetate as eluent.

¹H NMR (400 MHz, CDCl₃): δ 8.41 (s, 1H), 7.34 (d, J= 8.8 Hz, 1H), 6.59 (dd, J= 2.4 Hz, J= 6.8 Hz, 1H), 6.45 (d, J= 2.0 Hz, 1H), 4.36 (q, J= 7.2 Hz, 2H), 3.43 (dd, J= 7.2 Hz, J= 6.8 Hz, 4H), 1.38 (t, J= 7.2 Hz, 3H), 1.22 (t, J= 7.2 Hz, 6H). ¹³C NMR (CDCl₃, 100 MHz): δ 163.3, 157.4, 157.3, 151.8, 148.2, 130.0, 108.5, 107.9, 106.7, 95.7, 76.2, 76.0, 75.8, 60.1, 44.1, 13.4, 11.4. HRMS (ESI-MS): m/z calculated for C₁₆H₁₉NO₄ [M+H]⁺= 290.1387, observed 290.1395.

5.7.3 Synthesis of 7-(diethylamino)-2-oxo-2H-chromene-3-carboxylic acid (I2)

To a solution of ethyl-7-(diethylamino)-2-oxo-2H-chromene-3-carboxylate (1.0 g, 3.41 mmol) conc. HCl (25 mL) was added dropwise, and the mixture was stirred at room temperature for 48 h. The reaction mixture was transferred into an ice bath, and sodium hydroxide (10 M) was added dropwise into the reaction mixture; the precipitate formed was collected by suction filtration and dried under the vacuum.

¹H NMR (400 MHz, DMSO-*d*₆): δ 12.50 (s, 1H), 8.75 (s, 1H), 7.62 (s, *J* = 4 Hz, 1H) 6.77 (q, *J* = 12Hz, 1H), 6.55 (s, 1H), 3.47 (q, *J* = 24 Hz, 4H), 1.13 (t, *J* = 8 Hz, 6H). ¹³C NMR (DMSO-*d*₆, 100 MHz): δ 164.4, 159.6, 157.8, 152.8, 149.3, 131.7, 110.2, 107.1, 95.9, 44.3, 12.2. HRMS (ESI-MS): *m/z* calculated for C₁₄H₁₅NO₄ [M+H]⁺ = 262.1001, observed 262.1046.

5.7.4 Synthesis and Characterization of CM1

To a solution of 7-(diethylamino)-2-oxo-2H-chromene-3-carboxylic acid (0.5 g, 2.63 mmol) in DMF (10 mL), DIPEA (1.1 g, 10.52 mmol) HBTU (1.2 g, 3.15 mmol) and HOBT (0.42 g, 3.15 mmol) were added. The reaction mixture was allowed to stir for 15 min on the ice bath under nitrogen atmosphere and morpholine (275 mg, 3.15 mmol) was added, and the reaction mixture was further allowed to stir at room temperature for 12 h. After the completion of the reaction (monitored by TLC), DMF was evaporated under vacuum and the crude was diluted with water (30 mL), compound was extracted into DCM (3 X 30 mL). The collected DCM extracts was washed with water (1 X 20 mL), brine (1 X 20 mL), dried over Na₂SO₄ (anhydrous) and evaporated under vacuum. The crude product was purified by column chromatography using hexane : ethyl acetate as eluent.

¹ H NMR (400 MHz, DMSO-*d*₆): δ 7.99 (s, 1H), 7.50 (d, *J* = 8.9 Hz, H), 6.75 (dd, *J* = 8.9 Hz, 2.5 Hz, 1H), 6.56 (d, *J* = 2.3 Hz, 1H), 3.69-3.52 (m, 8H), 3.46 (dd, *J* = 14.0, 7.0 Hz, 4 H), 1.19-1.09

(m, 6H). ^{13}C NMR (DMSO- d_6 , 100 MHz): δ 164.1, 158.3, 156.6, 151.2, 143.9, 130.0, 115.7, 109.3, 107.1, 96.2, 66.2, 53.5, 47.1, 44.1, 41.8, 18.0, 16.7, 12.2. HRMS (ESI-MS): m/z calculated for $\text{C}_{18}\text{H}_{22}\text{N}_2\text{O}_4$ $[\text{M}+\text{H}]^+ = 331.1652$, observed 331.1649.

5.7.5 Synthesis and Characterization of CM2

To a solution of 7-(diethylamino)-3-(morpholine-4-carbonyl)-2H-chromen-2-one (100 mg, 3.89 mmol) in toluene (5 mL), Lawesson's reagent (157 mg, 3.89 mmol) was added and refluxed for 12 h. The solvent was evaporated under vacuum and the crude was diluted with water (20 mL), compound was extracted into DCM (3X 20 mL). The collected DCM extracts was washed with water (1 X 15 mL), brine (1 X 15 mL), dried over Na_2SO_4 (anhydrous) and evaporated under vacuum. The crude product was purified by column chromatography using hexane : ethyl acetate as eluent.

^1H NMR (400 MHz, DMSO- d_6): δ 7.96 (s, 1H), 7.55 (d, J= 8.9 Hz, 1H), 6.78 (dd, J= 8.9 Hz, 2.4 Hz, 1H), 6.60 (d, J= 2.3 Hz, 1H), 4.41-4.33 (m, 1H), 4.21 (m, 2H), 3.81-3.74 (m, 2H), 3.49 (q, J= 7.1 Hz, 4H), 1.16 (t, J= 7.0 Hz, 6H). ^{13}C NMR (DMSO- d_6 , 100 MHz): δ 191.8, 157.3, 156.3, 151.0, 143.1, 130.3, 121.9, 109.4, 107.3, 96.2, 66.1, 65.6, 52.2, 49.3, 44.1, 12.2. HRMS (ESI-MS): m/z calculated for $\text{C}_{18}\text{H}_{22}\text{N}_2\text{O}_4$ $[\text{M}+\text{H}]^+ = 347.1424$, observed 347.1434.

5.7.6 Absorption and Fluorescence Spectroscopy

UV-visible absorption and fluorescence spectroscopy measurements were carried out using single beam Agilent Cary series UV-Vis-NIR absorption and Agilent Cary eclipse fluorescence spectrophotometers at room temperature, respectively. 1 cm path length quartz cuvette (1 mL) was used for all the absorption and fluorescence measurements.

5.7.7 Preparation of Reactive Oxygen Species (ROS)

Various ROS (NO²⁻, NO³⁻, NO, t-BuOOH, H₂O₂, HO[·], ¹O₂ and ClO⁻) were prepared according to the following protocols. Calculated amount of NaNO₂, NaNO₃ and sodium nitroferricyanide (III) dihydrate were dissolved in PBS (pH= 7.4, 10 mM) to obtain NO²⁻, NO³⁻ and NO, respectively. Analytical grade t-BuOOH and H₂O₂ were obtained from Alfa Aesar and used as received. Hydroxyl radicals were generated in situ using Cu^{II}-Ascorbate redox pair. Singlet oxygen was generated using NaOCl and H₂O₂. NaOCl was used to generate ClO⁻ *in situ* and its concentration was measured using absorption study ($\epsilon = 350 \text{ M}^{-1} \text{ cm}^{-1}$ at 292 nm) at pH 9.0. The stock solutions of metal ions (Ni^{II}, Zn^{II}, Ca^{II}, Co^{II}, Na⁺, K⁺, Al^{III}, Fe^{III}, Cd^{II} and Pb^{II}) were prepared by dissolving calculated amounts of NiCl₂, ZnCl₂, CaCl₂, CoCl₂, NaCl, KCl, AlCl₃, FeCl₃, CdSO₄ and PbNO₃ salts, respectively, in deionized water (Milli Q). Similarly, the stock solutions of anions (Asc, S₂O₈²⁻, S²⁻, N³⁻, Cl⁻, I⁻, CO³⁻, OAc⁻, AsO₄³⁻, SO₄²⁻ and S₂O₃²⁻) were prepared by dissolving calculated amounts of sodium ascorbate, Na₂S₂O₈, Na₂S, NaN₃, NaCl, KI, Na₂CO₃, NaOAc, Na₃AsO₄, Na₂SO₄ and Na₂S₂O₃, respectively, in deionized water (Milli Q). Response of CM2 in Presence of A β 42. Response of CM2 was evaluated by measuring the fluorescence in presence of freshly prepared monomers (m), oligomers (o), and fibrils (f) of A β 42. A β 42 peptide (0.25 mg, Calbiochem, Merck) was dissolved in HFIP (200 μ L) and sonicated for 30 min. A β 42 sample was dried under the nitrogen flow and further dissolved in PBS (pH 7.4, 50 mM) containing NaCl (150 μ M). The A β 42 solution was incubated to produce oligomers and fibrils at 4 °C and 37 °C, respectively. Finally, CM2 (10 μ M) was added to different forms (monomers, oligomers, and fibrils) of A β 42 (10 μ M) and fluorescence ($\lambda_{\text{ex}} = 417 \text{ nm}$ and $\lambda_{\text{em}} = 485 \text{ nm}$) was measured using microplate reader (SpectraMax i3x).

5.7.8 Cell Culture

SHSY5Y cells were cultured using DMEM/F-12 (Dulbecco's Modified Eagle Medium / Nutrient Mixture F-12) medium (Gibco, Invitrogen) containing 10% of FBS (fetal bovine serum) and 1% PS (pen-strep) under the cell growing condition (37 °C temperature and 5% CO₂ atmosphere). For imaging experiments the cells were cultured in 35 mm petri dish under similar condition and the cells were fixed using 4% paraformaldehyde (PFA) solution.

5.7.9 Cytotoxicity Assay

To evaluate the cytotoxicity of CM2, we performed MTT assay in SHSY5Y cells. The cells were (15,000 cells/well) cultured in a 96-well plate using cell growing media and incubated with different concentrations of CM2 for 24 h. Further MTT (15 mL, 5 mg/mL) solution was added into the cell media and incubated for 3 h. Finally, the medium was exchanged with 100 μ L DMSO-MeOH (1:1) mixture and the absorbance were monitored at 570 nm using microplate reader (SpectraMax i3x, Molecular Devices).

5.7.10 Intracellular HOCl Imaging

To demonstrate the ability of CM2 for the detection and imaging of HOCl in cellular conditions, we performed imaging experiments with SHSY5Y cells. For this experiment, SHSY5Y cells were cultured in 35 mm petri dish with cell growing media. The cells were fixed with 4% PFA and incubated with CM2 (0.5 μ M) and DAPI for 30 min. The cells were washed three times with PBS and again incubated with NaOCl (400 μ M) for 30 min. Finally, the cells were washed and imaged under the confocal fluorescence microscope.

5.7.11 Genotyping of Mice

The mice were genotyped after attaining the age of weaning at 4-6 weeks. To collect genomic DNA, the tail was collected from each and every mouse and processed with NaOH and Tris-HCl buffer. The genotyping was performed according to the Jackson Laboratory's protocol and mice were confirmed as AD or WT mice. The primer sequences used for genotyping are as follows.

APP: 5'-GACTGACCACTCAGCCAGGTTCTG-3', 5'CTTGTAAGTTGGATTCTCATATCCG-3'; PSEN1: 5'-ATTAGAGAACGGCAGGAGCA-3', 5'-GCCATGAGGGGCACTAATCAT-3'.

5.7.12 Blood Brain Barrier (BBB) Crossing Experiment

For this BBB experiment, PBS (control) and CM2 were administered to WT C57BL/6 mice and sacrificed after 45 and 90 min to collect the brains. Then the brains were homogenized with equal amount (1.5 mL) of PBS and supernatants were collected for spectroscopy study. The absorbance and fluorescence of brain supernatants were measured in microplate reader in the absence and presence of ClO $^-$. All the data were plotted and analyzed in prism 6 software. Next, dichloromethane (DCM) extract of the brain lysate was further concentrated for mass analysis (MALDI) using α -cyano-4-hydroxycinnamic acid (CCA) matrix.

5.7.13 In Cellulo Imaging of HOCl Under AD-like Condition

SHSY5Y cells were treated with A β 42-Cu II complex to create AD like condition and excessive production of HOCl was imaged employing CM2 probe. For this experiment, SHSY5Y cells were cultured in 35 mm Petri dish and incubated with A β 42-Cu II (20 μ M) complex for 2 h. The cells were fixed with 4% PFA followed by incubation with CM2 (0.5 μ M) for 30 min and DAPI was used to stain the nucleus. The cells were imaged under the confocal fluorescence microscope.

5.7.14 Animal Model for *In Vivo* Experiment

B6.Cg-Tg(APP^{swe},PSEN1^{dE9})85Dbo/Mmjax mice (APP/PS1) were obtained from Jackson Laboratory (stock number 004462) and maintained and bred in the JNCASR animal facility under a 12 h light and dark cycle. All the studies were executed according to the guidelines of the Institutional Animal Ethics Committee (IAEC), JNCASR. The protocol (TG001) was approved by the IAEC and the Committee for the purpose of Control and Supervision of Experiments on Animals (CPCSEA).

5.7.15 *In Vivo* Administration of Probe

CM2 (1 mg/kg body weight) and vehicle (PBS) were administered into AD and WT mice (12 months, n = 3) through the nasal route. The probe (CM2) administration was performed twice over an interval of 12 h before sacrificing them for further studies.

5.7.16 Brain Collection and Immunohistochemistry

After the administration of CM2, the mice were sacrificed through cervical dislocation and their brains were collected. The collected brains were fixed with 4% PFA for 48 h and rehydrated with sucrose solution (30%). The brains were sectioned (40 μ m) using a cryostat with a -20 °C internal chamber temperature. Here, 2% BSA (bovine serum albumin) and 1% goat serum were used to block the brain sections. Following the blocking procedure, the sections were incubated with primary antibodies (1:1000) for 48 h at 4 °C with gentle shaking. The unbound primary antibody was washed, and the sections were incubated with fluorescently (red) labeled secondary antibody (1:300) for 4 h at room temperature in the dark with gentle shaking. These brain sections were incubated with 4',6-diamidino-2-phenylindole (DAPI) for 10 min and taken on a glass slide for

mounting with Vectashield mounting media and then imaged using a confocal fluorescence microscope (Olympus FV3000).

5.7.17 Image Analysis

All the brain images were analyzed and the intensity of green and red fluorescence was calculated using ImageJ software. GraphPad Prism was used to plot and analyze the results. Two-way ANOVA was used to analyze datasets with more than one independent variable. Further, Bonferroni's multiple comparisons Post hoc test was applied to determine the significant difference in the result ($P < 0.05$).

5.8 Appendix

- ❖ Single Crystal Analysis of CM2
- ❖ Crystallographic Data of CM2
- ❖ Compound I1, ^1H , ^{13}C NMR, and HRMS analysis
- ❖ Compound I2, ^1H , ^{13}C NMR and HRMS analysis
- ❖ Compound CM1, ^1H , ^{13}C NMR and HRMS analysis
- ❖ Compound CM2, ^1H , ^{13}C NMR and HRMS analysis
- ❖ Journal Cover Art

Datablock: CM2

Bond precision: C-C = 0.0089 Å Wavelength=0.71073

Cell: a=13.3839(5) b=19.2766(9) c=8.6173(3) alpha=90

beta=126.480(2) gamma=90

Temperature: 296 K

| | Calculated | Reported |
|----------------|-----------------|-----------------|
| Volume | 1787.62(13) | 1787.62(13) |
| Space group | C c | C c |
| Hall group | C -2yc | C -2yc |
| Moiety formula | C18 H22 N2 O3 S | ? |
| Sum formula | C18 H22 N2 O3 S | C18 H22 N2 O3 S |
| Mr | 346.44 | 346.43 |
| Dx,g cm-3 | 1.287 | 1.287 |
| Z | 4 | 4 |
| Mu (mm-1) | 0.199 | 0.199 |
| F000 | 736.0 | 736.0 |
| F000' | 736.80 | |
| h,k,lmax | 17,25,11 | 17,25,11 |
| Nref | 4430[2221] | 3467 |
| Tmin,Tmax | 0.947,0.976 | 0.947,0.976 |
| Tmin' | 0.909 | |

Correction method= # Reported T Limits: Tmin=0.947 Tmax=0.976 AbsCorr = MULTI-SCAN

Data completeness= 1.56/0.78 Theta(max)= 28.258

R(reflections)= 0.0641(2748)

wR2(reflections)= 0.1875(3467)

S = 1.040

Npar= 220

Alert level C

[ABSTY02_ALERT_1_C](#) An _exptl_absorpt_correction_type has been given without a literature citation. This should be contained in the _exptl_absorpt_process_details field.

Absorption correction given as multi-scan

[PLAT031_ALERT_4_C](#) Refined Extinction Parameter Within Range 2.526 Sigma

[PLAT094_ALERT_2_C](#) Ratio of Maximum / Minimum Residual Density 2.96 Report

[PLAT241_ALERT_2_C](#) High 'MainMol' Ueq as Compared to Neighbors of N2 Check

[PLAT242_ALERT_2_C](#) Low 'MainMol' Ueq as Compared to Neighbors of C16 Check

[PLAT242_ALERT_2_C](#) Low 'MainMol' Ueq as Compared to Neighbors of C18 Check

[PLAT340_ALERT_3_C](#) Low Bond Precision on C-C Bonds 0.00886 Ang.

[PLAT915_ALERT_3_C](#) No Flack x Check Done: Low Friedel Pair Coverage 57 %

Alert level G

[PLAT066_ALERT_1_G](#) Predicted and Reported Tmin&Tmax Range Identical ? Check

[PLAT072_ALERT_2_G](#) SHELXL First Parameter in WGHT Unusually Large 0.13

Report

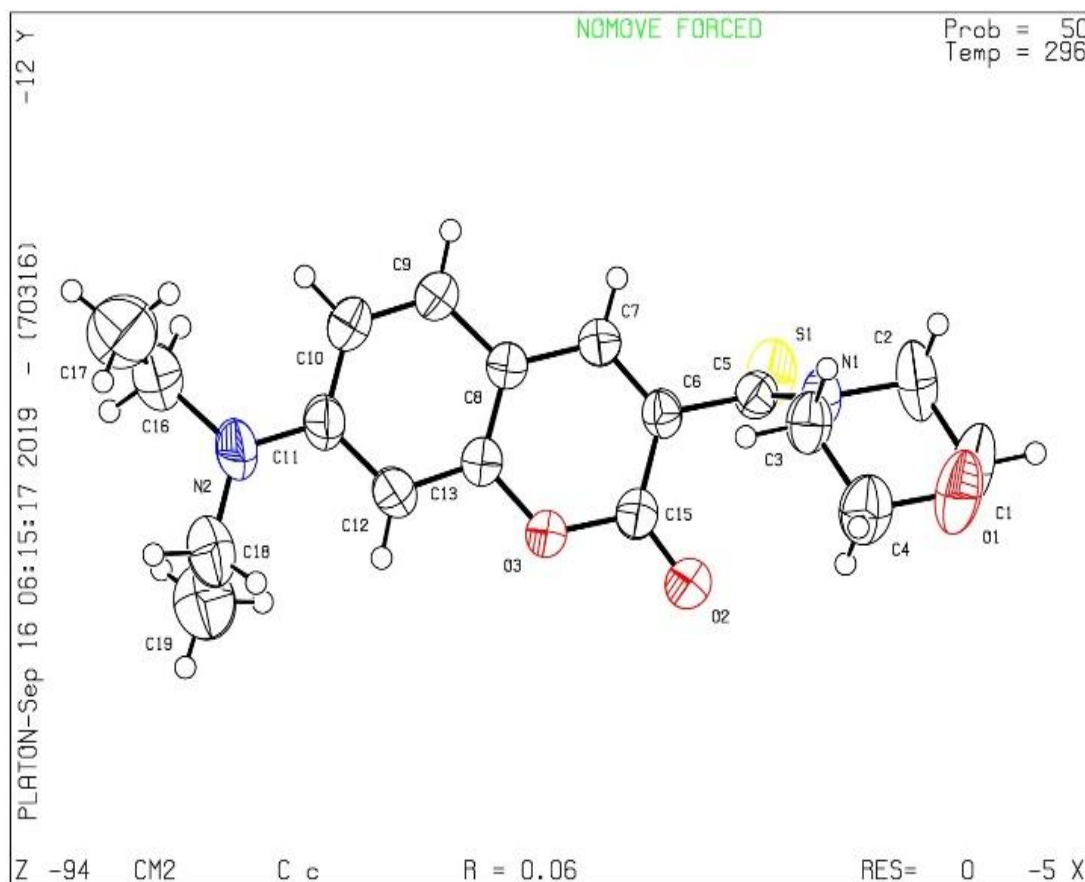
[PLAT128_ALERT_4_G](#) Alternate Setting for Input Space Group Cc Ic Note

[PLAT720_ALERT_4_G](#) Number of Unusual/Non-Standard Labels 3 Note

[PLAT883_ALERT_1_G](#) No Info/Value for _atom_sites_solution_primary . Please Do !

[PLAT910_ALERT_3_G](#) Missing # of FCF Reflection(s) Below Theta(Min). 3 Note

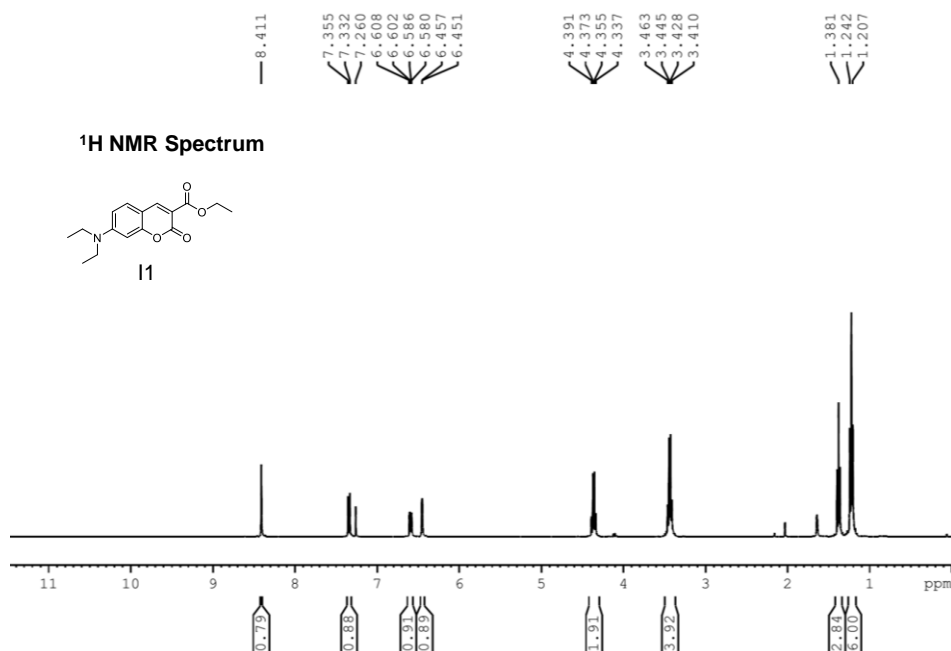
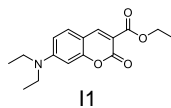
- [PLAT912 ALERT 4 G](#) Missing # of FCF Reflections Above STh/L= 0.600 5 Note
- [PLAT933 ALERT 2 G](#) Number of OMIT Records in Embedded .res File ... 7 Note
- [PLAT978 ALERT 2 G](#) Number C-C Bonds with Positive Residual Density. 1 Info
- [PLAT992 ALERT 5 G](#) Repd & Actual _reflns_number_gt Values Differ by 2 Check



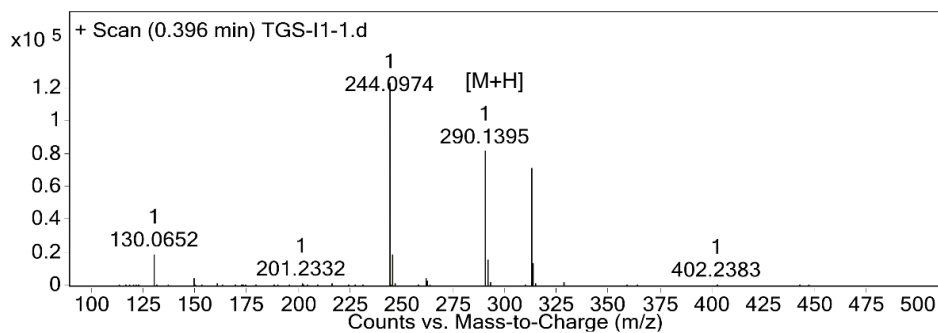
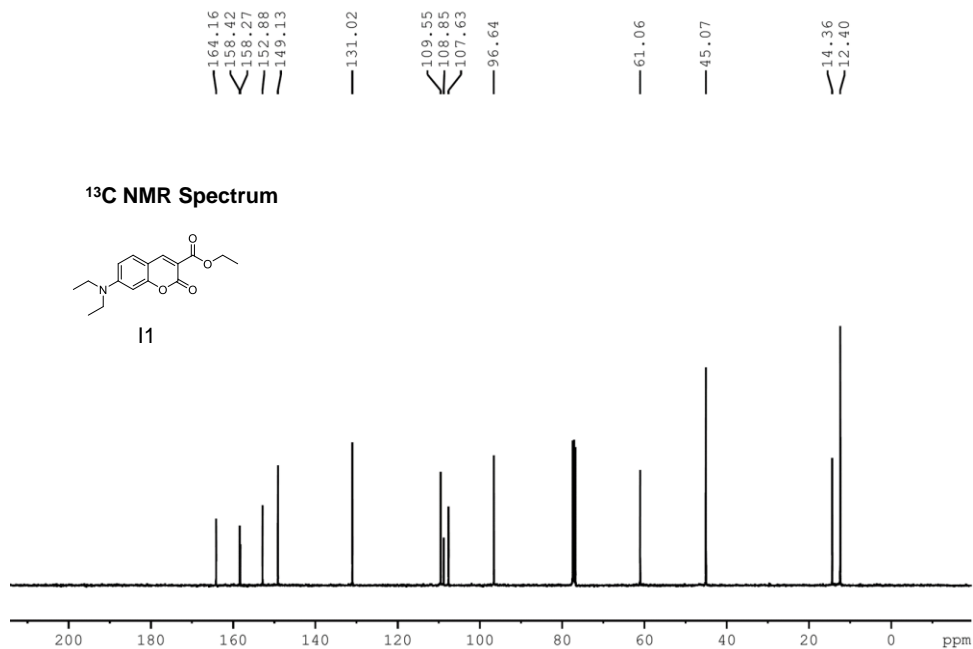
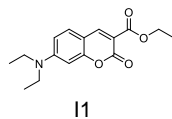
5.10 Crystallographic data of CM2 (CCDC Deposition Number 1955148)

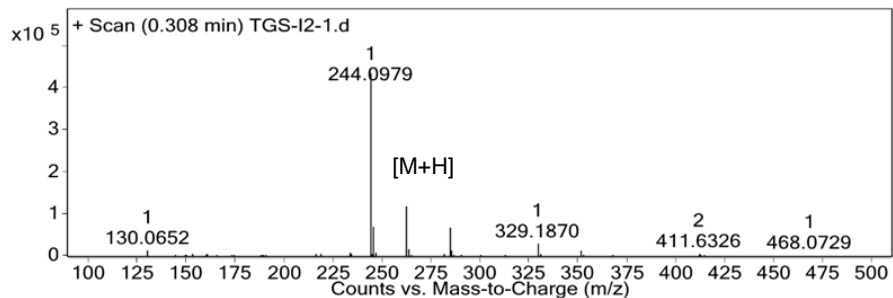
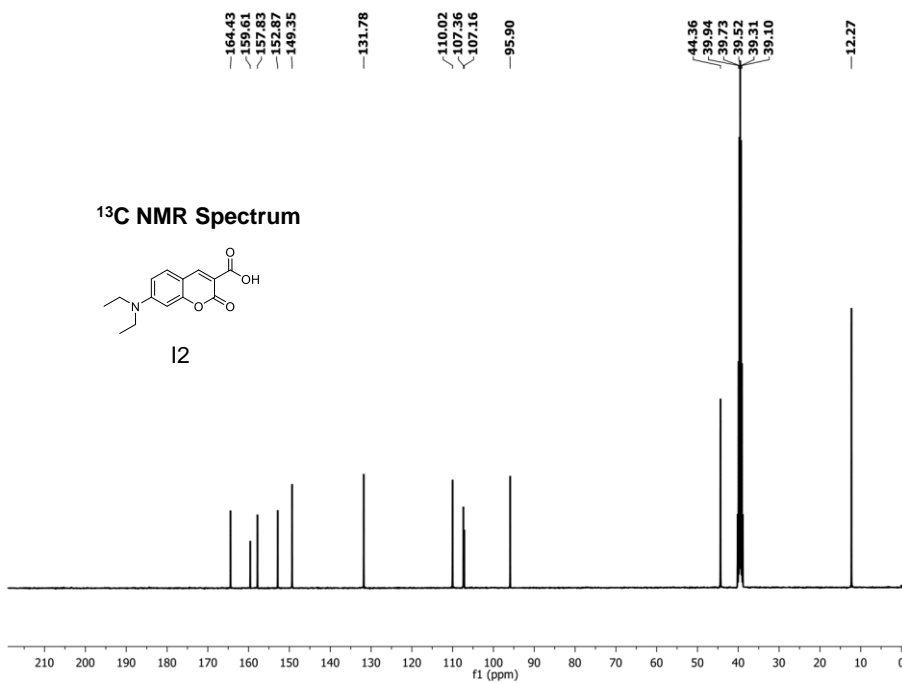
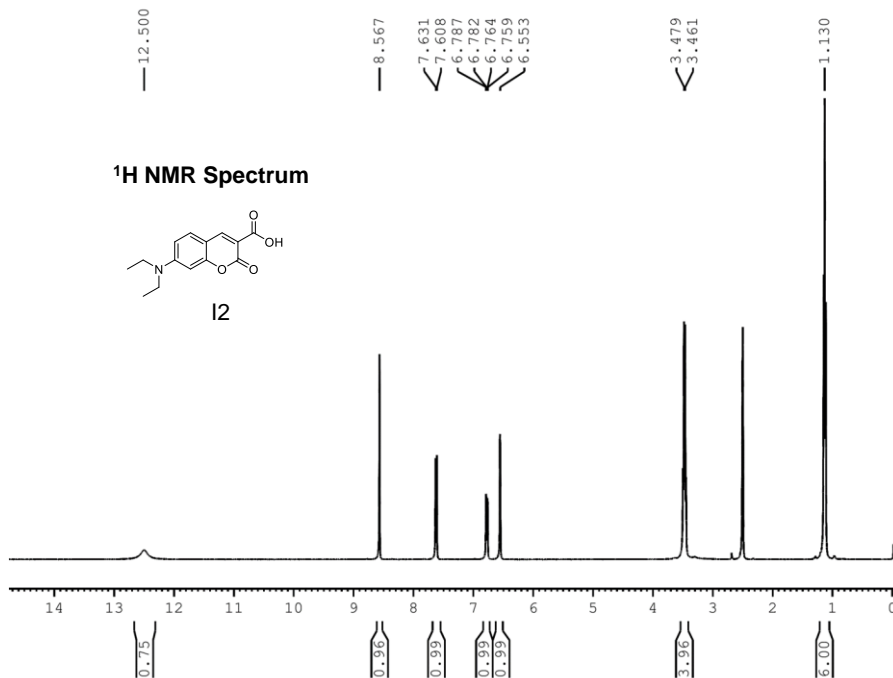
| <u>Crystallographic Parameters</u> | <u>Crystallographic Data</u> |
|---|---|
| Formula | C ₁₈ H ₂₂ N ₂ O ₃ S |
| Formula weight | 346.43 |
| Crystal system | Monoclinic |
| Space group | <i>C c</i> |
| <i>a</i> (Å) | 13.3839(5) |
| <i>b</i> (Å) | 19.2766(9) |
| <i>c</i> (Å) | 8.6173(3) |
| α (°) | 90 |
| β (°) | 126.480 |
| γ (°) | 90 |
| <i>Z</i> | 4 |
| <i>F</i> (000) | 736 |
| Temperature (K) | 296(2) |
| <i>V</i> (Å ³) | 1787.62(13) |
| Calculated density (μg·m ⁻³) | 1.287 |
| Crystal size (mm ³) | 0.48X 0.23 X 0.12 |
| μ (mm ⁻¹) | 0.199 |
| Limiting indices | -17 ≤ <i>h</i> ≤ 17, -25 ≤ <i>k</i> ≤ 25, -11 ≤ <i>l</i> ≤ 9 |
| Reflections collected/ Unique | 21010/ 3467 |
| <i>R</i> ₁ , <i>wR</i> ₂ [all data] | 0.0790, 0.1875 |
| <i>R</i> ₁ , <i>wR</i> ₂ [<i>I</i> > 2σ(<i>I</i>)] | 0.0641, 0.1718 |
| Largest diffraction peak and hole (e Å ⁻³) | 0.806/ -0.272 |

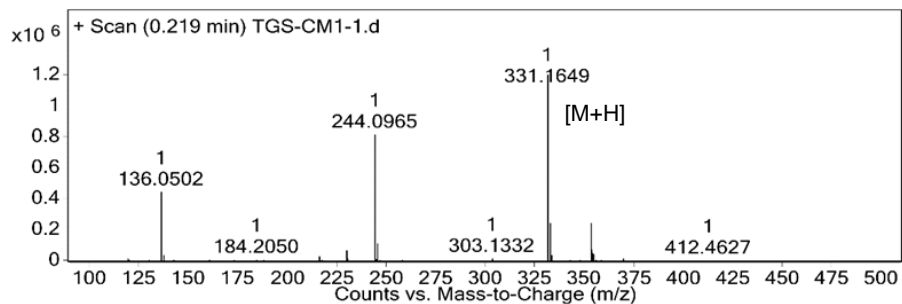
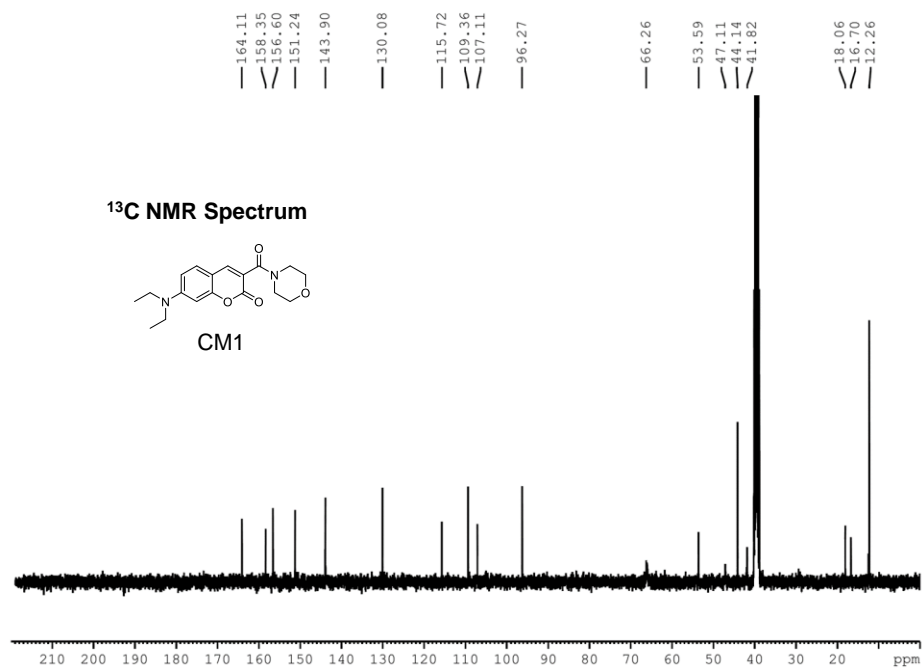
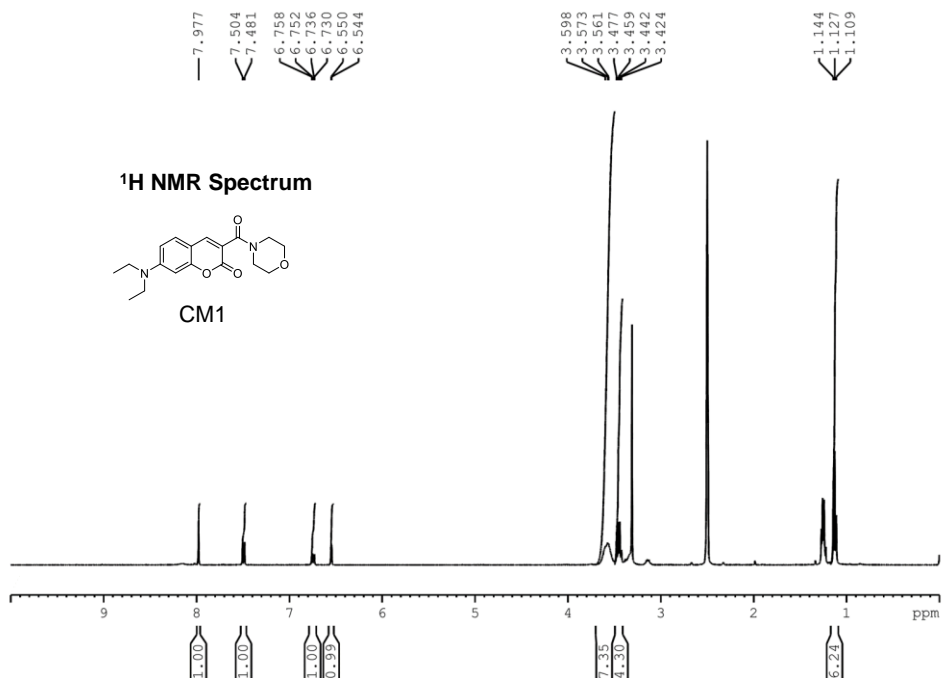
¹H NMR Spectrum

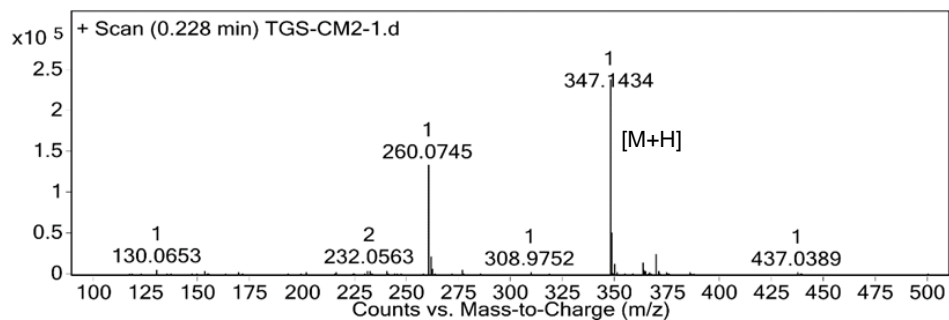
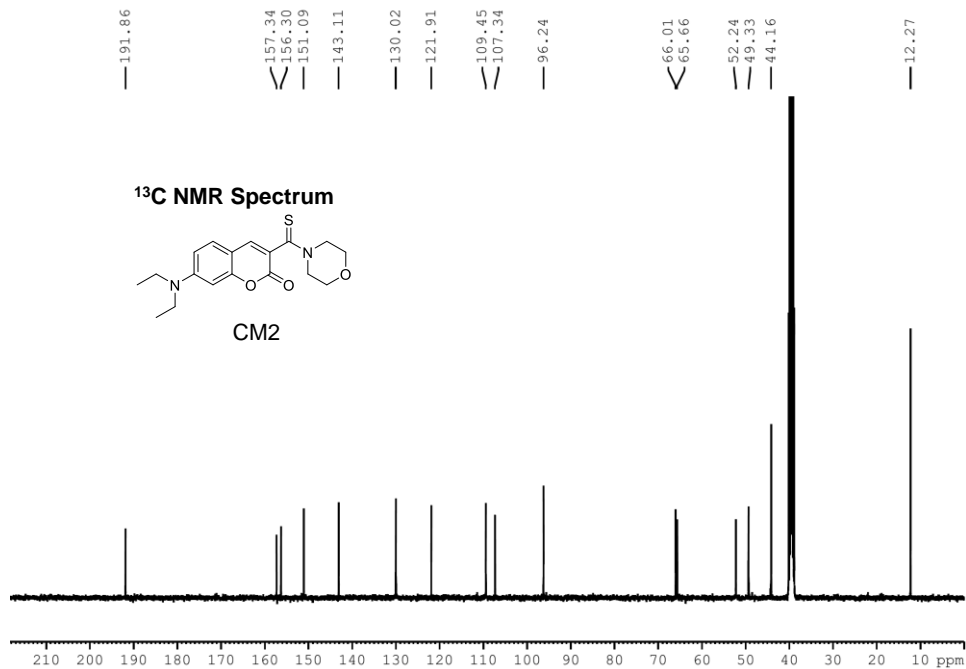
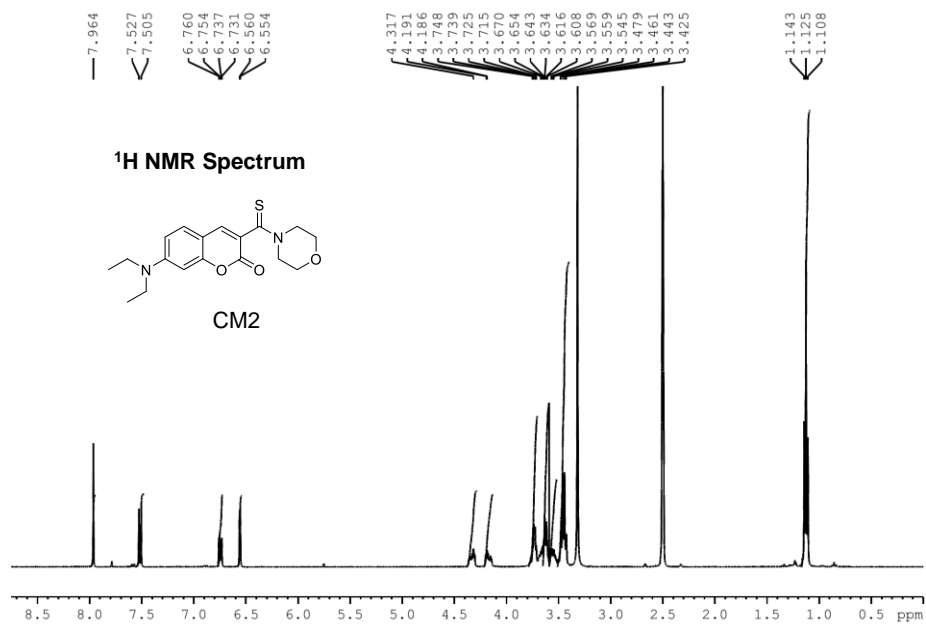


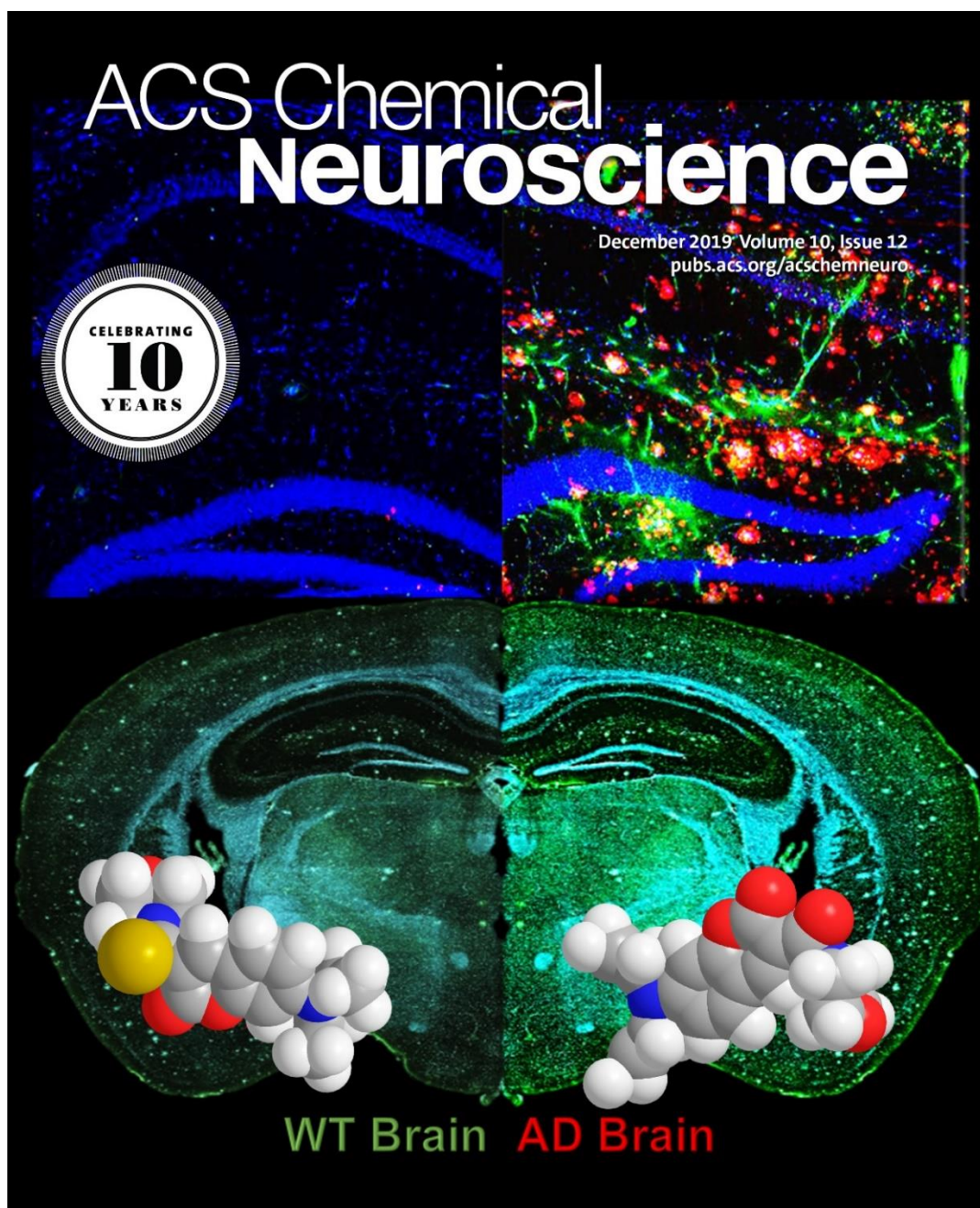
¹³C NMR Spectrum











The BBB crossing ability and thioamide-to-amide regioselective transformation of CM2 probe allowed unambiguous and differential detection, imaging and quantification of HOCl in the Alzheimer's disease (AD) and wild-type (WT) mice brains. This study established and validated the elevated level of HOCl (green) proximally localized with amyloid plaques (red) in the AD mouse brain as reliable marker to expand the repertoire of biomarkers for diagnosis of AD.

5.9 REFERENCES

1. Alzheimer's Association, 2015 Alzheimer's disease facts and figures. *Alzheimers Dementia* **2015**, *11*, 332-384.
2. Hardy, J.; and Selkoe, D. J. The amyloid hypothesis of Alzheimer's disease: progress and problems on the road to therapeutics. *Science* **2002**, *297*, 353-356.
3. Mandelkow, E. Alzheimer's disease. The tangled tale of tau. *Nature* **1999**, *402*, 588-589.
4. Reitz, C.; Brayne, C.; and Mayeux, R. Epidemiology of Alzheimer disease. *Nat. Rev. Neurol.* **2011**, *7*, 137-152.
5. Dobson, C. M. Protein folding and misfolding. *Nature* **2003**, *426*, 884-890.
6. Rajasekhar, K.; Chakrabarti, M.; and Govindaraju, T. Function and toxicity of amyloid beta and recent therapeutic interventions targeting amyloid beta in Alzheimer's disease. *Chem. Commun.* **2015**, *51*, 13434-13450.
7. Alzheimer's Association 2018 Alzheimer's disease facts and figures (vol 14, pg 367, 2018). *Alzheimers Dementia* **2018**, *14*, 701.
8. Huang, Y.; and Mucke, L. Alzheimer mechanisms and therapeutic strategies. *Cell* **2012**, *148*, 1204-22.
9. Rajasekhar, K.; and Govindaraju, T. Current progress, challenges and future prospects of diagnostic and therapeutic interventions in Alzheimer's disease. *RSC Adv.* **2018**, *8*, 23780-23804.
10. Hampel, H.; O'Bryant, S. E.; Molinuevo, J. L.; Zetterberg, H.; Masters, C. L.; Lista, S.; Kiddle, S. J.; Batrla, R.; and Blennow, K. Blood-based biomarkers for Alzheimer disease: mapping the road to the clinic. *Nat. Rev. Neurol.* **2018**, *14*, 639-652.
11. Hatai, J.; Motiei, L.; and Margulies, D. Analyzing amyloid beta aggregates with a combinatorial fluorescent molecular sensor. *J. Am. Chem. Soc.* **2017**, *139*, 2136-2139.
12. Rajasekhar, K.; Narayanaswamy, N.; Murugan, N. A.; Viccaro, K.; Lee, H. G.; Shah, K.; and Govindaraju, T. A beta plaqueselective NIR fluorescence probe to differentiate Alzheimer's disease from tauopathies. *Biosens. Bioelectron.* **2017**, *98*, 54-61.
13. Rajasekhar, K.; Narayanaswamy, N.; Murugan, N. A.; Kuang, G.; Agren, H.; and Govindaraju, T. A high affinity red fluorescence and colorimetric probe for amyloid beta aggregates. *Sci. Rep.* **2016**, *6*, 23668.

14. Jack, C. R. Jr.; Bennett, D. A.; Blennow, K.; Carrillo, M. C.; Dunn, B.; Haeberlein, S. B.; Holtzman, D. M.; Jagust, W.; Jessen, F.; Karlawish, J.; Liu, E.; Molinuevo, J. L.; Montine, T.; Phelps, C.; Rankin, K. P.; Rowe, C. C.; Scheltens, P.; Siemers, E.; Snyder, H. M.; Sperling, R.; *et al.* NIA-AA research framework: toward a biological definition of Alzheimer's disease. *Alzheimer's Dementia* **2018**, *14*, 535-562.
15. Nation, D. A.; Sweeney, M. D.; Montagne, A.; Sagare, A. P.; D'Orazio, L. M.; Pachicano, M.; Seppehrband, F.; Nelson, A. R.; Buennagel, D. P.; Harrington, M. G.; Benzinger, T. L. S.; Fagan, A. M.; Ringman, J. M.; Schneider, L. S.; Morris, J. C.; Chui, H. C.; Law, M.; Toga, A. W.; and Zlokovic, B. V. Blood-brain barrier breakdown is an early biomarker of human cognitive dysfunction. *Nat. Med.* **2019**, *25*, 270-276.
16. Maity, D.; Manna, A. K.; Karthigeyan, D.; Kundu, T. K.; Pati, S. K.; and Govindaraju, T. Visible-near-infrared and fluorescent copper sensors based on julolidine conjugates: selective detection and fluorescence imaging in living cells. *Chem. Eur. J.* **2015**, *17*, 1115261.
17. Bourassa, M. W.; and Miller, L. M. Metal imaging in neurodegenerative diseases. *Metallomics*. **2012**, *4*, 721-738.
18. Maity, D.; and Govindaraju, T. A differentially selective sensor with fluorescence turn-on response to Zn²⁺ and dual-mode ratiometric response to Al³⁺ in aqueous media. *Chem. Commun.* **2012**, *48*, 1039-1041.
19. Maity, D.; Kumar, V.; and Govindaraju, T. Reactive probes for ratiometric detection of Co²⁺ and Cu⁺ based on excitedstate intramolecular proton transfer mechanism. *Org. Lett.* **2012**, *14*, 6008– 11.
20. Plascencia-Villa, G.; Ponce, A.; Collingwood, J. F.; ArellanoJimenez, M. J.; Zhu, X.; Rogers, J. T.; Betancourt, I.; Jose-Yacaman, M.; and Perry, G. High-resolution analytical imaging and electron holography of magnetite particles in amyloid cores of Alzheimer's disease. *Sci. Rep.* **2016**, *6*, 24873.
21. Narayanaswamy, N.; Narra, S.; Nair, R. R.; Saini, D. K.; Kondaiah, P.; and Govindaraju, T. Stimuli-responsive colorimetric and NIR fluorescence combination probe for selective reporting of cellular hydrogen peroxide. *Chem. Sci.* **2016**, *7*, 2832-2841.

22. Jeitner, T. M.; Kalogiannis, M.; Krasnikov, B. F.; Gomlin, I.; Peltier, M. R.; and Moran, G. R. Linking inflammation and Parkinson disease: hypochlorous acid generates parkinsonian poisons. *Toxicol. Sci.* **2016**, *151*, 388-402.
23. Samanta, S.; Rajasekhar, K.; Babagond, V.; and Govindaraju, T. Small molecule inhibits metal-dependent and -independent multifaceted toxicity of Alzheimer's disease. *ACS Chem. Neurosci.* **2019**, *10*, 3611-3621.
24. Barnham, K. J.; and Bush, A. I. Biological metals and metal-targeting compounds in major neurodegenerative diseases. *Chem. Soc. Rev.* **2014**, *43*, 6727-6749.
25. Aratani, Y. Myeloperoxidase: Its role for host defense, inflammation, and neutrophil function. *Arch. Biochem. Biophys.* **2014**, *640*, 47-52.
26. Winterbourn, C. C. Reconciling the chemistry and biology of reactive oxygen species. *Nat. Chem. Biol.* **2004**, *4*, 278-286.
27. Wu, L.; Wu, I. C.; DuFort, C. C.; Carlson, M. A.; Wu, X.; Chen, L.; Kuo, C. T.; Qin, Y.; Yu, J.; Hingorani, S. R.; and Chiu, D. T. Photostable ratiometric pdot probe for in vitro and in vivo imaging of hypochlorous acid. *J. Am. Chem. Soc.* **2017**, *139*, 6911-6918.
28. Koide, Y.; Urano, Y.; Hanaoka, K.; Terai, T.; and Nagano, T. Development of an Si-rhodamine-based far-red to nearinfrared fluorescence probe selective for hypochlorous acid and its applications for biological imaging. *J. Am. Chem. Soc.* **2011**, *133*, 5680-5682.
29. Xu, Q.; Lee, K. A.; Lee, S.; Lee, K. M.; Lee, W. J.; and Yoon, J. A highly specific fluorescent probe for hypochlorous acid and its application in imaging microbe-induced HOCl production. *J. Am. Chem. Soc.* **2013**, *135*, 9944-9949.
30. Zhou, Y.; Li, J. Y.; Chu, K. H.; Liu, K.; Yao, C.; and Li, J. Y. Fluorescence turn-on detection of hypochlorous acid via HOCl-promoted dihydrofluorescein-ether oxidation and its application in vivo. *Chem. Commun.* **2014**, *48*, 4677-4679.
31. Jiao, X.; Huang, K.; He, S.; Liu, C.; Zhao, L.; and Zeng, X. A mitochondria-targeted near-infrared fluorescent probe with a large Stokes shift for real-time detection of hypochlorous acid. *Org. Biomol. Chem.* **2019**, *17*, 108-114.
32. Chan, J.; Dodani, S. C.; and Chang, C. J. Reaction-based small-molecule fluorescent probes for chemoselective bioimaging. *Nat. Chem.* **2012**, *4*, 973-984.

33. Zhu, H.; Zhang, Z.; Long, S.; Du, J.; Fan, J.; and Peng, X. Synthesis of an ultrasensitive BODIPY-derived fluorescent probe for detecting HOCl in live cells. *Nat. Protoc.* **2018**, *13*, 2348-2361.
34. Maity, D.; and Govindaraju, T. Highly selective visible and near-IR sensing of Cu²⁺ based on thiourea-salicylaldehyde coordination in aqueous media. *Chem. Eur. J.* **2012**, *17*, 1410-1414.
35. Maity, D.; and Govindaraju, T. Naphthaldehyde-urea/ thiourea conjugates as turn-on fluorescent probes for Al(III) based on restricted C=N isomerization. *Eur. J. Inorg. Chem.* **2011**, *2011*, 5479-5489.
36. Maity, D.; Karthigeyan, D.; Kundu, T. K.; and Govindaraju, T. FRET-based rational strategy for ratiometric detection of Cu²⁺ and live cell imaging. *Sens. Actuators, B* **2012**, *176*, 831-837.
37. Goldberg, J. M.; Batjargal, S.; Chen, B. S.; and Petersson, E. J. Thioamide quenching of fluorescent probes through photoinduced electron transfer: mechanistic studies and applications. *J. Am. Chem. Soc.* **2013**, *135*, 18651-18658.
38. Tang, J.; Robichaux, M. A.; Wu, K. L.; Pei, J.; Nguyen, N. T.; Zhou, Y.; Wensel, T. G.; and Xiao, H. Single-atom fluorescence switch: a general approach toward visible-light activated dyes for biological imaging. *J. Am. Chem. Soc.* **2019**, *141*, 14699.

❖ Publications

1. **Samanta, S.**; Rajasekhar, K.; Babagond, V.; Govindaraju, T. Small molecule inhibits metal-dependent and-independent multifaceted toxicity of Alzheimer's disease. *ACS Chem. Neurosci.* **2019**, *10*, 3611-3621. ([Cover Page](#))
2. **Samanta, S.**; Govindaraju, T. Unambiguous detection of elevated levels of hypochlorous acid in double transgenic ad mouse brain. *ACS Chem. Neurosci.* **2019**, *10*, 4847-4853. ([Cover Page, celebrating 10th year of ACS Chemical Neuroscience](#))
3. **Samanta, S.**; Rajasekhar, K.; Madhu, R.; Murugan, N. A.; Alam, S.; Shah, D.; Clement, J. P.; Govindaraju, T. Naphthalene monoimide derivative ameliorates amyloid burden and cognitive decline in a transgenic mouse model of Alzheimer's disease. *Adv. Therap.* **2021**, 2000225. (*BioRxiv*, 2020, doi: <https://doi.org/10.1101/2020.08.20.260166>.)
4. Rajasekhar, K.; **Samanta, S.**; Bagoband, V.; Murugan, N. A.; Govindaraju, T. Antioxidant berberine-derivative inhibits multifaceted amyloid toxicity. *iScience*, **2020**, 101005.
5. Datta, L. P.; **Samanta, S.**; Govindaraju, T. Polyampholyte-based synthetic chaperone modulate amyloid aggregation and lithium delivery. *ACS Chem. Neurosci.* **2020**, *11*, 18, 2812–2826.
6. Maity, B., **Samanta, S.**, Sarkar, S., Alam, S., Govindaraju, T. Injectable silk fibroin-based hydrogel for sustained insulin delivery in diabetic rats. *ACS Appl. Bio Mater.* **2020**, *3*, 3544–3552.
7. Ghosh, D.; **Samanta, S.**, Govindaraju, T. Dihydrophthalazinediones accelerate amyloid β peptide aggregation to nontoxic species *Bull. Mater. Sci.* **2020**. doi.org/10.1007/s12034-020-02223-2.
8. Kumar, A.⁺; Datta, L. P.⁺; **Samanta, S.**⁺; Govindaraju, T. Benzothiazole-phenothiazine Conjugate Based Molecular Probe for the Differential Detection of Glycated Albumin. *Isr. J. Chem.* **2021**, *61*, 1–10.

❖ Patents

1. Govindaraju, T.; Maity, B.; and **Samanta, S.** TEMP/E- 1/16027/2020-CHE.
2. Govindaraju, T.; Rajasekhar, K.; and **Samanta, S.** E-45/11310/2020/CHE.

❖ **Unpublished Works**

- **Samanta, S.**; Govindaraju, T. Differential microenvironment of Cu^{II} in A β oligomers and matured fibrils dictates their toxicity. (To be submitted)
- Maity, B.; **Samanta, S.**; Alam, S.; Sarkar, S.; Govindaraju, T. Antioxidant silk fibroin-melanin hydrogel composition for wound healing in diabetic rats. (To be submitted)
- Ghosh, D.; Konar, M.; **Samanta, S.**; Govindaraju, T. Remodelling of amyloid aggregation by CDP-peptidomimetic inhibitors. (To be submitted)
- Madhu, R.; **Samanta, S.**; Balachandra, C.; Govindaraju, T. Small molecule ameliorates multifaceted amyloid toxicity in Alzheimer's disease. (To be submitted)
- Mondal, T.; **Samanta, S.**; Govindaraju, T. Deciphering amino acid code and sequence in the modulation of protein amyloidogenicity. (To be submitted)

❖ **Book Chapters**

- **Samanta, S.**; Madhu, R.; Govindaraju, T. Alzheimer's is a multifactorial disease. (To be submitted)
- Madhu, R.; **Samanta, S.**; Govindaraju, T. Multiplexed and multimodal strategies for diagnosis of Alzheimer's disease. (To be submitted)
- Mondal, T.; **Samanta, S.**; Kumar, A.; Govindaraju, T. Multifunctional inhibitors of multifaceted A β toxicity of Alzheimer's disease. (To be submitted)
- **Samanta, S.**; Kumar, A.; Govindaraju, T. Gut microbiome and Alzheimer's disease. (To be submitted)

About the Author



The author, **Mr. Sourav Samanta**, was born on May 1st, 1991, at Natibpur, West Bengal, India. After his initial schooling at Natibpur Bhudeb Vidyalaya, he obtained his Bachelor degree in Chemistry in 2013 from Bangabasi College under Calcutta University, India. He obtained his Master Degree in Chemistry in 2015 from the Department of Chemistry, Indian Institute of Technology (IIT), Guwahati, Assam, India. He joined the New Chemistry Unit (NCU), Jawaharlal Nehru Centre for Advanced Scientific Research (JNCASR), Bangalore, India, for the PhD program in August 2015 under the guidance of Prof. T. Govindaraju. Currently, he is pursuing his PhD under the supervision of Prof. T. Govindaraju at JNCASR.